Title
Fundamental Study of Nanoparticle Effects on Functional Properties of Metals

Author
Pan, Shuaihang

Publication Date
2021

Peer reviewed|Thesis/dissertation

UNIVERSITY OF CALIFORNIA

Los Angeles

Fundamental Study of Nanoparticle Effects on Functional Properties of Metals

A dissertation submitted in partial satisfaction of the

requirements for the degree Doctor of Philosophy

in Mechanical Engineering

by

Shuaihang Pan

2021

ABSTRACT OF THE DISSERTATION

Fundamental Studies of Nanoparticle Effects on Functional Properties of Metals

by

Shuaihang Pan

Doctor of Philosophy in Mechanical Engineering

University of California, Los Angeles, 2021

Professor Xiaochun Li, Chair

The objective of this study is to provide insights and guidance for the rational design of high-performance metal matrix nanocomposites (MMNCs) with tunable functional properties for widespread applications. Microstructure-property relationship is a long-term focus for MMNCs, and incorporation of different nanoparticles would change these properties differently. Since the metals/alloys are unique with their high electron concentration and strongly coupled interaction between electrons and other configurational (micro-)structures, introducing nanoparticles into them will significantly influence electrical, thermal, chemical, and electrochemical properties. Given the various demands from industrial fields, MMNCs with predictable and reliable functional properties are urgently needed.

However, there still exist significant challenges in utilizing optimal functional properties with a suitable combination of metals/alloys and nanoparticles. Several reasons contribute to the

deadlock situations: First, the supreme functional properties would limit the selection of nanoparticles, but specific desired nanoparticles may be hard to fabricate, incorporate, and uniformly disperse in metals/alloys. Second, due to the lack of studies into nanoparticles-affected functional properties, the relationships between microstructures, processing routes, and final performance are too complicated to be determined. Therefore, though mechanical properties have been studied for decades, the lack of functional performance study hinders the use of metal matrix nanocomposites.

In this dissertation, a wide variety of MMNCs with a rational selection of nanoparticles were fabricated both *in situ* and *ex situ* to experimentally study the nanoparticle effects on their functional properties. Electrical, thermal, chemical (mainly anti-oxidation), electrochemical, and other selective functional properties (mainly tribological performance) were studied. The underlying mechanisms and (semi-)quantitative models have been investigated and developed to reveal nanoparticles' role in tuning these properties, providing insightful guidelines for the rational design of high-performance MMNCs.

The metal matrices in MMNCs are full of free electrons, and the high concentration of electrons is the most crucial factor to determine the electrical performance and other functional properties in MMNCs. In this study, the electrical performance of MMNCs fabricated by both *in situ* and *ex situ* methods have been investigated. Both Cu and Al alloys as the highly conductive matrices have been studied, and the metal-like ceramic nanoparticles such as WC, TiC, TiB_2, and ZrB_2 were used. First, the electron performance was measured with large temperature scanning on physical property measurement system (PPMS), and the role of the electron concentration and the electron diffusivity have been decoupled in the MMNC system. The experiments demonstrated that the reduced electrical conductivity is associated with a reduced electron concentration by the

interfacial electron localization. Second, with the understanding of the reduced apparent free electron concentration in MMNCs, a quantitative model was developed to depict the electrical conductivity change after the nanoparticle incorporation, and the feasibility of this model has been confirmed in Cu- and Al-based MMNC systems. This part of the study illustrates the fundamental role of the matrix-nanoparticle interface and explain the quantitative influences of the interfaces on the electronic parameters related to electrical conductivity. The developed model to predict electrical conductivity is necessary for the MMNC applications in electronic sectors.

With this understanding, since electrons are the dual carrier for both electricity and heat, the thermal performance of the MMNCs has been systematically investigated. In this study, *ex situ* nanocomposites of Cu alloy (i.e., Cu-Ag/WC) and *in situ* nanocomposites of Al (i.e., Al-TiC, Al-TiB_2, and Al-ZrB_2) were the primary focus. With the detailed microstructure investigation, matrix-nanoparticle interfacial characterization, and thermal parameter analyses, the influence of nanoparticles on the thermal performance of metal matrix nanocomposites has been clarified. The changes in heat capacity (by differential scanning calorimetry), thermal diffusivity (by laser flash method), and thermal conductivity have been decoupled. The contribution from electronic and phonic thermal transport has been compared. This part of the study confirms the electron behavior change by nanoparticles. It illustrates a semi-quantitative relationship and close links between the investigated electronic and thermal properties in MMNCs. The analyzed systems (i.e., Cu and Al nanocomposites) would be critical to rational design and applications of MMNCs in thermal management fields.

Similarly, due to the high concentration of electrons of metal matrices and their relatively high activity, even with the conductive ceramic nanoparticles, it is of interest to investigate how metal matrix nanocomposites respond to environments. Oxidation and corrosion are the two

primary degradation forms of metals in the environment, potentially compromising their service life and significantly limiting their applications in various conditions. This part of the study would be divided into two sections accordingly: Firstly, how the high-temperature oxidation process is influenced and how the temperature-dependent stability is tuned by nanoparticles have been investigated. Quantitative information about the thermal oxidation in Cu-based (i.e., Cu-40 wt.% Zn/WC) and Al-based (i.e., Al/ZrB_2) nanocomposites have been obtained via *ex situ* and *in situ* (mainly *in situ* XRD) measurement methods. Two distinctive oxidation layer growth modes (e.g., continuous growth in Cu-40 wt.% Zn/WC and self-limiting growth in Al/ZrB_2 nanocomposites) have been identified, respectively. The thermal oxidation kinetics and dynamics in MMNCs have also been clarified. The interactions among nanoparticles, microstructures, and oxidation driving force have been studied, and the potential applications and effective prevention measures have also been proposed. Second, metal corrosion is a process associated with electron transfer and ion transport. During the process, corroded by-products (mainly oxides and hydro-oxides) will appear on the metal surface as a protection layer. Therefore, to understand the corrosion performance in MMNCs, the electron behavior and oxide growth were integrated. In this part of the study, aluminum alloy 7075 and A206 nanocomposites (i.e., wrought AA7075-TiB_2 and AA7075-TiC as well as cast A206-TiC) were the main focus. During the experiments, the corrosion processes on the freshly exposed surface, passivated surface (with oxide layer), and passivated and then immersed surface (after being pitted) were compared, and their corrosion dynamical characteristics have been depicted with polarization potential scanning and electrochemical impedance scanning (EIS). Different corrosion performances, including pitting, intergranular corrosion, and stress crack corrosion, have been investigated under ASTM standards. The interplay between microstructures, oxidation, and corrosion has been quantitatively studied. In short, the corrosion

study of Al nanocomposites has advanced the understanding of the corrosive degradation process. It would also fundamentally shed light on possible measures of promoting the overall anti-corrosion performance in MMNCs.

Moreover, given other essential applications of MMNCs, other functional properties linked with tribological and manufacturing fields have been investigated.

In summary, this dissertation's extensive experimental studies have provided a useful fundamental understanding of the promising and tunable functional properties in various MMNCs. The starting point of electron behavior has created a unique angle to look into these functional properties by linking microstructures, electrons, and incorporated nanoparticles. Then, thermal properties, anti-oxidation performance, and anti-corrosion performance have been systematically studied, and the (semi-)quantitative models have been developed. Finally, tribological properties have been studied. This study advances the knowledge for rational design and manufacturing of high-performance MMNCs with desirable predictable functional properties for numerous applications.

The dissertation of Shuaihang Pan is approved.

Ajit Mal

John Hopkins

Yongje Hu

Xiaochun Li, Committee Chair

University of California, Los Angeles

2021

Dedicated to my parents and the beloved ones for their unconditional love and support.

TABLE OF CONTENTS

ACKNOWLEDGEMENTS

I would like to thank my advisor Prof. Xiaochun Li for his continuous support and guidance on my Ph.D. journey. It would be impossible for me to go through the Ph.D. study successfully without his patience and motivation. His advice encouraged me all the time. I am grateful to have the opportunity to investigate the exciting novel functional properties in nanoparticle-reinforced metals, which builds up my research attitudes and prepares me for my future career.

Besides my advisor, I would like to acknowledge the rest of my doctoral committee: Professors Ajit Mal, John Hopkins, and Yongje Hu, for their valuable inputs and insightful comments. Their knowledge and kindness help build my strengths and personalities during the Ph.D. study.

My sincere thanks also go to my colleagues in the lab. I must especially thank Drs. Chezheng Cao, Ting Chiang Lin, Zeyi Guan, Gongcheng Yao, Maximilian Sokoluk, and Abdolreza Javadi for their selfless help, useful guidance, and insightful discussions. Without their precious support, it would not have been possible to conduct this research well. I also must thank all my beloved supportive friends including Dr. Kaiyuan Jin, Tianlu Wang, and Haolun Chu from China and USA. Their unreserved care and help during my hard times are much appreciated. I am grateful to have all of them as good friends and excellent collaborators.

Finally, I must express my deepest gratitude to my parents for supporting me spiritually throughout the five-year Ph.D. journey and my life. Without their generous support and genuine understanding, I could not have achieved what I have done during these years.

VITA

2016-2021, Ph.D., Mechanical and Aerospace Engineering, UCLA, US

2012-2016, B.S., Mechanical Engineering, Shanghai Jiao Tong University, Shanghai, China

JOURNAL PAPERS

1. **Pan, S.**, Zheng, T., Yao, G., De Rosa, I., Li, X.* (2021): High-strength and high-conductivity in situ Cu-TiB_2 nanocomposites. *Materials Science and Engineering: A Structural Materials: Properties, Microstructure and Processing*.
2. **Pan, S.**, Zheng, T., Yuan, J., Li, X.* (2021): TiB_2 nanoparticle-regulated coupled oxidation behavior in aluminum alloy 7075. *Corrosion Science*.
3. **Pan, S.**, Yuan, J., Zheng, T., She, Z., Li, X.* (2021): Interfacial thermal conductance of in situ aluminum-matrix nanocomposites. *Journal of Materials Science*.
4. **Pan, S.**, Guan, Z., Yao, G., Yuan, J., Li, X.* (2020): Mo-enhanced chemical stability of TiC nanoparticles in molten Al. *Journal of Alloys and Compounds*.
5. **Pan, S.**, Guan, Z., Li, X.* (2020): Unusual Thermal Performance in Cu-60Ag by WC Nanoparticles. *Materials Science and Engineering: B Solid-State Materials for Advanced Technology*.
6. **Pan, S.**, Saso, T., Yu, N., Sokoluk, M., Yao, G., Umehara, N., Li, X.* (2020): New study on tribological performance of AA7075-TiB_2 nanocomposites. *Tribology International*, *152*, 106565.
7. **Pan, S.**, Yao, G., Guan, Z., Yu, N., Sokoluk, M., Li, X.* (2020). Kinetics and dynamics of surface thermal oxidation in Al-ZrB_2 nanocomposites. *Corrosion Science*, *176*, 108890.
8. **Pan, S.**, Yuan, J., Zhang, P., Sokoluk, M., Yao, G., Li, X.* (2020): Effect of electron concentration on electrical conductivity in in situ Al-TiB_2 nanocomposites. *Applied Physics Letters*, *116*(1), 014102.
9. **Pan, S.**, Yao, G., Sokoluk, M., Guan, Z., Li, X.* (2019): Enhanced thermal stability in Cu-40 wt% Zn/WC nanocomposite. *Materials & Design*, *180*, 107964.
10. **Pan, S.**, Sokoluk, M., Cao, C., Guan, Z., Li, X.* (2019): Facile fabrication and enhanced properties of Cu-40 wt% Zn/WC nanocomposite. *Journal of Alloys and Compounds*, *784*, 237-243.
11. **Pan, S.**, Guan, Z., Yao, G., Cao, C., Li, X.* (2019): Study on electrical behavior of copper and its alloys containing dispersed nanoparticles. *Current Applied Physics*, *19*(4), 452-457.
12. **Pan, S.**, Yao, G., Yuan, J., Sokoluk, M., Li, X.* (2020): Manufacturing of Bulk Al-12Zn-3.7 Mg-1Cu Alloy with TiC Nanoparticles. *Procedia Manufacturing*, *48*, 325-331.

13. **Pan, S.**, Yao, G., Yuan, J., Li, X.* (2019): Electrical Performance of Bulk Al–ZrB_2 Nanocomposites from 2 K to 300 K. In *Nanocomposites VI: Nanoscience and Nanotechnology in Advanced Composites* (pp. 63-70). Springer, Cham.
14. **Pan, S.**, Yao, G., Liu, J., Li, X.* (2019): Effect of Hot Rolling on Naval Brass/WC Nanocomposite. *Procedia Manufacturing*, *34*, 193-196.

PATENT

1. Li, X., Cao, C., Yao, G., **Pan, S.** (2020): Scalable manufacturing of copper nanocomposites with unusual properties. (WO Patent No. WO2020102539A1. International Application No. PCT/US2019/061485)

CHAPTER 1 INTRODUCTION

1.1 Background and motivation

Recently, metal matrix nanocomposites have emerged as a novel class of materials with tunable properties for various applications. After the long-standing problem of nanoparticle dispersion in metals/alloys was tackled [1], MMNCs now start to yield a considerable impact in practical applications, including electrical conductors [2], thermal management materials [3], and environmental service structural materials [4]. Since the nanoparticle incorporation into metal matrices already demonstrates advantageous mechanical strengthening effects [1], the combination with other tunable functional properties could open up more promising applications for MMNCs. For example, Cu- and Al-based MMNCs are expected to provide the next generation of electrical wires due to its enhanced mechanical properties and reasonable electrical conductivity [5].

The current selection of MMNCs depends on the empirically experimental results to determine their functional performance, and the suitable MMNC system for a specific application scenario relies heavily on trial-and-error. As a result, this inevitably adds to unpredictability in MMNCs functional properties. Several intrinsic and long-standing reasons are responsible for the dilemma of using MMNCs: First, the properties of metals/alloys would be significantly influenced by the manufacturing and processing techniques [6–8], which makes the predictable functional properties in MMNCs complicated. Second, though the mechanical properties and strengthening effects in MMNCs are mainly related to microstructure (e.g., modified secondary phase, tuned interface characteristics) and nanoparticle-defect interactions[9,10], the functional properties are also associated with the high concentration of free electrons in metals/alloys. In this case, understanding their functional properties and performances requires another degree of freedom from electrons. This requirement will result in a complex new angle to investigate the interplay between electrons

and nanoparticles. Last but not least, previous studies barely provided systematic discussion and analyses into the functional properties of MMNCs, and the obtained functional property data are scattered. For instance, even the nanoparticle volume dependence of these properties is not clear yet.

Since the recent applications of MMNCs require more balanced electrical conductivity, good thermal conductivity [11–13], supreme thermal stability [14], and outstanding anti-corrosion performance [4], it is urgently needed to examine these functional properties systematically and investigate the microscopic interaction among electron, microstructure, defects, and nanoparticle to develop predictable models of accurately depicting these functional properties quantitatively. Given the increasing diversity of the MMNCs, a more fundamental understanding, instead of mere phenomenology and experimental observation, is required to obtain the complete image of the coupled interaction among these multi-scale features for changed functional properties. Therefore, there is a great opportunity to acquire the knowledge of the nanoparticle effects on these functional properties and understand how to quantify the nanoparticle effects on these properties. This dissertation could provide us insights and guidance on how to understand and predict the tuned functional properties in MMNCs by the incorporation of nanoparticles, possibly broadening their application space and extending their potentials.

1.2 Research objectives

This study is to study the essential functional properties of MMNCs experimentally, systematically analyze their relationships with lattice microstructures, electrons (as well as their electronic properties), and defects, and scientifically understand their interactions for an accurate prediction of these properties. The fundamental understanding gained through this study will

provide irreplaceable insights and guidance for the rational design of high-performance MMNCs for various applications. More specifically, this study will start with investigating the electronic properties to clarify the electron behavior in MMNCs. Then, thermal performance will be studied to confirm the role of electrons in tuning the transportation properties and charateristics of MMNCs. After integrating electrons to understand the nanoparticle's interaction in MMNCs, the anti-oxidation and anti-corrosion performance of MMNCs will be discussed coherently. The engineering performance evaluation and microscopic fundamentals to understand the oxidation- and corrosion-resistance in MMNCs will be provided, and the characterization from microstructures, nanoparticles, and electrons will be used to support the understanding. Meanwhile, other properties like tribological performance will also be examined.

1.3 Work summary

The remaining chapters of this dissertation include

- Chapter 2 reviews the state of art into functional properties of MMNCs.
- Chapter 3 conducts ex situ and in situ fabrication/synthesis for MMNCs.
- Chapter 4 presents electrical and thermal properties of MMNCs.
- Chapter 5 demonstrates the general chemical stability (including oxidation- and corrosion-resistance) tuned by nanoparticles.
- Chapter 6 explores tribological properties in selective MMNCs.
- Chapter 7 draws conclusions.
- Chapter 8 provides the recommendation for future work

CHAPTER 2 LITERATURE REVIEW

2.1 Nanoparticle-reinforced metals

Nanocomposite materials refer to the systems with two or more different phases [15], which could provide distinct properties. For metal matrix nanocomposites (MMNCs), the matrix is usually metallic alloy, whereas the incorporated particles are normally inactive stable nanoscale phases (mainly ceramics like oxides [10,16], nitrides [17], carbides [18–21], silicides [22], and borides[23]). The major difference between MMNCs and alloys with nanoscale secondary phases is that the reinforcement phases in MMNCs are not generated via the dynamic interaction with the matrix and thus could hardly be predicted by the phase diagram [24]. With this definition, alloys themselves (e.g., AA7075 at T6 heat treatment state with the precipitated secondary phases [25,26]) are considered "matrix" in our study [25].

Currently, numerous material systems with different matrices and reinforced nanophases have been intensively investigated. The metallic matrices of copper [27,28], aluminum [29,30], iron [31], magnesium [32–34], zinc [35], and titanium [15,36] are among the most studied systems, and the used nano-reinforcements include particles, fibers, laminates, and so on. Due to the wide freedom of selection and mixture, these nanocomposite materials have been used in the various fields of automobile, aerospace, biomedical, and architecture industries.

With the huge needs of the MMNCs, different fabrication and manufacturing methods have been developed accordingly to guarantee the quality and performance of MMNCs. In general, the nanoparticle incorporation process could be divided into 2 categories: *ex situ* and *in situ* methods. *Ex situ* methods could provide more controllable incorporation process with potentially higher MMNC purity and more uniform size distribution, but the intrinsic limitations from materials' wettability and reactivity may limit the ex situ nanoparticles' dispersion. Comparatively, *in situ*

fabricated nanoparticles could have a smaller nanoparticle size (though the uniformity may not be guaranteed) and may potentially achieve a better distribution in the matrices [37]. The *in situ* process would be highly dependent on the thermodyamical processes [37], and the the synthesis of these nanophases usually require high temperature and reactive raw materials (e.g., KBF_4 and K_2TiF_6 for TiB_2 *in situ* synthesis in Al, or activated Ti and B for TiB_2 *in situ* synthesis in Cu) [2,23,37], which make the post-processing for purity and performance essential.

After the MMNCs are fabricated, most research focuses on the strengthening effects of the incorporated nano-reinforcements. To obtain satisfactory mechanical properties, the following strengthening mechanisms in MMNCs are normally applied, namely Orowan strengthening, dislocation interaction strengthening (by the coefficient of thermal expansion mismatch, i.e., CTE mismatch), load-bearing transfer, and Hall-Patch strengthening effect.

For Orowan strengthening, the spatial distance of nanoparticles is an important factor because it determines the resistance to the movement of dislocations [38]. Previous studies have already confirmed that uniformly dispersed dense nanoparticles with a size of ~10-100 nm could remarkably promote the matrix's mechanical properties. The Orowan strengthening effect is usually depicted with the relationship of [38–41]:

Eq. 2 - 1

$$\Delta\sigma_{Orowan} = \frac{0.13 G_m b}{\lambda} ln \frac{r}{b}$$

where r is the particle radius, and λ is the characteristic particle interspacing related to the nanoparticle volume fraction in the matrix. d_p denotes particle diameter, b the Burger's vector, and G the matrix shear modulus.

CTE mismatch strengthening requires the formation of the geometrically necessary dislocations (GNDs) during the temperature-specific processing. The mismatch of the CTEs

between matrices and nanophases will increase dislocation density and strengthen the materials by the description of [40–42]:

Eq. 2 - 2 $$\Delta\sigma_{CTE} = \sqrt{3}\beta Gb\sqrt{\frac{12\Delta\alpha\Delta TV_p}{bd_p}}$$

where $\Delta\alpha$ indicates the difference of the CTE. ΔT is the temperature difference between the testing and processing temperature. When the nanoparticles are too small to accommodate these GNDs, there are no enough strain can be generated and thus the CTE mismatch might be neglected [1].

Load bearing transfer would enhance the mechanical properties of MMNCs by the interfacial bonding between matrices and nano-reinforcement. The advantageous interface will help transfer the applied external loads from the soft matrix to the stronger nanoparticles [34]. Therefore, the nanoparticle size (as well as the interfacial coherency) would determine the load bearing strengthening effects [43]. Semi-quantitatively, the load bearing efficiency could be estimated with [40,41]:

Eq. 2 - 3 $$\Delta\sigma_{Load} = 1.5V_p\sigma_m$$

where V_p is the volume fraction of particles and σ_m is the original yield strength of matrix.

Additionally, as defined above, the nanophases in MMNCs are comparatively more stable and harder. Thus, when the solidification processing is used for MMNCs, the molten matrix could preferably nucleate on the nanophases, and the effective heterogeneous nucleation would be favorable for refined grain sizes; besides, during the processing of MMNCs, these nanophases could act as the pinning points which could stop or inhibit the grain growth (e.g, during recrystallization and heat treatment). With these phenomena refining the grains in MMNCs, the strengthen effect could be enabled by the equation [40,42]:

Eq. 2 - 4 $$\Delta\sigma_{H-P} = k_{H-P}\left(d_{MMNC}^{-\frac{1}{2}}\right) - k_{H-P}(d_m^{-\frac{1}{2}})$$

where k_{H-P} is the strengthening coefficient. Here, d_m is the average grain size of matrix without nanoparticles, and d_{MMNC} the average grain size of matrix after incorporating nanoparticles.

As shown in the abovementioned strengthening mechanisms, nanoparticles in the MMNCs will interact with the matrix, form the effective interfaces, influence the dislocation behavior, and change the systems' microstructure. Since these micro/nano-scale structures are also closely interacting with the high-concentration electrons in the MMNCs, the functional properties are inevitably influenced, and the dilemma between the enhanced mechanical properties and the tuned or even deteriorated functional properties needs to be resolved (as shown in **Figure 2 - 1**). Current research concerning MMNCs' functional properties will be reviewed in the following sections of the dissertation.

2.2 Effects of nanoparticles on electrical and thermal properties of metals

As mentioned in section 2.1, the strengthening interactions by nanoparticles will have non-negligible effects on the electron behavior (see **Figure 2 - 1**), and the electron behavior along with other microstructural/configurational factors would determine the functional properties as a result. The simplest case would be the tuned electrical and thermal properties, because the affected electrons directly control these performances.

2.2.1 Electrical properties in metal matrix nanocomposites

Electrical performance of MMNCs is mainly gauged by electrical conductivity. The supreme electrical conductivity in metals/alloys is owing to the high carrier density and the large carrier mobility and diffusivity, with no band gap requiring thermal or other activations.

With nanoparticle incorporation, the nanoparticles size [44], volume fraction [45], nanoparticle characteristics [46], and interfacial bonding [23,45] would greatly influence the MMNC's electrical properties. Except for the incorporation of reinforcement materials with higher electrical conductivity (e.g., graphene [47] and CNT [48]), the electrical performance will usually be deteriorated. For example, current studies agree that nanoparticles with over 1 vol.% decrease electrical conductivity by imposing multiple scattering effects and shortening the mean free path (MFP) of electrons [47,49] (as shown in **Figure 2 - 1**). The fundamental reason behind the synergic effect of the concentration, geometry, size, and type of nanoparticles on the electrical conductivity is complicated and not well understood.

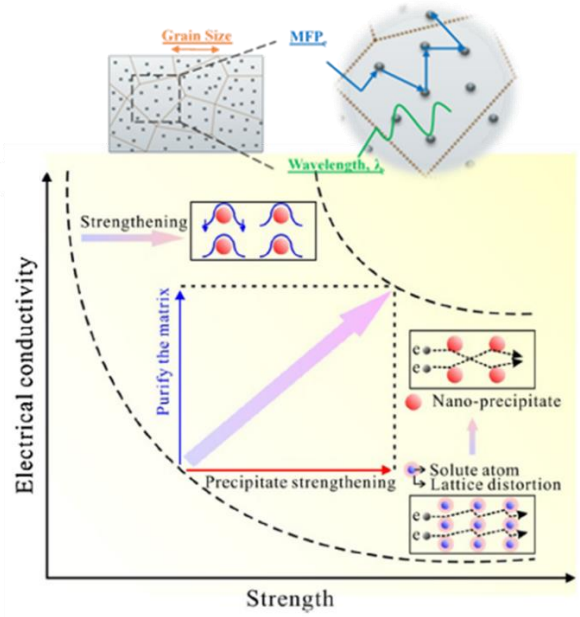

Figure 2 - 1 Illustration of electron scattering mechanism in MMNCs and the dilemma between high electrical conductivity and high strength in MMNCs [50].

Currently, two common methods are used to study the electrical conductivity of MMNCs: First, the Effective Medium Theory (EMT) is used to predict the electrical conductivity of MMNCs macroscopically with no need of any detailed microscopic electronic and structural information [51–

[53]. Second, via Matthiessen's law, the respective electrical resistivity contributions by grain boundaries and dislocations [27,53,54] are considered to be additive. While the method provides a better understanding microscopically, it usually depends on indirect electrical analyses from mechanical/configurational information. As nanoparticles create barriers to electron movement, an experimental study is much needed to gauge the electron behavior directly.

Furthermore, although existing theories and models are developed to understand electrical conductivity in MMNCs, few are broad enough to be applied to different systems. For example, in *in situ* Al-TiC, Al-TiB_2, Cu-Y_2O_3, and Cu-Al_2O_3 nanocomposites, electrical conductivities are far lower than theoretical prediction (by EMT, etc.), some even with a mismatch of up to ~50% [55,56]. Some studies reported that refined phases may recover certain electrical conductivity, if the metal/alloy compositions are dynamically evolving during processing [23,57]. More importantly, theoretical models are well established to determine the electrical properties of a composite material when a second phase dispersed in a metal matrix is at atomic scale (e.g., <<10 nm such as solid solutions) or at microscale (e.g., >>100 nm such as porosity or impurity). However, few models explore the influences if the second phase is at a size around 100 nm (e.g., nanoparticles) [58]. It is thus of significance to study how nanoparticles affect the electrical behaviour of metals.

All these cases demonstrate the complexity of electrical conductivity, due to the high and sensitive intrinsic carrier density in metal/alloy systems and the difficulty in directly analyzing their electronic properties in a wide temperature range.

2.2.2 Thermal properties in metal matrix nanocomposites

Thermal properties refer to heat capacity, thermal diffusivity, and thermal conductivity, and these three properties are linked by the relationship of:

Eq. 2 - 5 $$k = \alpha \cdot c_p \cdot \rho$$

Where k is the thermal conductivity, α indicates the thermal diffusivity, C_p the heat capacity, and ρ the density.

Microscopically, heat capacity is related to the materials phase and structure, because phonons as the Bosonic coherent lattice vibration responsible for heat transport are heavily influenced by lattice arrangements. Therefore, the microstructure modification in MMNCs could lead to the heat capacity change. Second, since electrons are dual carriers for heat and electricity and belong to Fermions, the tuned electronic properties in MMNCs could simultaneously lead to the heat capacity change, due to the interrupted density of states in nanoparticles, at matrix-nanoparticle interface, and by the introduced defects (as shown in **Figure 2 - 2**). The measurements for heat capacity in MMNCs are usually conducted by differential scanning calorimetry (DSC). For example, Ma et al. have experimentally measured the specific heat capacity of Al_2O_3/Ni nanocomposite with DSC techniques [59].

Similarly, as thermal diffusivity is measuring how rapidly the heat is able to be moved away in the materials, the sensitive phonon and electron thermal transport would be interactive with the incorporated nanoparticles. These coupled interactions in MMNCs will determine their thermal diffusivity (usually within a magnitude of ~10-100 mm^2/s for MMNCs) and thermal conductivity (usually within a magnitude of ~10-100 $W/m \cdot K$ in MMNCs). Current methods for thermal diffusivity measurement relies on flash heating (e.g., laser flash method [60]) to create a heat source and subsequently measure the thermal dissipation speed.

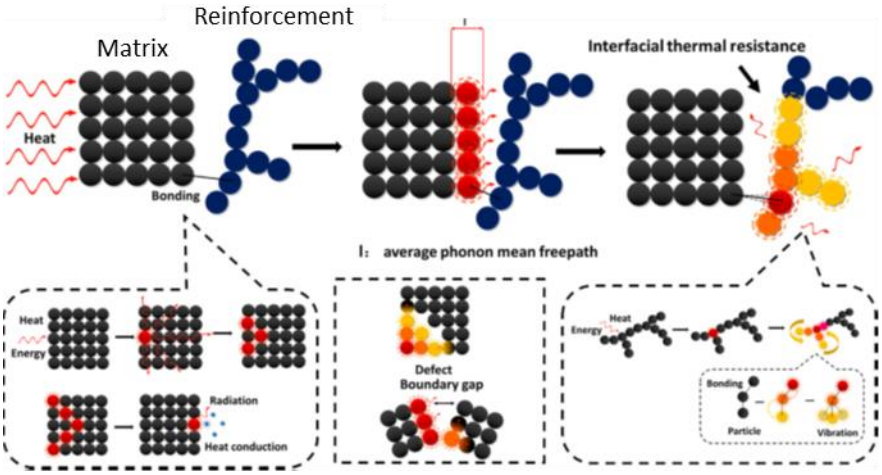

Figure 2 - 2 Illustration of thermal transport mechanism in MMNCs and various thermal transport barriers in MMNCs (the figure is adapted from Ref.[12] and Ref. [61]).

Currently, different models, including the Weiner and Hashin-Shtrikman (HS) bounds, are widely used to depict the thermal conductivities in composite materials [62].

The Weiner and Hashin-Shtrikman models are based on the similar EMT theories for electrical conductivity [12]. Since the Weiner model unrealistically assumes the non-interacting situation by the pure mixture law in composite materials, the HS model is more applicable for predicting the theoretical upper bounds of the thermal conductivity with the consideration of interfacial thermal resistance in composites. According to the HS and Weiner models, to enhance the thermal conductivity in materials, particles with supreme intrinsic thermal properties, such as diamond particles [13,63], graphene [12,64], and carbon nanotubes [65], are normally selected. However, the requirements for reinforcement coating [64,66] and extreme processing techniques [13] to overcome the wettability issues between metal and reinforcement phase [1] are problematic. When more defects, including voids and agglomerations, [67,68] are introduced, thermal transport is further deteriorated [3] and is usually significantly lower than the predicted HS and Weiner upper limits [69].

Recently, metallic ceramics including TiC,[25] WC,[70] TiB_2,[71] etc., have attracted much attention due to their metal-like behavior,[72] reasonable wettability with metals,[22] and high thermal stability[73,74]. Their incorporation into metals can also offer unique electrical and thermal behaviors to the nanocomposites,[75] due to the interaction between electrons, phonons, and other quasi-particles.[2] However, a lack of detailed fundamental understanding of these interactions could limit the rational design of metal matrix nanocomposites for thermal applications.

The difficulties of studying the thermal properties of metal matrix nanocomposites are rooted in the following aspects: first, multiple factors contribute to the altered thermal properties. Researchers have already shown that nanoparticles will affect the heat capacity and thermal diffusivity[76,77]. As interfacial thermal conductance is important for thermal performance, recent studies have also demonstrated that the Debye temperature ratio between metals and metallic ceramics will greatly influence interfacial conductance [78]. Second, as nanoparticles form interfaces with the matrices by severe chemical reactions (e.g., in Al-SiC systems), interfacial thermal conductance must consider the effects of the resulting intermediate layers [79,80]. Most significantly, as the interfacial coupling between electrons and phonons becomes more complicated,[81,82] the interfacial thermal conductance values predicted by the acoustic mismatch model (AMM) and the diffusive mismatch model (DMM) see a huge discrepancy.[82,83] Especially when metallic ceramic nanoparticles are used, electron-electron coupling may also play a role.[84,85] Since electron-electron coupling in heat transport is orders of magnitude more effective than other coupling transport mechanisms, an experimental estimation is still hard to obtain. As a result, many previous studies in metal matrix nanocomposites have used incorrect prediction models or dismissed the electron-electron coupling effects [80,86]. A systematic study on the interfacial thermal conductance between metal/alloy and metallic ceramic nanoparticles is urgently needed.

2.3 Effects of nanoparticles on chemical stability of metals

Unfortunately, in addition to the supreme electrical and thermal conductivity by carrier transportation, high concentration of free electrons in metals and alloys introduces another crucial problem for their long-term applications and service: materials' degradation owing to their high chemical reactivity [87]. With the comparatively high chemical reaction rate in various environments, the metallic system (e.g., the matrices in MMNCs) is sensitive to condition-dependent temperature [88], humidity [89], oxygen level [90], ion attack [91], compositional change [87,92], chemical reaction/element dissolution [92–94], and defects' interaction [95] etc., which could lead to a catastrophic failure.

Given the importantance of anti-oxidation (i.e., high-temperature chemical stability) and anti-corrosion (i.e., chemical instability introduced in corrosive media) performance of metals/alloys in the real industrial applications, the study into these two fields for MMNCs will be reviewed in this section.

2.3.1 Anti-oxidation performance of metal matrix nanocomposites

Anti-oxidation behavior of MMNCs is of great importance because metals/alloys, like Cu-Zn and various Al alloys, are widely used for coatings [96], heat exchangers [97], soldering media [98], catalysts, and solar cell electronics [99]. They will be inevitably exposed to the conditions of high temperature, high humidity, and/or in oxygen-abundant environments [97].

Currently, the metal/alloy oxidation process could be depicted, quantified, and classified by two common models: namely continuous growth mode (in metals and alloys like Cu, Zn) and self-limiting growth mode (in Al and its alloys) [100] (See **Figure 2 - 3** (c)-(f)).

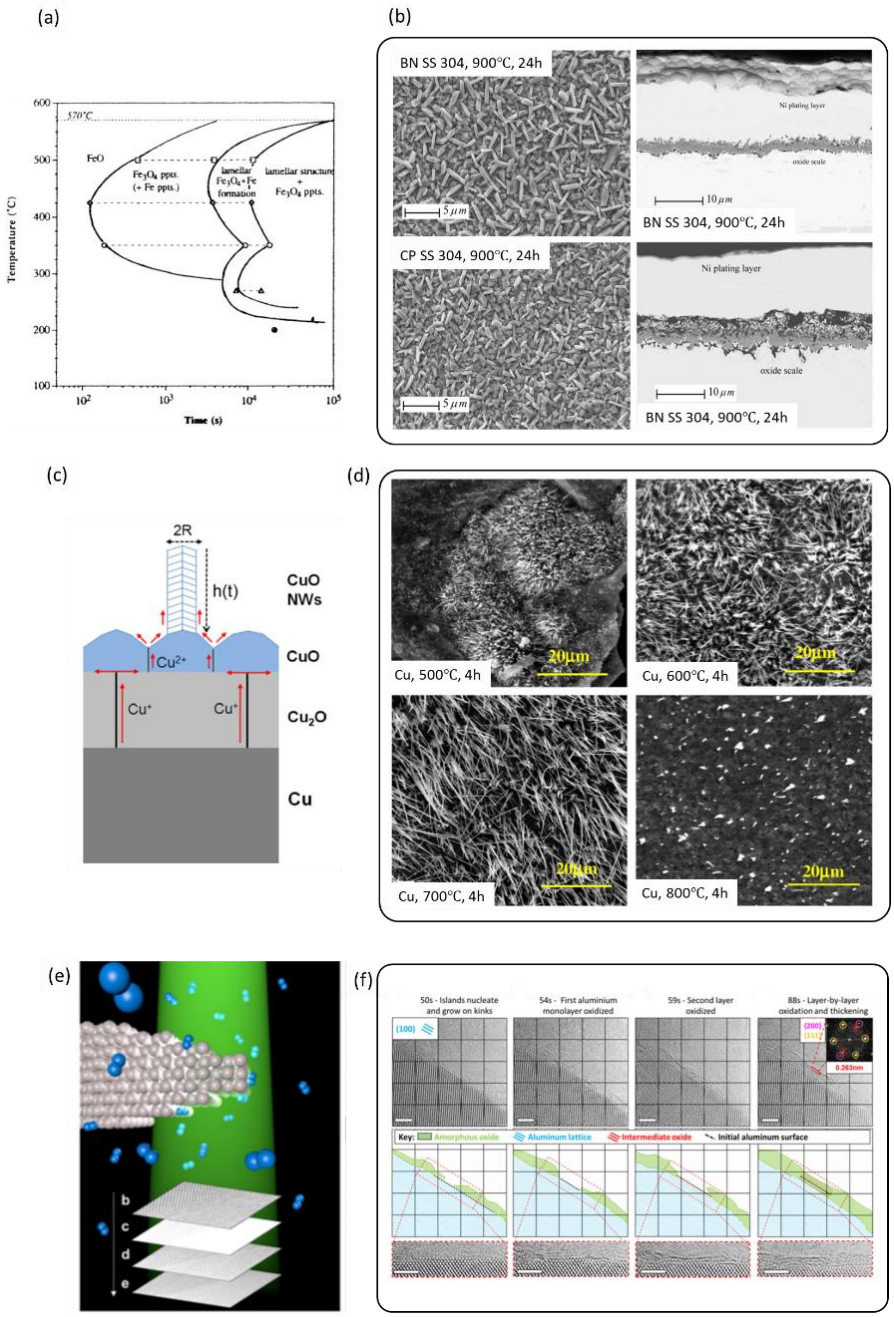

Figure 2 - 3 (a) Phase diagram for the temperature- and time-dependent oxidation behavior in iron system, and (b) oxidized surface morphology for stainless steel [101,102]. (c) Illustration of copper oxidation modes, and (d) temperature-dependent oxidized surface morphology for copper [88,103]. (e) Illustration of in situ measurement for Al oxidation, and (f) the observed alumina growth at Al surface during oxidation [104].

2.3.1.1 Non-limiting oxidation in metal matrix nanocomposites

For the non-limiting oxidation process, regardless of the oxidation layer morphology, the rate-laws will be followed with the general form of [105,106]:

Eq. 2 - 6 $$z^n \cdot \frac{dz}{dt} = k_{oxide}$$

Where z indicates the oxide layer's characteristic thickness, and k_{oxide} the oxidation rate constant. Here, n (usually with a value of $0 \leq n \leq 2$) [105] refers to the different non-stop oxidation modes with the linear, parabolic, and cubic oxidation rate.

For the non-limiting oxidation processes with Cu and Zn alloys, a diffusion-controlled mechanism is accepted as a quantitative description [103] (see **Figure 2 - 3** (c)). The effective diffusion flux responsible for the surface oxidation happens mainly along the grain boundary (GB). It is proportional to the GB diffusivity of the oxidized metallic element, the GB characteristic width, and the local stress gradient along the GB direction [103].

It is known that due to the pushing/capturing effects [107], the incorporated nanoparticles could reside at GBs of MMNCs. Considering the diffusion-controlled mechanism for Cu and Zn alloy oxidation, the anti-oxidation performance of their MMNCs could be potentially enhanced. However, due to the fabrication and manufacturing difficulties, there lack s a systematic study into Cu- and Zn-MMNCs' anti-oxidation performance.

2.3.1.2 Self-limiting oxidation in metal matrix nanocomposites

Self-limiting oxidation in Al is a coin with two sides: Al and its alloys are susceptible to surface oxidation due to their high chemical reactivity [106]. This susceptibility relates closely to the corrosion performance of Al alloys [108] and may induce degradation by a high oxidation rate [109]. Simultaneously, given the stability of the formed oxide Al_2O_3 itself, oxidation is also widely used

for applications in microelectronics and catalysts with high-quality oxide insulators and protection against wear and corrosion. For these applications, the oxidation-introduced Al_2O_3 thickness, morphology, and chemical composition are of great importance.

When it comes to the quantitative understanding of the thermal oxidation process in Al MMNCs, many difficulties regarding the thermal oxidation process of Al systems cannot be neglected. The following reasons contribute to the controversial understanding and unreliable prediction of the Al MMNC thermal oxidation process:

First, Al forms oxides with condition-dependent phases (e.g., amorphous Al_2O_3) and characteristics (e.g., dehydration process from the precursor $Al_2O_3 \cdot xH_2O$) [110–112]. The thermal oxidation process shows completely different mechanisms from other metals like Cu, Zn, and Fe. Previous studies and research on Al thermal oxidation mainly focus on the low-pressure conditions ($P_{O_2} = 10^{-6} \sim 10^{1}$ Pa) [113]. This environment has limits as it has been proved that air pressure will significantly influence the anti-oxidation performance [110,114].

Second, it is confirmed that Al will generate a self-limiting oxidation layer in the low-temperature thermal oxidation process [113]. However, when nanoparticles are incorporated into metal matrices, it is unclear how the anti-oxidation performance is altered.

Based on previous studies, the self-limiting Al oxidation demonstrates a strong surface composition- and oxide layer-dependent characteristics, irrelevant to the GB diffusion mechanism. Therefore, there is a strong need to investigate nanoparticles' role in the oxidation process of Al nanocomposites under air pressure for both high strength and tunable thermal stability.

2.3.2 Anti-corrosion performance of metal matrix nanocomposites

Corrosion in MMNCs would be more complicated than oxidation process, since the involving elements from the environment of O, Cl [91], and H [95], etc. could be more convoluted, and the electrochemical nature of the processes requires a thorough understanding on microstructures, nanoparticles, and electrons [115]. While MMNCs are gaining more interests for their strengthening effects, corrosion related to their mechanical behavior should be understood.

In this part, the review will focus on surface corrosion process and stress corrosion cracking (SCC), respectively. The discussion about surface corrosion considers the interaction between MMNCs and the corrosive environments without mechanical stimuli (e.g., pre-loading) (as shown in **Figure 2 - 4** (a)-(d)). As an important complementary, SCC will consider the anti-corrosion performance with mechanical stress intervention (as shown in **Figure 2 - 4** (d)-(f)). As a summary, the links between surface corrosion and SCC will be drawn to cast light on their close dependence on the microstructures, nanoparticles, and other behavior (electron behavior, oxidation performance, etc.) in MMNCs.

2.3.2.1 Corrosion in metal matrix nanocomposites

Surface corrosion in metals and alloys is happening mainly due to the chemical and electrochemical reactivity in the stimulated corrosive environments. Based on the corrosion conditions, it could happen in basic (pH>8), neutral (pH~6-8), and acidic (pH<6) solution. For example, Al alloys suffer from corrosion in all pH-range solutions, whereas most metals would be much more stable in basic solution than in acidic solution. In our review here and the dissertation research thereafter, the neutral solution corrosion behavior (i.e., in 3.5 wt.% NaCl non-degassed solution) should be our focus, because of its widet industrial applications and interests.

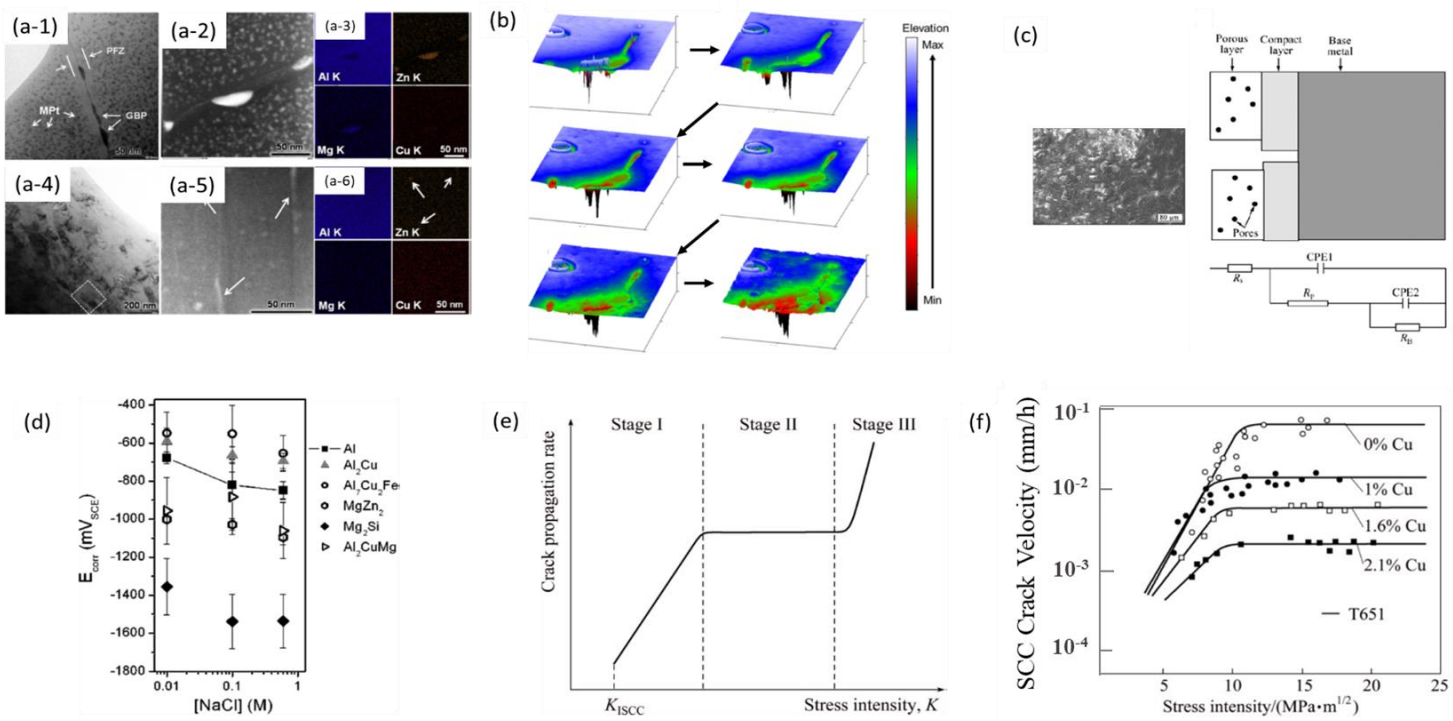

Figure 2 - 4 (a) Characteristic precipitate free zone (PFZ) and grain boundary precipitates (GBPs) in coarse-grain (a-1 to a-3) and nano-grain (a-4 to a-6) AA7075 alloy [94]; (b) Localized corrosion near the precipitates in AA7075 alloy [116]; (c) The characteristic EIS impedance equivalent circuit for the corrosion analysis of micro-arc oxidized AA7075 alloy [117]; (d) Corrosion potential of various precipitates in Al alloys responsible for localized corrosion [118]; (e) The typical SCC stages and the crack propagation speed-stress intensity relationship [92]; and (f) the element/composition (i.e., Cu concentration, here)-dependent SCC behavior in the modified AA7050 (with 6 wt.% Zn and 2 wt.% Mg as basis)-T6 alloy [92].

Surface corrosion itself is also classified into several categories, given its various corrosion forms. It could happen in the forms of non-localized surface electrochemical process (i.e., homogeneous surface corrosion), pitting corrosion (i.e., localized corrosion on specific surface locations), and intergranular corrosion (IGC, namely preferential penetrating corrosion behavior).

For non-localized surface electrochemical processes, it could be hard to realize, because alloying and nanoparticle incorporation would inevitably introduce local compositional, structural,

(**Figure 2 - 4** (a) and (b)) and electrochemical (**Figure 2 - 4** (d)) differences. Thus, pitting corrosion and IGC would be stressed here.

Pitting: Pitting corrosion (See **Figure 2 - 5**) has features of localized corrosion current, which cause a large-cathode but small-anode configuration. The initiation of pitting is usually associated with a ruptured passivation film on the surface [119] and a non-uniform local electrochemical potential (e.g., introduced by inert or active alloying element [120]), which leads to the exposure of easily corroded locations and the sudden increase of the corrosion current during the polarization potentiodynamic scanning (as shown in **Figure 2 - 5**(a)). More severely, the pitting sites could develop into crack initiation spots, which may cause the rapid failure of materials in service (as shown in **Figure 2 - 5** (c)). Generally speaking, pitting corrosion is influenced by the ion concentration (e.g., Cl ion in 3.5 wt.% NaCl solution) [121], pH [121], passivation film characteristics [119] (e.g., oxidation process would change the corrosion potential associated with TiB_2)[122], and microstructures (e.g., grain size, processing/manufacturing history) [120,123–125].

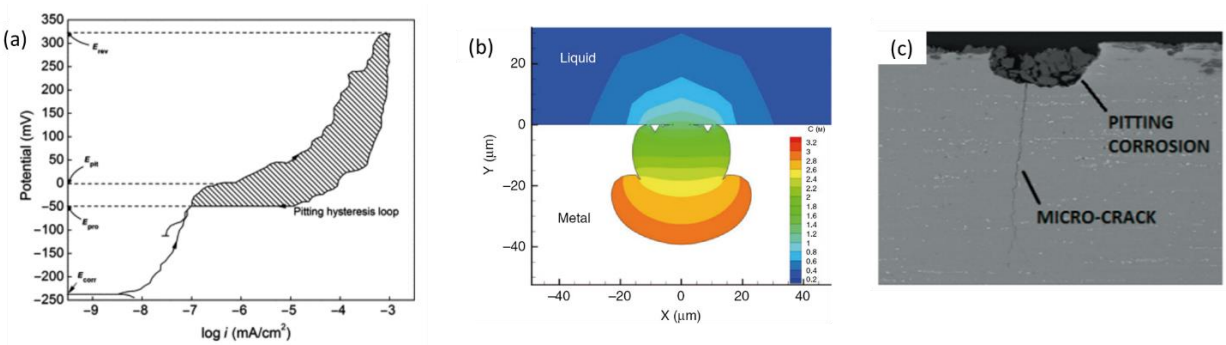

Figure 2 - 5 (a) The characteristic polarization curve showing the pitting corrosion process in materials [126]; (b) the typical current and ion concentration distribution near a pit in pitting corrosion [127]; and (c) Side effects of pitting corrosion like crack initiation in AA7075 alloy.

For MMNCs, after various nanoparticles are introduced into the metal matrices, the grains and secondary phases would be refined [25,128]. Thus, this change of microstructure signatures could

have effects on the pitting corrosion [124]. Moreover, since the nanoparticles are usually metallic ceramics like TiB_2, TiC, and WC, the electrical performance of MMNCs will be changed, and the matrix-nanoparticle interfaces will inevitably influence the electrochemical behavior and vary the pitting initiation locations accordingly. The study on the influence of incorporated nanoparticles on pitting resistance in various metal/alloy systems is urgently needed.

IGC Corrosion IGC corrosion is devastating, because of the rapid preferential attack at the grain boundaries (GB), which leads to the accelerated failure via the corroded GB as corrosion channels. Due to the GB-dependent nature of IGC, though many works have focused on quantifying and modeling IGC processes, [129] the results are far from being satisfactory.

For IGC corrosion, different processing and manufacturing routes would change the GB precipitates (GBP) greatly [130]. The GBPs would dynamically interact with the compositions, chemical natures, and structural features (e.g., PFZ zones by the solute atom depletion [131]) at or near the GB, which would contribute to the altered IGC susceptibility [130], as shown in **Figure 2 - 6**. Second, GB's misorientation angle is also an important factor to be considered for IGC susceptibility [132], because high angle GB (i.e., HAGB) is a preferential channel for corrosion crack propagation. Therefore, tuning the GBPs, minimizing the PFZ, reducing the HAGBs could be effective at suppressing IGC initiation and impede subsequent crack paths.

The IGC susceptibility is the most important factor to promote IGC failures and is determined by a standardized acceleration corrosion test by specific corrosion medium[4] (e.g., with the ASTM standards G100 for AA7075 alloy), as shown in **Figure 2 - 6** (a). This method is useful to determine the comparable engineering values of IGC susceptibility but may blur the microscopic signatures for the IGC initiating processes.

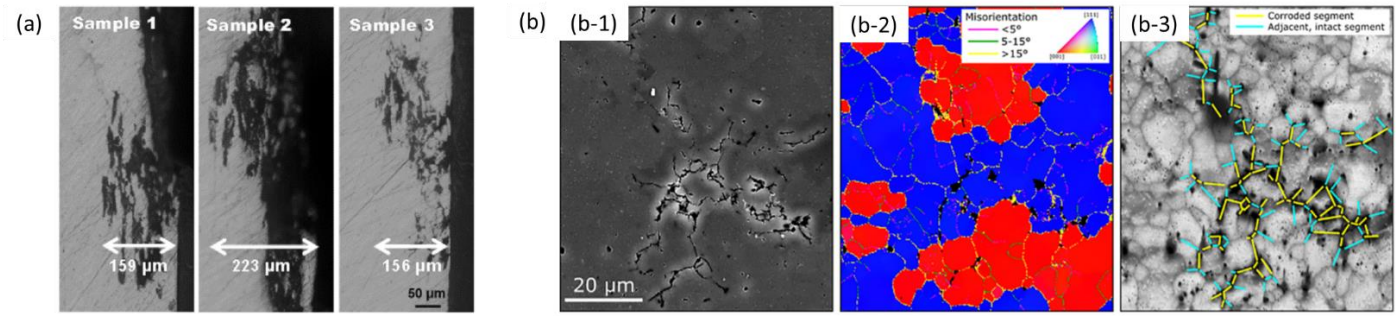

Figure 2 - 6 (a) The characteristic IGC cross-section view for AA7075 alloy [94]; (b) Methodology for statistically analyzing IGC using EBSD in Al-Mg-Si-Cu alloy: (b-1) Shows a secondary electron SEM image after 2 h exposure to the IGC test solution; (b-2) Inverse pole figure map with grain boundaries separated by misorientation angle. (b-3) EBSD image quality map, overlaid with corroded (yellow) and uncorroded (cyan) grain boundary segments [132].

As stated above, the IGC process is also heavily dependent on the GBPs, PFZ, and GB angles, whose influential factors overlap with the pitting corrosion. Thus, when it comes to the source of IGC and the interplaying driving forces in IGC propagation, pitting corrosion could be important in determining the IGC susceptibility. For example, pitting is usually severe near the oxide layer-ruptured area [125]; if these areas overlap with the GB areas, the interchange of corrosion modes between IGC and pitting could be mutually conducive [125]. As shown in **Figure 2 - 6** (b), the IGC paths are surrounded with a high density of pits [132].

Knowing all the factors and corrosion mode interactions, IGC behavior for metals/alloys after nanoparticle incorporation could be tuned due to the following reasons: 1) Microstructure change and structural refinement: Nanoparticle incorporation would usually introduce smaller grain size and more refined secondary phases/precipitates,[25,35] which could be advantageous toward an IGC-resistant composite; 2) Nanoparticles' location: Owing to the solidification kinetics and dynamics, nanoparticles might be pushed to the last solidified areas [107], where the secondary

phases, GBPs, etc. would be the last to nucleate and form. These local areas are often the IGC-weak locations because of the galvanic electromchemical potential difference[133] (depending on the compositional and configurational differences with the main lattices). Once the inert and noble nanoparticles like WC, TiC, and TiB_2 reside densely in these areas, it could provide a tougher corroded path, altered corrosion potential, and mitigated localized difference, all of which will be important in determining the ultimate IGC-resistance; 3) Passivation ability: As stated in **Section 2.3.1**, oxide layer characteristics and oxidation process might be influenced by nanoparticle incorporation. Since IGC initiation is inter-dependent on pitting evolution, the passivation film may serve as an effective barrier for anti-IGC performance [92], and the effects by the incorporation of nanoparticles into metals and alloys could be significant.

2.3.2.2 Stress corrosion cracking in metal matrix nanocomposites

SCC needs to be addressed with extra care, because its evolution is the consequence from both electrochemical interactions (e.g., corrosion, pitting, and IGC) and mechanical interruption (i.e., by stress, as shown in **Figure 2 - 7**). Given the corrosion nature of this process, its propagation and failure are similarly relying on variables like alloy composition,[109] ageing condition,[134] and subsequent microstructure changes [135], as shown in **Figure 2 - 7** (a)-(c). Due to the complex nature of the SCC, here, we limit our discussion to the alloy system of Al alloys (mainly 7xxx-series alloys with Al-Zn-Mg-Cu compositions and cast aluminum alloy A206 with Al-Cu as the main composition) in aqueous chloride solutions (e.g. 3.5 wt.% NaCl solution).

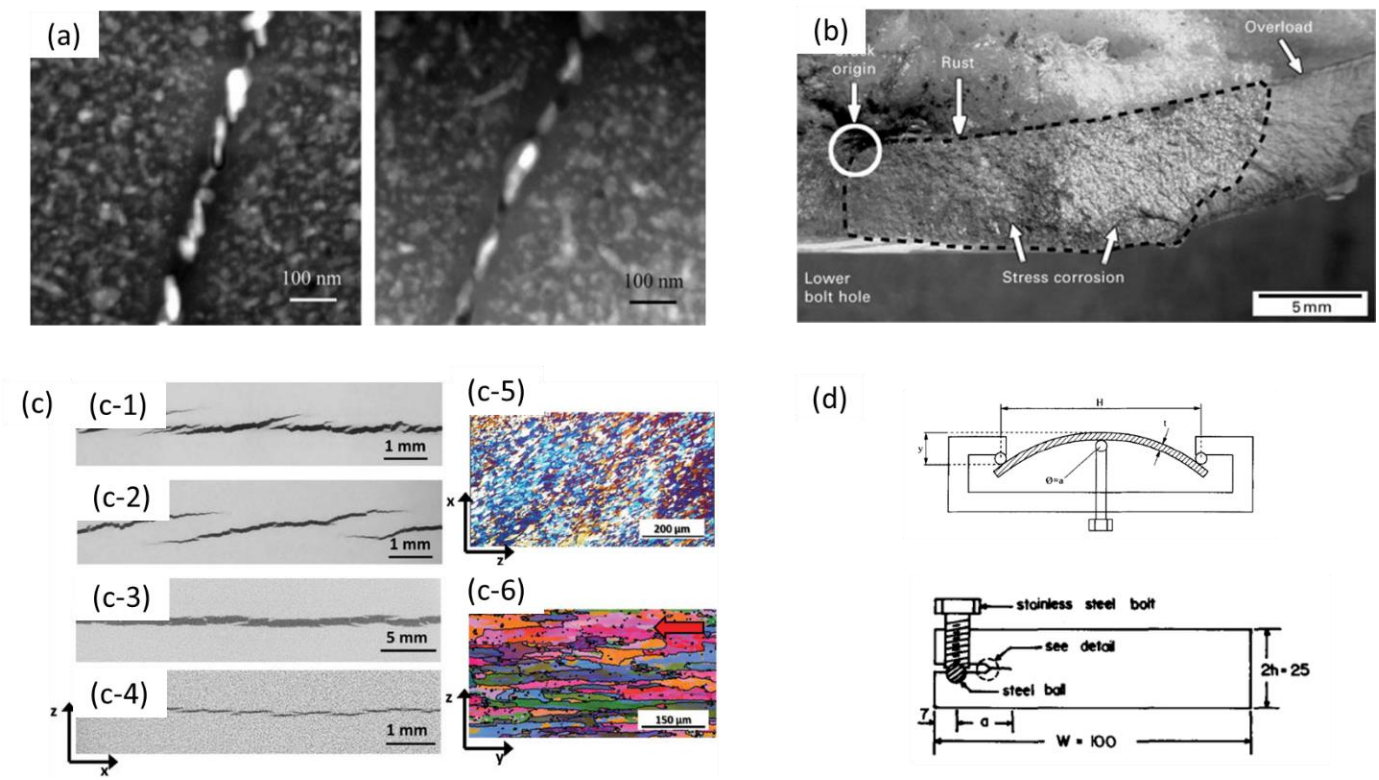

Figure 2 - 7 (a) Scanning TEM micrographs of 7075 (left) and 7079 (right). Both specimens in the overaged (T7) condition, showing GBPs, matrix (precipitates), and PFZ [136]; (b) Visualized SCC surface after failure [137]; (c) Virtual cross-sections of the stress corrosion crack perpendicular to the crack propagation direction (i.e. the Y-direction) for the AA7032 sample: (c-1) just below the notch and (c-2) 10 mm away from the notch (half-way down the sample). Virtual cross-sections of the AA5083 sample: (c-3) near the crack origin and (c-4) close to the crack front; (c-5) Polarised light micrograph showing the representative grain structure of the AA7032 sample; (c-6) EBSD orientation map in Euler colors showing the grain structure for the AA5083 sample.[138] (d) The representative methods to measure SCC susceptibility by double-cantilever setup [134,139].

When it comes to the influence of alloy composition, Cu is believed to have a critical role, because crack propagation speed (in stage II, as shown in **Figure 2 - 4** (e)) in low-Cu AA7079-T651 (with 0.4-0.8 wt.% Cu) is orders of magnitude higher than high-Cu AA7075-T651 (with 1.2-2.0 wt.% Cu) in aqueous NaCl solutions [140]. For Cu element alone, the difference in SCC performance is confirmed with TEM and electrochemical potential measurement. The conclusion is that Cu could substitute into $MgZn_2$ to form $MgZn_{2-x}Cu_x$ GBPs,[141] and the resultant tuned electrochemical properties of these precipitates with Cu could mitigate the hydrogen generation/uptake, increase the GP zone-stable temperature range,[92] and change the SCC propagation speed [136] (consistent with **Figure 2 - 4** (f)). More recently, it has been observed that higher Cu content (with higher Zn content) could also introduce more refined and denser strengthening precipitates [142,143]. Considering the effects of refinement on pitting and IGC, etc., the advantages of tuning Cu composition for a better SCC-resistance are understandable. For other elements like Mg, Zn, Mn, Fe, etc., they tend to tune the SCC-performance by changing the precipitates' anodicity during various heat treatment processes [92,144]. Nevertheless, it is incorrect to simply assume that adding inert elements like Cu, Ag, Zr, etc. would mitigate SCC cracking due to the potentially enhanced anti-corrosion behavior [145]. Previous study for Al-Cu system has shown that the addition of corrosion-beneficial Ag element could adversely introduce higher SCC-susceptibility [146]. The main reason for this phenomenon is the formation of high-density Ag-contained secondary phases. Their similar chemical composition with Al_2Cu makes Ag-containing secondary phases cathodes in corrosion, and the increased cathode area would increase the galvanic current through the PFZs (since the PFZs act as anodes) [146]. Thus, the SCC behavior is sensitive to the balance of the electrochemical potential by alloy composition [120], and, unfortunately, is not simply related to their different concentration.

Since ageing process (as part of the effective heat treatment for higher strength) is an inevitable processing technique influencing the compositional distribution and microstructural evolutions, ageing could also have dominant roles in determining the SCC susceptibility of Al-Zn-Mg-Cu alloys. For AA7075 alloy specifically, at peak aging, metastable η'($MgZn_2$) is dominant, and their anodic preferential corrosion (mainly in the form of pitting) will cause stress concentration [147]. Since some η'($MgZn_2$) and stable η phases could appear continuous along the GBs [147], once dissolved, it creates the cracking tunnels and accelerate SCC rate and hydrogen diffusion [148]. Therefore, as a common practice, overageing and RRA (namely retrogression and reageing treatments) could be conducive to achieving a higher SCC-resistance,[134] because these methods could favorably change the precipitation processes and tailor the precipitates' distribution, composition, and structural characteristics. Currently, to cater to the needs of different alloy systems, novel aging processes using time- and non-thermal control is developing. For instance, studies have used interrupted aging [149] and electrical pulses [150] as a way to introduce favorable precipitates and tune the SCC-behavior. By extending the control freedom of time elapse and electronic potential, these methods give triumphant trials, but the complexity of the processing sequence still limits their applications in SCC-reduction.

After nanoparticles are involved in the SCC observations and analyses, it is still not clear whether the SCC performance of Al-Zn-Mg-Cu nanocomposites will be enhanced or deteriorated. First, the incorporation of nanoparticles (such as TiC) will refine the secondary phases near or at the GBs, which will favorably break the precipitate continuity [25]. Second, the inert nanoparticle would be an effective barrier for diffusive processes including anodic dissolution and hydrogen transport. For example, it has been confirmed that carbides could make the adjacent precipitates nobler[151] and have more affinity to hydrogen via the thermal desorption spectroscopy (TDS) [95].

There are more benefits of nanoparticles in MMNCs, such as primary grain refinement, their intrinsic electrochemical stability, etc. However, the potential disadvantages could not be ignored. For instance, the matrix/reinforcement interface could lead to selective corrosion, if not chosen reasonably [92]. When the nanoparticles are conductive like TiC, WC, and TiB_2, galvanic dissolution and possible de-bonding at the interface would deteriorate SCC-resistance [139]. Moreover, the unexpected micro-segregation (of elements like Mg) at the matrix/nanoparticle interface could worsen the SCC scenarios [92].

2.4 Effects of nanoparticles on Tribological performance of metals

Alloys (including light-weight aluminum alloys) are widely utilized in the fields of aerospace, transportation, and construction. In particular, aluminum alloys after various heat-treatment are of great interests, due to their high ultimate tensile strength of 570 MPa and fracture toughness of up to 29 $MPa \cdot \sqrt{m}$ (as an example, in AA7075-T6 of Al-Mg-Zn-Cu series) [147,152,153]. Since it is also closely related to bearings, brake linings, and pistons for industrial applications, improving its friction and wear performance is highly desired [154,155].

Recently, aluminum matrix composites (AMCs) by adding metallic, ceramic or organic reinforcements have emerged as an important class of materials for tribological applications. For AMCs, commonly used reinforcement particles include silicon carbide (SiC), titanium carbide (TiC), titanium diboride (TiB_2), titanium oxide (TiO_2), alumina (Al_2O_3), carbon black (CB) and boron carbide (B_4C) [58,156], which can achieve friction reduction and wear resistance when compared to the original alloys [157–159] (as shown in **Figure 2 - 8** (a)).

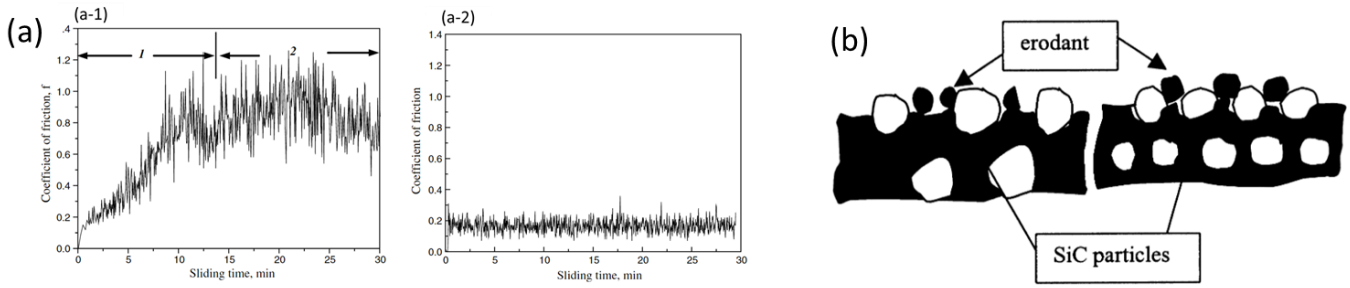

Figure 2 - 8 (a) Typical curves of friction coefficients of (a-1) SiC/Al composite and (a-2) TiB_2/Al composite against GCr15 bearing steel as a function of sliding time under dry sliding condition (P = 0.49 N and V = 0.8 m·s^{-1}) [160]; (b) Two friction/wear contact mode in SiC-reinforced Mg/Al composites: Erodant impinge effectively (left) or erodent prevented due to "short space" [161].

With this potential, the tribological properties of AA7075 AMCs have also been critically analyzed. For example, Roy et al. [162] reported that the addition of SiC and CB into AA7075 alloys significantly reduces the wear rate by the grain refinement effect. Bai et al. [163] also reported that the Al_2O_3 addition elevates the hardness of AA7075 composite to a level higher than that of the vermicular cast iron counterpart, thus significantly decreasing the wear rate. Kar et al. [164] used TiC as the reinforcement for AA7075 in their study. They found that the CoF is lowered by 20 % due to the improved strength and hardness with the optimal amount of TiC.

However, the reported tribological performance of AA7075 nanocomposites from these studies is inconsistent, owing to the diversity of the friction counterpart materials, the different surface roughness of the samples, and the resultant blurred distinction between friction and wear. For instance, UI Haq et al. [165] and Mistry et al. [166] reported contradictory results for the tribological properties of AA7075-Si_3N_4 composite against Fe-52100 (i.e. EN 31 steel in their study). As the amount of the reinforcement increased, UI Haq et al. reported higher CoFs for up to 6 wt.% of Si_3N_4, while Mistry et al. observed a decreasing trend in CoF. The controversial nature and

inconsistency of tribological performance is also observed in other AMCs due to the similar reasons (as shown in **Figure 2 - 8** (b)).

Secondly, among the available reinforcements, TiB_2 also has potential in superior tribological applications [167–169] owing to its supreme interface with AA7075, strengthening effect to the matrix and phase refinement for AA7075 [160,161]. Yet, no tribological studies have been reported to investigate the effects of nanoscale TiB_2 on AA7075 to the best of our knowledge. Both of these factors reduce the reliability of the tribological studies and limit the successful commercialization of AMC nanocomposites in tribological applications.

2.5 Summary

As discussed above, all the functional properties of metals/alloys show the microstructure-, composition-, and electron behavior-dependence. After the addition of nanoparticles, due to the microstructure change, compositional evolution, and increased matrix-nanoparticle interfaces, their functional properties are expected to change accordingly.

Owing the intrinsic complexity of influenced factors like grain, GBs, GBPs, PFZ, and defects (including dislocations), how the functional properties are changed in MMNCs is still not clear, and the previous studies have yielded controversial results (e.g., for chemical stability and tribological performance). A critical systematic study into these functional properties of MMNCs is urgently needed to enable their broad applications in industry. With the fundamental knowledge gained predicable, reliable, and quantitative description of functional properties in MMNCs under various scenarios would be possible in terms of processing, microstructure, and electron interactions.

CHAPTER 3 FABRICATION OF MMNCS

3.1 Experimental method

3.1.1 *Ex situ* molten salt assisted self-incorporation

3.1.1.1 Fabrication of copper alloy nanocomposite (naval brass)

The size distribution of the WC nanoparticles was characterized by Dynamic Light Scattering (DLS) on an *N4-PLUS DLS Machine*. Since WC is much heavier (**Table 4 - 7**), to ensure a good suspension and dispersion, 0.01% (wt./vol.) sodium polyphosphate solution was added to stabilize the WC nanoparticles. A suspension liquid with 100 µg of nanoparticles per liter was then subjected to ~2 hours of ultrasonic vibration before measurement. Each sample was repeated twice at 25℃. The size distribution of WC nanoparticles is shown in **Figure 3 - 1**.

Before the incorporation, WC nanoparticles with an average size of 100-200 nm were mixed with $KAlF_4$: NaCl salt (the volume ratio of latter is 1:1; the volume ratio of WC : salt mixture is 1:10). The mixture was mechanically mixed for 1 hour to ensure a uniform composition. $KAlF_4$ is utilized as an effective medium for metal oxide layer removal [170]. NaCl is used to help prevent the rapid evaporation of $KAlF_4$ and to ease the removal of residual salt mixture from the fabricated nanocomposite.

The incorporation is performed using a molten salt stirring method. In the experiment, the crucible was placed into a resistance furnace and fully covered with insulation material. It was pre-heated to 930°C and maintained isothermal for 5 mins. Hereafter, pure Cu-40 wt.% Zn (Commercial *C464 Naval Brass* by *OnlineMetals®*) was added, and argon protection was used with a flow rate of 10-20 ml/s. After Cu-40 wt.% Zn was fully molten, a boron nitride-coated stainless-steel stirring (*Caframo® Pitched Blade A511*) was positioned at the surface of the molten metal [171], and the nanoparticle-salt mixture was added. Upon the addition of the nanoparticle-salt

mixture, the mixing was started at 200 rpm/min. This incorporation process was continued for 30-45 mins and the samples were cooled to room temperature in air. The facile fabrication process is summarized in **Figure 3 - 2**.

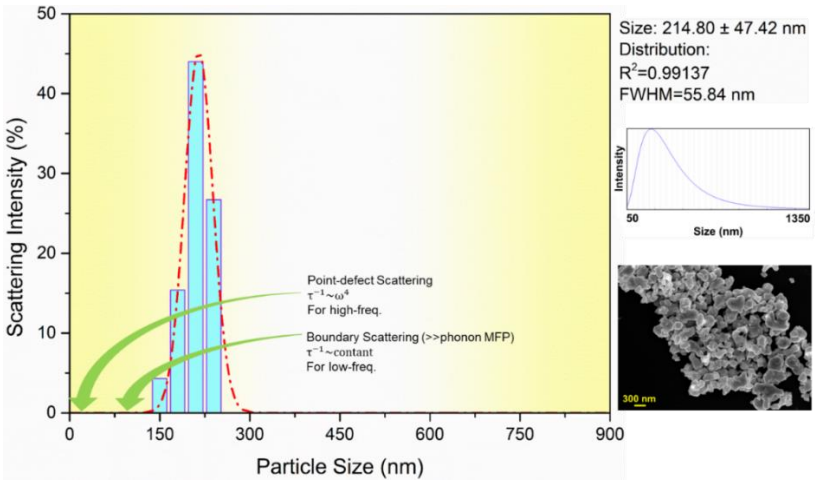

Figure 3 - 1 WC nanoparticle size distribution and SEM image with the depiction for different phonon scattering ranges

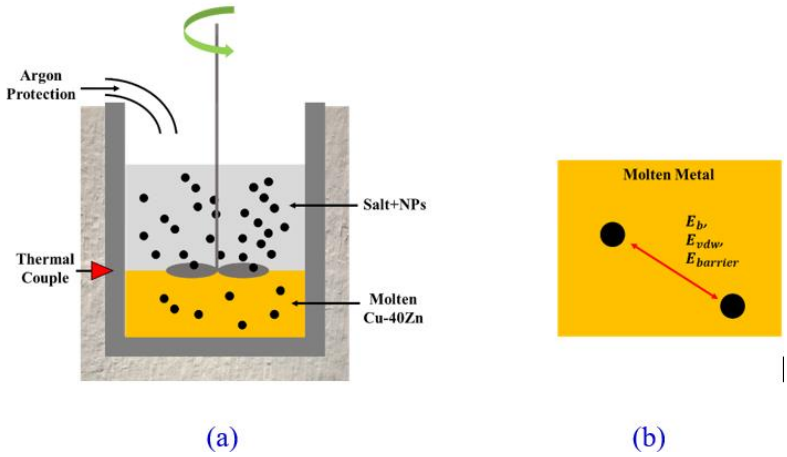

Figure 3 - 2 WC nanoparticle incorporation by molten salt stirring: (a) Experiment setup and (b) Dynamic model for incorporation stability.

3.1.1.2 Fabrication of copper alloy nanocomposite (Cu-Ag alloy)

First, Cu-60Ag with 10 vol.% of WC nanoparticles (with an average size of 214 nm, shown in **Figure 3 - 1**) was fabricated by a molten salt-assisted casting method (see **Figure 3 - 3**) [70, 172]. The Cu-60Ag/WC nanocomposites with high-purity elemental starting materials of Cu and Ag have been prepared. In the nanoparticle incorporation process, the crucible was first heated to the melting point of the alloy in a resistance-heated furnace. Then, the alloy (50-100 g, **Figure 3 - 3** (c)) was added, and argon protection (~10-15 mL/s) was provided. After the alloy was fully molten, the salt ($KAlF_4$) with WC nanoparticles of designed volume percentage was added to the molten metal. The temperature was held for 20 mins. The mechanisms for effective nanoparticle dispersion are discussed elsewhere [173]. The as-cast samples were ground, polished and ion milled to expose the microstructure. For comparison purposes, Cu-60Ag samples without nanoparticles and with different volume percentages of nanoparticles were also fabricated. The annealing heat-treatment is done in the heat-treatment furnace at 500±5°C for 48 hours; then, the samples will be furnace-cooling to the room temperature (~4h). The results of annealed Cu-60Ag and Cu-60Ag/10 vol.% WC are summarized in **Figure 4 - 23** (a) and (b).

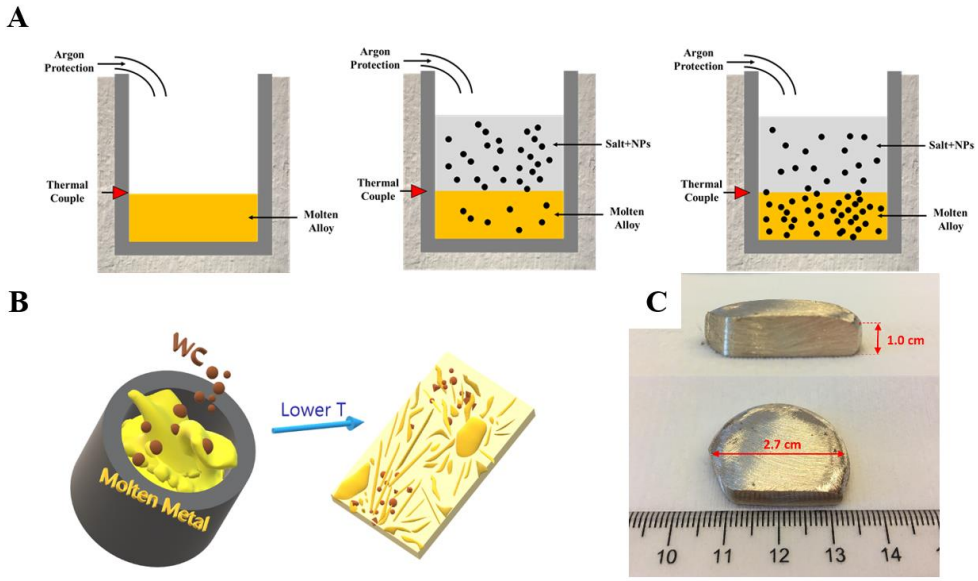

Figure 3 - 3 (a) The molten salt-assisted incorporation process; (b) The illustrative casting process for Cu-60Ag/WC nanocomposites; (c) The sample dimensions for as-cast Cu-60Ag/10 vol.% WC after surface polishing and slicing.

To better understand the trend of thermal conductivity and test the evolution of thermal behavior in Cu-Ag systems (see **Chapter 4**), Cu-Ag nanocomposites with 10 vol.% WC and varied Ag content are fabricated via the same fabrication process.

3.1.2 *In situ* nanoparticle generation and incorporation

3.1.2.1 Fabrication of aluminum matrix nanocomposite (AMNC)

Here, Al-TiB_2, Al-ZrB_2, and Al-ZrB_2 nanocomposites with nanoparticle volume percentage less than 5 vol.% were fabricated via the *in situ* route.

The *in situ* Al-TiB_2 samples were first prepared: the crucible was heated to 750℃ in an induction furnace. After the aluminum metal became molten, $KAlF_4$ was added [41,70]; When the $KAlF_4$ fully melted, the pre-mixed reactants, KBF_4 and K_2TiF_6 (with amounts for desired TiB_2 volume percentage) were poured in. After 20 mins under 750℃, the samples were cast out and air-cooled, as shown in **Figure 3 - 4**.

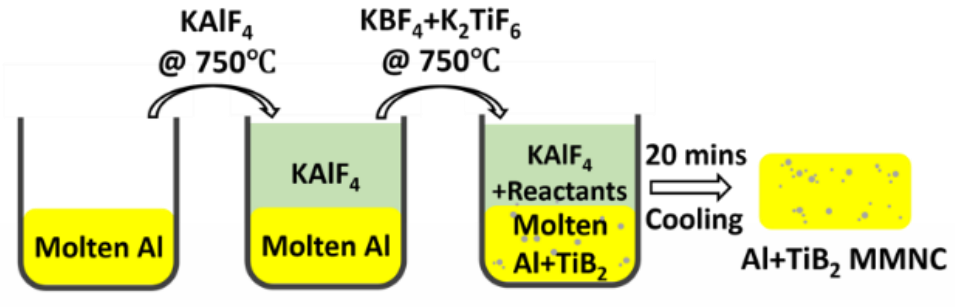

Figure 3 - 4 In situ synthesis process for Al-*x* vol.% TiB_2 nanocomposite.

The *in situ* Al-ZrB_2 and Al-TiC samples were prepared via the similar fabrication route with $KAlF_4$ covering and under Ar protection. The processing time varies with the different nanoparticle types. We should also note that the *in situ* processing for nanocomposites is favorable because of the optimal bonding interfaces between metals and ceramic nanoparticles. In addition, these ceramic nanoparticles can be successfully synthesized and stabilized with excess molten aluminum [79,174].

3.1.2.2 Fabrication of aluminum alloy nanocomposite (AA7075 and A206)

Al alloys are mostly strengthened via precipitation hardening, and the various precipitates (e.g., typical η phase in AA7075 alloy and typical θ phase in A206 alloy) contribute to the unique properties in different high-strength Al alloys. In this study, 2 kinds of Al alloys were focused, i.e., traditionally uncastable AA7075 alloy (Al-Zn-Mg-Cu series) and castable high-strength A206 alloy (Al-Cu series).

AA7075 nanocomposites: For AA7075 alloy, AA7075-TiB_2 and AA7075-TiC nanocomposites were fabricated. To obtain the optimal performance of AA7075 nanocomposites, based on the previous studies [26,175], the TiB_2 and TiC volume percentage in AA7075 has been designed to be both 1.5 vol.% for the current study.

The AA7075 nanocomposites were derived from the high-volume percent Al nanocomposite precursors (e.g., master nanocomposites like Al-TiB_2 and Al-TiC with over 3 vol.%). The precursor nanocomposites were melted at ~900 ℃, and the corresponding alloying elements (including Zn, Mg, Cu, and other trace elements) were added and manually stirred to

achieve the same and reasonably homogeneously distributed composition as AA7075 alloy. After alloying, the samples were first cast out into bulk ingots.

For the extruded AA7075-TiC and -TiB_2 nanocomposites, the hot extrusion was done by Shenchun Co. Ltd. The process was completed with the following parameters: The AA7075-TiC and -TiB_2 nanocomposite ingots in a diameter of 150 mm was hot-extruded with an extrusion ratio of ~30; The extrusion speed was set at 1.5 mm/s; the monitored extrusion temperature was set at ~400-430°C.

After obtaining the as-cast and as-extruded samples of AA7075-TiC and AA7075-TiB_2 nanocomposites, T6 heat-treatment (i.e., homogenization and solutionizing at 475°C for 2 hours, then quenching in water at 25°C, finally aging at 120°C for 24 hours) was used to obtain both the AA7075(T6)-TiC and AA7075(T6)-TiB_2 nanocomposites under as-cast and as-extruded states. Commercial AA7075(T6) was used as the reference material.

A206 nanocomposites The cast pure A206 was melt in an induction furnace under argon protection of 15 mL/s and alloyed under 750 ℃ for 15 min. For A206-1.5 vol.% TiC nanocomposites (hereafter, A206-1.5TiC), the cast samples were derived from the dilution of the pure Al-3.5 vol.% TiC composite master (hereafter, Al-3.5TiC) by *MetaLi LLC*. Due to the reaction between Al and TiC at a temperature lower than 780 C temperatures,[176] the graphite crucible was first heated to 850 ℃ under argon protection. Pure alloying elements were added first and isothermally kept for 15 min. Then, Al-TiC was added, and the mechanical stirring with graphite stirrer blades was applied with a speed of 300 rpm for 10 min. The A206-TiC was cast out into a cylinder-shape mold and air-cooled.

The heat treatments of T4 and T6 was applied after the cast samples were cut into thin pieces of ~2 mm thickness. T4 heat treatment followed the route of step-solutionizing at 515 ℃

for 1 h and 530 ℃ for 8 h, water quenching, and naturally aging for 36 h. T6 heat treatment used the recipe of step-solutionizing at 515 ℃ for 1 h and 530 ℃ for 8 h, water quenching, and artificially aging at 155 ℃ for 24 h.

After the heat treatment, the samples were cut into the desired shape and size by waterjet. The microhardness was measured by *Microhardness Tester LM 800AT* with a dwelling time of 10 sec and a loading of 200 gf, and each sample was tested for at least 5 times. For the electrical conductivity, all the samples were grinded to ~100-150 um thick and polished up to 1200 grit with anhydrous ethanol. The measurement was conducted on *Prometrix Omnimap RS-35 Four Point Probe Station*. Each sample was measured for 5 times. The microstructure and surface morphology was characterized with electron microscopy and energy dispersion scanning on a *Zeiss Supra 40KV* model, and the secondary electron imaging was used with a 12 KV acceleration voltage.

3.2 Experimental results

3.2.1 Naval brass/WC nanocomposite by molten salt assisted self-incorporation

Naval brass/WC samples taken from the ingots were ion milled for 2 hours to clean the surface. Scanning Electron Microscopy (SEM) imaging and Electron Diffraction Scanning (EDS) mapping (See **Figure 3 - 5** and **Figure 3 - 6** (a) and (b)) were used to confirm the nanoparticle dispersion and volume percentage. X-Ray Diffraction scanning (XRD, see **Figure 3 - 6** (c)) further confirmed the existence of WC nanoparticles in the metal matrix. As shown in **Figure 3 - 5**, even though pseudo-dispersed, the nanoparticles show a reasonable distribution with no sintering, agglomeration or severe clustering.

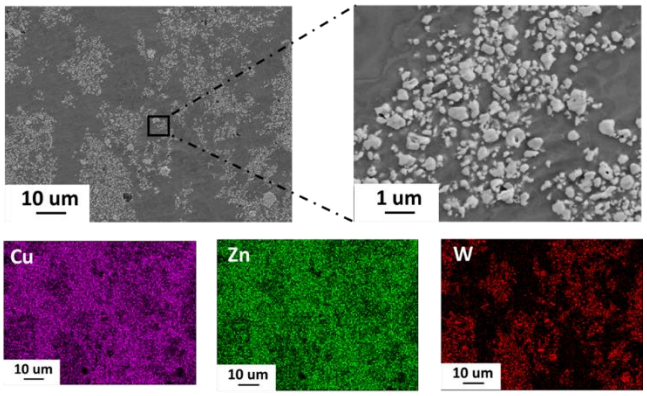

Figure 3 - 5 SEM Imaging and EDS Mapping for Cu-40 wt.% Zn with 12.5 vol.% WC nanoparticles. (High-magnification image shows the localized pseudo-dispersion area)

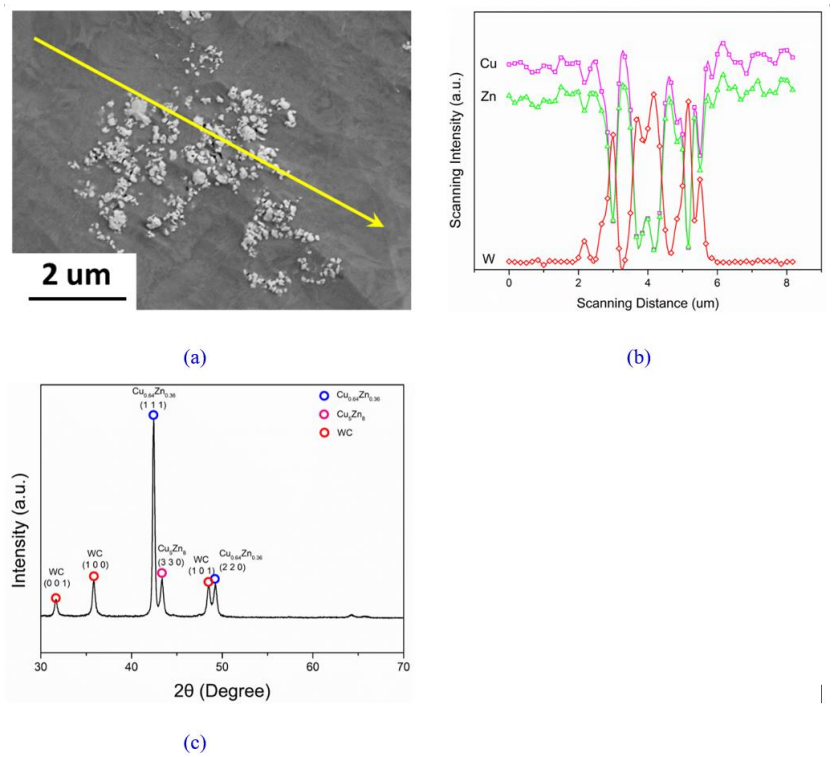

Figure 3 - 6 (a) and (b) Element line-scanning for Cu-40 wt.% Zn/12.5 vol.% WC to confirm the existence of WC; (c)XRD Scanning for Cu-40 wt.% Zn/12.5 vol.% WC

3.2.2 Cu-Ag/WC nanocomposite by molten salt assisted self-incorporation

Similar to the results of naval brass/WC nanocomposites, SEM imaging and EDS mapping (See **Figure 3 - 7** and **Figure 3 - 8**) were used to confirm the nanoparticle dispersion, volume percentage, and nanoparticle-rich zone boundaries. **Figure 3 - 7** has confirmed the existence of WC nanoparticles in the metal matrix. even though pseudo-dispersed, the nanoparticles show a reasonable distribution with no sintering, agglomeration or severe clustering. Since Cu-60Ag alloy has Cu-rich phase and Cu-Ag eutectic phase, it also shows that the preferential existence of WC nanoparticles near the boundary of Cu-rich phase, and the WC nanoparticles concentrate in the eutectic phase.

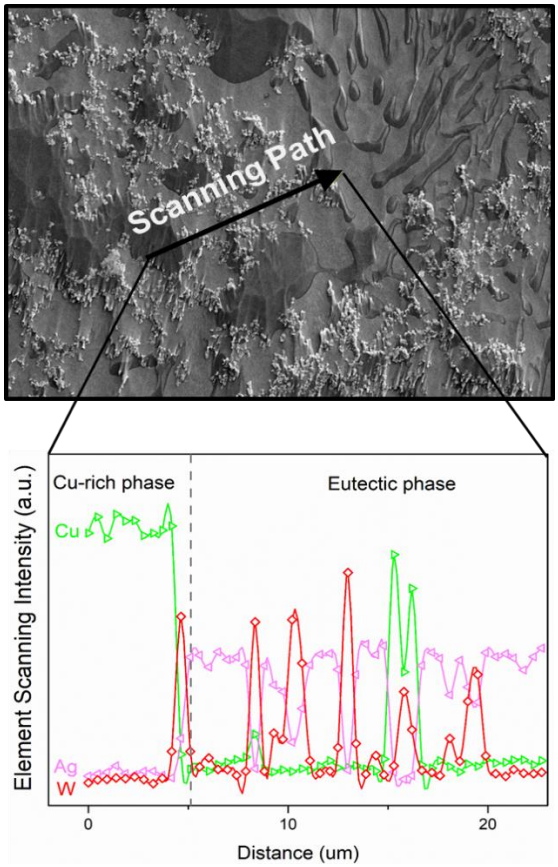

Figure 3 - 7 Line-scan for the WC nanoparticle distribution in eutectic and Cu-rich phases of a Cu-60Ag/10 vol.% WC nanocomposite.

When looking at the fabricated Cu-Ag/10 vol.% WC nanocomposites with various Ag compositions, as shown in **Figure 3 - 8**, this preferential distribution of WC nanoparticles into the eutectic phase and at the boundary of the eutectic phase and main phase (i.e., Cu-rich phase for Ag wt.%<71.9 wt.%, or Ag-rich phase for Ag wt.%>71.9 wt. %).

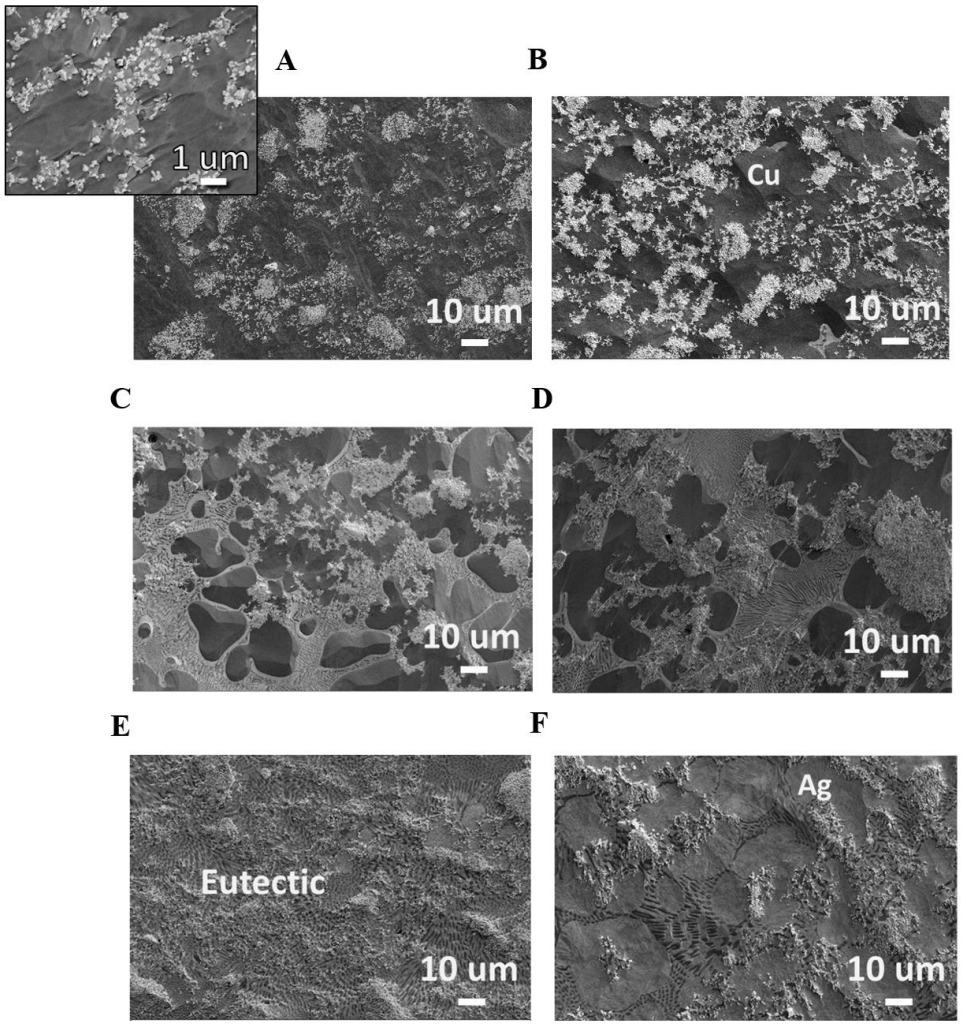

Figure 3 - 8 SEM images of microstructures for the WC nanoparticle distribution of **(A.)** Cu-10Ag, **(B.)** Cu-20Ag, **(C.)** Cu-40Ag, **(D.)** Cu-50Ag, **(E.)** Cu-71.9Ag (eutectic point), and **(F.)** Cu-80Ag all with 10 vol.% WC.

3.2.3 Al/TiC, Al/TiB_2, and Al/ZrB_2 nanocomposites by in situ incorporation

The *in situ* synthesized Al-TiC, -ZrB_2, and -TiB_2 samples were scanned with X-ray diffraction (XRD) to confirm and ensure the purity of the reaction products. The XRD scanning was operated on a *PANalytical Pro* model with Cu Kα radiation and standard 40 kV accelerating voltage; the scanning angle range was 30° to 90°, and the step size was 0.05° with a scanning speed of 2°/min. Afterward, the samples were ground and polished with grinding paper (up to 1200 grit) by anhydrous ethanol (200 proof) rinsing, and their microstructures were exposed via ion milling (20 min under 4.5 kV with a tilt angle of 4°). Scanning electron microscopy (SEM) imaging on a *Zeiss Supra 40KV* was used to measure the *in situ* formed nanoparticle size under secondary electron (SE) and InLens modes. The volume percentage of the synthesized nanophases was estimated by energy dispersive spectrum (EDS) mapping (since slow *in situ* synthesis reaction dynamics controls the TiC generation process,[177] all TiC volume percentages are shown with error bars). Detailed interfacial structures and morphologies were revealed by transmission electron microscopy (TEM) (*FEI T20 iCorr* model with a 120 kV accelerating voltage and a sample thickness of ~150 nm) to provide structural and configurational information for the altered thermal conductivity.

Microhardness and room-temperature electrical conductivity were measured by micro-indentation and four-point probing. For microhardness tests, the sample was cut into $5mm$-diameter shapes with thicknesses $> 1\ mm$, and measurements were done with a square-based diamond pyramid indenter on *Microhardness Tester LM 800AT* (100 gf applied for 10s). The electrical conductivity of all samples was measured using a *Prometrix Omnimap RS-35 4-point probe station*, with more than 3 measurements at each site and more than 3 sites for each sample. All samples were mechanically ground and polished by 1200-grit SiC paper with 200 proof

anhydrous ethanol, and the final thickness of the samples was between 100 µm to 200 µm, to guarantee a better figure of merits during the measurements

With the XRD scanning for Al-3.68 vol.% TiC, Al-3 vol.% ZrB_2, and Al-3 vol.% TiB_2 in **Figure 3 - 9**, it is confirmed that the *in situ* Al-based nanocomposites have high-purity TiC, ZrB_2, and TiB_2 nanoparticles via this molten-salt assisted method. The nanoparticle purity can rule out the by-product's effects on thermal performance.

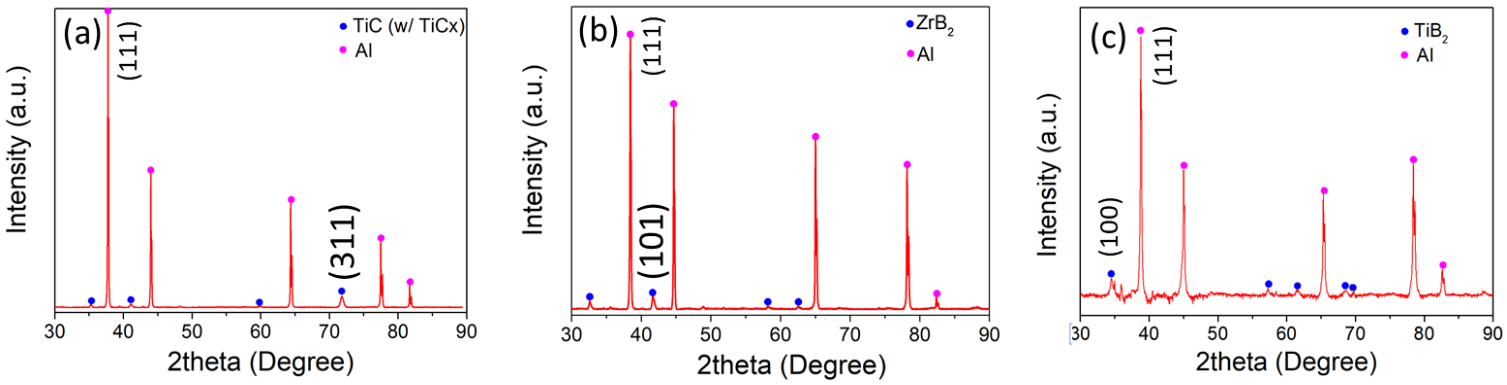

Figure 3 - 9 XRD scanning for in situ (a) Al-3.68 vol.% TiC nanocomposite, (b) Al-3 vol.% ZrB_2 nanocomposite, and (c) Al-3 vol.% TiB_2 nanocomposite.

When the sizes of TiC, ZrB_2, and TiB_2 are analyzed in **Figure 3 - 10**, **Figure 3 - 11**, and **Figure 3 - 12**, they obey the same distribution model and have similar statistical average size: the diameter of TiC is ~58 nm, the diameter of ZrB_2 is ~78 nm, and the diameter of TiB_2 is ~44 nm. Since the nanoparticles are all in size range of 10 nm-100 nm, this will give similar scale effects on electron and phonon transport,[75,178] which can significantly reduce the analysis complexity. Besides, as shown in **Figure 3 - 9** and **Figure 3 - 11**, the prominent (111) plane of Al could have coherent or semi-coherent interfaces with (311) planes in TiC, (101) planes in ZrB_2, and (100) planes in TiB_2 (all with an interface mismatch far less than ~20%), and this common coherency

(as denoted by the yellow dashed lines in **Figure 3 - 12**) could preclude the influence of drastically different interface types in thermal transport.

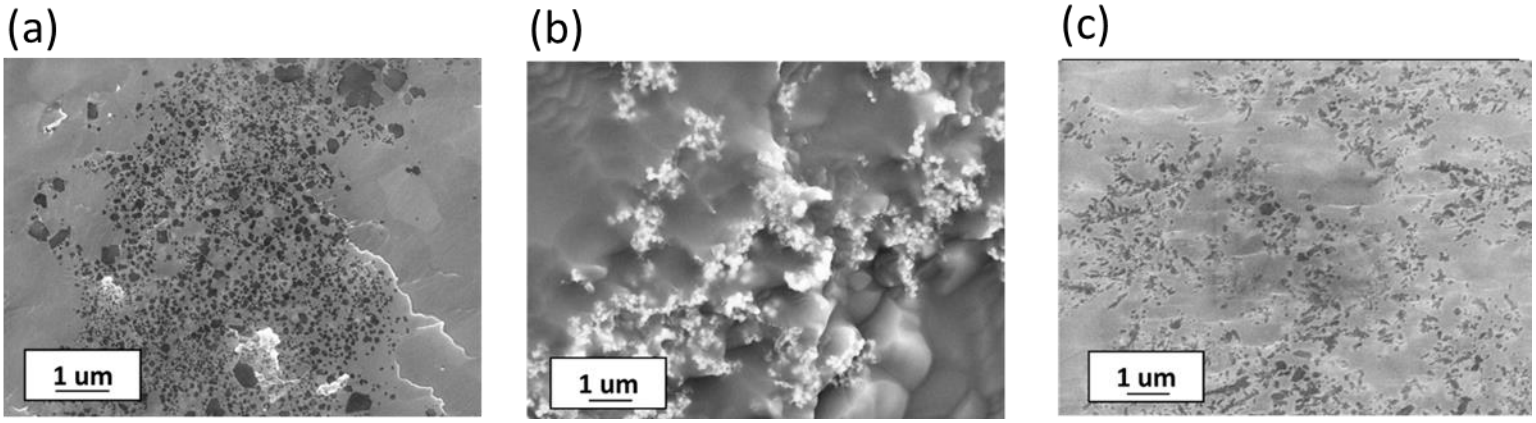

Figure 3 - 10 High-magnification SEM imaging for in situ (a) Al-3.68 vol.% TiC nanocomposite (InLens mode), (b) Al-3 vol.% ZrB_2 nanocomposite (combined SE and InLens mode), and (c) Al-3 vol.% TiB_2 nanocomposite (InLens mode).

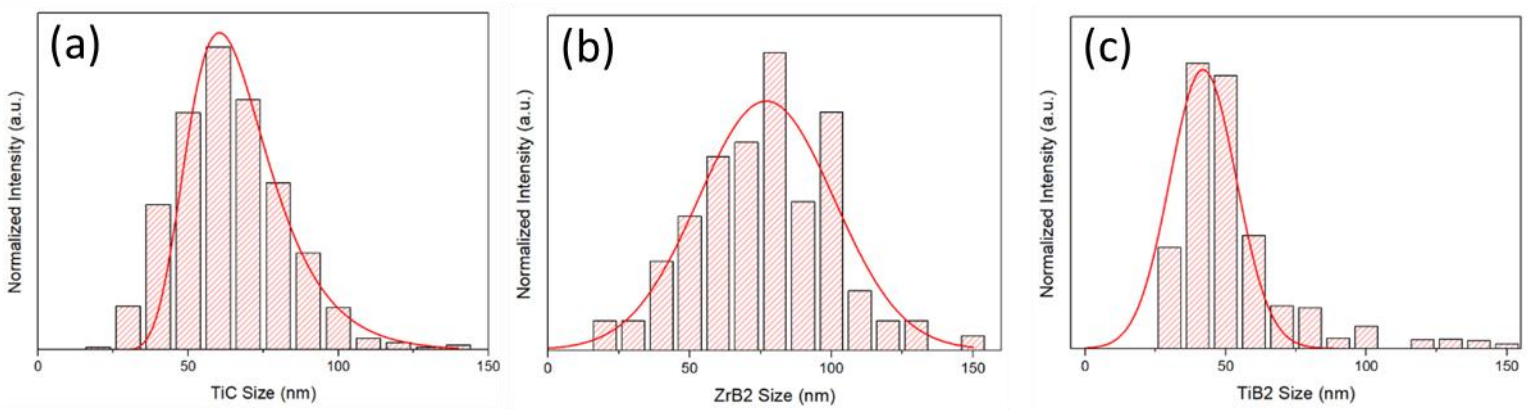

Figure 3 - 11 Nanoparticle size statistics for *in situ* (a) Al-3.68 vol.% TiC nanocomposite (~58 nm in diameter), (b) Al-3 vol.% ZrB_2 nanocomposite (~78 nm in diameter), and (c) Al-3 vol.% TiB_2 nanocomposite (~44 nm in diameter).

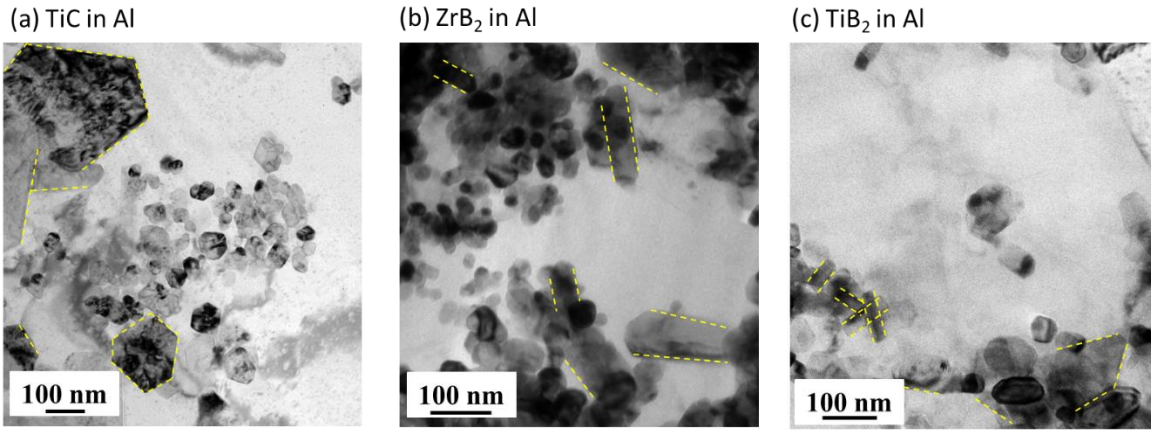

Figure 3 - 12 TEM observation of interfaces for in situ (a) Al-3.68 vol.% TiC nanocomposite, (b) Al-3 vol.% ZrB_2 nanocomposite, and (c) Al-3 vol.% TiB_2 nanocomposite; Inserted yellow dash lines show the energy-favorable coherent or semi-coherent interfaces.

By measuring the microhardness in **Figure 3 - 13** (a)-(c), reasonable linearity with nanophase volume percentage is observed and the increasing strength proves the samples' good quality. The main reason for the different strengthening effects results from the nanoparticle pseudo-clustering and the ratio of coherent, semi-coherent, and incoherent interfaces, as shown in **Figure 3 - 12**.

The measured electrical conductivity of Al-TiC, -ZrB_2, and -TiB_2 nanocomposites (See **Figure 3 - 13** (d)-(f)) shows that with the incorporation of nanoparticles, aluminum's electrical conductivity will decrease.[2] As the electron mean free path in metals is less than or comparable to the measured nanoparticle sizes, the scattering of electrons at the Al-nanoparticle interface is inevitable.[2,179] The effect of the reduced electrical conductivity will be further discussed in the following sections for the investigation of thermal performance of Al-based nanocomposites (in **Section 4.2.2.1**).

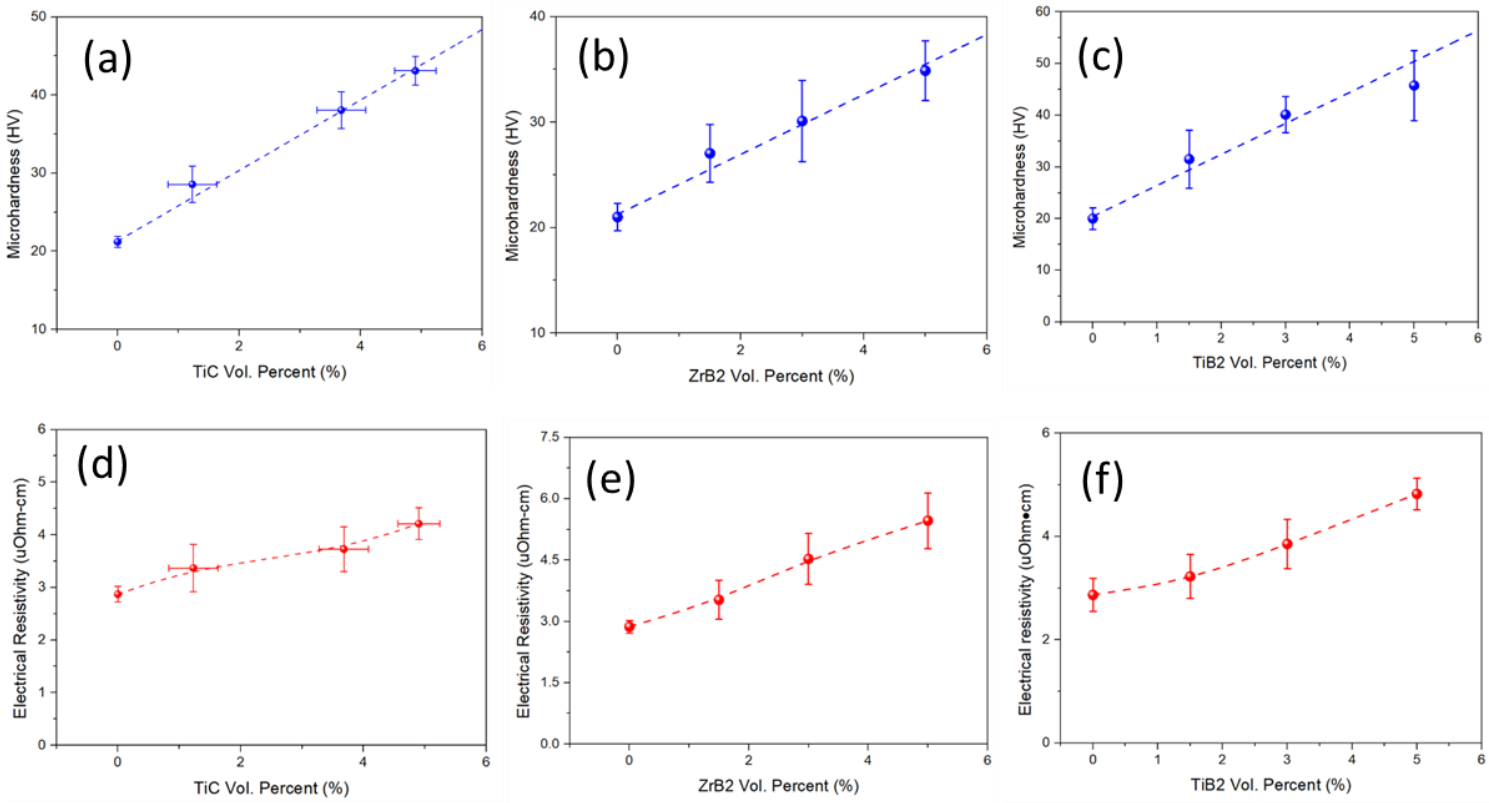

Figure 3 - 13 Microhardness for *in situ* (a) Al-TiC nanocomposites, (b) Al-ZrB_2 nanocomposites, and (c) Al-TiB_2 nanocomposite; and room-temperature electrical resistivity for in situ (d) Al-TiC nanocomposite, (e) Al-ZrB_2 nanocomposite, and (f) Al-TiB_2 nanocomposite.

3.2.4 AA7075 nanocomposites by in situ incorporation

To guarantee the successful and accurate incorporation of nanoparticles, the elemental composition of AA7075 alloy system has been measured and calibrated with ICP-MS. The results of the element composition of the designed AA7075 and its nancomposites have been summarized in **Table 3 - 1**.

Table 3 - 1 The measured element composition in AA7075 alloy system

Element	Zn	Mg	Cu	Cr	Zr	Mn	Al
Ratio (wt.%)	6.03±0.05	2.71 ±0.03	1.38±0.01	0.36±0.01	0.02±0.00	0.42±0.01	Bal.

Cast AA7075 nanocomposites: As shown in **Figure 3 - 14** and **Figure 3 - 15**, the nanoparticles (TiC and TiB_2) are mainly residing in or near the GB precipitates. The line scan of **Figure 3 - 14 (b)** and **Figure 3 - 15 (b)** confirms the co-existence of nanoparticles and the precipitates. Meanwhile, the XRD results **Figure 3 - 14 (c)** and **Figure 3 - 15 (c)** proves the phase composition in T6-heat treated cast AA7075 alloy with TiB_2 and TiC nanoparticles. The similar nanoparticle size distribution (see **Figure 3 - 14 (d)** and **Figure 3 - 15 (d)**) could rule out the influence of nanoparticle size difference on the corrosion performance.

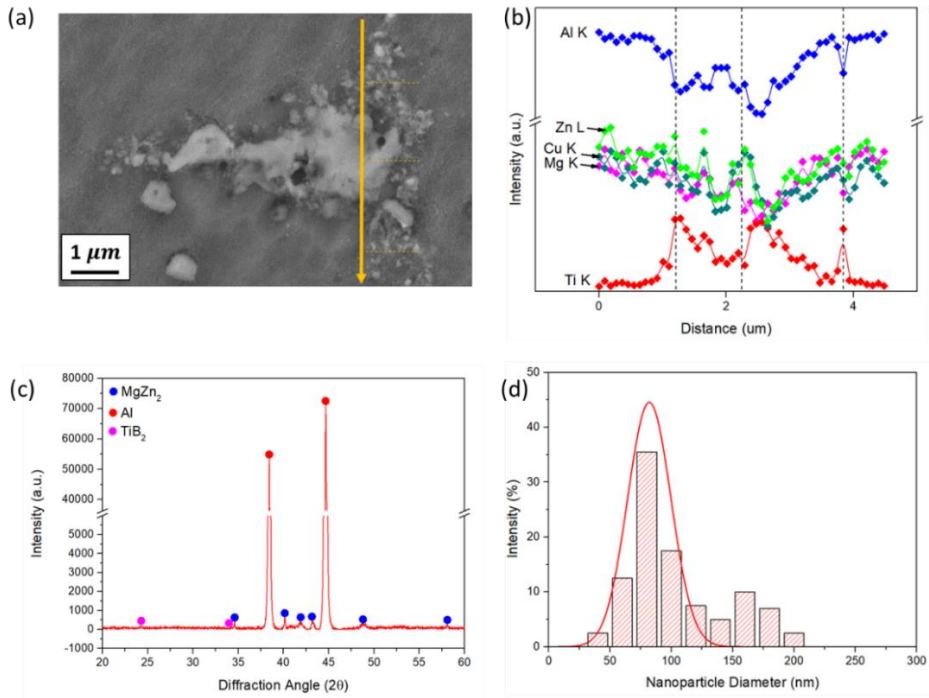

Figure 3 - 14 Microstructure analysis for cast AA7075-1.5 vol.% TiB_2 (cast, T6) **(a)** SEM imaging of nanoparticle-contained secondary phase; **(b)** EDS line-scanning for Al, Zn, Mg, Cu, and Ti element composition; **(c)** XRD; **(d)** TiB_2 nanoparticle size distribution.

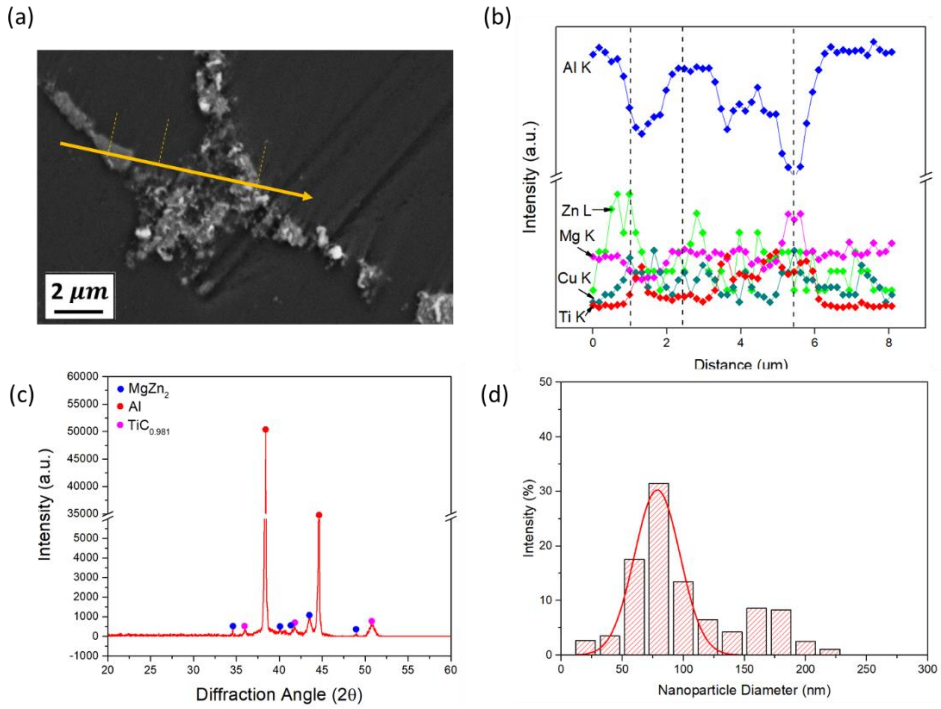

Figure 3 - 15 Microstructure analysis for AA7075-1.5 vol.% TiC (cast, T6) **(a)** SEM imaging of nanoparticle-contained secondary phase; **(b)** EDS line-scanning for Al, Zn, Mg, Cu, and Ti element composition; **(c)** XRD; **(d)** TiC nanoparticle size distribution.

Extruded AA7075 nanocomposites As shown in **Figure 3 - 16** and **Figure 3 - 17**, both TiC and TiB_2 share the similar size distribution as in their cast T6 state, and refine the secondary phases in AA7075 (extruded, T6) to a small size. However, due to the extrusion procedure, the nanoparticles will be regulated in a band-like shape in a pseudo-dispersion fashion.[180]

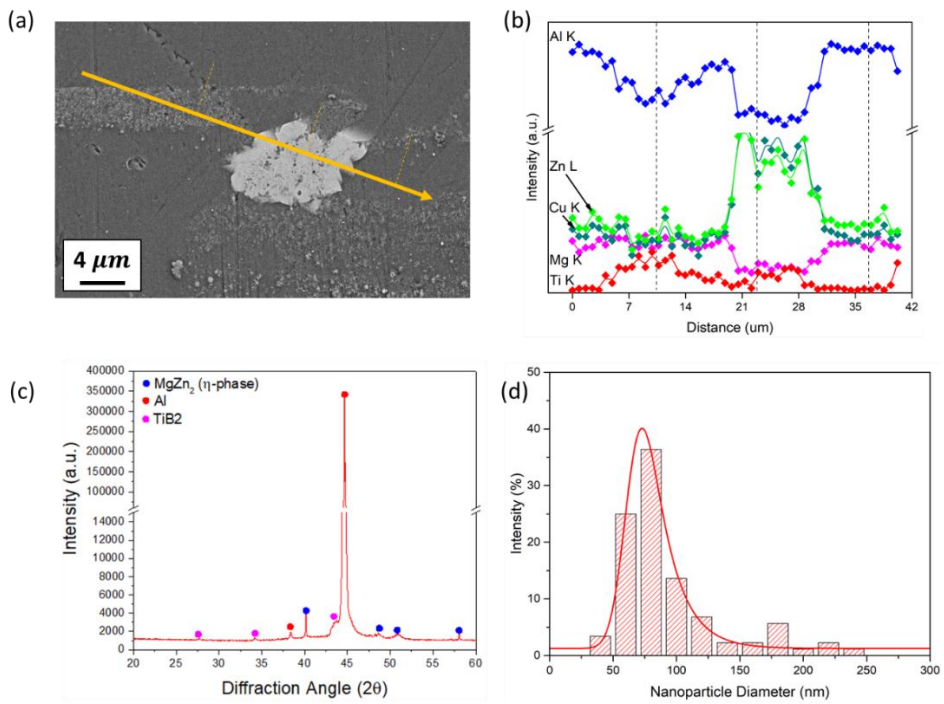

Figure 3 - 16 Microstructure analysis for AA7075-1.5 vol.% TiB_2 (extruded, T6) **(a)** SEM imaging of nanoparticle-contained secondary phase; **(b)** EDS line-scanning for Al, Zn, Mg, Cu, and Ti element composition; **(c)** XRD ; **(d)** TiB_2 nanoparticle size distribution.

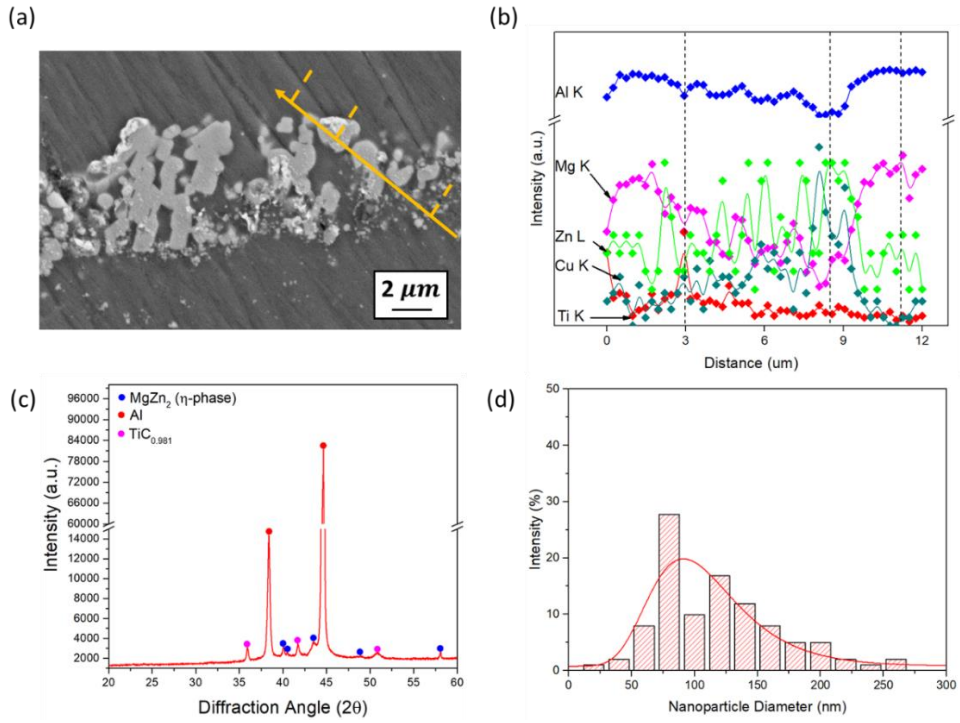

Figure 3 - 17 Microstructure analysis for AA7075-TiC (extruded, T6) **(a)** SEM imaging of nanoparticle-contained secondary phase; **(b)** EDS line-scanning for Al, Zn, Mg, Cu, and Ti element composition; **(c)** XRD ; **(d)** TiC nanoparticle size distribution.

After confirming the nanoparticle size, composition, and distribution in AA7075 alloy after various processing, the microhardness and electrical conductivity of AA7075-1.5 vol.% TiB_2 and AA7075-1.5 vol.% TiC have been measured for comparison (see **Figure 3 - 18**). For cast and extruded AA7075 nanocomposites, the incorporated 1.5 vol.% TiB_2 and TiC nanoparticles would increase the microhardness by the strengthening effects and retain a reasonable lowered electrical conductivity. The consistent trend for cast and extruded samples confirm the good processing quality for the AA7075 nanocomposites used in our study.

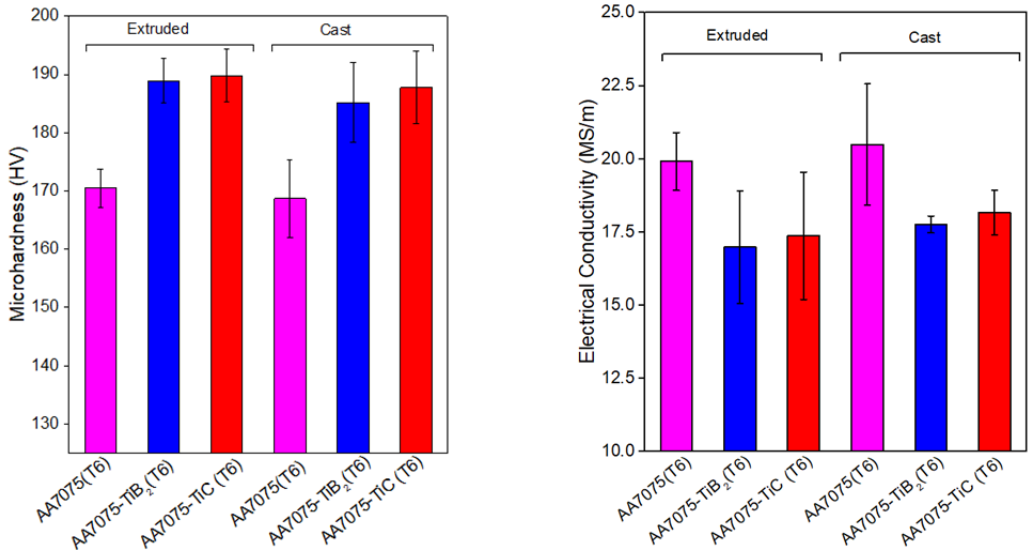

Figure 3 - 18 (a) Microhardness and **(b)** electrical conductivity of AA7075 (T6), AA7075-1.5 vol.% TiB_2 (T6), and AA7075-1.5 vol.% TiC (T6) by cast and extrusion.

3.2.5 A206 nanocomposites by in situ incorporation

As shown in **Table 3 - 2**, the alloying process could give a standardized composition in our designed A206 and its nanocomposites. After the T4 and T6 heat treatment, the microstructure of A206 and A206-1.5 vol.% TiC is compared in **Figure 3 - 19** (a) and **Figure 3 - 20** (a). The element line-scan in **Figure 3 - 19** (b) and **Figure 3 - 20** (b) reveals the pseudo-dispersion of TiC nanoparticles near the Al-Cu precipitates. The GB precipitates in A206-1.5 vol.% TiC of T4 and T6 states also did not show a clear difference in size.

However, when the microhardness is measured, the difference caused by heat treatments stands out. The microhardness of A206 (T6) is ~15 HV higher than A206 (T4), whereas A206-1.5 vol.% TiC (T6) is ~11 HV higher than A206-1.5 vol.% TiC (T4), as shown in **Figure 3 - 19** (c) and **Figure 3 - 20** (c). When it comes to the electrical conductivity, since the aging process is useful to precipitate out the atomic solutes of Cu and reduce the scattering of electrons by these solutes,[2,179] the electrical conductivity in A206 and A206-1.5 vol.% TiC of T6 state is ~2.50% and ~3.35% higher than their T4 counterparts, respectively (see **Figure 3 - 19** (d) and **Figure 3 - 20** (d)). The microhardness and electrical conductivity of A206 in T4 and T6 states also fall into the commercial range, which proves the good quality and consistency of our alloying methods.

Table 3 - 2 The measured element composition in A206 alloy system

Element	**Cu**	**Mg**	**Ti**	**Mn**	**Al**
Ratio (wt.%)	4.429±0.037	0.354±0.004	0.292±0.010	0.160±0.001	Bal.

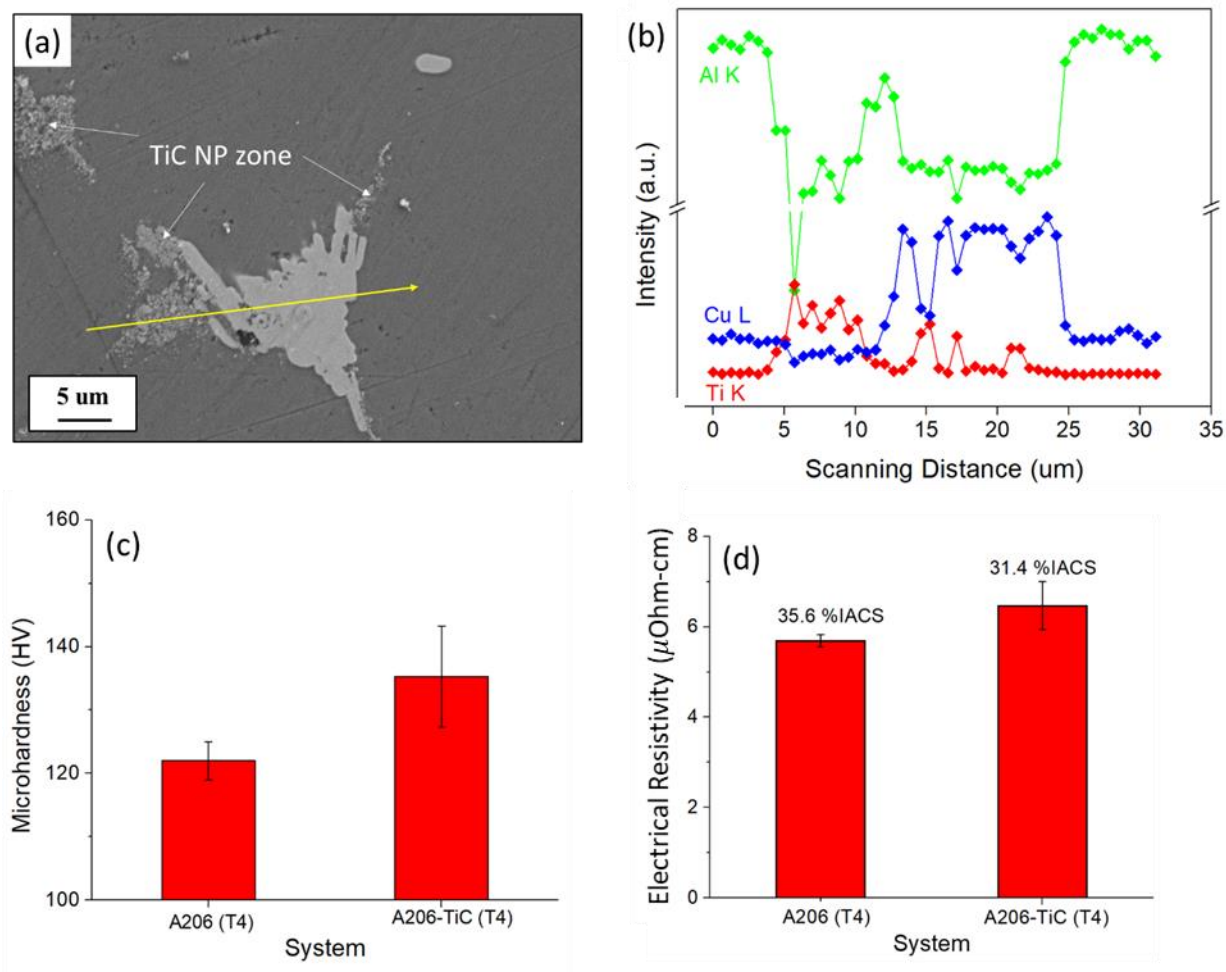

Figure 3 - 19 (a) The microstructure and (b) the element line-scan of A206-1.5 vol.% TiC (T4); (c) the microhardness and (d) the electrical conductivity of A206 (T4) and A206-1.5 vol.% TiC (T4).

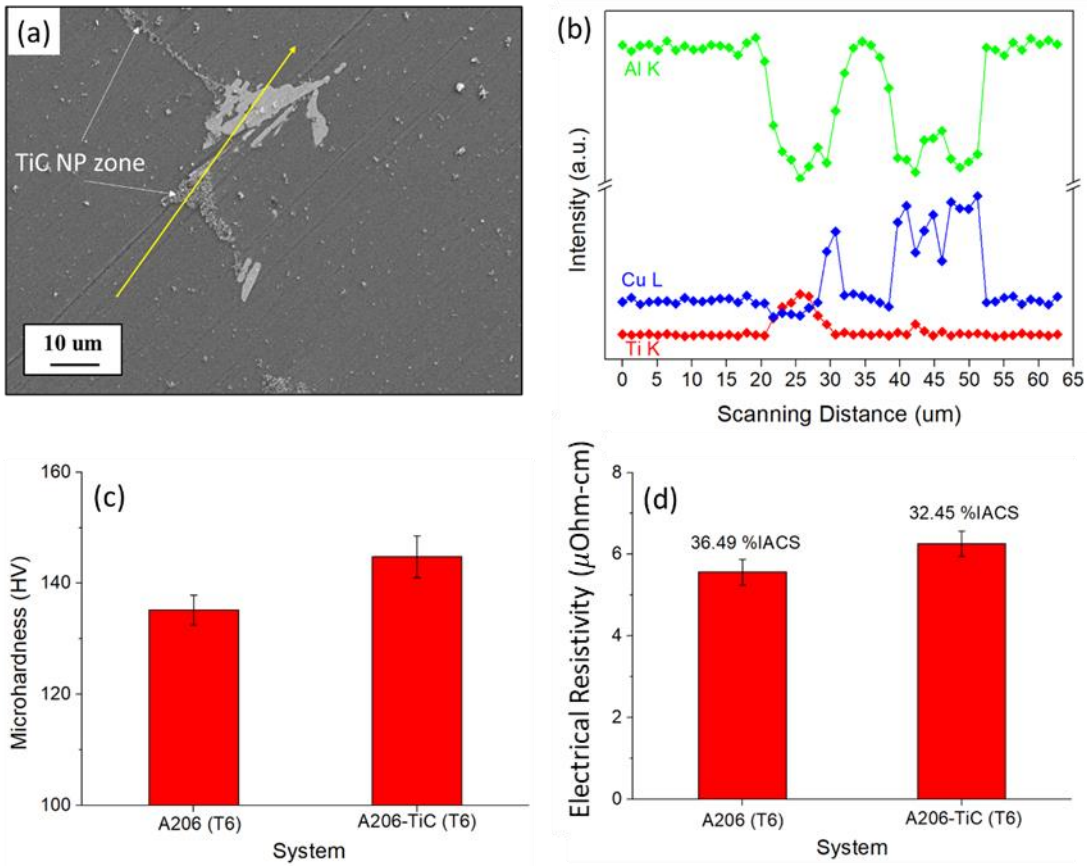

Figure 3 - 20 (a) The microstructure and (b) the element line-scan of A206-1.5 vol.% TiC (T6); (c) the microhardness and (d) the electrical conductivity of A206 (T6) and A206-1.5 vol.% TiC (T6).

In section **3.2.4** and **3.2.5**, the microstructure of the synthesized and processed AA7075 and A206 nanocomposites is to show the synthesis quality via the *in situ* route. The detailed microstructural study directly linked with the functional properties would be further presented in **Chapter 5** and **Chapter 6**.

3.3 Summary

In this chapter, both the *in situ* and *ex situ* methods to fabricate metal matrix nanocomposites have been summarized, and the successful incorporation of WC, TiB_2, TiC, and ZrB_2 nanoparticles has been demonstrated.

For the following fundamental study on the electrical, thermal, chemical, and other engineering properties in metallic nanocomposites, the Cu-based nanocomposites are mainly fabricated by an *ex situ* method. Due to the wettability between Cu matrix and WC nanoparticles (which could be tuned by alloying elements of Zn and Ag), reasonable pseudo-dispersion of WC into Cu-based nanocomposites is achieved.

In comparison, Al-based nanocomposites are mainly fabricated via an *in situ* route, and the successful incorporation of nano- to submicron-scale nanoparticles like TiC, TiB_2, and ZrB_2 is achieved. This method is feasible in Al systems, given the reasonable reactivity of Al with the element-containing salts. The general good wettability between Al with TiC, TiB_2, and ZrB_2 facilitates their dispersion. It has been further demonstrated that with the *in situ* synthesized Al nanocomposites (as master), Al alloy nanocomposites like AA7075/TiB_2 and AA7075/TiC could be fabricated in a facile way.

In summary, the universally feasible incorporation methods could efficiently incorporate nanoparticles into different metals and alloys. Generally speaking, the developed synthesis methods and the resultant reasonable dispersion of nanoparticles could serve a reliable basis for the fundamental study into the functional properties of the focused nanocomposite systems.

CHAPTER 4 EFFECT OF NANOPARTICLES ON ELECTRICAL AND THERMAL PROPERTIES OF METALS

4.1 Experimental methods

4.1.1 Room-temperature measurement for electrical conductivity

The electrical conductivity of all samples was measured using a *Prometrix Omnimap RS-35 4-point probes*, with more than 3 measurements at each site and more than 3 sites for each sample. All the samples were mechanically grinded and polished by 1200-grit SiC paper with 200 proof anhydrous ethanol, until the surface was freshly exposed with no indents. The final thickness of the samples was between 100 um to 200 um, to guarantee a better figure of merits during the measurements on the four-point probe station.

During the measurement, all samples were placed on a silicon wafer. The measurement temperature was fixed at 25°C in the clean room environments.

4.1.2 Low temperature measurement for electrical performance

All the samples were made into Hall bar shapes via *wire EDM*. After EDM, the samples were etched in the highly diluted HCl solution (0.01 mol/L) for 2 min to get rid of the possible heat-affected surface. After that, the sample was mechanically polished down to the required thickness with the pure ethanol rinsing. Then, ion-milling was used to get rid of the attached contaminants. These samples were measured on *PPMS* (*Quantum Design PPMS Model-698*) to reveal the low temperature electrical properties with a 50 mA current pump under 8 Hz under the helium-purged atmosphere, as illustrated in **Figure 4 - 4** (b). The magnetic scanning in PPMS for the apparent carrier (i.e., free electron) density is in the range of $\pm 6.0\,T$. This can help rule out noise due to the high charge carrier density, while preventing possible electromigration and skin

effects. During the measurement, the sample electrical properties are measured from 10K up to 300K at the speed of 2K/min; At 10K and 300K, the magnetic field is exerted from $-6.0\,T$ to $+6.0\,T$ isothermally.

4.1.3 Measurement for thermal performance

4.1.3.1 Heat capacity

DSC Heat Flux Method on a *Perkin DSC* was used to obtain the data for metal matrix nanocomposites. All the samples were made into nearly cylindrical 50-100 mg pieces. The focused scanning temperature ramped from 0-50 ℃ by step-scan method, since room-temperature properties are of interests. The scanning recipe included an isothermal treatment at 0℃ for 3 minutes (to achieve thermal relaxation), an increasing stepwise temperature scanning, and an isothermal treatment under 50℃ for 1 min. Each sample was characterized three times.

4.1.2.2 Thermal diffusivity

Thermal conductivity measurement is dependent on the measurement for thermal diffusivity as follows:

Eq. 4 - 1 $$k = \alpha \cdot c_p \cdot \rho$$

Where k is the thermal conductivity. α indicates the thermal diffusivity, C_p the heat capacity, and ρ the density. The density is estimated by the law of mixture:

Eq. 4 - 2 $$\rho \cong \rho(matrix) \cdot (1 - x) + \rho(np) \cdot x$$

Where x denotes the WC nanoparticle volume fraction.

Laser Flash Method was used to determine α. The samples were made into rods/bars of high aspect ratio up to ~10:1 with lengths of 1.5-2.0 cm, as demonstrated in **Figure 4 - 1**. This

aspect ratio provided an efficient heat guide for sensitive measurement. All the measured temperature is normalized to $< T >$ by:

Eq. 4 - 3 $$< T >= \frac{T(t)-T_0}{T_1-T_0}$$

Where T_0 and T_1 are the initial temperature and peak temperature, respectively.

By finding the half-maximum temperature point $T_{0.5}$, the tangent line at $T_{0.5}$ intersects with the x-axis to provide the time period from the initial laser flash pulse, as shown in **Figure 4 - 1**. The diffusivity can be calculated by the relationship of:

Eq. 4 - 4 $$\alpha = \frac{0.48L^2}{\pi^2 t_{0.5}}$$

where L is the sample length. The laser's wavelength was 1075 nm, and its pulse duration was 0.01 s, which is far less than the estimated thermal signal transmission time. The temperature sampling time interval was 0.0001 s. Each sample was characterized three times.

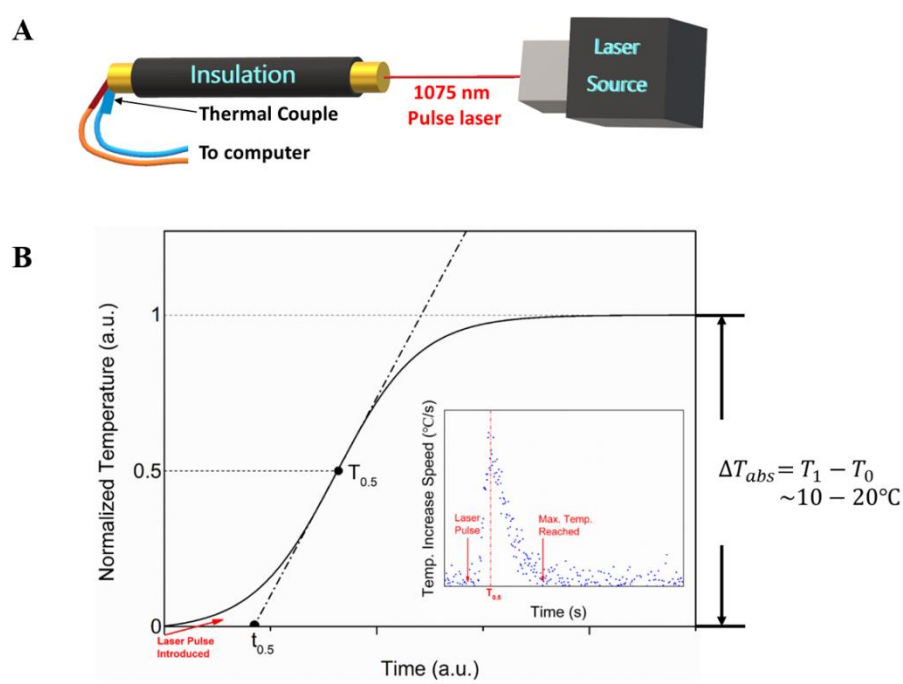

Figure 4 - 1 (a) Illustration for thermal measurement setup; (b) The temperature curve during laser flash pulse and the real temperature gradient in measurements

4.2 Experimental results

4.2.1 Electrical Properties

4.2.1.1 Al-TiB_2 nanocomposites

The samples were etched by a mixture of 50 mL Poulton's reagent, 25 mL HNO_3 (aq), and 40 mL chromic acid (0.3g/mL with distilled water) as the dye for 5-10 s [181]. The etched surface with exposed grain sizes were analyzed under polarized light. As shown in **Figure 4 - 2**, with an increasing volume percentage of TiB_2 nanoparticles, the grain size of the Al-matrix decreases from ~1100 um in pure Al to ~80 um of Al-3 vol.% TiB_2 nanocomposite.

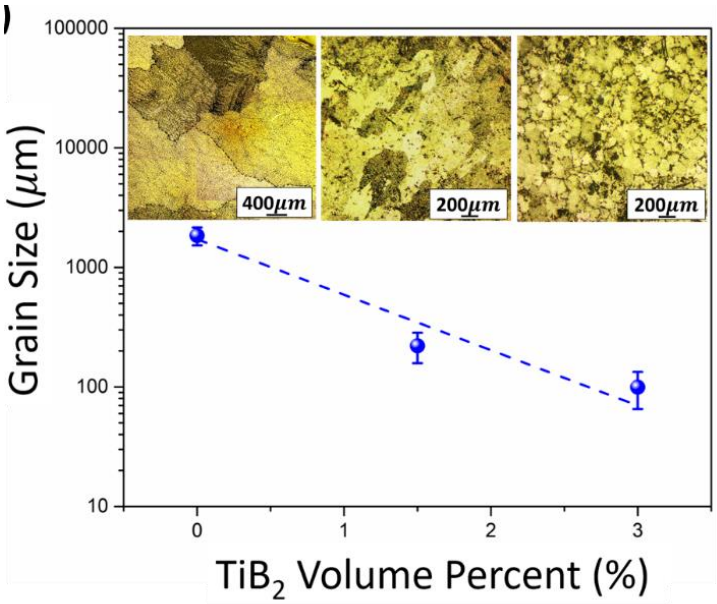

Figure 4 - 2 Grain size of Al-*x* vol.% TiB_2 nanocomposite (*x*=0, 1.5, 3), with the inserted after-etching surface of the nanocomposites.

Examination of the TiB_2 nanoparticle distribution in the Al matrix under low-magnification SEM is summarized in **Figure 4 - 3** (a): It's clear that the nanoparticles are mainly uniformly dispersed either in the grain boundaries or in the pseudo-clusters without significant clustering or agglomeration [1,107]. As proof of the reasonable dispersion of TiB_2 in the Al matrix, the

microhardness was measured on a *Microhardness Tester LM800A* (200Kgf with 10s dwell time), and the Young's modulus was measured on an *MTS Nanoindenter XP* (9 measurements per sample, with the penetration depth into surface of 2000 nm under 45 Hz and 0.05 s^{-1} strain rate), as shown in **Figure 4 - 3** (d). Since the strengthening effects of nanoparticles can be Taylor expanded for the low volume percentage nanocomposites, the good linearity of the microhardness and Young's modulus rules out the possibility of TiB_2 having a highly inhomogeneous distribution[1,41].

The chemical composition of the Al-TiB_2 nanocomposite was verified through XRD on a *PANalytical X'Pert Pro* (Cu Kα), as summarized in **Figure 4 - 3** (c). Since 1.5 vol.% TiB_2 is out of the resolution limit of XRD, pure Al and Al-3 vol.% TiB_2 were scanned for comparison. According to **Figure 4 - 3** (c), by in-situ methods, the TiB_2 is stabilized in the Al matrix with undetectable impurities and causes FWHM widening of the main Al (111) and (200) peaks. Besides, the interface of Al-TiB_2 tends to be more favorable along Al (111), since it has the least lattice mismatch with major TiB_2 planes of (100) and (001),[7] shown in **Figure 4 - 3** (b).

The nanoparticle size distribution was mapped under high-magnification SEM and processed with *ImageJ*, as shown in **Figure 4 - 3** (e) and (f). It is clear the in-situ TiB_2 nanoparticles have a reasonably uniform size of ~40-60 nm in diameter, and the Al-1.5 vol.% TiB_2 and Al-3 vol.% TiB_2 have the polydispersity index (PDI) of ~0.4472 and ~0.3047, respectively.

For electrical properties, the electrical conductivity was first measured on a Four-point Probe under room temperature for comparison (see **Figure 4 - 4** (a)). Meanwhile, the samples were made into Hall bar shapes via *wire EDM*. When EDM is done, the samples were etched in the highly diluted HCl solution (0.01 mol/L) for 2 min to get rid of the possible heat-affected surface. After that, the sample was mechanically polished down to the required thickness with the pure ethanol rinsing. Then, it was ion-milled to get rid of the attached contaminants. These samples

were measured on *PPMS* (*Quantum Design PPMS Model-698*) to reveal the low temperature electrical properties with a 50 mA current pump under 8 Hz under the helium-purged atmosphere, as illustrated in **Figure 4 - 4** (b).

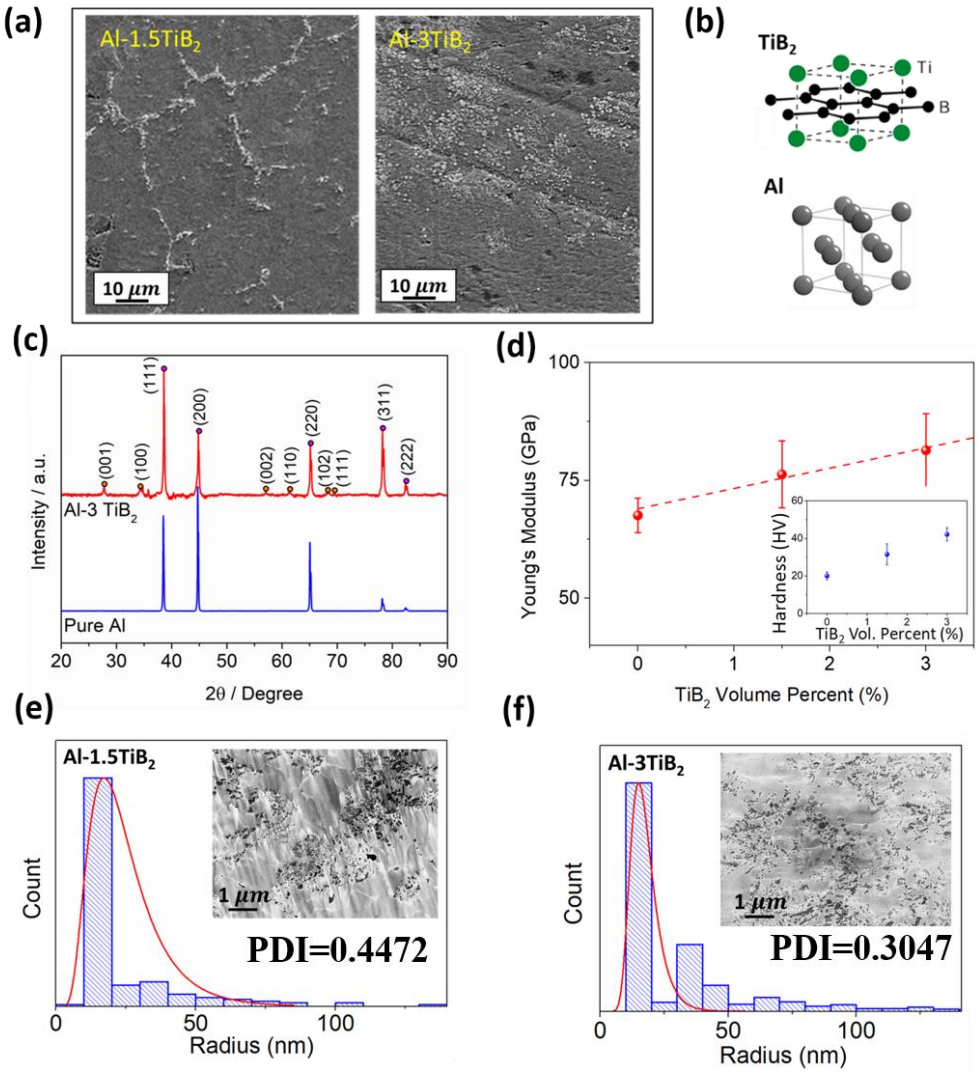

Figure 4 - 3 (a) Low-magnification SEM images showing the TiB2 distribution in Al-1.5 vol.% TiB_2 and Al-3 vol.% TiB_2; (b) Crystal structure illustrations for Al and TiB_2; (c) XRD scanning for pure Al and Al-3 vol.% TiB_2 nanocomposites; (d) Microhardness values and Young's moduli of Al-*x* vol.% TiB_2 nanocomposites; In-situ TiB_2 nanoparticle size distributions in (e) Al-1.5 vol.% TiB_2 and (f) Al-3 vol.% TiB_2 (Inserted: the corresponding SEM images in InLens mode).

The magnetic scanning in PPMS for the apparent carrier (i.e., free electron) density is in the range of $\pm 6.0\,T$. This can help rule out noise due to the high charge carrier density, while preventing the possible electromigration and skin effect. During the measurement, the sample electrical properties are measured from 10K up to 300K at the speed of 2K/min; At 10K and 300K, the magnetic field is exerted from $-6.0\,T$ to $+6.0\,T$ isothermally. Then, the apparent (free) electron concentration and electron mobility are calculated via the equations of **Eq. 4 - 5** and **Eq. 4 - 6** below:[182]

Eq. 4 - 5

$$\frac{dRxy}{dB} = \frac{1}{n_e \times d \times q_e}$$

Eq. 4 - 6

$$\mu_e = \frac{\sigma}{n_e \times q_e}$$

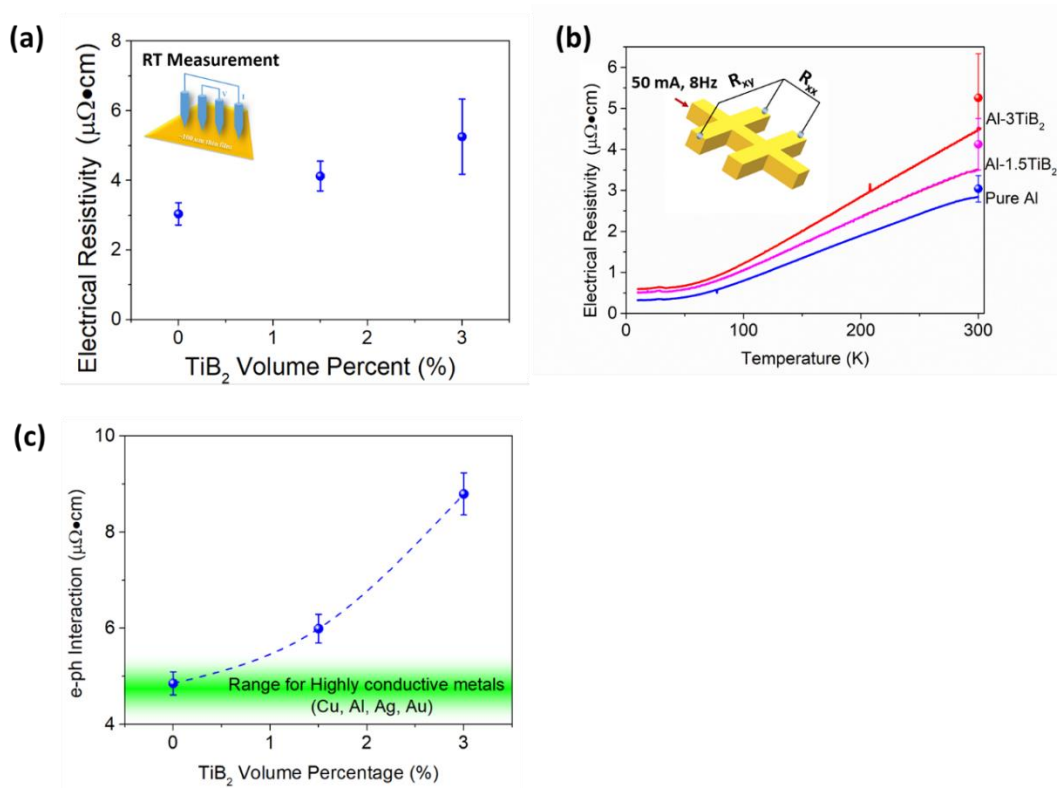

Figure 4 - 4 (a) Room temperature electrical resistivity of Al-*x* TiB_2 nanocomposites (*x*=0, 1.5, 3) by four-point probe measurements; (b) Temperature dependence (10-300 K) of electrical

resistivity in Al-x TiB_2 nanocomposites (x=0, 1.5, 3) by PPMS measurements; (c) The electron-phonon interaction coefficient in **Eq. 4 - 7**.

The four-point probe and PPMS results match reasonably well. With the increasing volume percentage of TiB_2 nanoparticles in the Al matrix, electrical conductivity of Al-TiB_2 decreases. Also, the electrical conductivity of Al-TiB_2 shows a temperature dependence with clear metallic signatures, as summarized by **Eq. 4 - 7**:

Eq. 4 - 7

$$\Delta\rho(T) \propto T^5 \times \int_0^{\frac{T_\theta}{T}} \frac{x^5}{(e^x-1)\times(1-e^{-x})}\,dx$$

Here, T_θ is the Debye temperature. As shown in **Figure 4 - 4** (c), with increasing TiB_2 nanoparticle volume percentage, the electron-phonon interaction coefficient increases and demonstrates a stronger effect of phonons on electrons when phonons are not suppressed under higher temperatures. This is understandable because the enhanced Young's modulus shown in **Figure 4 - 3** (d) imply a phonon transport enhancement by the relation of group velocity $v_g \propto \sqrt{\frac{E}{\rho_{sys}}}$ (where E denotes the Young's modulus, and ρ_{sys} denotes the system density).

However, by measuring the electron concentration (see **Figure 4 - 5** (a)), though with a low volume percentage (<10 vol.%) of TiB_2 nanoparticles, the (apparent) electron concentration decreases from $1.24 \times 10^{29}\ m^{-3}$ to $9.11 \times 10^{28}\ m^{-3}$ for 1.5 vol.% TiB_2 and $7.66 \times 10^{28}\ m^{-3}$ for 3 vol.% TiB_2. In contrast, as shown in **Figure 4 - 5** (c), the electron mobility shows negligible change at different temperatures with the increased volume of TiB_2 nanoparticles. As summarized in **Figure 4 - 5** (b), the electrical conductivity ratio with pure Al in response to temperature is roughly constant, except for the significant phonon-electron interaction range from 50-150K. This is consistent with the previous study [179].

By identifying the contributions of different factors to the reduction of electrical conductivity in the Al-TiB_2 nanocomposites, the ratios are summarized in **Figure 4 - 5** (d) and (e). The description of EMT in terms of the volume percentage of TiB_2 nanoparticles is summarized by **Eq. 4 - 8** [52,183]:

Eq. 4 - 8

$$\rho_{Al-TiB_2} = \rho_{Al} \times \left[\frac{1+\frac{2\rho_{Al}}{\rho_{TiB_2}}-2f\times(\frac{\rho_{Al}}{\rho_{TiB_2}}-1)}{1+\frac{2\rho_{Al}}{\rho_{TiB_2}}+2f\times(\frac{\rho_{Al}}{\rho_{TiB_2}}-1)}\right]$$

Where ρ_{Al-TiB_2}, ρ_{Al}, and ρ_{TiB_2} are the electrical resistivity for the nanocomposite, Al matrix, and TiB_2 respectively. f is the volume percentage of TiB_2 nanoparticles in the nanocomposites.

Together with the information from the XRD and grain size studies in **Figure 4 - 2** and **Figure 4 - 3**, according to the Matthiessen's Law, the contributions from grain boundaries and dislocations[27,53] are calculated via **Eq. 4 - 9** and **Eq. 4 - 10**, respectively:

Eq. 4 - 9

$$\Delta\rho_{GB} \cong \frac{2}{3}\alpha_T \times \Omega_{Al-GB} \times (\frac{2.37}{D})$$

Eq. 4 - 10

$$\Delta\rho_{dis} = \begin{cases} \frac{2\sqrt{3}\Omega_{Al-dis}\times\left|\frac{\beta\times cos\theta-\frac{0.9\lambda}{D}}{sin\theta}\right|}{D\cdot b} \ (by\ XRD) \\ 6\Omega_{Al-dis} \times \frac{f\times\Delta CTE\times\Delta T}{r\times b\times(1-f)} \ (by\ \Delta T) \end{cases}$$

Where Ω_{Al-GB} and Ω_{Al-dis} refer to the grain boundary resistance ($1.9 \times 10^{-16}\ \Omega \cdot m^2$) [184] and dislocation resistance ($3.3 \times 10^{-25}\ \Omega \cdot m^3$) [185]. D, r, and b are the grain size of Al, the radius of a TiB_2 nanoparticle, and the Burgers vector for Al, respectively. In **Eq. 4 - 9**, the coefficient $\alpha_T = 1 + \frac{MFP(T)}{D}$ compensates for the temperature dependence of the electron mean free path.[186,187] β is the peak broadening at certain peak θ under X-ray wavelength of λ. ΔCTE is the mismatch between Al and TiB_2, and ΔT is the temperature difference between the in-situ synthesis temperature and the compared temperature.

The electron mobility contribution is demonstrated by **Eq. 4 - 11** and directly plotted with the experimental data in **Figure 4 - 5** (a).

Eq. 4 - 11

$$\frac{1}{\mu_e} = \sum \frac{1}{\mu_i}$$

Thus, **Figure 4 - 5** (d) and (e) depict the expected electrical conductivity if any one of the various factors act alone. According to **Figure 4 - 5** (d) and (e), grain boundaries, dislocation resistivity, TiB_2 volume percentage, and electron mobility all seem to affect the electrical conductivity of Al-TiB_2 slightly [184,185], and the reduction in (apparent) electron concentration stands out.

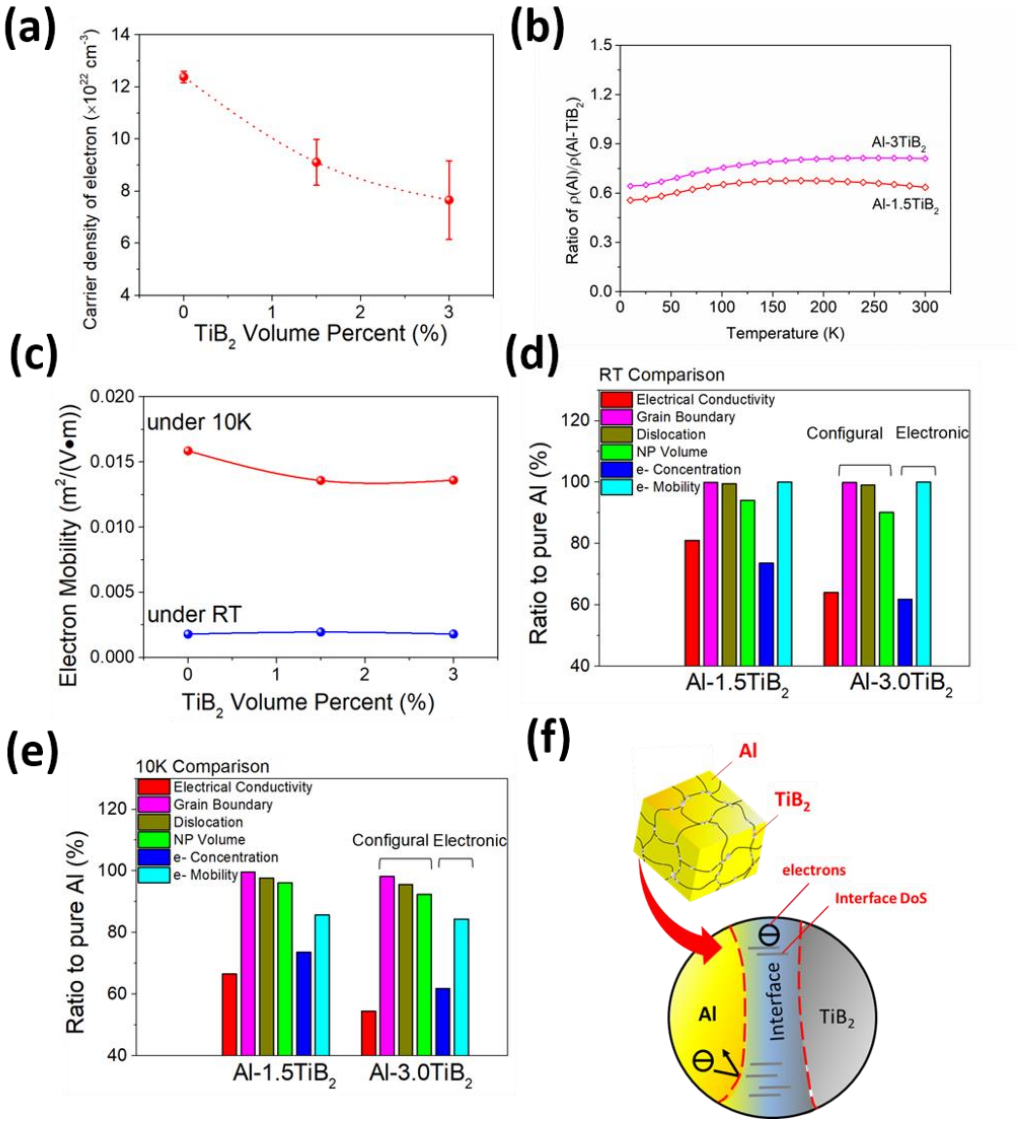

Figure 4 - 5 (a) Electron concentrations in Al-*x* vol.% TiB_2 nanocomposites (*x*=0, 1.5, 3); (b) Ratio of electrical resistivity in Al-TiB_2 nanocomposites compared to pure Al; (c) Electron mobilities in Al-*x* vol.% TiB_2 nanocomposites (*x*=0, 1.5, 3) under RT and 10 K; The contributions to the reduction in electrical conductivity in Al-*x* vol.% TiB_2 nanocomposites (*x*=1.5, 3) by mechanical/structural and electronic considerations at (d)RT and (e)10K; (f) Illustration of electron behavior in Al-TiB_2 nanocomposites.

Table 4 - 1 Electronic configuration near Fermi level in Al and TiB_2

Materials	Structure	Fermi Velocity ($\times 10^6\ m/s$)	DOS near Fermi Energy (eV^{-1})	Mismatch
Al	FCC	2.03	0.31	-
TiB_2	HCP	-	0.16	-47%

This study shows that the reduction in (apparent) electron concentration is crucial in the reduction of electrical conductivity of in-situ Al-TiB_2 nanocomposites. In contrast to previous studies and research,[27,53,54] this study reveals that the mechanical/configurational factors are not directly correlating to the electrical properties, and the electrical properties are directly influenced via the significant electron concentration decrease in Al-TiB_2 nanocomposites. Based on this study, the incorporation of TiB_2 nanoparticles creates defects, including interfaces and dislocations, and changes the preferred growth modes of Al grains [174,185]. These defects create a defect density of states to accommodate more free electrons and to enhance lattice effects on electrons [188]. These interfaces also have mismatches and discontinuity in Fermi velocity and density of states, as shown in **Table 4 - 1**. Both of these effects contribute to the bound states of electrons and a significant scattering of free electrons [189]. The electron mobility is less affected because the lowered (apparent) electron concentration reduces the possibility of electron scattering within the MFP (especially at room temperature). In short, for metal matrix nanocomposites with a low volume percentage of nanoparticles, electron concentration and electron mobility should be decoupled for electrical conductivity analyses, as the direct correlation between the mechanical/configurational changes and the tuned electrical performance fails. This finding is important for a more rational design of

metal matrix nanocomposites for applications that demand both high mechanical strength and good electrical conductivity.

4.2.1.2 Al-ZrB_2 nanocomposites

The Al-3 vol.% ZrB_2 nanocomposites were prepared via an in situ molten salt assisted method following the reaction route below:

$3K_2ZrF_6+6KBF_4+10Al \rightarrow 2KF+10KAlF_4+3ZrB_2$ (750℃, 20 min)

3 vol.% ZrB_2 is selected for good castability of samples. The ZrB_2 nanoparticle size and distribution in Al were studied via scanning electron microscopy (SEM), and the result is shown in **Figure 4 - 6**. It's clear that the ZrB_2 nanoparticles have a pseudo-dispersion (**Figure 4 - 6** (a)) but without agglomeration or sintering (**Figure 4 - 6** (b)).[1,41] The diameter of the synthesized ZrB_2 nanoparticles is ~112 nm on average. For the grain size, the samples were etched by a mixture of 50 mL Poulton's reagent, 25 mL HNO_3 (aq), and 40 mL chromic acid (3g/10 mL distilled water) as the dye for 5-10 s.[181] The etched surface with exposed grain sizes were analyzed under polarized light. As shown in **Figure 4 - 7**, with the incorporation of ZrB_2 nanoparticles, the grain size of the Al-matrix decreases from ~1100 um in pure Al to about 179 um in the Al-3 vol.% ZrB_2 nanocomposite (**Figure 4 - 7** (c)).

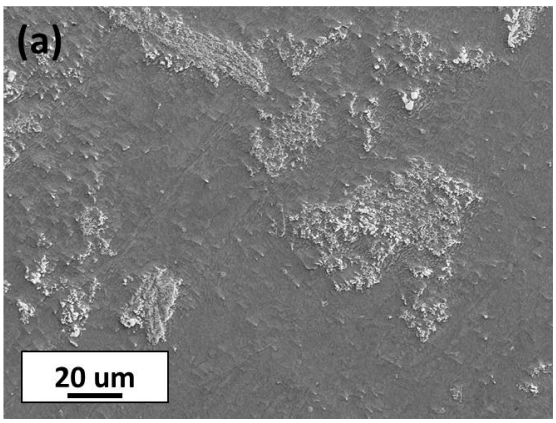

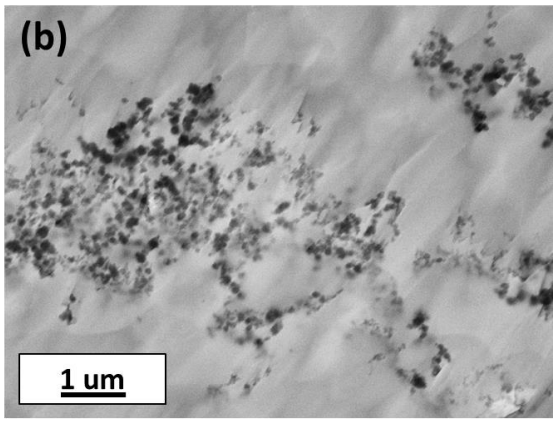

Figure 4 - 6 (a) The microstructure for Al-3 vol.% ZrB_2 nanocomposites; (b) The ZrB_2 nanoparticle size distribution in the Al-3 vol.% ZrB_2 nanocomposites.

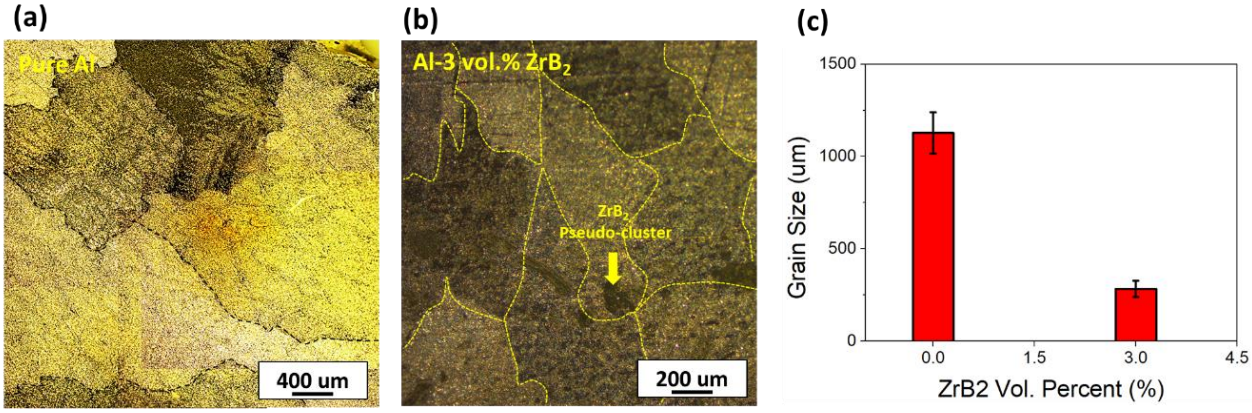

Figure 4 - 7 The grain structure after etching for (a) pure Al and (b) Al-3 vol.% ZrB_2 nanocomposites; (c) The grain size comparison for pure Al and Al-3 vol.% ZrB_2 nanocomposites.

The sample for electrical conductivity measurement was machined by wire EDM into Hall bar shapes with a thickness of ~100-150 um, and then measured on physical property measurement system (PPMS) to reveal the low temperature electrical properties with a 50 mA current pump under 8 Hz. The temperature scanning starts from 2K up to 300K, covering the reported possible ZrB_2 superconductivity transition temperature.[190] The magnetic scanning in PPMS for the apparent carrier (i.e., free electron) density and electron mobility is in the range of ±6.0 T.[191] The results are summarized in **Figure 4 - 8** to **Figure 4 - 10** and **Table 4 - 2**, respectively.

The electrical conductivity of pure Al and Al-3 vol.% ZrB_2 nanocomposites from 2K to 300K are summarized in **Figure 4 - 8**. At room temperature, the electrical resistivity of Al-3 vol.% ZrB_2 is 4.1 uOhm-cm, larger than 2.6 uOhm-cm in pure Al. However, Al-3 vol.% ZrB_2 still shows

characteristic metallic electron behavior following **Eq. 4 - 7**, as the electrical conductivity increases with the decreased temperature and saturates when the temperature approaches 0K.

Moreover, when gauging the electron concentration at 2K, 10K, and 300K, it is found that the electron concentration has little change in both pure Al ($\sim 12 \times 10^{28}\ m^{-3}$) and Al-3 vol.% ZrB_2 nanocomposites ($\sim 9 \times 10^{28}\ m^{-3}$). This confirms that the metallic collective behavior of electrons in Al-3 vol.% ZrB_2 is kept.

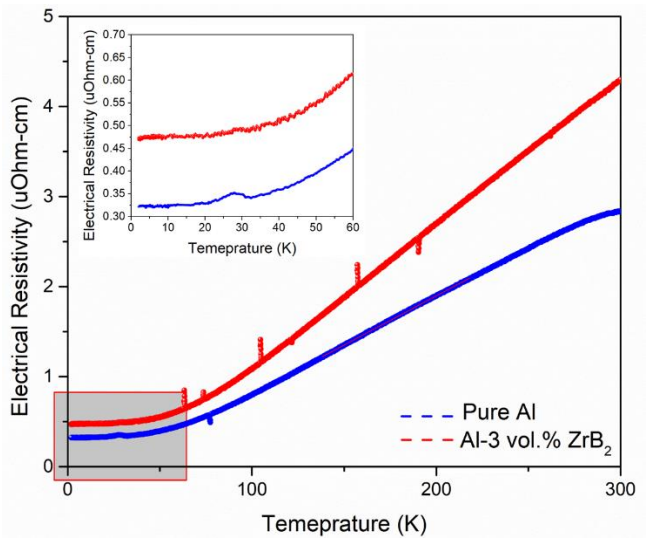

Figure 4 - 8 Electrical conductivity in pure Al and Al-3 vol.% ZrB_2 nanocomposite from 2K-300K. (Inserted: The detailed scanning for electrical conductivity from 2K to 50K)

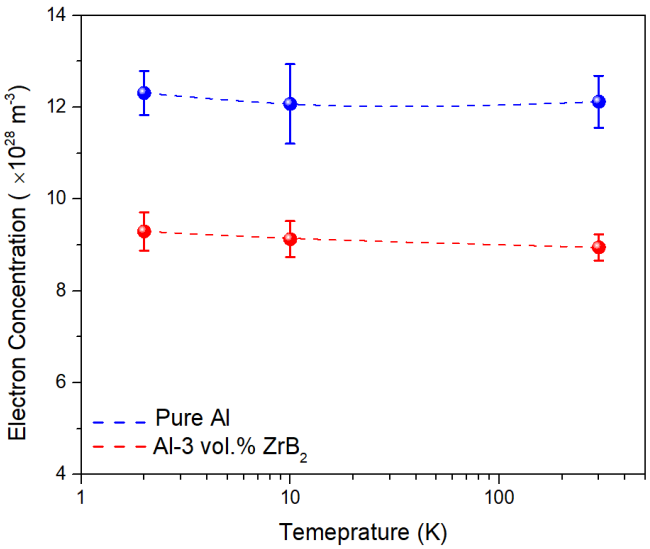

Figure 4 - 9 Electron concentration of pure Al and Al-3 vol.% ZrB_2 at 2K, 10K, and 300K

However, when the temperature is lower, the electron mobility is higher in both pure A and the Al-3vol%ZrB_2 materials; Furthermore, for pure Al and Al-3 vol.% ZrB_2 at 2K, 10K, and 300K, the electron mobilities are comparable, especially when the temperature is high when the phonon is not suppressed. Moreover, at 2K, the electron mobility does not suffer a steep drop due to the possible electron localization in the Al-3 vol.% ZrB_2 nanocomposites, implying that the reported superconductivity in ZrB_2 play little role in the nanocomposites.

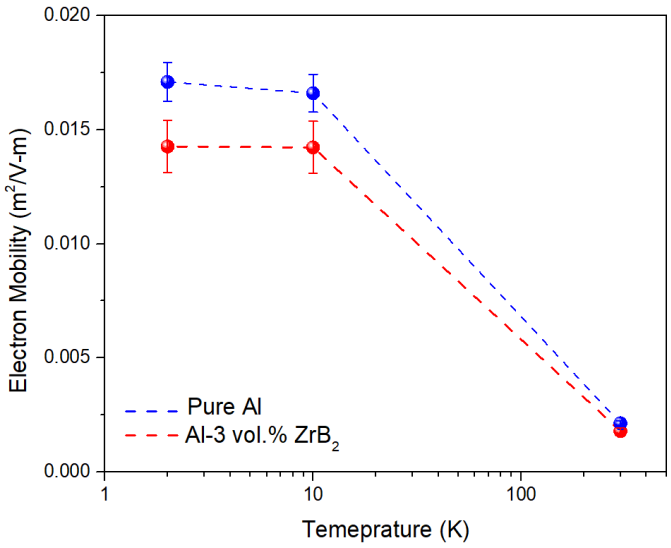

Figure 4 - 10 The electron mobility of pure Al and Al-3 vol.% ZrB_2 at 2K, 10K, and 300K.

When we calculated the Bloch-Grueneisen Factor in terms of the temperature-dependence of their electrical conductivity (See **Table 4 - 2**), the Al-3 vol.% ZrB_2 nanocomposites have a higher value than pure Al, which indicates a larger electron-phonon interaction after ZrB_2 nanoparticles are introduced.

Table 4 - 2 Reported Superconductivity Temperature and Measured Bloch-Grueneisen Factor for Al and Al-3 vol.% ZrB_2[190]

Materials	**Reported Superconductivity Temp. at 0T** **K**	**Bloch-Grueneisen Factor** **uOhm-cm**
Pure Al	1.2	4.26
Al-3ZrB₂	5.6 for ZrB_2	6.33

To separate the effects from configurational and electronic contributions, the electrical resistivity from grain boundary and dislocation change is calculated for Al-3 vol.% ZrB_2 nanocomposites via the following **Eq. 4 - 9** and **Eq. 4 - 10** (the second line) [192].

By the comparison shown in **Figure 4 - 11**, it is clear that, with a low volume percentage of ZrB_2 nanoparticles in Al, the configurational contributions by changed grain boundaries and dislocations are not directly correlated with the reduction of electrical conductivity in the Al-3 vol.% ZrB_2 nanocomposites. It could infer that the electrical conductivity reduction is larger than that of the electron concentration. It indicates that the electrical performance is affected via the indirect effect of the configurational defects on the electron concentration and electron mobility.

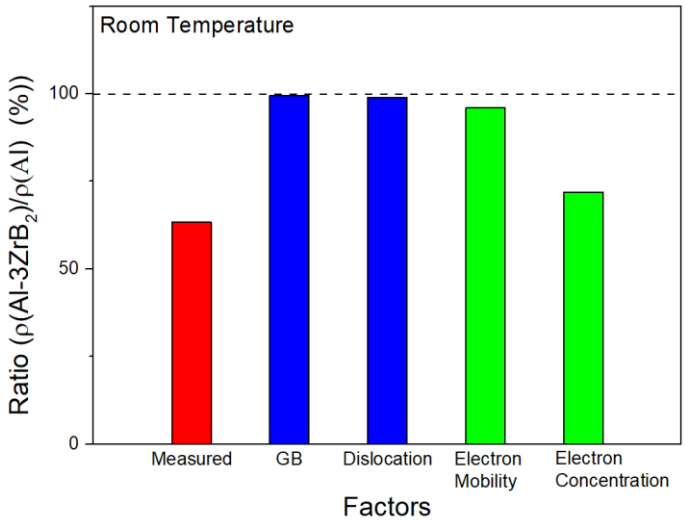

Figure 4 - 11 Comparison between the factors contributing to the reduction of electrical conductivity in Al-3 vol.% ZrB_2 nanocomposites

This study provides a quantitative study into the electrical behavior of Al-ZrB_2 nanocomposites. The 3 vol.% ZrB_2 nanoparticles are synthesized in-situ in the molten Al. The nanoparticles are pseudo-dispersed, and the Al grains are refined. After obtaining the electrical

conductivity, electron mobility, and electron concentration via Hall measurement, the contributions to the reduced electrical conductivity from configurational (i.e., grain boundary, and dislocation) and electronic (i.e., electron mobility, and electron concentration) aspects are separated and quantitatively analyzed. It is confirmed that the altered grain boundaries and dislocations are not the major reason for the reduction of electrical conductivity in the Al-3 vol.% ZrB_2 nanocomposites. The major role of the incorporated ZrB_2 nanoparticles is to introduce the above mentioned defects that increase the phonon-electron interactions, thus leading to a significant decrease in (apparent) free electron concentration.[193] This understanding can help eliminate the errors and inaccuracy from determining MMNC electrical conductivity purely by configurational considerations. Moreover, a quantitative determination of electronic parameters in Al-ZrB_2 can guide the rational design in MMNC materials for electrical applications.

4.2.1.3 Cu alloy nanocomposites

WC nanoparticles were efficiently incorporated into molten copper and its alloys by a salt assisted incorporation method [70,194]. The molten salts, including chloride salts and potassium aluminium fluoride helped remove the oxide layer of the metals and provided a medium for the nanoparticles to disperse.

Scanning electron microscopy (SEM) on *Zeiss SUPRA 40KV* and Electron Dispersive Spectroscopy (EDS) mapping were used to characterize the samples. As shown in **Figure 4 - 12**, the nanocomposite samples contain well-dispersed WC nanoparticles of high concentrations. However, there are some pseudo-dispersion zones showing locally higher loadings of dispersed nanoparticles with nanoparticle-sparse zones, while the nanoparticles are still well separated from each other [195]. Since the size of WC nanoparticles is about 100 - 200 nm (>10 nm), it rules out the

possible effects of dominant short-range atomic interaction for electrical conductivity, e.g., bonding reactions and solid solutions [196,197]. Moreover, negligible defects (e.g., porosities) and impurities are observed in the samples; Other crucial factors detrimental to the electrical conductivity of the nanocomposites could also be eliminated for discussion.

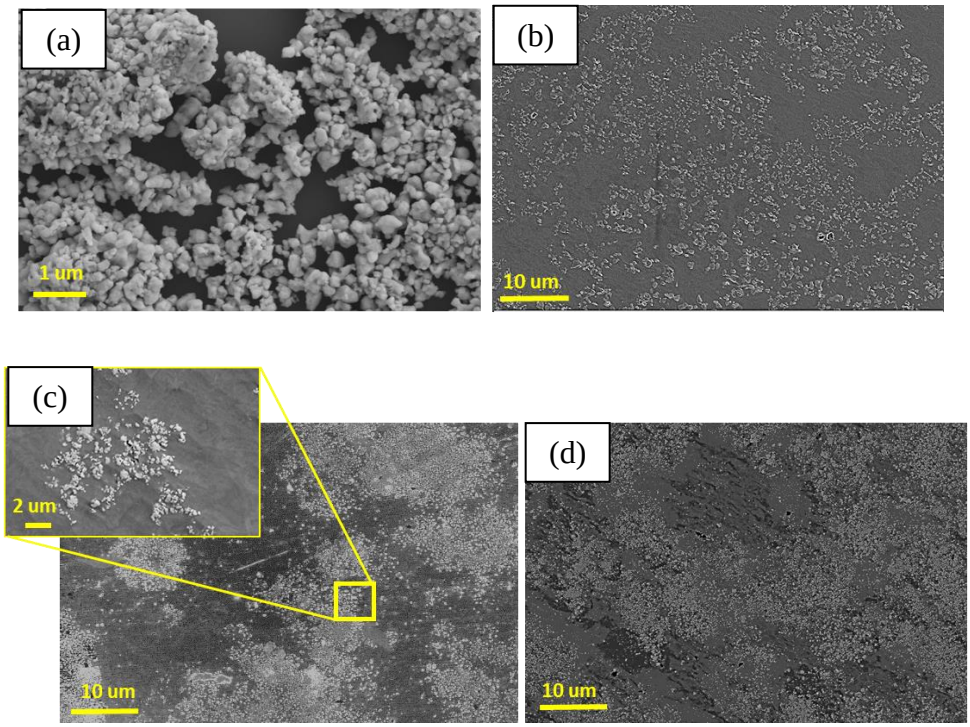

Figure 4 - 12 (a) SEM scanning image of WC nanoparticles of 100-200 nm in size (distributed and measured on silicon wafer); SEM scanning images of WC nanoparticles incorporated in (b) Cu/14 vol.% WC; (c) Cu-40 wt.% Zn/18 vol.% WC, and (d) Cu-60 wt.% Ag/11 vol.% WC. (the brighter phase is WC, all in *In-Lens* mode)

The electrical conductivity of all samples was measured using a *Prometrix Omnimap RS-35 4-point probes*, as shown in **Figure 4 - 13**, with more than 3 measurements at each site and more than 3 sites for each sample. With a higher volume percentage of WC nanoparticles, the electrical conductivity of the Cu, Cu-60wt.% Ag, and Cu-40 wt.% Zn nanocomposite samples

decayed significantly. For the pure Cu system, the electrical resistivity changed from 54.59 $\times 10^6$ S/m (1.83 μOhm · cm) for the sample containing 0 vol.% WC, to 13.68 $\times 10^6$ S/m (8.23 μOhm · cm) for the sample containing 45 vol.% WC. For the Cu-60 wt.% Ag samples, the electrical conductivity decreased from 41.92 $\times 10^6$ S/m (2.41 μOhm · cm) for the sample containing 0 vol.% WC, to 6.37 $\times 10^6$ S/m (15.86 μOhm · cm) for the sample containing 22 vol.% WC. For the Cu-40 wt.% Zn samples, the electrical conductivity changed from 16.22 $\times 10^6$ S/m (6.18 μOhm · cm) for the sample containing 0 vol.% WC, to 12.46 $\times 10^6$ S/m (8.27 μOhm · cm) for the sample containing 14.65 vol.% WC.

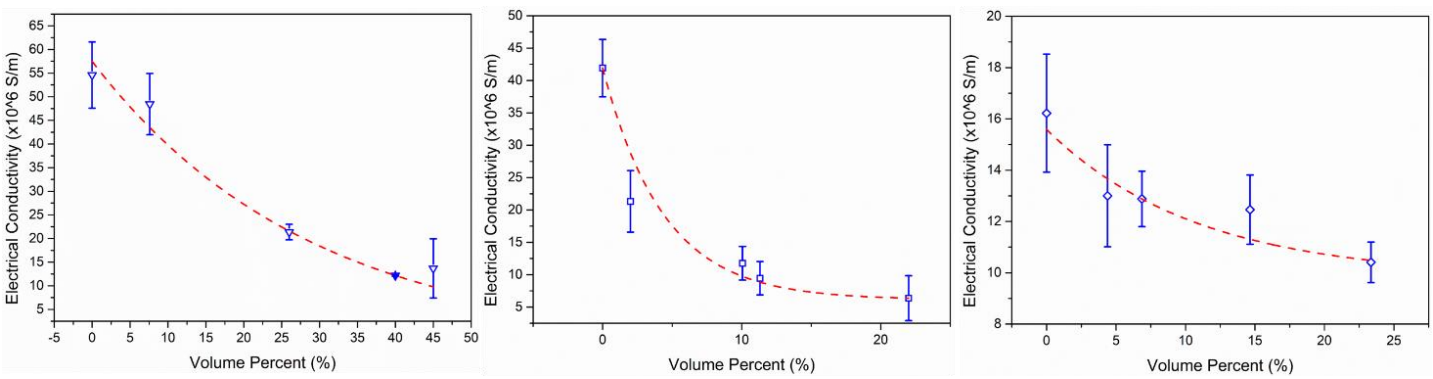

Figure 4 - 13 Electrical conductivity for systems containing different volume percentage of WC for: (a) Cu; (b) Cu-60 wt.% Ag; (c) Cu-40 wt.% Zn under room temperature of 25℃

<u>*Prediction model setup*</u> It is well known that metal and metallic ceramics such as WC have a high concentration of (nearly) free electrons [198,199]. Therefore, both material classes exhibit high electrical conductivity, even though the incorporated WC nanoparticles have very different atomic configuration. In these metallic systems, high-energy electrons near the Fermi surface (i.e.,$\varepsilon_F \pm 4k_B$T by Landauer formalism [200]) will greatly influence the transport phenomena, as shown in **Figure 4 - 14**. Therefore, the electron's transport characteristics are mostly governed by strong

electronic interactions during interfacial scattering. These electronic interactions are normally about 10 to 100 times stronger than the pure thermal interactions (e.g. diffusion scattering) [201,202].

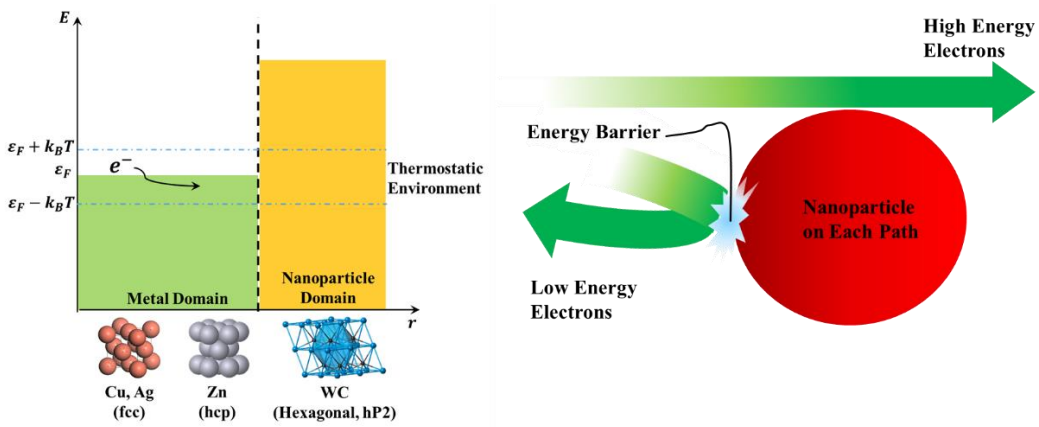

Figure 4 - 14 Energy structure at the interface of metal matrix and nanoparticles, as well as the scattering pattern of electrons at the interface (As the drifting electrons are effective for electrical transport near the fermi surface, a thermostatic environment is appropriate near the Fermi level. The other electrons, in the energy states far from the Fermi level can be considered as "isolated" from the thermostatic environment.) [203]

Different metals (including alloy systems) have different Fermi Surface energy levels. For instance, copper has its Fermi Surface at 7.00 eV, whereas metallic tungsten carbide (WC) at 22~25 eV, as shown in **Table 4 - 3** [204,205]. Here, the Fermi energy for WC is estimated from previous Fermi level studies, work function measurements, and ionization energy analyses. Since the interaction environment can be isolated from the electrons with an energy lower than $\varepsilon_F - k_B$T, the thermostatic environment can be considered as "bathed" in a constant Fermi temperature, which results in $8.16 \times 10^4\ K$ for Cu-matrix [203,206].

Table 4 - 3 Electronic Properties of Cu, Zn, Ag and WC [204–206]

Material	Fermi Level ε_F / eV	Fermi Temperature T_F / K
Cu	7.00	8.16×10^4
Zn	9.47	11.04×10^4
Ag	5.19	6.40×10^4
WC	22.0 ~ 27.5	-

Whenever constant electric currents occur in metals, electrons will travel in a specific direction at dynamical equilibrium, and current density analysis can be applied. When the conductive WC nanoparticles are uniformly dispersed in the metal, some electrons traveling within the metal will certainly interact with the metal-nanoparticle interfaces. The possibility for whether an electron will be blocked in the thermostatic layer or transport through the nanoparticle follows the probability of its partition functions, as shown in **Eq. 4 - 12** and **Eq. 4 - 13** [206].

Eq. 4 - 12 $$\zeta(E) = exp\left(-\frac{E}{k_B T}\right)$$

Eq. 4 - 13 $$P(E) = \frac{exp\,(-\frac{E}{k_B T})}{\sum \zeta(\varepsilon)}$$

Where $P(E)$ indicates the possibility for electrons to be in a certain energy state E and T depicts the environmental temperature in the system.

As implied in the equations, electron disturbance can only occur along the Fermi surface and is of very small magnitude for $\varepsilon_F \pm k_B$T. Even if we consider$\varepsilon_F \pm 4k_B$T, its value remains within a small range and can be treated as a discrete energy level (or a bandwidth of $2k_B$T~$8k_B$T) for effective electron transport [200,206]Thus, **Eq. 4 - 13** can be reduced to **Eq. 4 - 15**.

Eq. 4 - 14 $$\sum \zeta(\varepsilon) = \exp\left(-\frac{\varepsilon_{WC}}{k_B T}\right) + \frac{1}{2\delta k_B T}\int_{-\delta k_B T}^{+\delta k_B T} \exp\left(-\frac{\varepsilon_{metal}+\delta E}{k_B T}\right) dE$$

$$\approx \exp\left(-\frac{\varepsilon_{WC}}{k_B T}\right) + \exp\left(-\frac{\varepsilon_{metal}}{k_B T}\right)$$

Eq. 4 - 15 $$P(E) = \frac{exp\left(-\frac{\varepsilon_{WC}}{k_B T}\right)}{exp\left(-\frac{\varepsilon_{WC}}{k_B T}\right) + exp\left(-\frac{\varepsilon_{metal}}{k_B T}\right)} \approx exp\ (-\frac{\varepsilon_{WC} - \varepsilon_{metal}}{k_B T})$$

where ε_{WC} is the Fermi energy for WC nanoparticle, and ε_{metal} the Fermi energy for metal matrix, respectively. In this sense, the possibility of electron transmission through the interface is governed by the energy of the system and the energy barrier it must overcome.

Another important consideration for the model is the nanoparticle concentration. The concentration x (in vol.%) will conjugate with the pure energy state probability, thus yielding a diffusion free energy of activation, as shown in **Eq. 4 - 16**.

Eq. 4 - 16 $$\Delta E \approx x \cdot (\varepsilon_{WC} - \varepsilon_{metal})$$

In other words, in this model, the WC nanoparticles can be simplified as "homogeneous" (uniformly distributed) or "periodically homogeneous" (pseudo-uniformly distributed) in the metal or alloy matrix. This implies that the conductivity can be analyzed by current density and electron transport. The probability for the electrons to scatter at the nanoparticle-metal interface is proportional to the concentration percentage (i.e., $100 \cdot x$).

Therefore, for an electron floating in a metal lattice, the theoretical electrical conductivity must obey the Arrhenius Relationship:

Eq. 4 - 17 $$\sigma = \sigma_0(T) \cdot \left[exp\left(-\frac{\varepsilon_{F-WC} - \varepsilon_{F-metal}}{k_B T_F}\right)\right]^x = \sigma_0(T) \cdot exp\ (-\frac{\varepsilon_{F-WC} - \varepsilon_{F-metal}}{k_B T_F} \cdot x)$$

where T_F denotes the Fermi temperature of free electrons in metals.

By plotting the gathered experimental data in logarithmic scale, the electrical conductivity of nanoparticle reinforced copper and copper alloys (Cu, Cu-60 wt.% Ag, and Cu-40 wt.% Zn) is decaying exponentially with increasing volume fraction WC nanoparticles, as shown in **Figure 4 - 15**. The fitted equations for the curves are shown in **Table 4 - 4**.

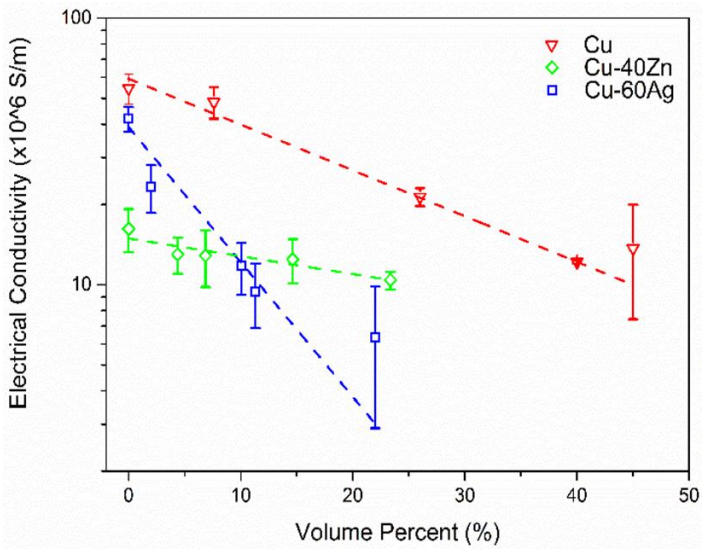

Figure 4 - 15 Electrical conductivity against nanoparticle volume percent in Cu, Cu-40 wt.% Zn, and Cu-60 wt.% Ag under room temperature of 25℃

To further validate this theory, it was further tested in both low (the temperature of liquid N_2) and high temperature environments (the temperature above Debye temperature) regarding electrical and thermal aspects.

For the low temperature range, a Hall effect measurement setup was used to characterize the electrical conductivity of WC nanocomposites. The temperature range is 80-270 K and was achieved by liquid nitrogen cooling, and the temperature scanning speed was set to 0.1 K/s. The constant current was set as 0.05 mA (i.e., ~5×10^4 $A/_{m^2}$) to cause an obvious voltage change in the experiments results. All connections are linked by silver (pure, ~1.6 uOhm-cm), which is ~10 times more conductive than that of Cu-40 wt.% Zn and its nanocomposites. Therefore, the contact effect for electrical conductivity measurement minimized. During the experiment, the electron density in each system does not change with temperature but with the nanoparticle concentration, which rules out temperature-sensitive factors like thermal activation for carrier number variation.

The results are shown in **Figure 4 - 16**. (a). It is clear that for both pure Cu-40 wt.% Zn and Cu-40 wt.% Zn/13.5 vol.% WC, with the increasing temperature, the electrical resistivity increases, due to the stronger lattice scattering. The typical shape memory phase change (at ~215-225 K) of Cu-40 wt.% Zn was resulted in a change of electrical conductivity in both samples. If the electrical resistivity ratio of pure and 13.5 vol.% WC-incorporated samples (i.e., the ratio of the electrical conductivity between 13.5 vol.% WC-incorporated samples and pure) is considereed, it's found to be almost constant with a value of 0.71 ± 0.03. By applying **Eq. 4 - 17**, the theoretically predicted ratio is ~0.76, which fits the experimental observation well. The invariance of the electrical resistivity ratio of pure matrix and 13.5 vol.% WC nanocomposites proved the important role of the Fermi level mismatch in our theory.

For the high temperature range (i.e., above Debye temperature), the Differential Scanning Calorimetry (DSC) was conducted for pure Cu-40 wt.% Zn and Cu-40 wt.% Zn/16 vol.% WC samples to obtain the electronic heat capacity change, as shown in **Figure 4 - 16** (b). Since the Debye temperature for Cu, Zn and Ag is about -50~30 ℃, the heat capacity below 0-100 ℃ (i.e., 273-373 K) should result in:

Eq. 4 - 18

$$\frac{\partial C_{ve}}{\partial T} \cong \frac{\pi^2 \cdot \overline{n_e} \cdot k_B^2}{2\varepsilon_F}$$

In this case, $\frac{\partial C_{ve}}{\partial T}$ for pure Cu-40 wt.% Zn system was derived as ~$3.6 \times 10^{-4}\ \mathrm{J/(g \cdot K^2)}$ and for Cu-40 wt.% Zn/16 vol.% as ~$2.5 \times 10^{-4}\ \mathrm{J/(g \cdot K^2)}$. By using the following predicted relationship:

Eq. 4 - 19

$$\frac{\left(\frac{\partial C_{ve}}{\partial T}\right)_{np}}{\left(\frac{\partial C_{ve}}{\partial T}\right)_{pure}} \cong {(\overline{n_e})_{np}}\Big/{(\overline{n_e})_{pure}} \approx \exp\left(-1.86 \cdot \mathrm{x}\right)$$

Therefore, the theoretical calculated volume percentage of the Cu-40 wt.% Zn/16 vol.% WC resulted in ~19 vol.%. This further confirmed the feasibility of our theory.

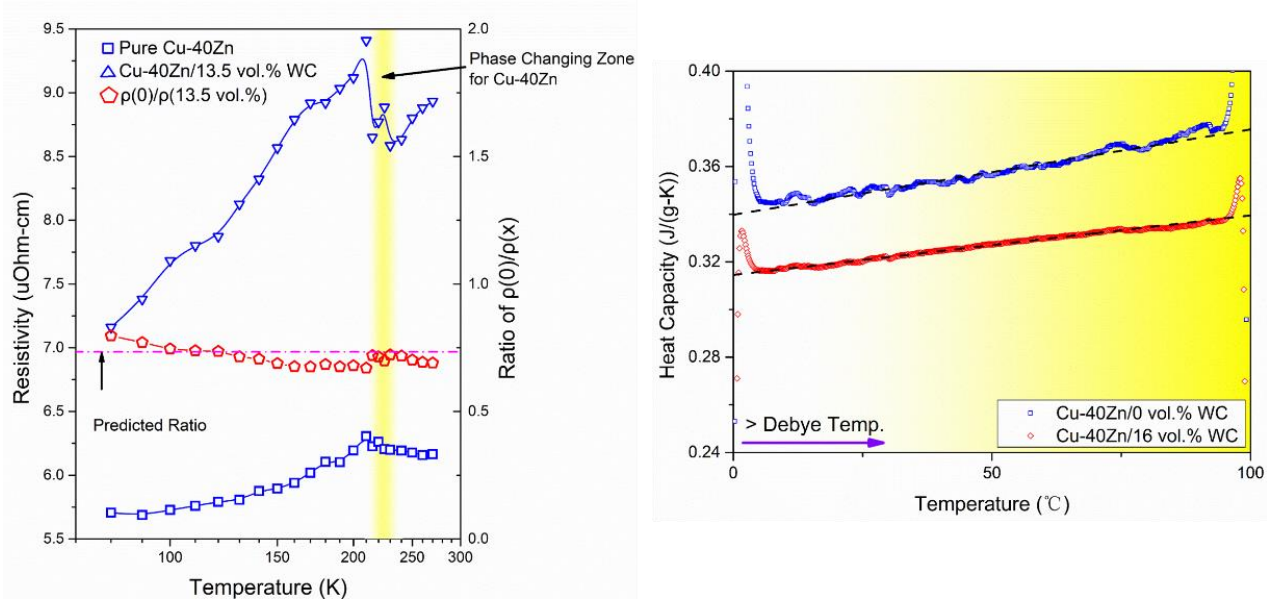

(a) (b)

Figure 4 - 16 (a) Electrical resistivity for Cu-40 wt.% Zn and Cu-40 wt.% Zn/13.5 vol.% WC between 80 K and 270 K, as well as the electrical resistivity ratio between the pure and 13.5vol.% WC samples; (b) Electronical heat capacity change above the Debye temperature for Cu-40 wt.% Zn and Cu-40 wt.% Zn/16 vol.% WC.

Table 4 - 4 Fitted Equations for Electrical Conductivity of the nanocomposites (the Fermi level for alloy systems is set at the average value; σ is in unit of $\times 10^6\ S/m$)

Matrix	Fitting Equation	Calculated from Equation
Cu	$\sigma \cong 59.18 \cdot \exp(-3.95 \cdot x)$	$\sigma \cong 54.59 \cdot \exp(-2.34 \cdot x)$
Cu-60 wt.% Ag	$\sigma \cong 41.98 \cdot \exp(-9.07 \cdot x)$	$\sigma \cong 41.92 \cdot \exp(-5.50 \cdot x)$
Cu-40 wt.% Zn	$\sigma \cong 15.21 \cdot \exp(-1.62 \cdot x)$	$\sigma \cong 15.22 \cdot \exp(-2.06 \cdot x)$

More importantly, by performing a Taylor expansion of the trend term (i.e., around zero volume percent of WC), the electrical resistivity trend could be derived, as shown in **Eq. 4 - 20**.

Eq. 4 - 20 $$\rho = \frac{1}{\sigma} = \frac{1}{\sigma_0(T)} \cdot exp\left(\frac{\varepsilon_{F-WC} - \varepsilon_{F-metal}}{k_B T_F} \cdot x\right)$$

$$= \rho_0 \cdot \left[1 + \frac{\varepsilon_{F-WC} - \varepsilon_{F-metal}}{k_B T_F} \cdot x + \frac{1}{2}\left(\frac{\varepsilon_{F-WC} - \varepsilon_{F-metal}}{k_B T_F} \cdot x\right)^2 + o(x^2)\right]$$

Since the size of the WC nanoparticles used in this study ranges between 100 nm - 200 nm in diameter, it is considered appropriate to model latter as impurities in the metal matrix. This simplification allows us to assume that the application of Nordheim's rule, and therefore the possibility to empirically determine the electrical resistivity of the system, is viable. The transformation of the expansion series shown in **Eq. 4 - 20Eq. 4 - 13** into the standard (quasi-) binary system using the Nordheim formula resulted in **Eq. 4 - 21**.

Eq. 4 - 21 $$\rho = \rho_0 \cdot \left[1 + \frac{\varepsilon_{F-WC} - \varepsilon_{F-metal}}{k_B T_F} \cdot x + \frac{1}{2}\left(\frac{\varepsilon_{F-WC} - \varepsilon_{F-metal}}{k_B T_F} \cdot x\right)^2\right]$$

$$= \rho_0 + k_1 \cdot x + k_2 \cdot (1 - x) \cdot x$$

Since Nordheim’s rule considers the potential perturbation and different scattering centers to determine the scattering probability using the Born approximation (see **Eq. 4 - 22** and **Eq. 4 - 23**), it is found highly compatible with the presented macroscopic electrical conductivity trends and suggests that our model for interface scattering by energy difference is valid, as shown in **Eq. 4 - 23**.

Eq. 4 - 22 $P(scattering) \propto x \cdot P(A) + (1 - x) \cdot P(B) = \sum_i x_i \cdot [(1 - x_i)^2 \cdot p^2]$

Eq. 4 - 23 $$p = \int \varphi_{k1} \cdot (E_{pi} - E_p) \cdot \varphi_{k2} dV$$

where $(E_{pi} - E_p)$ is the potential difference in 2 components, and p depicts the single-direction scattering probability density from state φ_{k1} to φ_{k2}. x_i is the corresponding volume fraction for component A or B.

Limitations on the new model This new model, however, has some limitations regarding its ability to explain the collective electron transport behavior in nanocomposites. First, one of the assumptions made indicates that the moving electrons can always reach an equilibrium, at which the electron density is not a function of space or time. This equilibrium ensures that the electrical conductivity is determined by the material's electron concentration (i.e., from **Eq. 4 - 12** to **Eq. 4 - 17**). Second, the used nanoparticle is of metallic nature, which makes Fermi energy a very important factor for electronic transport. This implies that, for nanocomposites containing dielectric nanoparticles, e.g., Al_2O_3, the new model's predictions my not be satisfactory. Moreover, the physical explanation for this trend does not consider the effect of the nanoparticle size since the nanoparticle size is larger than the electron mean free path in the matrix [186]. If the used nanoparticle is small (~10 nm [186]), electron tunnelling effects etc. may play a non-negligible role in the material's electronic behaviour. The interfaces shown in **Figure 4 - 14** may therefore be invalid and the energy barrier must be viewed as a continuum.

In summary, our study proposes the first model to predict the decaying electrical conductivity in copper matrices (of Cu, Cu-40 wt.% Zn, and Cu-60 wt.% Ag) containing WC nanoparticles with a diameter of about 100-200 nm. This model considers the electronic structure difference, the interface scattering, and the Nordheim equation. The new model suggests that scattering at the metal-nanoparticle interface in the samples with higher nanoparticle loadings will reduce the probability for the collective electrons to pass the electronic interfacial energy barrier. This results in an exponentially decaying electrical conductivity. The model is experimentally validated by resistivity measurements at different temperatures and electronic heat capacity measurements above the Debye temperature.

4.2.2 Thermal Properties

4.2.2.1 Al-TiC, Al-TiB_2, and Al-ZrB_2 nanocomposites

Thermal performance The thermal diffusivity (shown in **Figure 4 - 17** (a)-(c)) by the laser flash method shows the same decaying trend as with the electrical conductivity. The thermal diffusivity for pure Al is $\sim 10.5 \times 10^{-5}\ m^2/s$; the value for Al-TiC nanocomposite changes to $\sim 8.3 \times 10^{-5}\ m^2/s$ for 3.68 vol.% TiC; Al-ZrB_2 nanocomposite changes to $\sim 7.5 \times 10^{-5}\ m^2/s$ for 3 vol.% ZrB_2; and Al-TiB_2 nanocomposite changes to $\sim 8.4 \times 10^{-5}\ m^2/s$ for 3 vol.% TiB_2.

After scanning the heat capacity of all the nanocomposites up to the aluminum's Debye temperature (see **Figure 4 - 17** (d)-(f)), the room temperature heat capacity for all nanocomposites is extracted from the measruements and plotted in the inserted figures of **Figure 4 - 17** (d)-(f). It is interesting to note that: at room temperature, with the increasing volume percentage of nanophases, the heat capacity will decrease; as the temperature increases, the heat capacity of the nanocomposites will surpass that of pure Al. This trend occurs because TiC, ZrB_2, and TiB_2 have much lower heat capacity than pure Al at low temperature; as the temperature goes higher, heat capacity in TiC, ZrB_2, and TiB_2 contributed by phonons will increase rapidly with thermal activation until it exceeds that of pure Al [73,207,208].

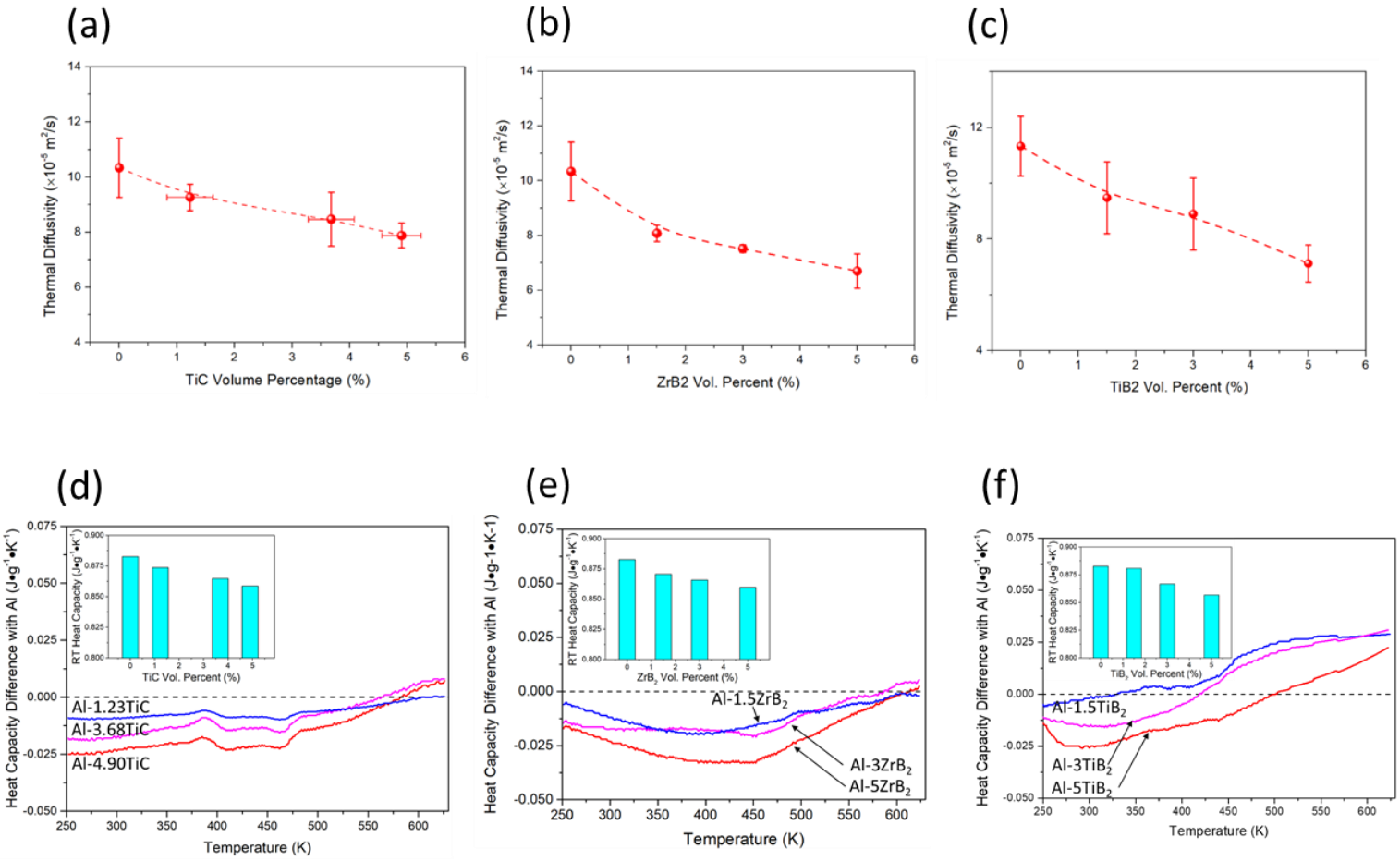

Figure 4 - 17 Room-temperature thermal diffusivity for in situ (a) Al-TiC nanocomposites, (b) Al-ZrB_2 nanocomposites, and (c) Al-TiB_2 nanocomposites; temperature scanning for the heat capacity in *in situ* (d) Al-TiC nanocomposites, (e) Al-ZrB_2 nanocomposites, and (f) Al-TiB_2 nanocomposites, demonstrated by the difference with the pure Al.

The nanocomposites' room-temperature thermal conductivity is calculated and plotted in **Figure 4 - 18** (a)-(c) with the information from thermal diffusivity and heat capacity. Pure Al has a thermal conductivity of $\sim 251.01\ W/m \cdot K$; With 3.68 vol.% TiC nanoparticles, the value is $\sim 190.49\ W/m \cdot K$; With 3 vol.% ZrB_2 and 3 vol.% TiB_2, it changes to $\sim 187.83\ W/m \cdot K$ and $\sim 212.28\ W/m \cdot K$, respectively. Together with the nanoparticle sizes from **Figure 3 - 11**, via the

EMT illustrated in **Figure 4 - 18** (d) and material properties from **Table 4 - 5**, the thermal conductance at the Al-TiC, Al-TiB_2, and Al-ZrB_2 interfaces are estimated to be $\sim 3.89 \times 10^8\ W/m^2 \cdot K$, $\sim 3.44 \times 10^8\ W/m^2 \cdot K$, and $\sim 2.60 \times 10^8\ W/m^2 \cdot K$, respectively (See **Figure 4 - 19**).

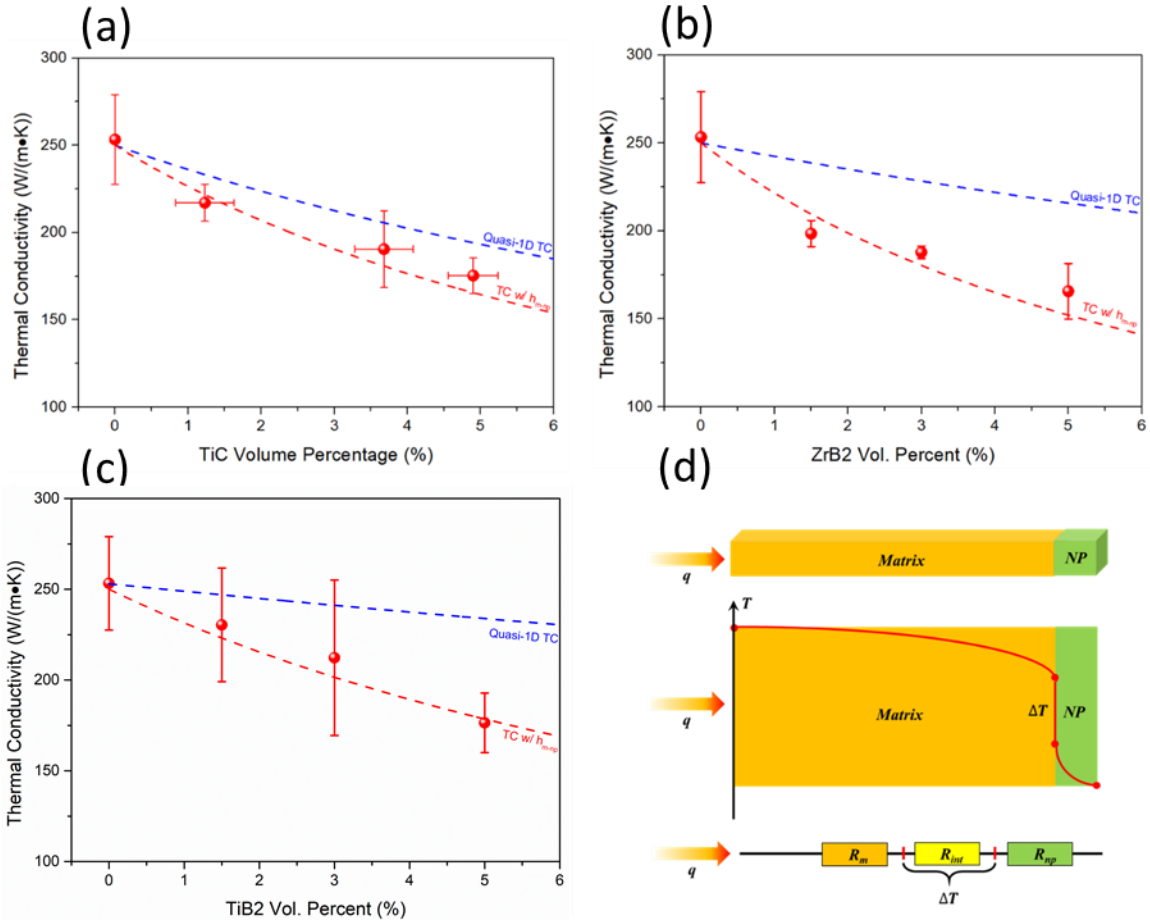

Figure 4 - 18 Room-temperature thermal conductivity for *in situ* (a) Al-TiC nanocomposite, (b) Al-ZrB_2 nanocomposite, and (c) Al-TiB_2 nanocomposite (all shown with the Quasi-1D Model by mixing rule and Interfacial Thermal Conductance Model by EMT); (d) schematic illustration for Interfacial Thermal Conductance Model by EMT and the method for calculating interfacial thermal conductance.

Table 4 - 5 Wettability, room-temperature thermal conductivity, and room-temperature heat capacity of three different nanoparticles in this study[72,73,209,210]

	Contact Angle with Al at 900℃ (°)	**RT Thermal Conductivity (W/m^2-K)**	**RT Heat Capacity (J/g-K)**	**Sommerfeld Coeff. (mJ/mol-K^2)**	**Fermi Velocity ($\times 10^5$ m/s)**	**Sound Velocity (m/s)**
TiB_2	~60	96.0	0.923	0.9	5.7	7640
TiC	~50	36.4	~0.60	0.68	18.3	6200
ZrB_2	~75	53.0	~0.45	0.65	3.2	9233

Theoretical study The AMM- and DMM-predicted values for various interfacial thermal conductance are also summarized in Figure 4 - **19**.[83,86] It is clear that compared with the literature values, Al-AlN and Al-Al_2O_3 nanocomposites fit the AMM and DMM models reasonably well. The main cause is the lack of effective electron transport inside AlN and Al_2O_3 nanophases, which simplifies the thermal transport coupling process at Al-nanoparticle interfaces. However, for TiC, ZrB_2, and TiB_2 nanoparticles, a huge mismatch among experimental values, AMM models, and DMM models is observed. This discrepancy implies that a significant coupling thermal transport process involving electrons takes off at the Al-ceramic nanoparticle interface, given their supreme electrical conductivity.

Since electron-electron (e-e) and electron-phonon (e-ph) coupled thermal transports are orders of magnitude more effective than pure phonon-phonon (ph-ph) coupled thermal transport at interfaces (as shown in **Table 4 - 6**), the predicted electron coupling DMM values are higher

than the experimental values and much higher than the expected phonon coupling AMM and DMM values (See **Figure 4 - 19**).

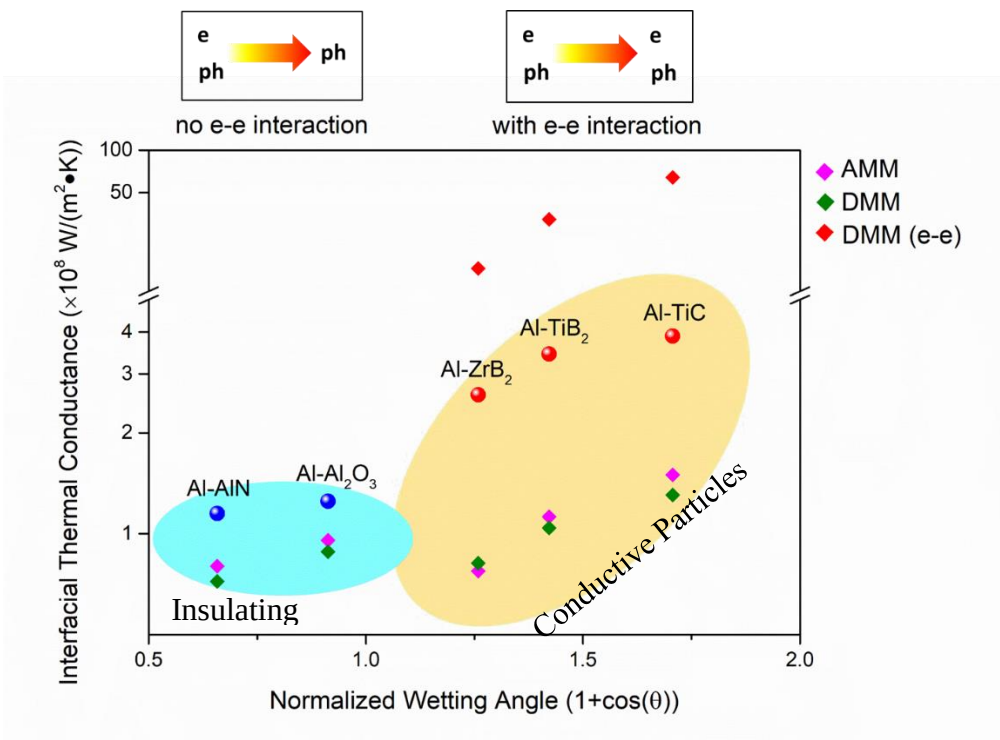

Figure 4 - 19 Dependence of interfacial thermal conductance on matrix-nanoparticle wettability (i.e., interfacial interaction strength) for *in situ* Al-TiC, Al-ZrB_2, and Al-TiB_2 nanocomposites, as compared with other literature data.[81,85]

Table 4 - 6 The typical magnitudes for interfacial thermal conductance by couplings between phonons and electrons

Coupling Factors	Estimated h_c
Phonon-phonon (ph-ph)	$\sim 10^7 - 10^8\ W/m^2 \cdot K$
Electron-phonon (e-ph)	$\sim 10^8 - 10^9\ W/m^2 \cdot K$
Electron-Electron (e-e)	$\sim 10^9 - 10^{10}\ W/m^2 \cdot K$

When the electronic thermal contribution in Al-TiC, Al-ZrB_2, and Al-TiB_2 is calculated in **Figure 4 - 20**, it is clear that Al-TiC has the highest electronic thermal transport among them. This difference also indicates that the electron-involved thermal transport features are more obvious at Al-TiC interfaces.

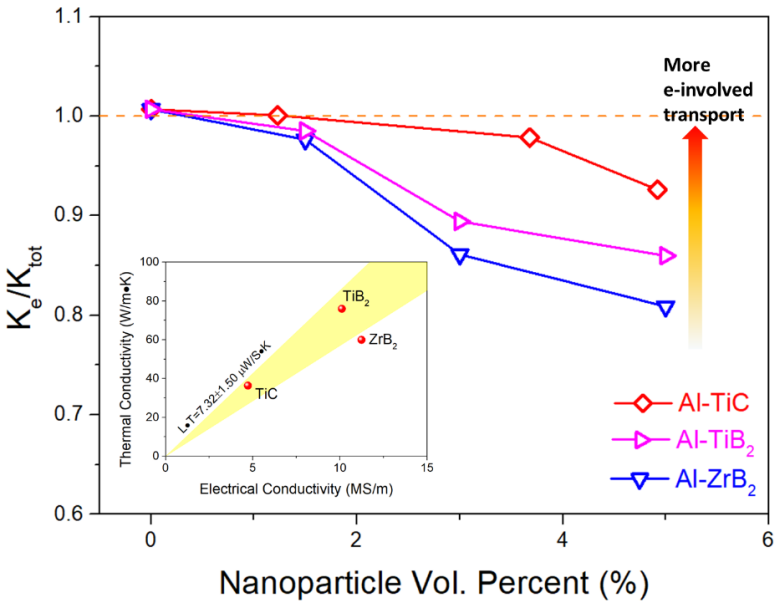

Figure 4 - 20 Electronic thermal conductivity contribution of in situ Al-TiC, Al-ZrB_2, and Al-TiB_2 nanocomposites.

<u>*New model*</u> After confirming the electron's and phonon's roles in interfacial thermal transport, the next objective is to assess their heat transport characteristics quantitatively in a facile and accurate way.

Microscopically, the interfacial thermal conductance is mainly determined by interfacial bonding strength (which can be characterized by interfacial separation energy w_{sep}), effective bonding numbers and types,[211] and the effective coupled thermal conducting paths (tuned by bonding characteristics)[85].

For nanoparticles incorporated into an Al matrix, the adhesion free energy can be depicted as:[174,212]

Eq. 4 - 24 $$E_a(\mathrm{RT}) \cong (1+\cos(\theta(T_0)) \cdot \gamma_{Al} - \int_{T_0}^{RT} S_{interface} dT$$

Where $\theta(T_0)$ is the contact angle θ under *in situ* processing temperature T_0 and γ_{Al} is the liquid Al surface tension. The interface entropy change $S_{interface}$ will be composed of vibrational, configurational, and fusion components, mainly determined by the solidification phase change of Al.[212] In this sense, the matrix-dependent term $\int_{T_0}^{RT} S_{interface} dT$ could be treated as a constant. Therefore, as θ goes lower, the adhesion energy (depicting the pre-formed interfaces at T_0) will be more prominent; when E_a is larger, the interfacial interaction will effectively change to chemical bonds and tune the electron/phonon behavior at interfaces.[79] Therefore, the magnitude of E_a is a good assessment of bonding extent and numbers by the relationship of:

Eq. 4 - 25 $$E_a(\mathrm{RT}) \propto (1+\cos(\theta(T_0)) \propto \mathrm{N}$$

Where N denotes the effective bonding numbers (which are also responsible for tuning transport phenomena). As mentioned above (see **Figure 3 - 9**), the strongest XRD peaks of pure Al like (111) show better lattice matching with specific strong XRD peaks of TiC, ZrB_2, and TiB_2, which validates the formation of effective and stable interfacial bonding between Al and three ceramic nanoparticles.[174]

Given that the bonding strengths for all these nanoparticles are at about the same order (~1 J/m^2), the interfacial thermal conductance can then be estimated semi-quantitatively by:

Eq. 4 - 26 $$h_c \propto N \cdot w_{sep} \propto E_a(RT) \cdot w_{sep}$$

The data of the expected magnitude of $E_a(RT) \cdot w_{sep}$ is summarized in **Figure 4 - 21**. Compared with the literature, we should note that even though Al_2O_3 has a very high bonding

strength (i.e., large w_{sep}) with Al, it has a poor wettability (i.e., small E_a); the low wettability leads to the low possibility for interfacial bonding [22]. Further considering the insulating characteristics of Al_2O_3 (see **Figure 4 - 21**), the interfacial thermal conductance is not comparable to metallic nanoparticles (i.e., TiC, ZrB_2, and TiB_2), as indicated in **Figure 4 - 19**.[84] This proves the feasibility of **Figure 4 - 19** for interfacial thermal conductance comparison and prediction.

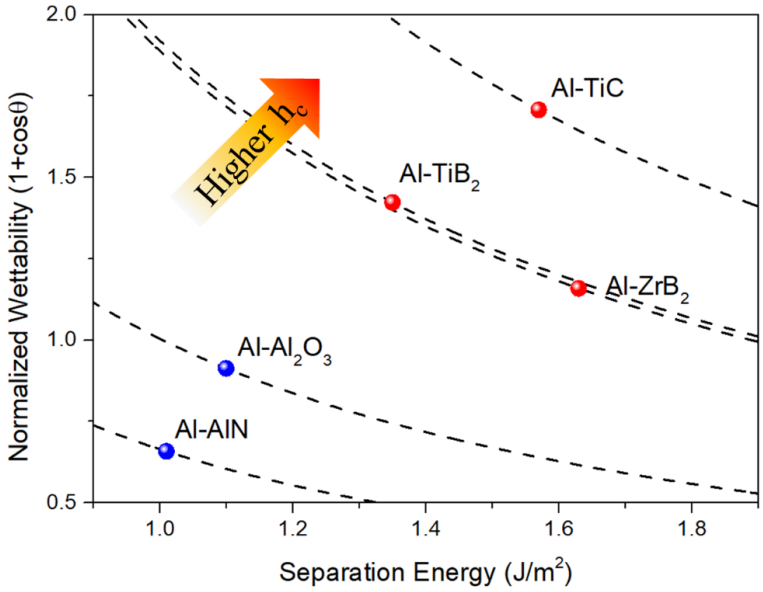

Figure 4 - 21 The dependence of interfacial thermal conductance h_c on interfacial wettability and separation energy; the examples are TiC, TiB_2, ZrB_2 (in our experimental study), Al_2O_3, and AlN (from literature values) in Al matrix.

In conclusion, the thermal properties (including thermal diffusivity, heat capacity, and thermal conductivity) of *in situ* Al-TiC, Al-ZrB_2, and Al-TiB_2 nanocomposites are systematically studied. The interfacial thermal conductance between Al and these metallic ceramics are quantitatively determined via EMT models. Due to their electrical conductivity, the interface's electronic thermal conductance is confirmed to play an important role for different ceramic nanoparticles in the Al-based nanocomposites. By evaluating the AMM and DMM models with

the different coupling transport interpretations, electrons and phonons are believed to be tuned by their interfacial characteristics, including wettability (showing the possible effective bonding number) and separation energy (showing their interaction strength). The relatively higher interfacial thermal conductance between Al and metallic ceramic nanoparticles like TiC is attributed to the more efficient interfacial electron coupling transport. For a quantitative interfacial thermal conductance prediction on the metal matrix nanocomposites with metallic ceramic nanoparticles, the interface wettability and interface separation energy are correlated to determine the interfacial coupling intensity and the interfacial thermal conductance, which yield a good match with experimental results. This understanding of interfacial thermal conductance in metal matrix nanocomposites into interfacial transport behavior will greatly guide the rational design of metal matrix nanocomposites for thermal management and heat transport applications.

4.2.2.2 Cu-Ag/WC nanocomposites

Thermal Properties of Cu-60Ag/WC Nanocomposite To determine the thermal conductivity of the materials, differential scanning calorimetry (DSC) and laser flash methods were used to measure heat capacity and thermal diffusivity, respectively (see ***Appendix*** of this section and **Figure 4 - 1**). Thermal conductivity, heat capacity, and thermal diffusivity of Cu-60Ag/WC nanocomposites are summarized in **Figure 4 - 22** (a), (b), and (c), respectively. The thermal conductivity witnesses a surprising enhancement to the highest 420.5 W/m·K when the WC nanoparticle volume percentage approaches 10 vol.%, breaking the upper-limits of thermal conductivity for nanocomposites set by both the HS and Weiner models. According to **Figure 4 - 22** (b) and **Figure 4 - 30** (a), the heat capacity of Cu-60Ag/WC nanocomposites shows a similar trend to thermal conductivity in **Figure 4 - 22** (a). In light of the structural parameters (see **Table**

4 - 7) and the temperature scanning of heat capacity (see **Figure 4 - 30** (b)), the heat capacity changes accordingly with the increased WC volume percentage because WC has a heat capacity between copper and silver and a higher atomic density than both. It suggests that phonons, originally secondary in metals or alloys, can be tuned and enhanced in the nanocomposite. It should be noted that WC keeps its phase composition and atomic ratio without any non-stoichiometric transition to WC_x,[70] as shown by the X-ray pattern of the composition of Cu-60Ag and Cu-60Ag/10 vol.% WC in **Figure 4 - 22** (d). Most importantly, together with the annealing heat-treatment results as shown in **Figure 4 - 23** (a) and (b), the DSC and XRD results rule out the possibility of phase transition, composition change, and existence of metastable phase to tune thermal conductivity.

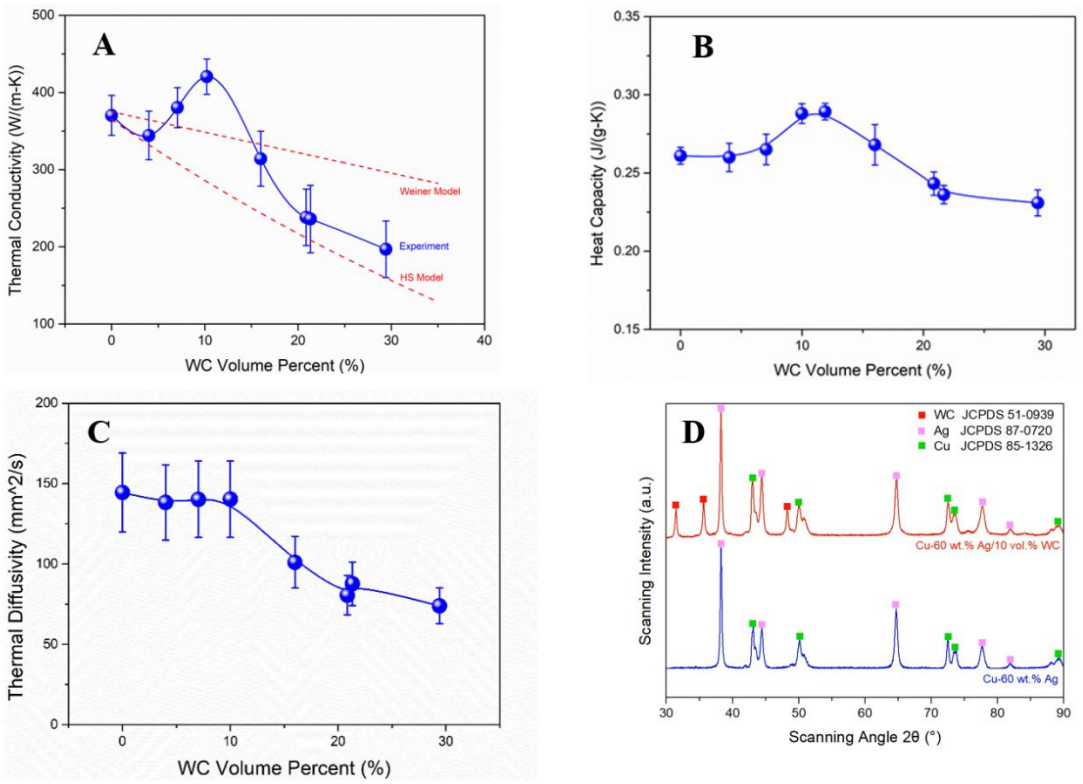

Figure 4 - 22 (a) Thermal conductivities of Cu-60Ag/WC nanocomposites with different volume percentages of WC nanoparticles, in comparison with HS and Weiner models; (b) Heat

capacities at room temperature for Cu-60Ag/WC nanocomposites; (c) Thermal diffusivities of Cu-60Ag/WC nanocomposites by laser flash method; (d) XRD analyses and JCPDS references of Cu-60Ag and Cu-60Ag/10 vol.% WC nanocomposites.

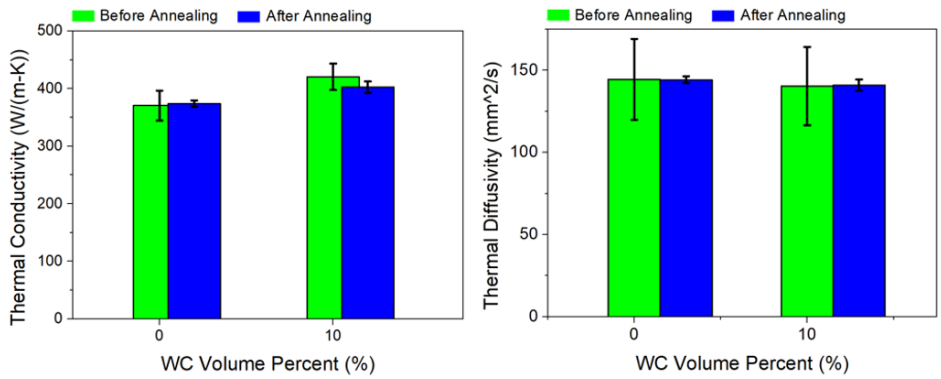

Figure 4 - 23 (a) Thermal conductivity and (b) thermal diffusivity of long-term annealed Cu-60Ag and Cu-60Ag/10 vol.% WC.

<u>*Electron and Phonon Contributions*</u> In metals and alloys, thermal conductivity is mainly determined by heat capacity (**Figure 4 - 22** (b) and **Figure 4 - 30** (a)) and electrical conductivity macroscopically. The tuned heat capacity as shown in **Figure 4 - 22** (b) indicates that the importance of matrix-nanoparticle interactions to create more energy absorbing states. To further discern the possible underlying mechanisms for the unusually enhanced thermal conductivity in the nanocomposites with about 10 vol.% WC, it is of significance to determine the heat transport contributions from phonons and electrons (**Figure 4 - 24** (a) and (b)), respectively, via the Wiedmann-Franz law,[213–216] because the long-term study of transport phenomena yields the expressions for the thermal conductivity in the form:

Eq. 4 - 27 $$k = \alpha \cdot C_p \cdot \rho = k_e + k_{ph}$$

As shown in **Eq. 4 - 27**, the total thermal conductivity could also be expressed from the contribution of electronic thermal conductivity k_e and phonon thermal conductivity k_p.

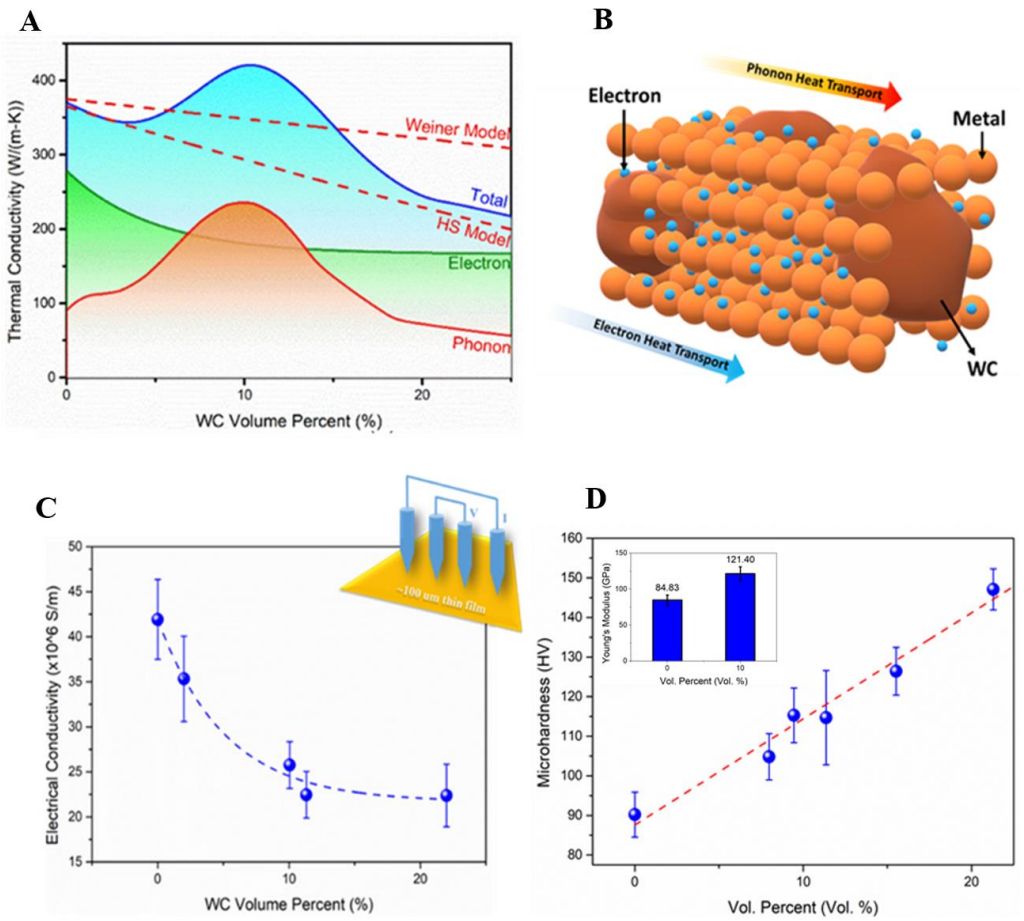

Figure 4 - 24 (a) Phononic and electronic thermal conductivity analyses for Cu-60Ag/WC nanocomposites; (b) Descriptive illustration for microscopic thermal transport in a metal matrix nanocomposite; (c) Electrical conductivities at room temperature of Cu-60Ag/WC nanocomposites; (d) Microhardness of Cu-60Ag/WC nanocomposites (Inserted: Young's modulus of Cu-60Ag and Cu-60Ag/10 vol.% WC).

<u>*Electron Contribution*</u> The electrical conductivity of the samples has been measured (see ***Appendix*** of this section), and the result is shown in **Figure 4 - 24** (c). The Wiedemann-Franz law was then used to calculate the theoretical thermal contribution from electrons. Thereby, the

separate thermal contributions from phonons and electrons have been determined, as shown in **Figure 4 - 24** (a).

For electron transport analyses (i.e., k_e), the decrease in electrical conductivity with the increasing WC volume fraction (**Figure 4 - 24** (c)) is associated with the scattering barriers imposed by the incorporated WC nanoparticles. For Cu-60Ag systems, 10 vol.% WC nanoparticles scattered away ~30% electrical conductivity from the pure alloy. Given the nanoparticle size of about 200 nm (see **Figure 3 - 1**), this decaying trend is inevitable because the mean free path of electrons as fermions are 10-100 nm in metals and alloys [179,217].

Phonon Contribution The phononic thermal transport is governed by the following equation:

Eq. 4 - 28

$$k_{ph} \cong \frac{1}{3} \cdot C_v \cdot v_g^2 \cdot \tau$$

Where v_g is the group velocity, and the average scattering time is determined by $\frac{1}{\tau} = \sum_i \frac{1}{\tau_i}$ including scattering from phonon-phonon, electron-phonon, mass inconsistency (e.g. fourth order point-defect scattering), and interfacial boundaries [44,178,218].

First of all, for group velocity v_g, the addition of WC nanoparticles has a positive effect: by the continuum theory in solids, the group velocity can be estimated by $\overline{v_g} = \sqrt{E/\rho}$, [219,220] given the correlation in metal matrices of $HV = \alpha \cdot E^m$. [219,221] A substantial enhancement in the microhardness (**Figure 4 - 24** (d)) indicated the potential increase of the group velocity in Cu-60Ag/10 vol.% WC nanocomposites [222].

Second, in terms of the decreased electrical conductivity in Cu-60Ag/WC nanocomposites (**Figure 4 - 24** (c)), this reduction in electrical conductivity can potentially reduce the phonon-electron scattering when the highly dense electrons get scattered in the alloy matrices (i.e. τ_{e-ph}) [218].

Third, WC nanoparticles of size ~200 nm could rarely scatter phonons as point defects, whose frequency in metals is mostly very high (~1-10 THz [223,224]) (**Figure 3 - 1**); this may also help as the advantageous prerequisite for phonon recovery. Atomically, according to other simulation theories, WC has a larger phononic band gap between acoustic and optical phonon branches, [225] which also helps minimize acoustic-optical phonon scattering (i.e. τ_{ph-ph}) of the nanocomposite system compared with the pure alloys [218]. This also gives WC more superior and favorable properties over other nano-reinforcements like TiC, CrB_2, etc, as demonstrated in **Figure 4 - 25** (a). Meanwhile, in comparison to other highly conductive metallic ceramics, including other common carbides, borides, and silicides, WC, similar to elemental tungsten, has a large Lorentz constant of about $77.3\ \mathrm{mW \cdot u\Omega \cdot K^{-2}}$, as shown in **Figure 4 - 25** (b). Since the Lorentz constant gives the correlation between thermal conductivity carried by electronic carriers, these characteristics could help restore the thermal transport in alloys and minimize the effect of reduced electrical conductivity on thermal conductivity (**Figure 4 - 25** (b)) [226].

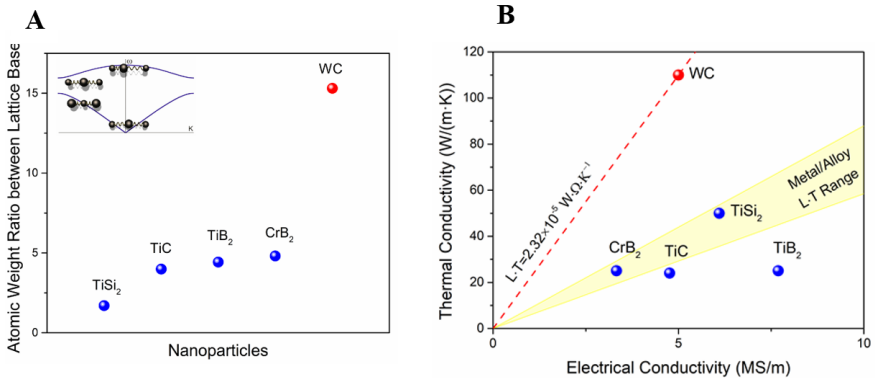

Figure 4 - 25 (a) Atomic weight ratio between lattice bases in different nano-reinforcemenst; (b) Lorentz Constant of WC compared with metallic system (metal/alloy) range and other usual highly conductive ceramics.

Besides, the alloy concentration and atomic ratio in the eutectic phase of Cu-60Ag/10 vol.% WC nanocomposite compares favorably to those of pure Cu-60Ag. The presence of WC nanoparticles purifies the eutectic structures and reduces the concentration variation, [16] which will effectively reduce the scattering from mass inconsistency of the Cu-Ag metal matrix [218] (See **Figure 4 - 26**). The high-purity Ag and Cu phases can then offer a better thermal transport.

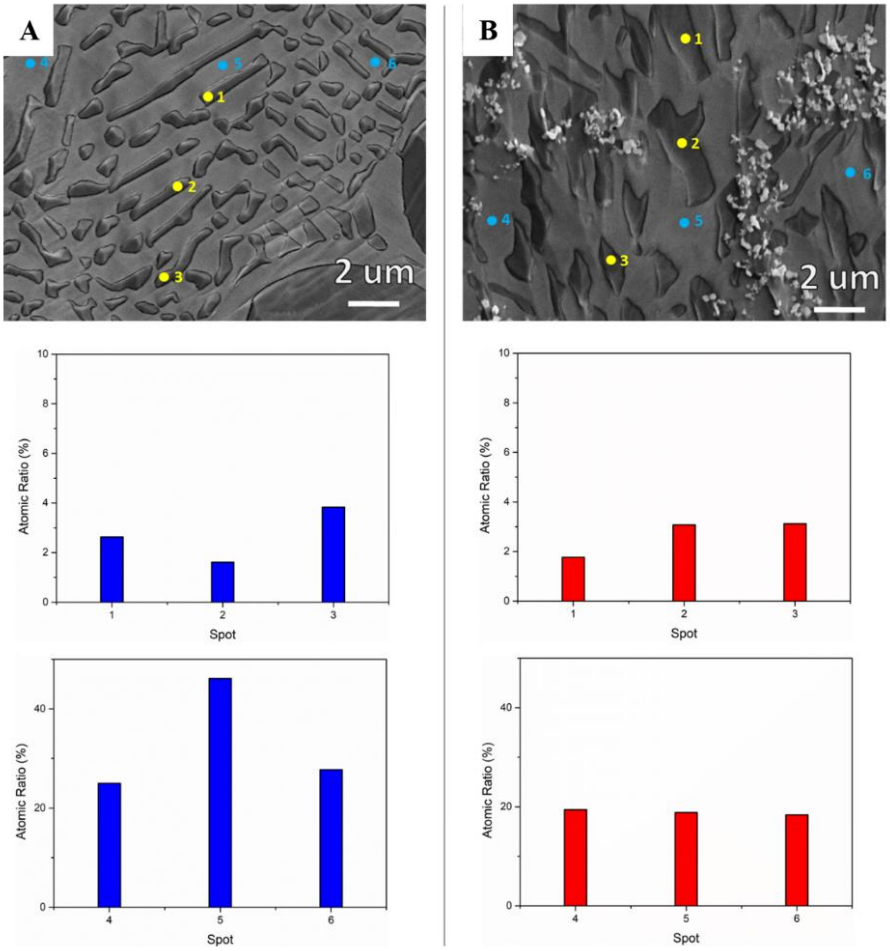

Figure 4 - 26 The eutectic phase element concentrations and atomic ratios of Cu in Ag-rich zones (spots 1-3) and Ag in Cu-rich zones (spots 4-6) in Cu-60Ag alloys (a) and Cu-60Ag/10 vol.% WC (b).

To gain a more complete picture of possible phonon enhancement, the microstructure of the materials by scanning electron microscopy (SEM) with EDS mapping has been further charaterized. The morphological variations are shown in **Figure 4 - 27**. It suggests that the effect of WC nanoparticles on phonons by means of boundary modification [8] could also partially induce the unusual thermal behavior. **Figure 4 - 27** (b) and (d) present a typical divorced eutectic phase in pure Cu-60Ag. In comparison, WC nanoparticles modified the eutectic phase morphology and induced ultrafine grains (with certain ultrafine twin grains in the Cu-rich phase [227]) in the nanocomposite as shown in **Figure 4 - 27** (c) and (e) (also see **Figure 4 - 31** and **Figure 3 - 7**) [228]. This twin-like structure will minimize the scattering effect for thermal transport, especially when the dispersed WC nanoparticles are also more distributed in/along the eutectic phase (**Figure 4 - 31**) [107]. In brief, WC nanoparticles reshape the phase structures by demolishing the clear phase boundary [229], introducing some ultrafine twin grains [230,231], and linking the strip-like phase structures [16,228,229,231] (**Figure 4 - 27** (c) and (e) and **Figure 4 - 31**).

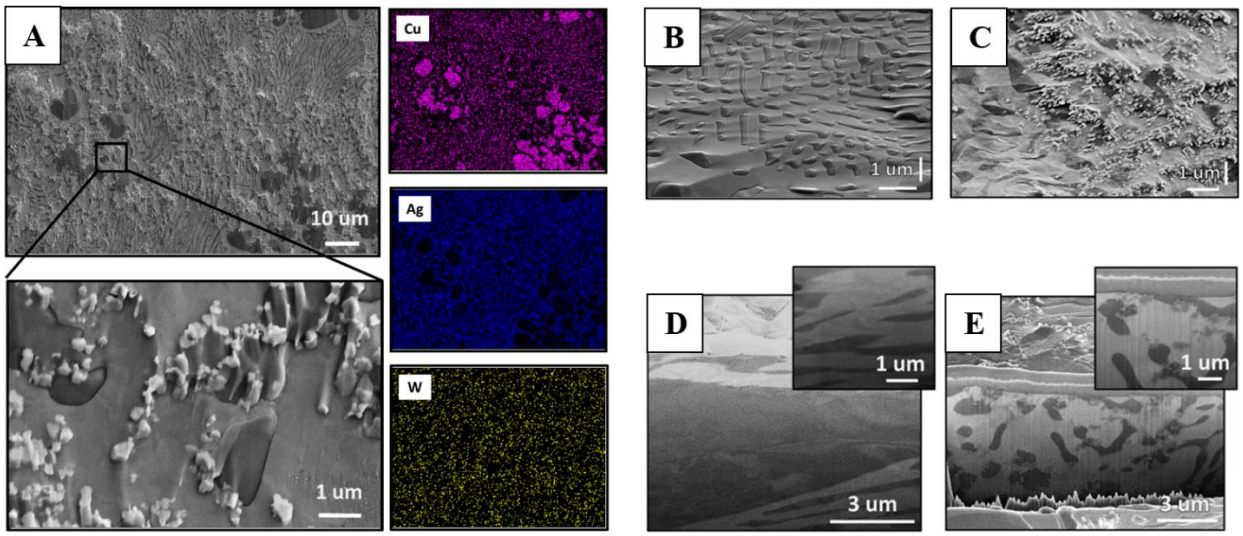

Figure 4 - 27 (a) Low and high magnification SEM images for Cu-60Ag/10 vol.% WC nanocomposites with EDS mapping for element analysis; SEM images of surface morphology

after 52° tilt for (b) Cu-60Ag alloy and (c) Cu-60Ag/10 vol.% WC nanocomposite; FIB cross-section images for (d) Cu-60Ag alloy and (e) Cu-60Ag/10 vol.% WC nanocomposite.

In summary, the thermal conductivity of Cu-60Ag alloy with 10 vol.% dispersed nanoparticles of less-conductive tungsten carbide (WC) breaks the theoretical upper limits. As analyzed above, the unusual enhancement of thermal transport in Cu-60Ag by the WC nanoparticles is possibly attributed to the tuned phonons thermal behavior [232] by the reduction of scattering with WC's supreme characteristics and the modified microstructures including phase composition [233] with WC nanoparticles. However, for Cu-60Ag with much less than 10 vol.% of WC, the thermal conductivity follows the HS model well, because the thermal transport enhancement by the lower volume percentage of WC cannot compensate for the more rapid reduction in electrical conductivity. For Cu-60Ag with a far higher volume percentage of WC than 10 vol.%, thermal transport deterioration by defects like dislocations and dense boundaries may dominate phonon enhancement by WC nanoparticles.

Study on Cu-x Ag/10vol%WC The nanoparticle distribution and microstructure of the Cu-x Ag/10 vol.% WC nanocomposites are shown in **Figure 3 - 8** (a) to (f). It shows that the WC nanoparticles are more densely dispersed into the eutectic phases near/along their boundaries. As illustrated in the enlarged SEM image of **Figure 3 - 8** (a), no clustering or agglomeration is observed.

To check if a similar phenomenon exists in other Cu-Ag systems, the thermal conductivity of Cu-x Ag/10 vol.% WC nanocomposites is shown in **Figure 4 - 28** (a). When compared with the pure copper-silver alloys and their nanocomposites, Cu-60Ag/10 vol.% WC has the most unusual

thermal conductivity enhancement. **Figure 4 - 28** (b) shows the variation of heat capacity, which varies with the Ag content. Due to the intermediate heat capacity of WC between Cu and Ag, the heat capacity ratio of the nanocomposites to their pure alloy changes. Then, according to **Eq. 4 - 27**, the evolving trend in the thermal conductivities shown in **Figure 4 - 28** (a) is predictable.

As mentioned before, the electrical conductivity (**Figure 4 - 28** (c)) of the Cu- *x* Ag/10 vol.% WC nanocomposites has been measured (See ***Appendix*** of this section). Then, these data were used to calculate the phononic and electronic thermal transport with **Eq. 4 - 27**,[234] as summarized in **Figure 4 - 28** (e) and (f).

For pure Cu and Ag, phonons do not contribute much to heat transportation,[214] as shown in **Figure 4 - 28** (e). Although phonons in Cu-x Ag alloys contribute to a larger fraction of thermal conductivity, near-eutectic alloy concentrations (71.9 wt.% of Ag) give rise to the highest ratio between phonon to electron thermal transport. Aside from the separate roles of electrons and phonons, the total thermal conductivity of Cu-60Ag is higher than that of any other concentration. While the 10 vol.% of dispersed WC nanoparticles attenuate the electrical conductivity in Cu-*x*Ag alloys, the improved hardness, as shown in **Figure 4 - 28** (d), can enhance the thermal transport from phonons, as depicted in **Figure 4 - 28** (f).

Also, **Figure 3 - 8** would be useful to understand the microhardness trend in **Figure 4 - 28** (d), because the reasonably dense yet not linked eutectic phase with (almost) fully filled WC nanoparticles could give the most efficient strengthening.[235]

Comparison to Other Metals/Alloys and Their Composites Compared to other metals and alloys, including their (nano-) composites, the Cu-60Ag/10 vol.% WC nanocomposites have the advantages of higher mechanical properties, higher thermal conductivity, and more reasonable

electrical conductivity, as illustrated by **Figure 4 - 29** (a) and (b). Different from most of the other metals, alloys, and compounds, Cu-60Ag/10 vol.% WC nanocomposites expand the range of the Lorentz constant to correlate electrical and thermal conductivities in metallic systems (**Figure 4 - 29** (b)). When compared with the carbon-based metal matrix nanocomposites that depend mostly on phonons,[13,220] since the high thermal conductivity of our materials come from both electrons and phonons, retaining a much higher electrical conductivity is advantageous for a wider variety of applications.

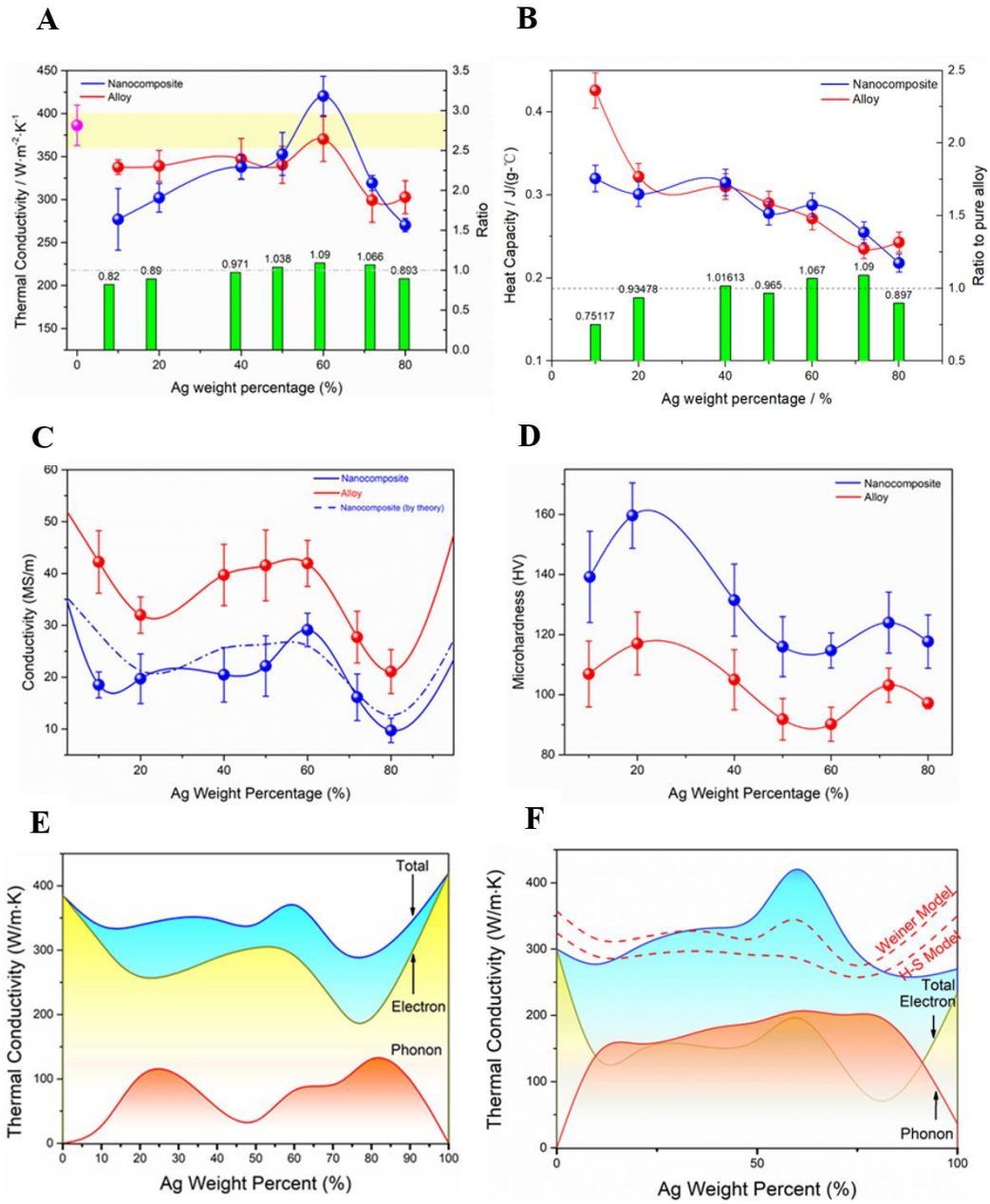

Figure 4 - 28 (a) Thermal conductivities of Cu-*x* Ag alloy and Cu-*x* Ag/10 vol.% WC nanocomposites (*x*=10, 20, 40, 50, 60, 71.9, 80), with the yellowish zone showing the available pure Cu thermal conductivity; (b) Heat capacities of Cu-*x* Ag alloy and Cu-*x* Ag/10 vol.% WC nanocomposites (*x*=10, 20, 40, 50, 60, 71.9, 80); (the green bars shows the ratio of the corresponding property in Cu-*x* Ag/10 vol.% WC nanocomposite to that in Cu-*x* Ag alloy) (c) Electrical conductivities of Cu-*x* Ag alloy and Cu-*x* Ag/ 10 vol.% WC nanocomposites (*x*=10,

20, 40, 50, 60, 71.9, 80); (d) Mechanical properties of Cu-*x* Ag alloy and Cu-*x* Ag/ 10 vol.% WC nanocomposites (*x*=10, 20, 40, 50, 60, 71.9, 80); (e) Phononic and electronic thermal conductivity analyses for Cu-x Ag alloys (*x*=0, 10, 20, 40, 50, 60, 71.9, 80, 100); (f) Phononic and electronic thermal conductivity analyses for Cu-x Ag/10 vol.% WC nanocomposites (*x*=0, 10, 20, 40, 50, 60, 71.9, 80, 100).

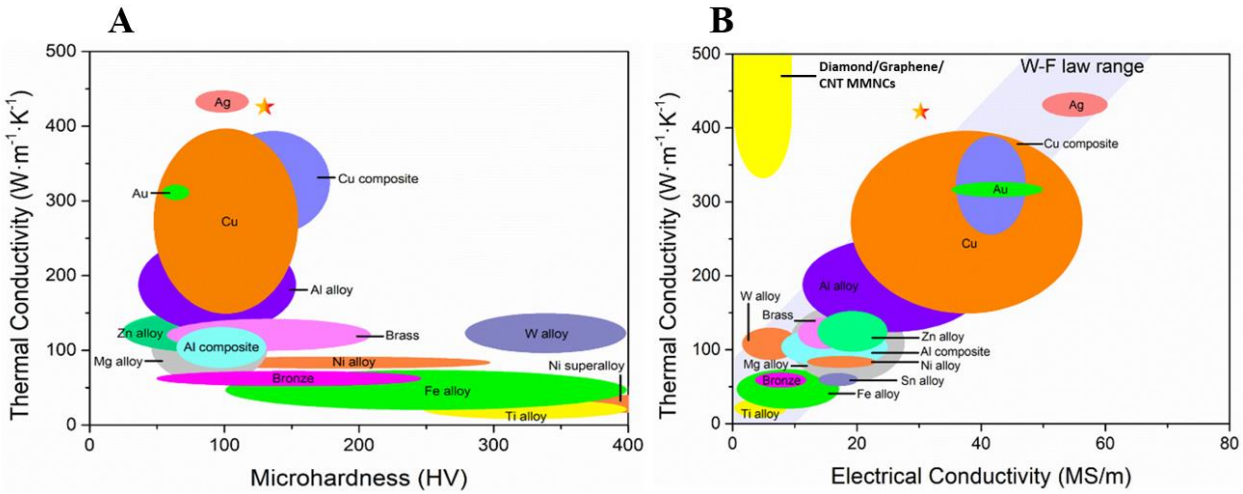

Figure 4 - 29 (a) Ashby chart of microhardness vs thermal conductivity of all major metals, alloys, and metal-based materials; (b) Ashby chart of electrical conductivity vs thermal conductivity of all major metals, alloys, and metal-based materials (with $\mathrm{L} = 24.4 \pm 4.9\ \mathrm{mW} \cdot \mathrm{u}\Omega \cdot \mathrm{K}^{-2}$ from Wiedmann-Franz Law)

<u>*Summary:*</u> In conclusion, we report an unusually high thermal conductivity in Cu-60Ag/WC nanocomposites, which is far beyond the upper bound of the interfacial models based on the Hashin-Shtrikman and Weiner limits. Possible mechanisms include phonon enhancement by a reduction in overall scattering and microstructure modification by WC nanoparticles with favorable thermal structures. These characteristics contribute to an unusual enhancement of phonon transport in Cu-60Ag by the less conductive WC nanoparticles. It has to be admitted that

more direct microscopic thermal analysis including 3ω-method may be needed to decouple thermal conductivity, heat capacity and thermal diffusivity, and more deterministic theoretical modeling could help confirm the dominant effects from phonon enhancement. Despite of this, the new finding is of significance for the development and application of nanoparticle-reinforced metals with both superior strength and high thermal conductivity.

Appendix

Microhardness Measurement The microhardness of the samples was measured with a *Microhardness Tester LM 800AT* under 200 gf loading for 10 sec. The samples were cut into ~0.5 cm thick plates and polished to obtain a flat surface. Each sample was characterized 10 times at different surface locations. The microhardness for all the samples is summarized in **Figure 4 - 24** (d) and **Figure 4 - 28** (d).

Electrical Conductivity Measurement The measurement for electrical conductivity was operated on a *Prometrix Omnimap RS-35* under a constant temperature of ~25°C. All the samples were made to 100 µm thick films, which provided a reasonable Merit of Number on the machine. Each sample was characterized three times. The final results of the electrical conductivity testing are shown in **Figure 4 - 24** (c) and **Figure 4 - 28** (c)**.**

Materials' General Characterization The scanning electron microscopy was operated on a *Zeiss Supra 40VP SEM*, with EDS mapping as an integrated part (See **Figure 4 - 27** and **Fig. S9**). The SEM scanning voltage and the EDS mapping voltage were both 10 kV. The cross-section analyses were done with a *Nova 400 Focused Ion Beam*. The X-Ray Diffraction was operated on a *Panalytical Pro* to check the material composition and provide semi-quantitative values for

composition ratio with a Cu K_α radiation source. All the samples were made into flat pieces. Since it's a metal-matrix nanocomposite, XRD peaks from 2θ=30~90° are analyzed (See **Figure 4 - 22**).

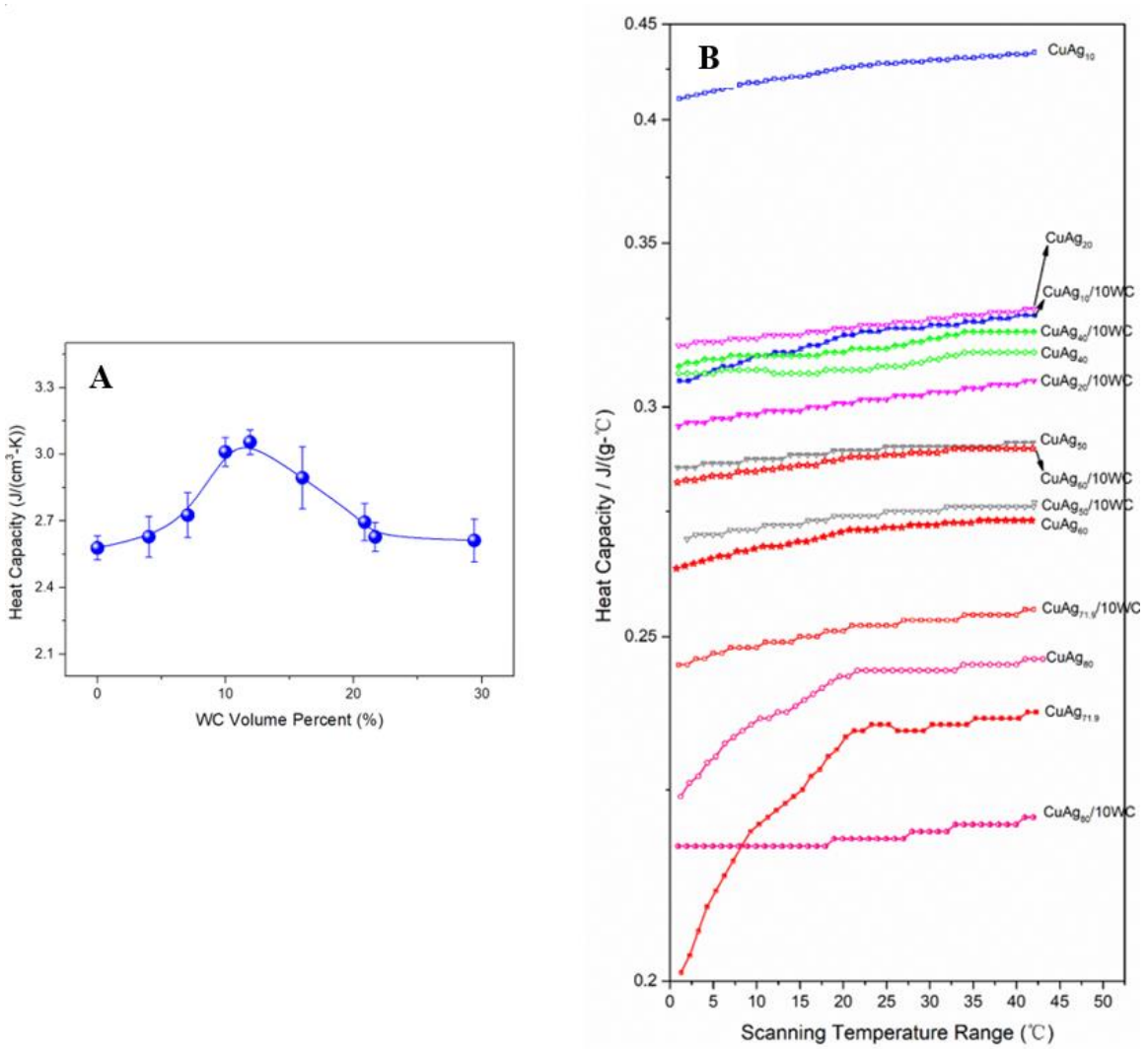

Figure 4 - 30 (a) Volumetric specific heat capacity of Cu-*x*Ag alloy and Cu-*x*Ag/10 vol.% WC nanocomposites (*x*=10, 20, 40, 50, 60, 71.9, and 80); (b) Temperature dependence of heat capacity of Cu-*x*Ag alloy and Cu-*x*Ag/10 vol.% WC nanocomposites (*x*=10, 20, 40, 50, 60, 71.9, and 80).

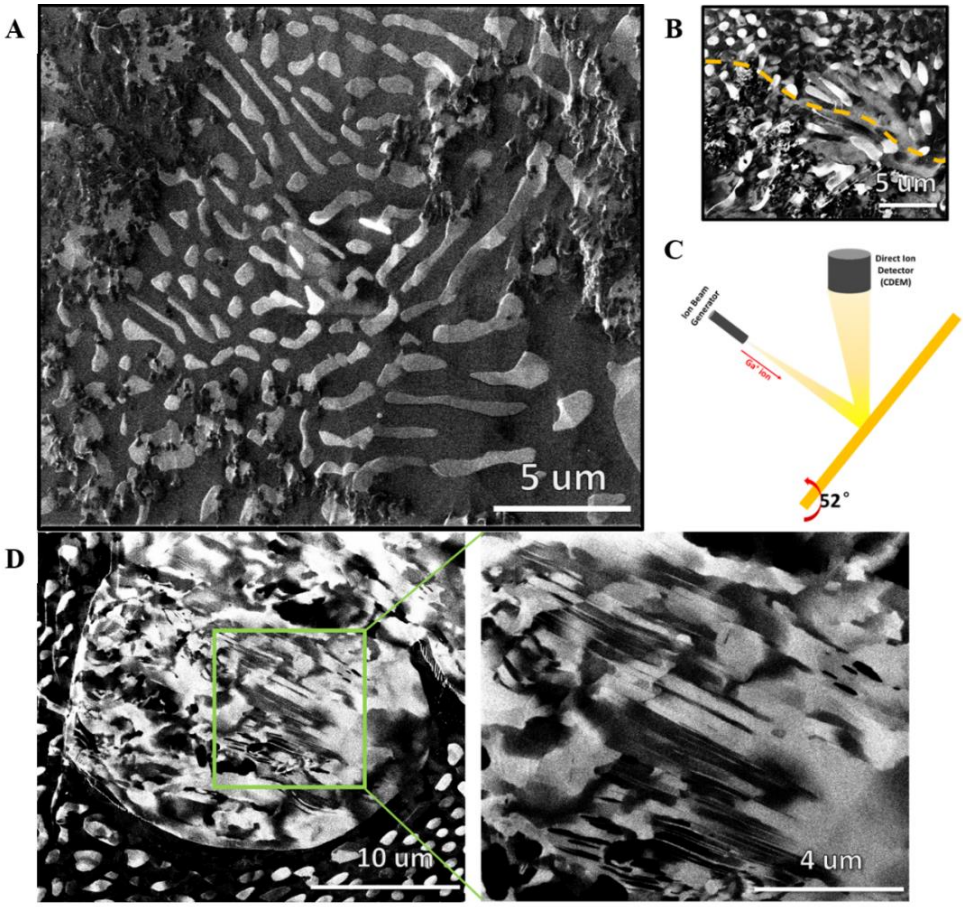

Figure 4 - 31 (a) The direct ion image of the eutectic phase in a Cu-60Ag/10 vol.% WC nanocomposite; (b) The morphology comparison between WC-rich area and WC-deficient area of the eutectic phase in a Cu-60Ag/10 vol.% WC nanocomposite; (c) The schematic illustration of Ga^+ ion imaging and the continuous dynode electron multiplier (CDEM) detecting mode. (d) The direct ion image of Cu-rich phase in a Cu-60Ag/10 vol.% WC nanocomposite to show local ultrafine twin grains and twin boundaries.

If the Cu-Ag systems with Ag concentration nearest to Cu-60Ag were compared, it could be noted that: As shown in **Figure 4 - 30**, for Cu-71.9Ag (both with and without 10 vol.% WC nanoparticle), it has a significantly lower heat capacity than Cu-60Ag; Moreover, the innate lower

electrical conductivity in Cu-71.9Ag (**Figure 4 - 28** (e) and (f)) also results in a lower electronic thermal conductivity and thus a lower total thermal conductivity.

Second, although Cu-50Ag and Cu-60Ag have comparable heat capacity, after incorporating 10 vol.% WC, the heat capacity of Cu-50Ag is lower than the pure CuAg50. This means that the WC incorporation will not have the same effect as in the Cu-60Ag system.

Table 4 - 7 Thermal properties of Cu, Ag, and WC at room temperature [236,237]

	Material	**Debye Temp.** **K**	**Heat Capacity** **J/(g-K)**	**Thermal Cond.** **W/(m-K)**	**Atomic Density** $\times 10^{28}$ **m**$^{-3}$	**Density** g/cm^3
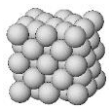	**Ag**	221	0.233	400-450	5.02	10.7
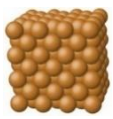	**Cu**	310	0.386	370-400	8.78	8.96
	**WC**	-	0.292	110	9.62	15.63

Considering that **Eq. 4 - 27** is used to calculate thermal conductivity with heat capacity and thermal diffusivity, the clear difference of the heat capacity among Cu-Ag systems with Ag concentration near Cu-60Ag determines the different thermal conductivity change with WC incorporation.

This understanding from heat capacity could further be linked to the difference in microstructure modification and electronic/phononic thermal contributions, as mentioned in the

previous sections. This is the ultimate reason why Cu-10Ag/WC could observe the phenomenon, while other Cu-Ag systems may not.

4.3 Summary

In this chapter, by focusing on the electron behavior, the effects of nanoparticles on the electrical and thermal performances in Cu- and Al-based nanocomposites have been studied.

First, by investigating the low-temperature electrical performance (down to 2K) of Al-based nanocomposites (i.e., Al-TiB_2 and Al-ZrB_2), the effects of nanoparticles on the electron concentration and electron mobility have been decoupled. Given the common nanoparticle size of 10-100 nm, the interfacial electron localization has been proposed to understand the reduced apparent free electron concentration. This study shows that the reduction in the (apparent) electron concentration is crucial for the reduction of electrical conductivity of *in situ* Al-TiB_2 and Al-ZrB_2 nanocomposites. In contrast to previous studies and research, this study reveals that the mechanical/configurational factors do not directly correlate with the electrical properties, and the electrical properties are directly influenced via the significant electron concentration decrease in Al-TiB_2 and Al-ZrB_2 nanocomposites. Based on this study, the incorporation of TiB_2 and ZrB_2 nanoparticles creates defects, including interfaces and dislocations, and changes the preferred growth modes of Al grains. These defects create a defect density of states to accommodate more free electrons and to enhance lattice effects on electrons. These interfaces also have mismatches and discontinuity in Fermi velocity and density of states. Both these effects contribute to the bound states of electrons and a significant scattering of free electrons. The electron mobility is less affected because the lowered (apparent) electron concentration reduces the possibility of electron scattering within the MFP (especially at room temperature).

With this understanding, the quantitative description of electrical conductivity in Al- and Cu-based nanocomposites have been proposed. Our study proposes the first model to predict the decaying electrical conductivity in copper matrices (of Cu, Cu-40 wt% Zn, and Cu-60 wt% Ag) containing WC nanoparticles with a diameter of about 100-200 nm. This model considers the electronic structure difference, the interface scattering, and the Nordheim equation. The new model suggests that scattering at the metal-nanoparticle interface in the samples with higher nanoparticle loadings will reduce the probability for the collective electrons to pass the electronic interfacial energy barrier. This results in an exponentially decaying electrical conductivity. By combining the Fermi level fluctuation at the matrix-nanoparticle interface, the relationship between electrical conductivity and nanoparticle volume fraction has been made clear. Further thermophysical observation proves the feasibility of the proposed model.

Given the link between electron behavior, electrical conductivity, and thermal performances, the thermal properties (mainly thermal diffusivity and thermal conductivity) in the nanocomposites have been systematically investigated. Using Al-based nanocomposites (i.e., Al-TiC, Al-TiB_2, and Al-ZrB_2) as the model system, the contribution from the electronic and phononic thermal conductance has been decoupled. How the heat capacity, thermal diffusivity, and thermal conductivity change with the nanoparticle volume fraction has been quantitatively determined. By the comparison with the AMM, DMM, and EMT models, the advantages of using metallic ceramic nanoparticles stands out, and an EMT model considering matrix-nanoparticle interfacial thermal conductance has been proposed.

With all the understanding from electrical and thermal behavior in nanocomposites, the final section investigates an abnormal thermal performance in Cu-*x*Ag/WC nanocomposites. Possible mechanisms for the abnormal thermal behavior include phonon enhancement by a

reduction in overall scattering and microstructure modification by WC nanoparticles with favorable thermal structures. The main evidence lies on the increased heat capacity in the Cu-Ag/WC systems, and further experimental study compatible with nanocomposite systems (like 3ω-method) could be helpful to decouple all these contributing factors.

In brief, the study in the chapter has systematically analyzed the electron contribution in the electrical and thermal behavior of metal matrix nanocomposites, and has built engineering prediction model for the thermophysical properties in metal matrix nanocomposites (mainly Al- and Cu-based nanocomposites in this study). This quantitative study would be important for the further discussion of tuned chemical stability in these nanocomposites.

CHAPTER 5 EFFECT OF NANOPARTICLES ON CHEMICAL STABILITY OF METALS

5.1 Experimental method

5.1.1 Nanoparticle stability

The nanoparticle stability is mainly studied for the industrial application of Al-TiC systems. Thus, the discussion for the experimental methods would be limited to Al(-Mo)-TiC and Al-Si-TiC (including Al-Si-Mg) system.

During the experiment, the nanoparticle stability is reflected in the nanoparticle reaction rate. The XRD scanning (on a *PANalytical Pro* model with Cu Kα radiation with standardized 40KV accelerating voltage; the scanning angle is from 30 to 70° and then zoomed in from 35° to 40°; the step size is 0.05°, with the scanning speed of 2°/min) together with the EDS mapping (on a *Zeiss Supra 40KV* model) was used to quantify formed intermetallic phase concentration (derived from the rate of nanoparticle depletion) in the systems after the chemical reaction between nanoparticle (here, TiC) and matrix (here, Al, Al-Mo, Al-Si, and Al-Si-Mg).

5.1.2 Thermal oxidation measurement

Similarly, the thermal oxidation process is the chemical reaction between matrix and oxygen (O_2), and its kinetics and dynamics are a subcategory of chemical stability. Therefore, the study could also use the reaction rate as an index to demonstrate the anti-oxidation performance. In our experiments, both the pure alloy and the nanocomposite were analyzed via *in situ* XRD from room temperature to over 80% of its melting temperature of the alloy (700℃ for Cu-40 wt.% Zn/WC nanocomposites and 600℃ for Al-ZrB_2 nanocomposites) to obtain information on matrix crystal plane stability, phase transition, and oxidation.

Further, to quantitatively analyze the anti-oxidation performance, the XRD peak intensity and EDS surface mapping were used to quantify the oxidized surface ratio. Since the thermal oxidation created various observable oxide layer structures, FIB milling (on a *FEI Nova 600 SEM/FIB System*) was utilized to show the oxidation cross-section for layer properties.

Since the Al oxidation has the unique characteristic of being self-limiting, weight gain/loss will be a direct index to reflect this feature. To achieve this, TGA measurement (on a *Perkin Elmer Diamond TG/DTA model*) was added to analyze the dynamic and kinetic evolution of the Al_2O_3 oxide layer. The scanning temperature was set from 325K to 875K at 4K/min for 150 min (with 13 min for isothermal keeping at 875K before cooling to guarantee the mass measurement stabilization) and isothermal scanning for 90 min. Each sample has been scanned for 3 times under each investigated condition. The results were summarized as Al_2O_3 weight gain and Al_2O_3 layer thickness. The air flow was set to be 30 mL/min to guarantee the enough oxygen and efficient heating in TGA. All the oxidation was introduced under air condition ($P_{tot} = 10^5\ Pa$; $P_{O_2} = 2.1 \times 10^4\ Pa$).

5.1.3 Electrochemical measurement

AA7075 corrosion performance The electrochemistry measurement was done on *VersaSTAT 4* machine with graphite as counter electrode and Ag/AgCl as reference electrode.

For intrinsic corrosion-resistance and pitting-resistance measurement, all the samples (with the size of $1.0 \times 1.5\ cm^2$) were immediately tested after the polishing and ultrasonic cleaning with anhydrous ethanol (200 proof). For intrinsic corrosion-resistance measurement, the freshly exposed sample surface was used in the experiments; the experiment was following the sequence

of open current potential measurement (OCP), linear polarization current measurement (LPC), and potentiodynamic scanning (from -0.25V v.s. OCP to 1.6V v.s. OCP, then back to 0V OCP).

For pitting-resistance measurement, all the samples were first passivated in 70.0 wt.% concentrated HNO_3 to form a thin homogeneous passivation Al_2O_3 layer for 1 min; then, the experiment was following the sequence of open current potential measurement (OCP), electrochemical impedance scanning (EIS) back and forth between 0.1 Hz and 100 KHz), linear polarization current measurement (LPC), and potentiodynamic scanning (from -0.25V v.s. OCP to 1.0V v.s. OCP, then back to 0V OCP). To gauge the pitting effects on the passivation film, the comparison group was used, with AA7075 (T6), AA7075-TiB_2 (T6), and AA7075-TiC (T6) samples first passivated in 70.0 wt.% concentrated HNO_3 for 1min and immersed in 3.5 wt.% NaCl for 24 hours. After the pitting immersion, the electrochemical measurements were repeating the same recipe for the pitting-resistance measurements. The experiments all used aerated non-N_2 purged 3.5 wt.% NaCl solution (pH=~6.5-7) under 25℃.

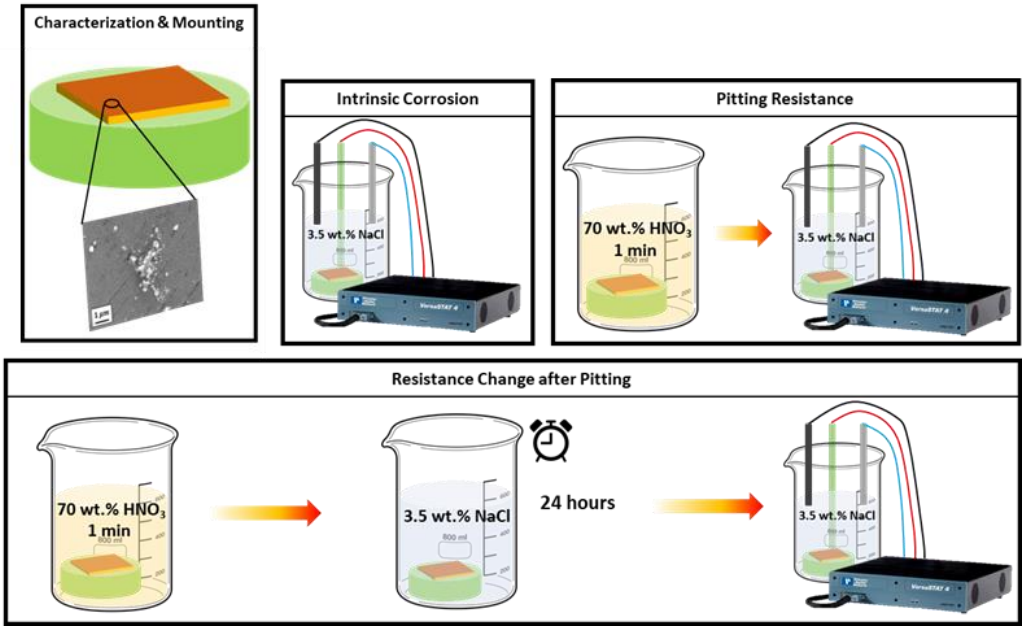

Figure 5 - 1 EIS corrosion measurement and sample preparation procedures.

With the understanding from pitting corrosion, the IGC susceptibility was also investigated to support the pitting observation and the proposed explanation. IGC susceptibility was gauged with the ASTM standards G100. All samples were degreased with 1200 proof anhydrous ethanol after polishing; then, they were immersed in 5 wt.% NaOH solution for 1 min, followed by the neutralization immersion in 30 wt.% HNO3 for 1 min; afterwards, the samples were put into the mixed solution with 57g/L NaCl and 10 mL/L H_2O_2 for 24 hours. To quantify the IGC susceptibility, the sample cross-section was cut open, and the IGC penetration depth was compared.

A206 corrosion performance The evaluation of the corrosion performance has been using the similar techniques with AA7075 nanocomposite systems.

For corrosion performance evaluation, the electrochemical impedance scanning technique was used on a *VersaSTAT 4* machine with graphite as counter electrode and Ag/AgCl as reference electrode. All the samples (with the size of $1.0 \times 1.5\ cm^2$) were tested following the sequence of open current potential measurement (OCP) for 10 min, electrochemical impedance scanning (EIS) back and forth between 0.1 Hz and 100 KHz), linear polarization current measurement (LPC), and potentiodynamic scanning (from -0.25V v.s. OCP to 1.0V v.s. OCP, then back to 0V v.s. OCP). All the measurements used aerated non-N_2 purged 3.5 wt.% NaCl solution (pH=~6.5-7) under 25℃. Three kinds of surfaces have been tested and compared, namely freshly exposed surface, passivated surface, and immersed/pitted surface. To make passivated surface, all the samples were immersed in 70.0 wt.% concentrated HNO_3 to form a thin homogeneous passivation Al_2O_3 layer for 1 min, and the surfaces were rinse with 200 pf anhydrous ethanol and air-dried. The quality of the passivated surfaces has been checked in **Figure 5 - 93**(using A206-TiC in T4 and T6 states as

an example). The immersed and pitted surface was made by immersing the passivated surface into 3.5 wt.% NaCl for 24 hours.

In addition, the IGC susceptibility was tested via an immersion method. All samples were degreased with 1200 proof anhydrous ethanol after polishing; then, they were immersed in 5 wt.% NaOH solution for 1 min, followed by the neutralization immersion in 30 wt.% HNO_3 for 1 min; afterwards, the samples were put into the mixed solution of 57g/L NaCl and 10 mL/L H_2O_2 for 24 hours. To quantify the IGC susceptibility, the sample cross-section was cut open, and the IGC penetration depth was compared. During all the solution-based tests, the liquid was larger than the requirements of 100 mL/cm^2 for every 24 h.

5.1.4 SCC determination

SCC susceptibility is gauged with the measurement of induced crack propagation speed in 3.5 wt.% NaCl solution (pH=~6.5-7.0) at 25 °C. All the samples have been measured with the double cantilever bending (DCB) method, as shown in **Figure 5 - 2**. Here, the AA7075 (extruded, T6) is used as an example, where the normal direction S-T plane is set as the crack propagation direction. All the extruded samples have used the same setup for SCC tests. For cast AA7075 and nanocomposites, since the grains have no specific orientation preference, the test direction has no specific requirements.

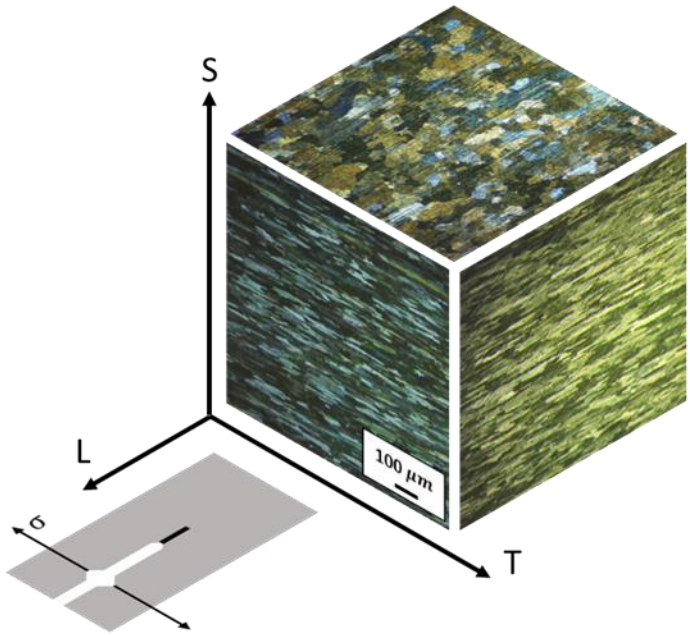

Figure 5 - 2 The DCB measurement setup for SCC susceptibility and the characteristic grain shapes in commercial AA7075 plate (extruded; T6), as well as the associated 3 directions of (S, T, L)

For the sample preparation, all the test pieces were cut out by wire EDM to guarantee the precision. During the test, a BN-coated tungsten screws has been notched into the small cut opening notch to guarantee the same deflection distance. According to Ref. [238], the applied stress intensity k could be estimated by the screw-induced deflection with the equation of:

Eq. 5 - 1

$$k = \frac{\delta \cdot E \cdot h \cdot [3h \cdot (a+0.6h)^2 + h^3]^{0.5}}{4 \cdot [(a+0.6h)^2 + h^2 \cdot a]}$$

where E represents the elastic module, h the half specimen height, a the crack length from the notched point, and δ the constant displacement at the load point.

During the test, each piece was immersed in at least 500 mL NaCl solution. The NaCl was replaced every 2 days to guarantee a stable pH range of the solution; The measurement duration was set for the cracks to achieve 1 cm (with 30 days' maximum time for low-stress intensity range

and possible through-cracking for high-stress intensity range). During this process, the reduction of stress intensity after the crack propagated was compensated with the negative error bar to reflect the values more accurately.

After the SCC immersion test, the sample surface would be polished to exposed total crack trace. After the surface characterization, the two cantilevers would be torn apart, and the surface on the crack trace (particularly the crack tip) would be characterized with SEM and EDS to expose the microstructural and compositional features.

5.2 Experimental results

5.2.1 Chemical reactivity of Al-Mo/TiC nanocomposite

Fabrication and Reaction Process During the experiments, the Al-2 vol.% TiC samples (hereafter, Al-TiC, from *MetaLi*®; the size of the TiC nanoparticles is shown in **Figure 5 - 3** (a)) were used to add Mo to form Al-0.5 wt.% Mo-2 vol.% TiC (hereafter, Al-Mo-TiC) under 900℃. As the first step, 900℃ was chosen to avoid the possible Al and TiC reaction during the initial alloying process, because TiC is reported to be stable in molten Al at above ~810-900℃ [239]. 0.5 wt.% pure powder-form Mo (>99.9% purity from Sigma-Aldrich® with the calibrated diameter of ~10 μm) was chosen by a scaling relationship to guarantee no Al-Mo intermetallic phases and full melting [240,241]. When alloying Mo into the system, a graphite crucible was used as the container and pre-heated to 900$\pm$5 ℃ by a resistance furnace. Since the Mo concentration is low, no stirring was introduced during the alloying process. The alloying time was set to be 10 min. When alloying was finished, the Al-Mo-TiC sample was cast out into a graphite mold and air-cooled. Afterward, the samples were re-melt at 750℃ isothermally for 1 and 4 hours to investigate the reaction process between Al and TiC. During the alloying process and the isothermal reaction process, to avoid

heavy thermal oxidation, pure argon (Ar) gas was used as the protective gas with a flow rate of ~20 mL/min on top of the molten system.

After obtaining the data for Al-Mo-TiC alloyed at 900℃, to further confirm the feasibility of stabilizing Al-TiC under industrially favorable 750℃ with Mo addition, samples of Al-Mo-TiC directly alloyed under 750℃ have been prepared, and the reaction process would be gauged with the same way as Al-Mo-TiC alloyed under 900℃. The summary of the experimental design could be referred to in **Figure 5 - 3** (b).

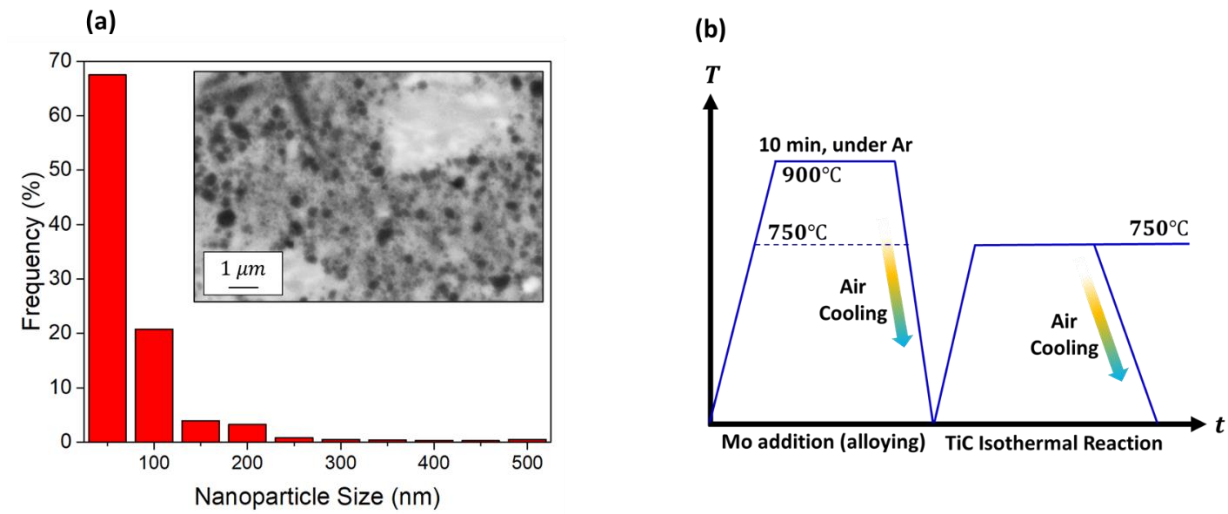

Figure 5 - 3 (a) Nanoparticle size distribution of TiC nanoparticles in as-received Al-TiC nanocomposite (Inserted: Enlarged SEM image for TiC nanoparticle pseudo-cluster under InLens mode); (b) Illustration of the time-sequential experiment design.

After the experiments, the samples' microhardness and electrical conductivity have been measured on *Microhardness Tester LM 800AT* (100 gf for 10s dwelling) and *ResMap 4-Point Station*, respectively. For microhardness tests, the sample was cut into $5mm \times 10\ mm$ shape with a thickness $> 1\ mm$, and the measurement was done with a square-based diamond pyramid indenter. When measuring electrical resistivity, four-point probing based on film resistance

measurement was used; all samples were mechanically thinned to be $150\ \mu m$ with a probing area of $1\ cm \times 1\ cm$ and sat on a flat silicon wafer during the electrical measurement. For each measurement, three samples processed with the same condition have been prepared. Each sample has been measured three times; all sample surfaces have been mechanically ground using up to 1200 grit with anhydrous ethanol (200 proof) rinsing. The mechanical properties from micropillar compression tests were measured on *MTS Nanoindenter XP* [242]. Considering the ductility of pure Al, a 3000 nm displacement was chosen for the flat punch probe with a size of 10 μm at room temperature with a strain rate of $1 \times 10^{-3}\ s^{-1}$. All the samples have been tested three times, and the characteristic engineering stress-strain curve has been shown. With the micropillar results, the local mechanical slip behavior of the materials could be visualized. By this method, we could more directly gauge Mo's influence on the interface properties of Al(Mo)-TiC before isothermal reaction and Al_3Ti(Mo)-Al after the isothermal reaction.

Microstructure images were taken from *Zeiss Supra 40KV SEM* under SE and InLens modes. For the nanoparticle size distribution, the enlarged SEM images were processed with *ImageJ* to obtain the TiC diameter. The sample was also etched in 1.0 M/L dilute HCl to extract the TiC nanoparticles, and the TiC nanoparticle suspension solution was measured with DLS (Dynamic Light Scattering) to confirm the size distribution. Furthermore, to reveal the Mo-enrichment in the Al-Mo-TiC system, TEM images were taken on an *FEI T20 iCorr* model with the 120 kV accelerating voltage, with the sample thickness of ~150 nm.

Meanwhile, the XRD scanning (on a *PANalytical Pro* model with Cu Kα radiation with standardized 40KV accelerating voltage; the scanning angle is from 30 to 70° and then zoomed in from 35° to 40°; the step size is 0.05°, with the scanning speed of 2°/min) together with the EDS mapping (on a *Zeiss Supra 40KV* model) was used to quantify intermetallic phase concentration

in the systems after the isothermal holding at 750℃. It should be noted that the time axis is all drawn in the square root scale to reflect the diffusion nature of the chemical reaction process at 750℃ [239]. Afterward, to validate our fundamental understanding, the Al-Mo-TiC system processed under 750℃ (e.g., Mo is alloyed to Al-TiC under 750℃ for 10 min) and kept isothermal under 750℃ for the same reaction time has been used for comparison.

Figure 5 - 4 (a) and (b) show the TiC nanoparticle pseudo-dispersion in the Al-Mo-TiC nanocomposite (also indicated by **Figure 5 - 9**). The pseudo-dispersion of TiC in the system is enabled by the balance among the Brownian thermal energy, van der Waals interaction, and interfacial energy, where TiC nanoparticles will scatter in a cluster shape without agglomeration [1,243]. The X-ray line scan in **Figure 5 - 4** (c) indicates that the larger TiC nanophase has a higher Mo signal in the EDS mapping. This suggests that the addition of Mo does not form large dendrite-like $Al_{12}Mo$ in the Al-Mo-TiC system, if *in situ* synthesized simultaneously [240]. With the size distribution analysis in **Figure 5 - 4** (d), it is confirmed that the TiC nanoparticles are synthesized mainly with a mean diameter of 116 nm, and the small bump tail from 400-500 nm corresponds to the Mo-coated sub-micron TiC particles (similar to the X-ray line scan result in **Figure 5 - 4** (c)).

To further confirm this observation, the TEM images in **Figure 5 - 4** (e) and (f) have been used to reveal the bimodal size distribution in Al-Mo-TiC. In the TiC nanoparticle dense zone (as shown in **Figure 5 - 4** (e)), the TiC nanoparticle diameter is within the range of 50-100 nm, and this is consistent with the size distribution by the SEM image processing and DLS measurement in **Figure 5 - 4** (d). At the sub-micron TiC phase interface, **Figure 5 - 4** (f) shows a coated interlayer with Mo-enrichment (as demonstrated by the X-ray line scan in **Figure 5 - 4** (c)).

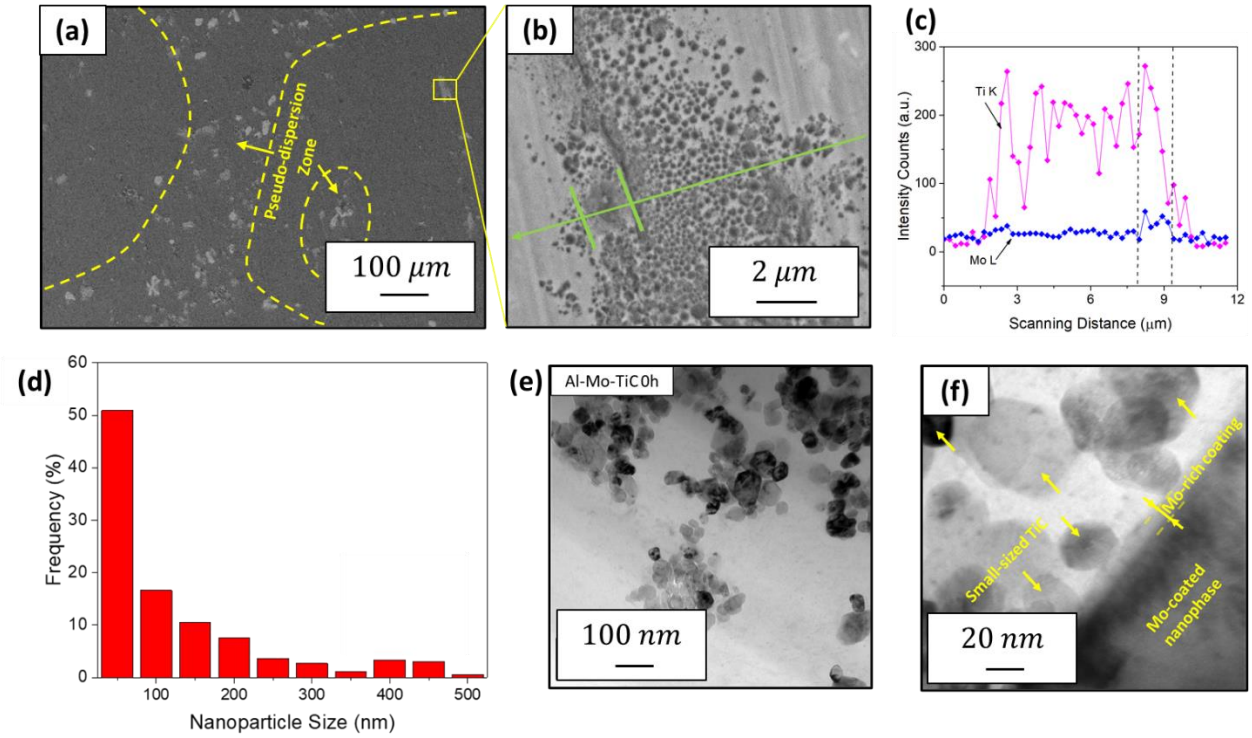

Figure 5 - 4 (a) The nanoparticle pseudo-dispersion in Al-Mo-TiC nanocomposites after synthesis; (b) Magnified SEM image of TiC dense zone in Al-Mo-TiC and (c) the corresponding EDS line scan; (d) TiC nanoparticle size distribution in Al-Mo-TiC nanocomposites; TEM image of nano-sized TiC particles

Then, all the samples have undergone the isothermal reaction process under 750℃. As shown in **Figure 5 - 5** (a) and (c), before held at 750℃, the Al-TiC and Al-Mo-TiC both have the TiC nanoparticle pseudo-clusters (with the dense zone size of ~10 um, also as evidenced by **Figure 5 - 9**), with no observable Al-Ti or Al-Mo intermetallic dendrite. When maintained at 750℃ for 4 hours, the TiC pseudo-cluster transformed into larger intermetallic pieces in both Al-TiC and Al-Mo-TiC systems, as shown in **Figure 5 - 5** (c) and (d). However, compared in **Figure 5 - 5** (e), the intermetallic phase of Al_3Ti in Al-TiC is much larger than $Al_3Ti(Mo)$ in Al-Mo-TiC. After 4h isothermal reaction, Al-TiC forms the intermetallic phases of size ~41.9 μm, whreas Al-Mo-TiC

only yields an intermetallic phase of size ~24.3 μm. The EDS scanning in **Figure 5 - 5** also demonstrates a growth mode with reacting and piece-merging in the observed large intermetallic phase.

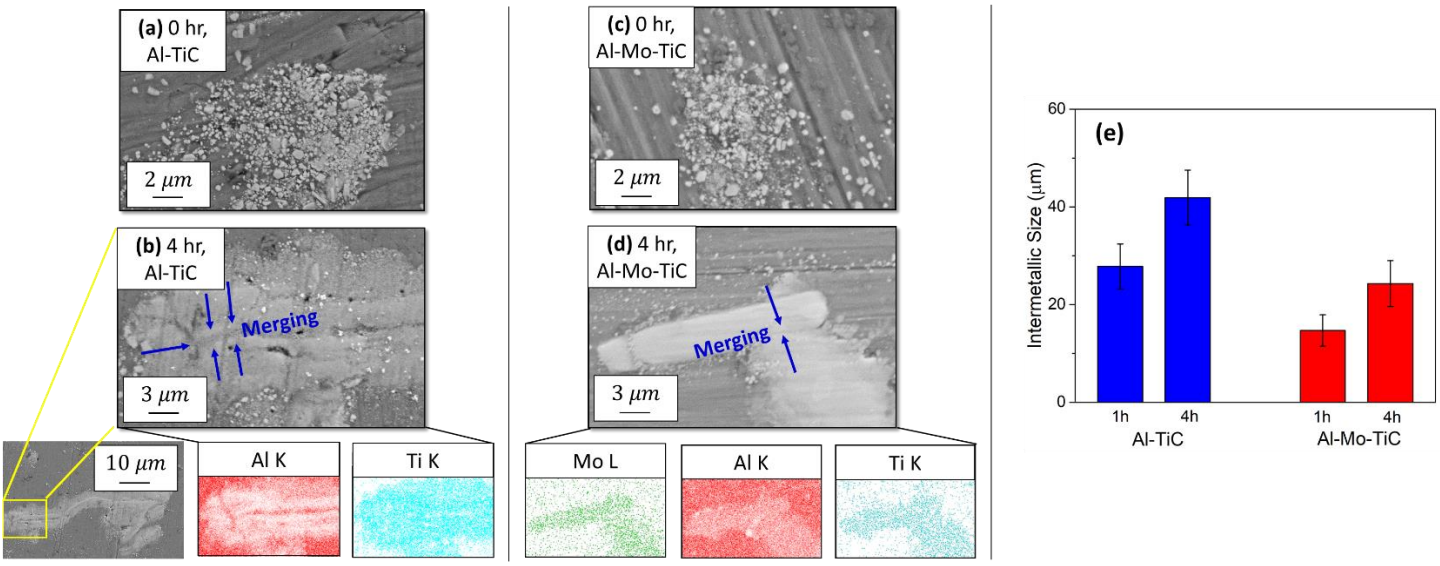

Figure 5 - 5 The size of nanoparticle pseudo-cluster in (a) Al-TiC and (b) Al-Mo-TiC nanocomposites before chemical reaction; The intermetallic phase and the corresponding EDS mapping for (c) Al-TiC and (d) Al-Mo-TiC nanocomposites after 4 h holding at 750℃; (e) Comparison of the $Al_3Ti(Mo)$ intermetallic size in Al-TiC and Al-Mo-TiC nanocomposites after 1h and 4h at 750℃.

Except for the size of the intermetallic phases, the mechanical properties have also been modified with the addition of Mo. As shown in **Figure 5 - 6**, the compressive mechanical property of Al-TiC and Al-Mo-TiC after 0h (in **Figure 5 - 6** (a) and (b)) and 4h isothermal reaction (i.e., at the matrix-intermetallic interface in **Figure 5 - 6** (c) and (d)) has been compared. It could be seen from **Figure 5 - 6** (e) that the Mo addition gives the comparable mechanical strength in Al-TiC before isothermal reaction. However, after 4h reaction, the advantage of the Mo addition becomes

clear, as the Al-Mo-TiC system could get a reasonable strengthening effect from the formed intermetallics, while keeping the matrix ductility. Two reasons contribute to this difference: First, the Mo addition gives a smaller Al3Ti(Mo) phase (**Figure 5 - 5**) and stronger matrix-intermetallic interface (see the almost defect-free interface after compression test in **Figure 5 - 6** (d)); Second, Mo is reported to be an essential element to enhance ductility in Al-Ti intermetallics, [107,244] which indicates that the Mo enrichment in the formed intermetallic phases (**Figure 5 - 5** (d)) could help minimize the brittleness and mitigate the crack propagation (**Figure 5 - 10**) from the bulky Al_3Ti. Three times of pillar compression tests confirm this result.

After the isothermal reaction process at 750 ℃, the microhardness and electrical conductivity evolution are measured in **Figure 5 - 7** (a) and (b), respectively. Before the isothermal reaction at 750℃, the Al-Mo-TiC has a higher microhardness and electrical conductivity than Al-TiC. This difference indicates that the Mo addition is potentially strengthening the Al and TiC interface in a solute atom state [240] instead of directly forming the $Al_{12}Mo$ intermetallic phase. Also, since the used Mo powder is of size ~10 μm, the hardness increase is not from Mo particle directly, because single large particles (>>1 μm, as shown in **Figure 5 - 4** (b), (d), and (e)) has not been observed, and only concentrated Mo as a coating interlayer could be found (as shown in **Figure 5 - 4** (f)).

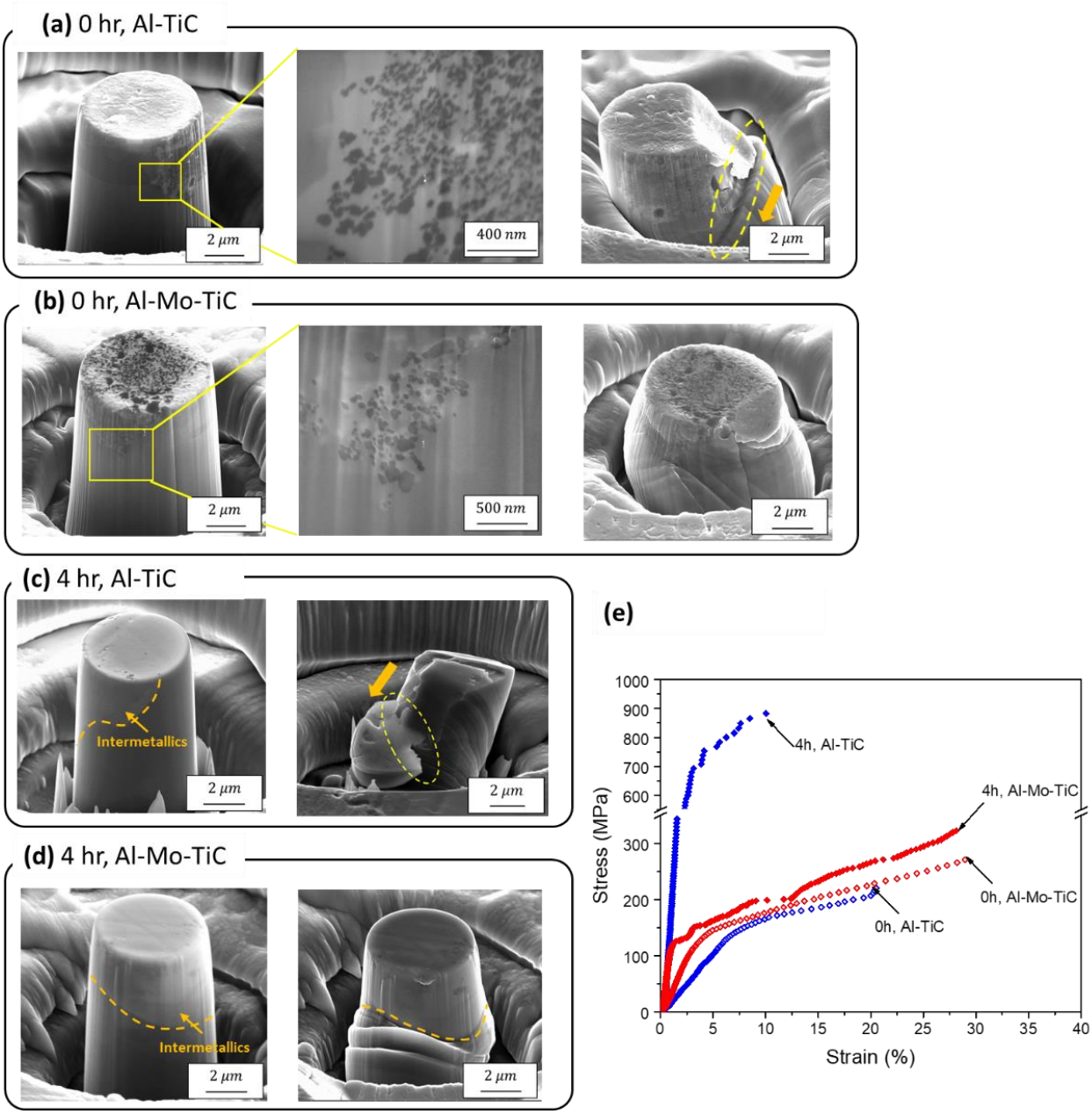

Figure 5 - 6 Micropillar before and after compression tests for (a) Al-TiC with 0h isothermal reaction, (b) Al-Mo-TiC with 0h isothermal reaction, (c) Al-TiC after 4h isothermal reaction, and (d) Al-Mo-TiC after 4h isothermal reaction. (e) Engineering stress-strain curves for micropillar compression tests for Al-TiC and Al-Mo-TiC under 0h and 4h isothermal reaction, respectively.

With the prolonged isothermal reaction at 750°C, the microhardness of Al-Mo-TiC changes more rapidly and finally gets closer to Al-TiC. This is because Mo is transitioning from the Al-TiC interfacial atom to the element in the intermetallic phase (i.e., with $Al_3Ti(Mo)$ composition), leading to the same intermetallic strengthening as in Al-TiC (i.e., Al_3Ti); Besides, as mentioned in **Figure 5 - 6** (c) and (d), the Mo addition could also reduce the brittleness by constantly diffusing and segregating into the intermetallic secondary phase, with the reaction continuing. This is also why a sharper microhardness decrease in Al-Mo-TiC during the isothermal reaction in **Figure 5 - 7** (a).

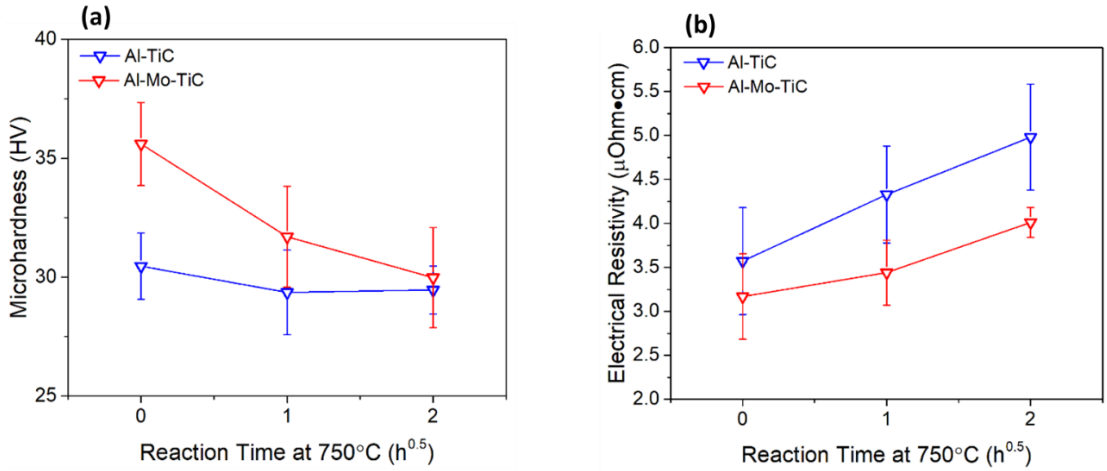

Figure 5 - 7 (a) The microhardness and (b) the electrical resistivity of Al-Mo-TiC and Al-TiC nanocomposites after synthesis, 1 h holding, and 4 h holding at 750°C.

For the electrical conductivity in **Figure 5 - 7** (b), with the prolonged isothermal reaction, the electrical resistivity of both Al-TiC and Al-Mo-TiC is increased, since the formed $Al_3Ti(Mo)$ phase (~60 μOhm · cm) [245] has a much higher electrical resistivity than TiC (~30.3 μOhm · cm) [246]. Besides, as shown in **Figure 5 - 5** (b) and (d), the transitional interface between the intermetallic $Al_3Ti(Mo)$ and Al could lead to severe electron localization, which is also

disadvantageous for electrical conductivity after 750℃ isothermal reaction [2,247]. To compare the effect of Mo addition, the properties of Al-TiC and Al-Mo-TiC before the isothermal reaction and after the 4-hour isothermal reaction have been listed in **Table 5 - 1**. By this table, it should be noted that the compression yield strength shows the largest difference among the samples after 4h isothermal reaction. This is because the micropillar tests focus on the localized properties within ~5×5 μm^2, and the effects of the role of the local intermetallics and Al matrix's interface would be enlarged or even dominant. Given the abovementioned advantages like ductility enhancement and superior interface by Mo addition, the compressive yield strength difference for Al-TiC and Al-Mo-TiC after 4h isothermal reaction would be expected.

Later, the XRD peak intensity in **Figure 5 - 8** (a) and (b) at various reaction stages together with the EDS element scanning is used to quantify the $Al_3Ti(Mo)$ formation rate under 750℃ in **Figure 5 - 8** (c). As shown in **Figure 5 - 8** (b), in both Al-TiC and Al-Mo-TiC systems, with the prolonged isothermal reaction at 750℃, more and more TiC will be consumed to form the intermetallic $Al_3Ti(Mo)$ phase. However, with the Mo addition, Al-Mo-TiC has a slower TiC reaction rate than Al-TiC at 750℃ (see **Figure 5 - 8** (c)).

Table 5 - 1 Overall comparison of the properties of Al-TiC and Al-Mo-TiC before the isothermal reaction and after the 4-hour isothermal reaction

	Reaction time	Al-TiC	Al-Mo-TiC
Microhardness (HV)	0 hr	30.5 ± 1.4	35.6 ± 1.8
	4 hr	29.5 ± 1.0	30.0 ± 2.1
Compressive yield strength (MPa)	0 hr	142 ± 9	145 ± 7
	4 hr	757 ± 38; brittle	150 ± 8; ductile
Electrical resistivity	0 hr	3.57 ± 0.61	3.17 ± 0.49

$(\mu Ohm \cdot cm)$	4 hr	4.98 ± 0.60	4.01 ± 0.17
Intermetallic size (μm)	4 hr	42 ± 6	24 ± 5

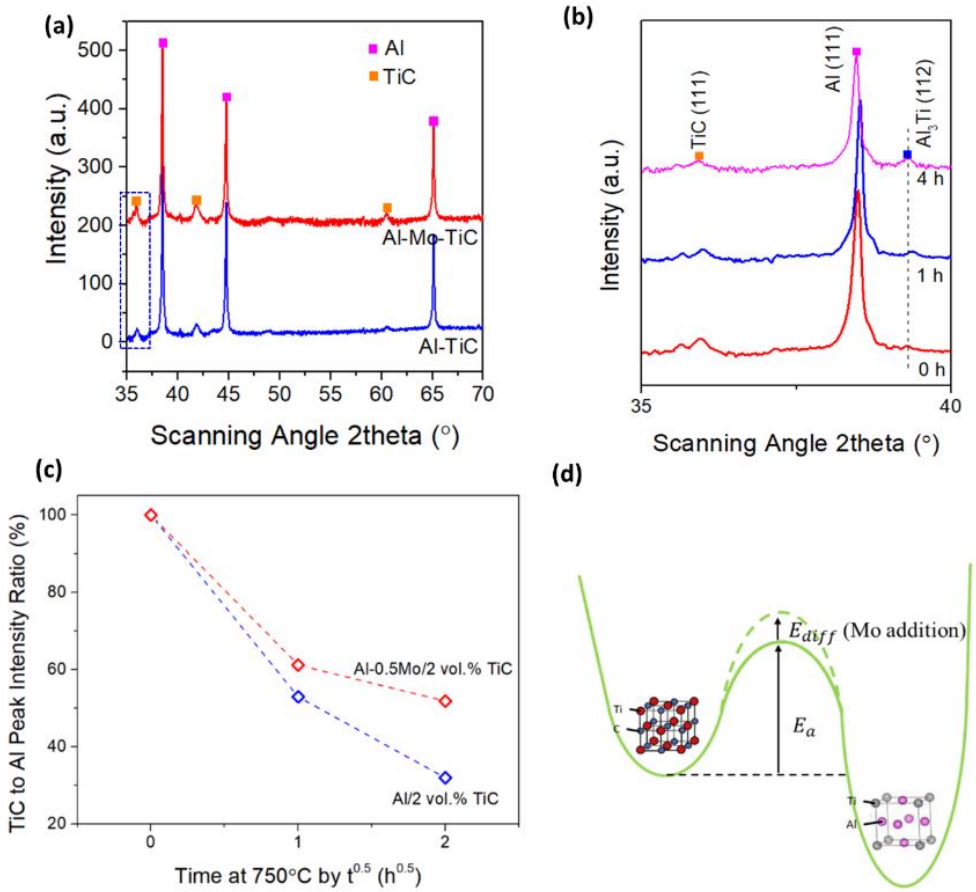

Figure 5 - 8 (a) The XRD scanning for Al-TiC and Al-Mo- TiC nanocomposites after synthesis, and (b) The enlarged XRD images for the comparison of the peak intensity of TiC and $Al_3Ti(Mo)$ during the 750℃ holding in Al-Mo-TiC. (c) The TiC reaction rate at 750℃ with the prolonged reaction time; (d) The illustration of the effect of adding Mo on the Al-TiC reaction at 750℃.

From **Figure 5 - 4** (f), it could be seen that Mo forms an interlayer on the surface of TiC nanoparticles. This interlayer will separate the direct contact of Al and TiC, which means that element diffusion by Al and Ti is needed before the chemical reaction process would happen. Therefore, as shown in **Figure 5 - 8** (c), since the reaction is a diffusion-controlled process with a similar enthalpy (see **Table 5 - 2**),[239] the formation of Al_3Ti through the reaction between Al (or Al-Mo) and TiC will be governed by:

Eq. 5 - 2

$$\frac{\partial V}{\partial t} = D_{Al-TiC} \cdot \frac{\partial^2 V}{\partial r^2}$$

Where V is the characteristic volume of the formed Al_3Ti, D_{Al-TiC} the reaction-related coefficient to reflect the diffusion nature of the process, and r the characteristic interlayer thickness of Al_3Ti (or Al_3Ti(Mo) for Al-Mo-TiC system).

Table 5 - 2 Energy of the related chemical reactions at ~750℃ [248–250]

Reaction	**Formation Enthalpy ΔH (KJ/mol)**	**Product Gibbs Free Energy ΔG (KJ/mol)**
Al+Ti→Al_3Ti	-153	-298
Ti+C→TiC	-156	-175

Then, with a quasi-1D solution, $r \cong 2\sqrt{D \cdot t}$. Since it is in the diffusion-controlled time scale, it could be simplified when $r \ll R$, where R (~10μm) denotes the TiC nanoparticle pseudo-cluster size. Therefore, the growth of Al_3Ti will be governed by the approximation of:

Eq. 5 - 3

$$V \cong 8\pi R^2 \sqrt{D \cdot t}$$

We should note that this characteristic size does not consider the merging agglomerations of multi-piece Al_3Ti (as shown in **Figure 5 - 5** (c) and (d)). As mentioned above, the original TiC

total volume could be estimated from the visible pseudo-clusters by R (~10μm). The reaction rate calculated via the percentage of residual TiC to fit the trend in **Figure 5 - 8** (c) will be:

Eq. 5 - 4 $$\rho \cong 1 - \frac{V}{V_0} = 1 - \frac{\sqrt{\mathrm{D}\cdot\mathrm{t}}}{6\mathrm{R}}$$

Where ρ is the residual TiC content percentage in **Figure 5 - 8** (c), and V_0 gives the original TiC volume by the estimation of $\frac{4}{3}\pi R^3$.

Hence, by using **Eq. 5 - 4** to fit the reaction curve of **Figure 5 - 8** (c), the reaction diffusion coefficient D in the reaction of the Al-TiC system can be determined as $\sim 1.33 \times 10^{-13}\ \mathrm{m^2/s}$, whereas the reaction diffusion coefficient for the Al-Mo-TiC system is only $\sim 6.08 \times 10^{-14}\ \mathrm{m^2/s}$. It should be noted that the calculated diffusivity is comparable to the range of the solute diffusivity of Mo/Ti mentioned in Ref. [251]. This comparison proves that the addition of Mo, even though a small amount, could effectively hinder the chemical reaction by a lower diffusion rate and thus enhance the thermal stability at the interface of Al and TiC at 750℃.

Furthermore, in thermally triggered chemical reaction related to Gibbs free energy as the stability criterion (see **Table 5 - 2**), the kinetics parameters (e.g., $\mathrm{D_{Al-TiC}}$ here) could be used to extract energy-controlled dynamic terms (e.g., activation energy). In our case, after the reaction-related coefficient of $\mathrm{D_{Al-TiC}}$ is quantified for Al-TiC and Al-Mo-TiC systems under 750℃, respectively, the reaction diffusion coefficient is directly related to the thermal activation with the Arrhenius relationship in Ref. [252] by:

Eq. 5 - 5 $$\mathrm{D} \propto \exp\left(-\frac{E_a}{k_B \cdot T}\right)$$

Thus, under the same temperature (i.e., 750℃ in our case), the difference in the reaction diffusion coefficient of Al-Mo-TiC indicates an activation energy escalation ΔE_a by the slower-

diffusing Mo addition (with $\Delta E_a \cong E_{diff}$) (as illustrated in **Figure 5 - 8** (d)). E_{diff} associated with Mo addition is estimated to be 0.069 eV.

With this understanding, since E_a is relatively insensitive to temperature, the positive effects from Mo addition would also be expected if Al-TiC is directly alloyed with Mo under 750℃. As shown in **Figure 5 - 11**, the reaction rate between Al and TiC after the Mo addition at 750℃ is comparable to Al-Mo-TiC fabricated under 900℃, still indicating a beneficial reaction suppression over Al-TiC systems.

In conclusion, the addition of Mo into the Al-TiC system is advantageous for its chemical stability at the favorable Al processing temperature range (~750℃). With Mo addition, Mo increases the reaction activation energy by about 0.069 eV and introduces a lower reaction diffusion coefficient during the reaction between Al and TiC. During the reaction, Mo will form intermetallic products with $Al_3Ti(Mo)$ more slowly, thus making the intermetallic phase finer. This study offers a novel insight into how Mo and other suitable micro-alloying elements can help stabilize TiC in the aluminum melt at a more industry-favorable processing temperature.

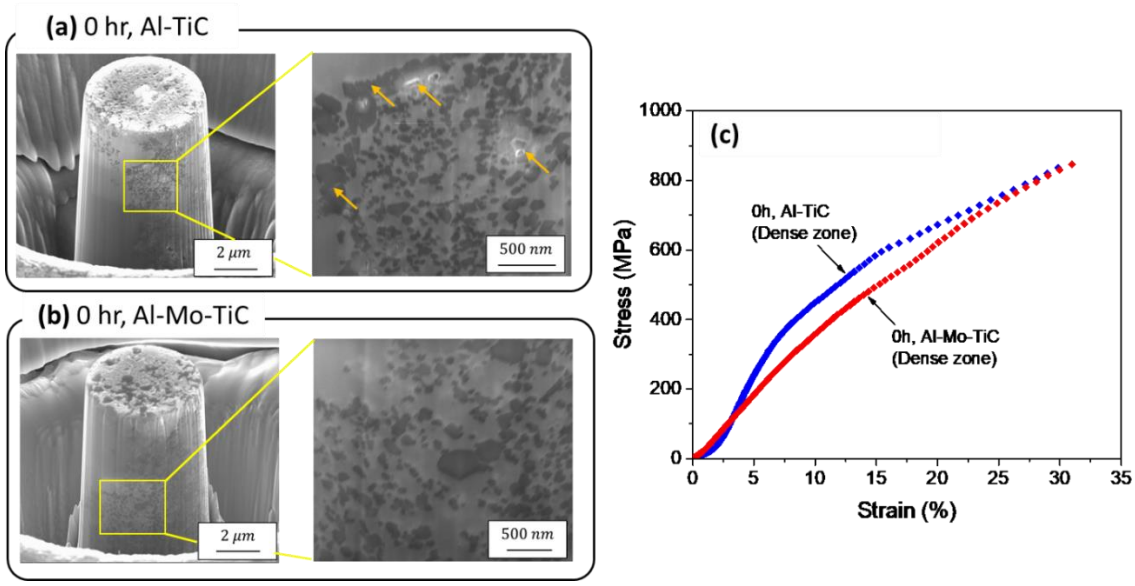

Figure 5 - 9 Micropillars for (a) Al-TiC with 0h isothermal reaction (with arrows indicating defects and large TiC particles) and (b) Al-Mo-TiC with 0h isothermal reaction to show the TiC nanoparticle pseudo-dispersion situation. (c) The compression stress-strain curve for micropillars at TiC nanoparticle dense zone of Al-TiC and Al-Mo-TiC with 0h isothermal reaction.

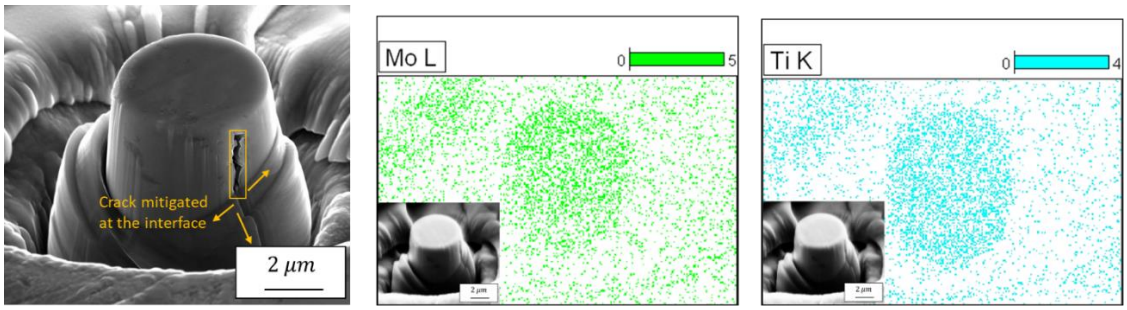

Figure 5 - 10 (a) Crack propagation mitigated at the matrix-intermetallic phase interface and EDS mapping for (b) Mo L peak and (c) Ti K peak for the Al-Mo-TiC micropillar in **Figure 5 - 6** (d) after compression test.

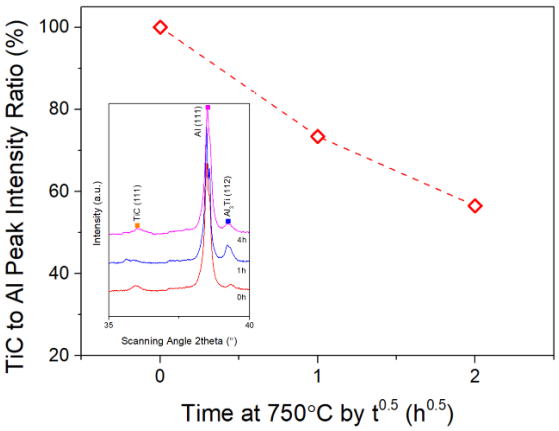

Figure 5 - 11 The TiC reaction rate at 750℃ with the prolonged reaction time for Al-Mo-TiC with Mo addition at 750℃ for 10 min alloying and then under 750℃ isothermal reaction. (Inserted: the enlarged XRD images for comparing the peak intensity of TiC during the 750℃ holding in Al-Mo-TiC).

5.2.2 Chemical reactivity of Al-Si/TiC nanocomposite

To fabricate the AlSi10Mg-2 vol.% TiC nanocomposites (hereafter, AlSi10Mg-TiC), the Al-3.5 vol.% TiC master (hereafter, Al-TiC) was first synthesized *in situ* via the previously reported recipe from Ref. [253,254]. The dispersion and size distribution were checked before use, as summarized in **Figure 5 - 12 (b)-(d)**. Then, the pure Al (with the purity >99.99%, from *American Elements Inc.*) was first melt at 850 ± 15 ℃ isothermally with a graphite crucible under Ar protection in an induction furnace. After 10 mins, Al-50 wt.% Si master alloy (from *Belmont Inc.*, USA) was added as designed. Until the alloy was fully melt, Al-TiC master was added slowly, in case of the temperature drop to the Al-TiC reaction range, [176] as shown in **Figure 5 - 12 (a)**. Pure Mg (with the purity >99.99%, from *American Elements Inc.*) was added simultaneously. Afterwards, the molten pool was kept for 30 min with a mechanical stirring at 100 rpm, cast into a permanent mold, and air-cooled. The pure AlSi10Mg, AlSi10-TiC, and AlSi10Ag-TiC (with Ag from *Umicore Precious Metals Canada Inc.*, grain fine with minimum purity of 99.99%) was prepared via the similar route.

In addition, previous studies have confirmed the critical influence of T6-like heat treatment [255,256]. In our study, the similar T6 heat treatment has been conducted for all the Al-Si alloys and nanocomposites. [256–258] During the process, the solution treatment was carried out in a heat treatment furnace at 540 °C for 2 h. Then, the samples were immediately water-quenched. After water quenching, the samples were later artificially-aged for 12 h at 160 °C [258,259].

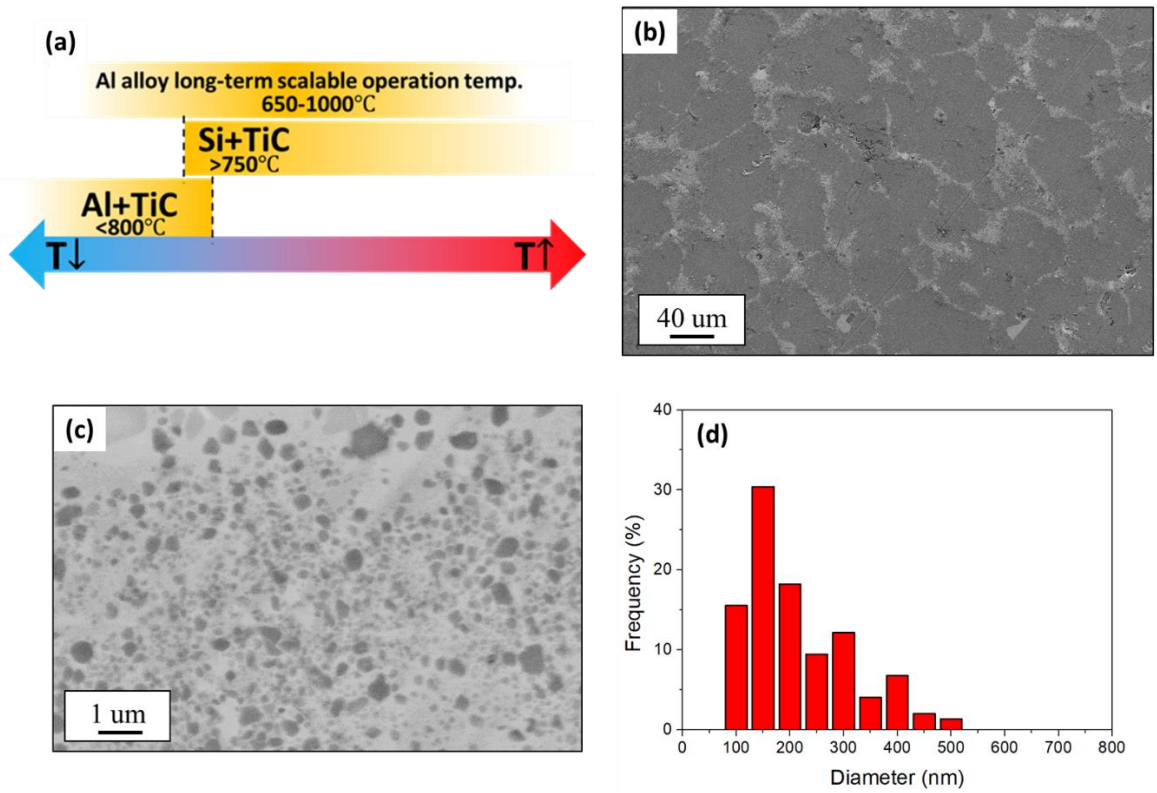

Figure 5 - 12 (a) The temperature-dependent reactive instability in Al-Si and TiC system. The microstructure of **(b)** Al-3.5 vol.% TiC master. **(c)** The enlarged image for the TiC morphology and **(d)** the TiC size distribution in Al-3.5 vol.% TiC master.

Phase and microstructure change As shown in **Figure 5 - 12 (b)-(d)**, the TiC nanoparticles are pseudo-dispersed homogeneously in the original Al-TiC master, and the average diameter of the TiC nanoparticles is ~121 $\pm$ 35 nm. The XRD scanning in **Figure 5 - 13** also proves the good purity of the synthesized TiC nanoparticles.

When looking at the products after 30 min casting process, it could be seen that an obvious composition difference among as-cast AlSi10Mg, Al-3.5TiC, AlSi10Mg-TiC, and AlSi10-TiC, as scanned by XRD in **Figure 5 - 13**. The pure AlSi10Mg includes the typical Si-rich eutectic peaks, with a little Mg_2Si phases. However, for both AlSi10Mg-TiC and AlSi10-TiC, the peaks of the

chemical reaction product from Si and TiC stand out. No clear TiC peaks are observable, and the complex compounds of $Al_3TiSi_xC_y$ (mainly Ti_3SiC_2) are formed.

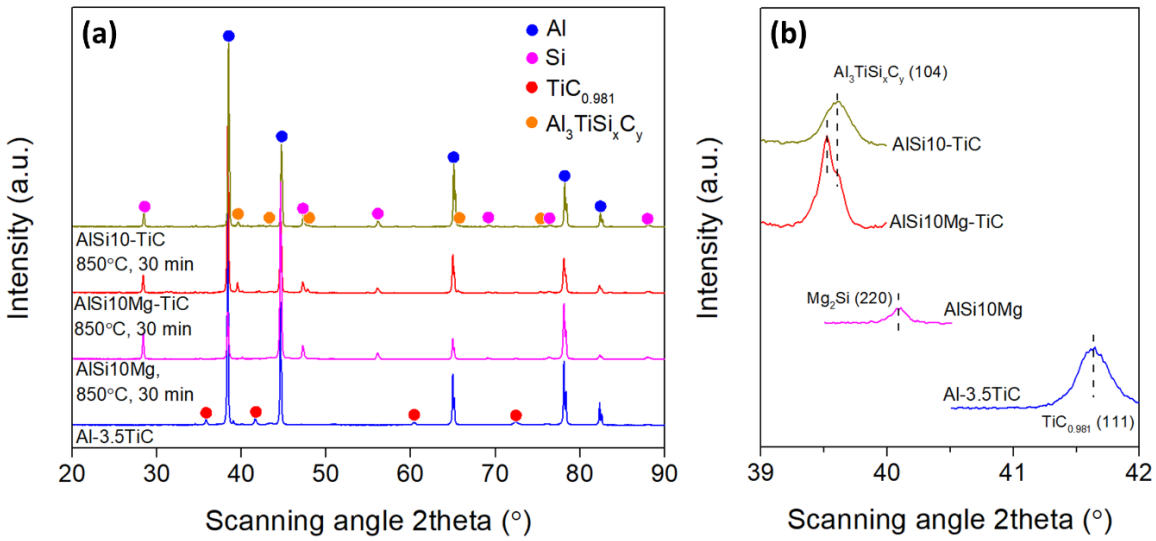

Figure 5 - 13 (a) The phase composition of as-cast AlSi10Mg alloy, AlSi10Mg-TiC nanocomposites, and the original Al-TiC master, and **(b)** the zoomed-in image of the strongest peak of TiC, Mg_2Si, and $Al_3TiSi_xC_y$ phases

Further investigating the post-reaction microstructure in **Figure 5 - 14 (a)**, it could be seen that pure AlSi10Mg is stable during the processing. Only eutectic phases with some Mg_2Si of 1-10 um in size are observable, and these eutectic phases form a network-like structure. However, AlSi10Mg-TiC nanocomposites show a different microstructure (see **Figure 5 - 14 (b)** and **(c)**). In the areas without long bulky $Al_3TiSi_xC_y$ pieces (see **Figure 5 - 14 (b)**), when the initial reaction stage happens, the pseudo-dispersed TiC nanoparticles are attracting more Si into the area, and they start to merge and agglomerate. One interesting observation is that the added Mg would concentrate near or at the interface of these initial reaction zones (see the Mg K element mapping in **Figure 5 - 14 (b)**). On the contrast, in the areas where the bulky $Al_3TiSi_xC_y$ pieces have already formed, these intermetallic pieces are dispersed into the eutectic phase zones more uniformly with

a length of ~10 um. Near these intermetallic-forming zones, Mg does not form Mg_2Si secondary phase, and their solid solution into Al shows a uniform distribution (see **Figure 5 - 14 (c)**). It should also be noted that due to Si reaction, TiC nanoparticles may not have enough nucleation potency[260], so the changed microstructures and mechanical properties would be more related to the formed intermetallics.

Given the importance of the Si-TiC reaction and the resultant products, understanding how the more rapid TiC consumption by Si in AlSi10Mg system is needed. According to the XRD, microstructure analysis and other previous studies [261], for Al-Si system without Mg, the reaction with TiC could be summarized as:

Eq. 5 - 6 $$(1+7x)\ Si+8TiC+29Al \xrightarrow{850\ ℃} 7Al_3Ti(Si_x)+Al_8C_7Si$$

However, in AlSi10Mg-TiC system, the reaction carries a different signature. Since Mg is more concentrated near the initial TiC-dense zone at the initial reaction interface by diffusion (see **Figure 5 - 14 (b)**), it could be deduced that the accelerated reaction process is due to the Mg addition. Given the higher melting temperature of Mg_2Si (~1081.4℃), this increased reaction speed could be sustained by the constant Si supply through the interfacial Mg_2Si and the tendency to nucleate and precipitate, as shown in **Eq. 5 - 7** and **Eq. 5 - 8**:

Eq. 5 - 7 $$(7+x)Mg_2Si+21TiC+8Al \xrightarrow{850\ ℃} 7Ti_3SiC_2+Al_8C_7(Si_x)+2(7+x)Mg\ (Sol.)$$

Eq. 5 - 8 $$2Mg\ (Sol.)+Si\ (Sol.) \xrightarrow{850\ ℃} Mg_2Si\ (\Delta H_f < 0)$$

This Mg-induced reaction is supported by the phase diagram calculation in **Figure 5 - 22 (b)**.[259] As shown by the 10 wt.% Si contour line in **Figure 5 - 22**, the segregation of Mg could fluctuate and cross the Mg_2Si range, which raises the thermal probability for the reaction accelerated by Mg_2Si. Particularly, the formation enthalpy associated with **Eq. 5 - 8** is negative, indicating a favorable energy supply to help activate the chemical reaction (see **Figure 5 - 21**).

Therefore, the role of Mg would be continuously supplying reactive Mg_2Si (**Figure 5 - 13**), segregating to the nucleating site near the TiC-dense zone (**Figure 5 - 14 (b)** Mg K peak), and attracting more Si to the TiC-dense zone to form the $Al_3Ti(Si_xC_y)$ intermetallics (**Figure 5 - 14 (b)** Si K peak). The thermal stability of Ti_3SiC_2-like phases in Al-Si system [262] supports the proposed reaction mechanism.

To prove this observation, the microstructure of as-cast AlSi10Mg-TiC (**Figure 5 - 14 (b)** and **(c)**) and AlSi10-TiC (**Figure 5 - 14 (d)** and **(e)**) has been further compared. Without Mg in AlSi10-TiC, **Figure 5 - 14 (d)** shows that the reaction rate is slower, since the TiC-dense zone still has residual particles, and the intermediate reaction product is observable in the enlarged SEM image. Compared with **Figure 5 - 14 (b)**, Si has no clear concentration into the TiC-dense zone. The more rapid reaction in AlSi10Mg-TiC than in AlSi10-TiC confirms the crucial role of Mg's addition.

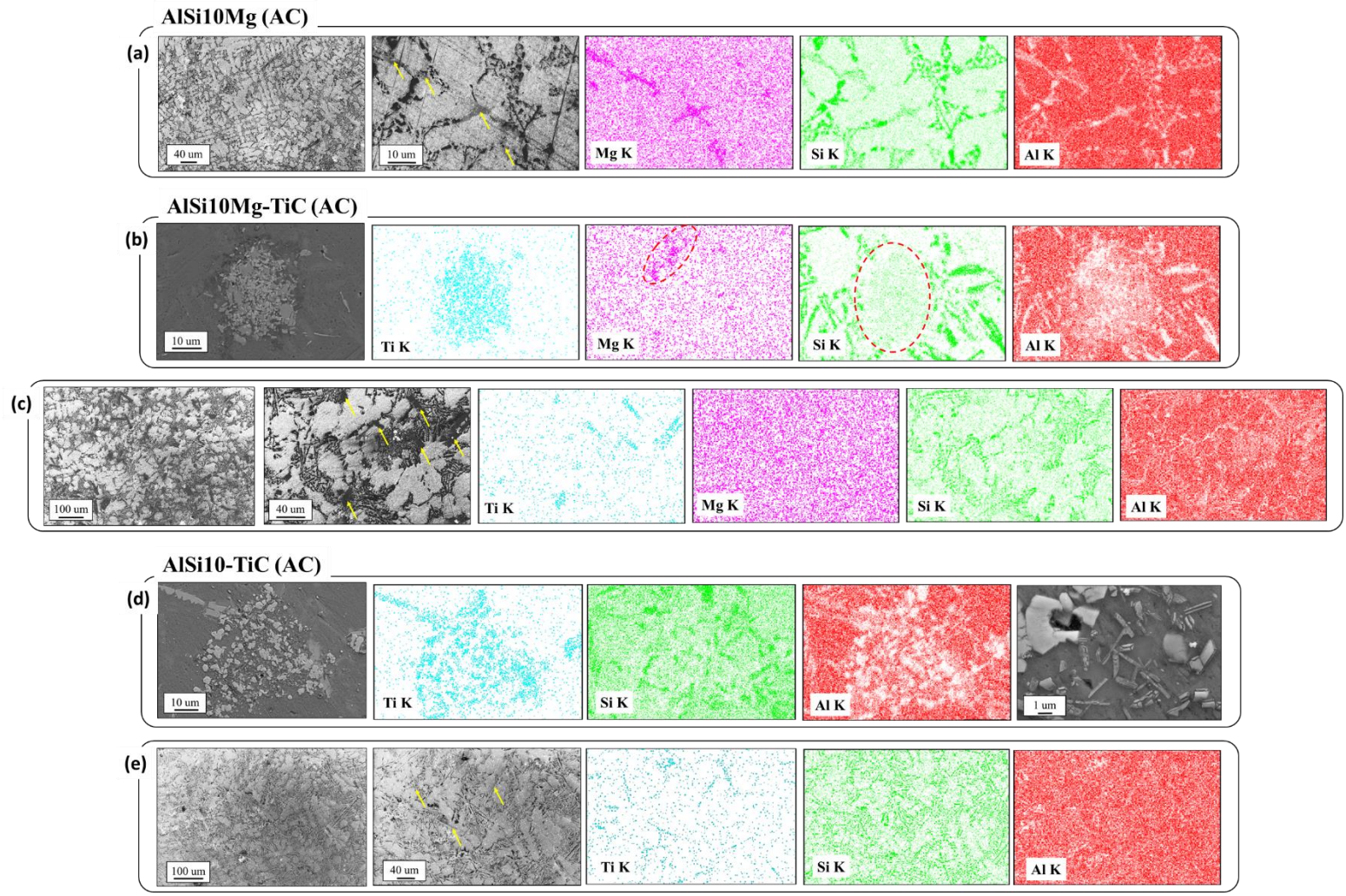

Figure 5 - 14 The microstructure and the elemental mapping of **(a)** as-cast AlSi10Mg alloy, **(b)** and **(c)** as-cast AlSi10Mg-TiC nanocomposites, and **(d)** and **(e)** as-cast AlSi10-TiC nanocomposites. **(b)** and **(d)** are showing the initiation of the chemical reaction near the nanoparticle-dense zone in as-cast AlSi10Mg-TiC and AlSi10-TiC, respectively.

<u>*Mechanical property change*</u> **Figure 5 - 15 (a)-(f)** shows the etched morphology of as-cast AlSi10Mg, AlSi10Mg-TiC, and AlSi10-TiC surfaces. According to the microhardness results in **Figure 5 - 15 (g)**, the AlSi10Mg-TiC system has ~7HV higher hardness than the AlSi10Mg system. As shown in the SEM images for the indent marks, the rapidly formed $Al_3Ti(Si_xC_y)$ intermetallics contributes to this hardness increase.

Besides, after etching, the AlSi10Mg-TiC has long bulky $Al_3Ti(Si_xC_y)$ intermetallic pieces mostly (see **Figure 5 - 15 (d)**), whereas the AlSi10-TiC still shows particle-dense zones with irregular perimeter (see **Figure 5 - 15 (f)**).

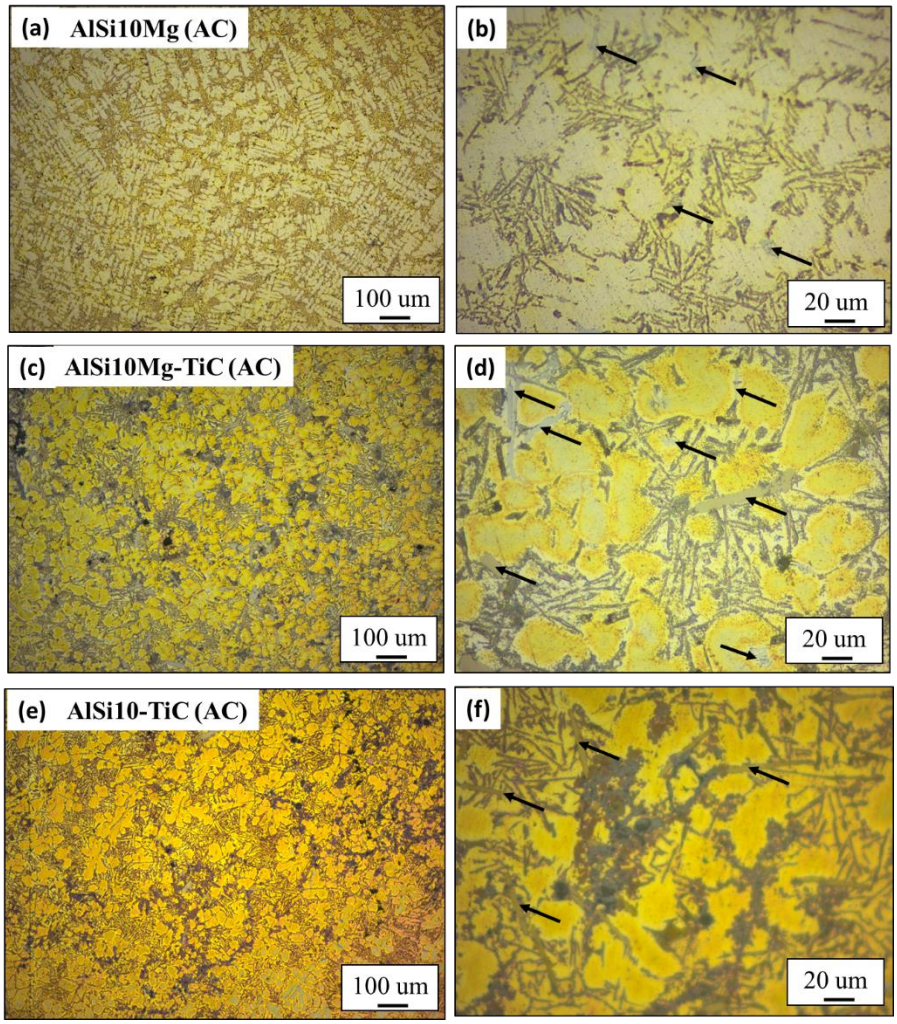

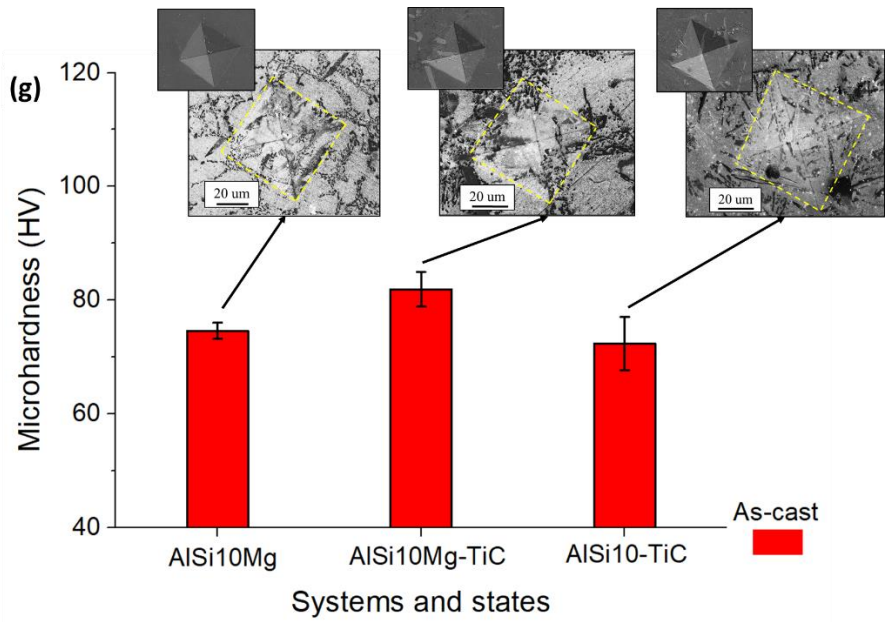

Figure 5 - 15 The etched microstructure and grain size comparison among as-cast **(a)** and **(b)** AlSi10Mg alloy (black arrow indicates Mg_2Si phases), **(c)** and **(d)** AlSi10Mg-TiC nanocomposites (black arrow indicates the formed intermetallic phases), and **(e)** and **(f)** AlSi10-TiC nanocomposites (black arrow indicates the formed intermetallic phases); **(g)** The microhardness and indentation mark of as-cast AlSi10Mg alloy and as-cast AlSi10Mg-TiC nanocomposites.

The similar observation is found in T6 heat treated samples for AlSi10Mg, AlSi10Mg-TiC, and AlSi10-TiC. As shown in **Figure 5 - 16**, after the T6 heat treatment, the eutectic phases have been modified into small pieces with a more regular morphology in AlSi10Mg, AlSi10Mg-TiC, and AlSi10-TiC. However, there exists large bulk pieces of $Al_3TiSi_xC_y$ in AlSi10Mg-TiC, and Mg_2Si is adjacent to these formed intermetallics (see **Figure 5 - 16 (b)** and **Table 3 - 3**). This observation also supports the Mg2Si-induced reaction mechanism. In comparison, though bulk pieces of $Al_3TiSi_xC_y$ are also appearing in T6-heat treated AlSi10-TiC, some of the reaction product still keeps the irregular perimeter like the particle-dense morphology (see **Figure 5 - 16 (c)**). The etched microstructure in **Figure 5 - 16 (a)-(f)** validates the same observation and gives the consistent proof to **Figure 5 - 15** in as-cast state.

Similarly, the microhardness in **Figure 5 - 17 (g)** confirms the effectiveness of Mg_2Si precipitation strengthening in AlSi10Mg and AlSi10Mg-TiC and this trend is consistent with the results in **Figure 5 - 15 (g)**.

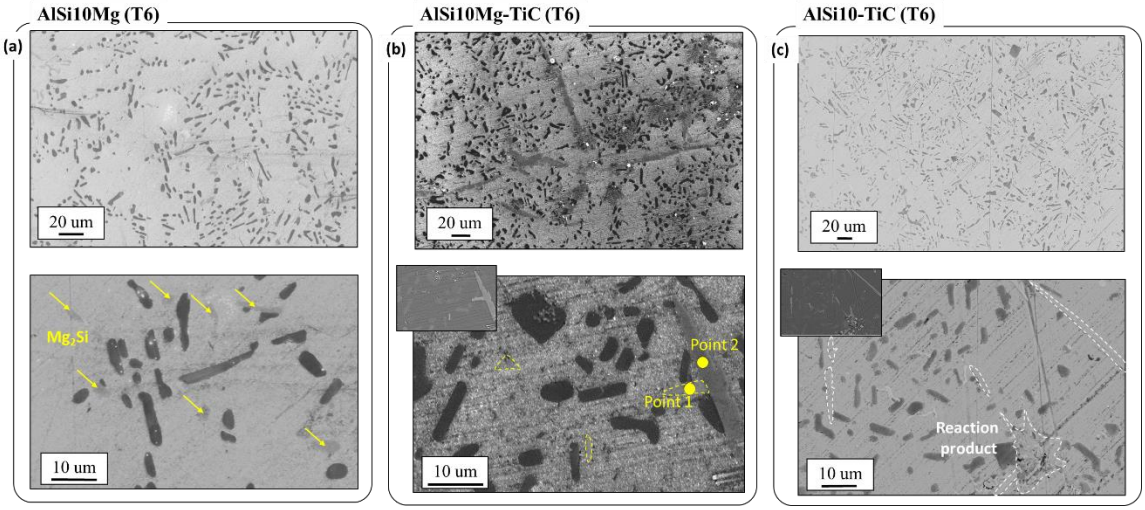

Figure 5 - 16 The microstructure of **(a)** T6 heat-treated AlSi10Mg alloy, **(b)** T6 heat-treated AlSi10Mg-TiC nanocomposites, and **(c)** T6 heat-treated AlSi10-TiC nanocomposites.

Table 3 - 3 EDS elemental point scanning for locations in **Figure 5 - 16 (b)** for T6 heat-treated AlSi10Mg-TiC nanocomposites

Location	Al (wt.%)	Mg (wt.%)	Si (wt.%)	Ti (wt.%)	Possible compounds
Point 1	42.32	16.31	41.17	0.20	Mg_2Si
Point 2	78.47	0.00	8.11	13.42	$AlSiTi/Al_3TiSi_xC_y$

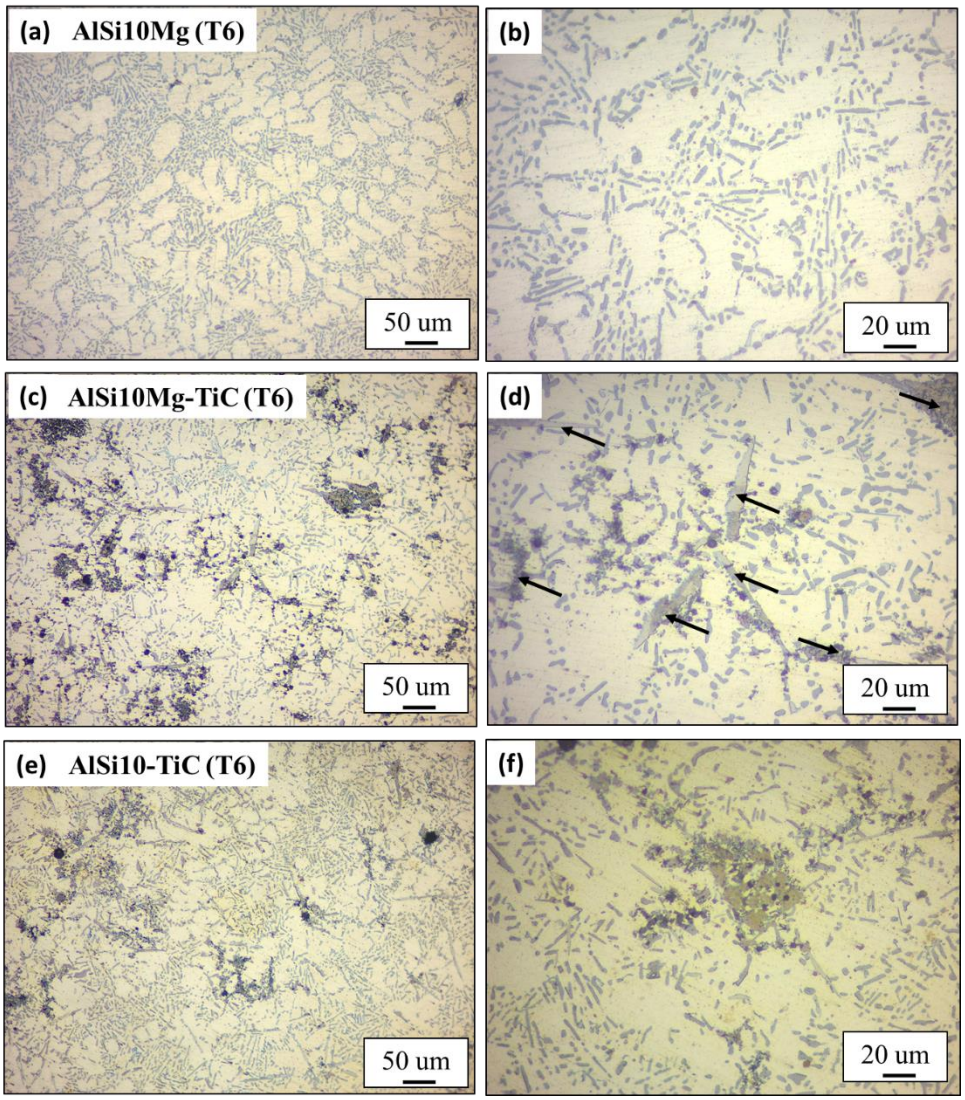
(a) AlSi10Mg (T6)
50 um
(b)
20 um
(c) AlSi10Mg-TiC (T6)
50 um
(d)
20 um
(e) AlSi10-TiC (T6)
50 um
(f)
20 um

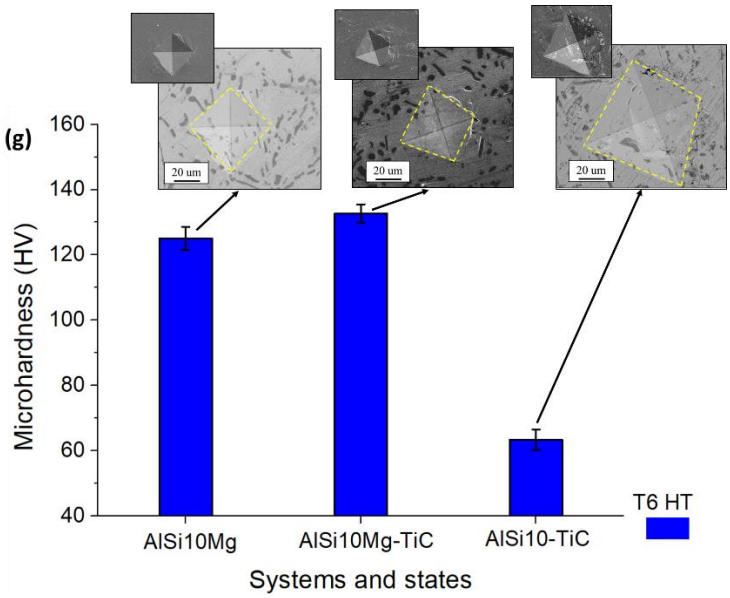
(g)
Microhardness (HV)
160
140
120
100
80
60
40
20 um
20 um
20 um
AlSi10Mg
AlSi10Mg-TiC
AlSi10-TiC
Systems and states
T6 HT

Figure 5 - 17 The etched microstructure and grain size comparison amongT6 heat-treated **(a)** and **(b)** AlSi10Mg alloy (yellow arrow indicates Mg_2Si phases), **(c)** and **(d)** AlSi10Mg-TiC nanocomposites (yellow circle indicates Mg_2Si phases), and **(e)** and **(f)** AlSi10-TiC nanocomposites (yellow circle indicates the formed intermetallic phases); **(g)** The microhardness and indentation mark of T6 heat-treated AlSi10Mg alloy and as-cast AlSi10Mg-TiC nanocomposites.

Figure 5 - 19 shows the tensile test results for the as-cast and T6 heat-treated samples of AlSi10Mg, AlSi10Mg-TiC, and AlSi10-TiC. We should note that the tensile properties of as-cast AlSi10Mg is similar to the literature values [258]. For AlSi10Mg and AlSi10Mg-TiC after T6 heat treatment, the ductility is sacrificed in both the systems, and the strength is increased greatly by the T6 heat-treatment. However, the AlSi10-TiC samples have a different mechanical performance after the heat treatment and show a slightly increased strength and an almost doubled ductility [263]. We should also note that the heat-treatment induced strengthening is contrary to the age-softening of AlSi10Mg alloys by 3D-printing [255,264], because the eutectic phases in AlSi10Mg alloys or nanocomposites are stable in their size and the heat treatment will not cause noticeable coarsening.

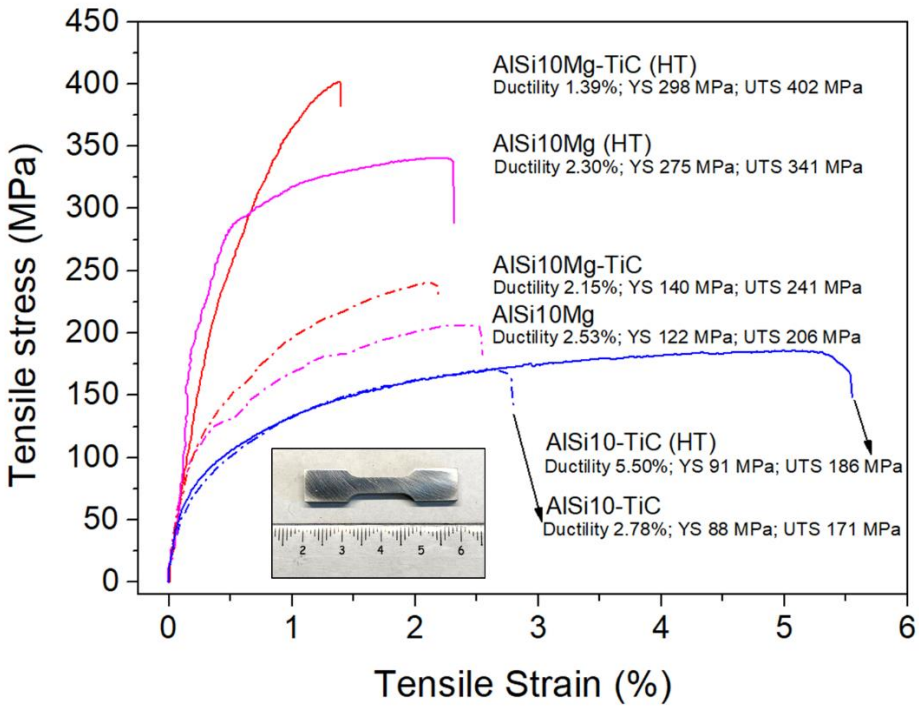

Figure 5 - 18 The stress-strain curve for as-cast and heat-treated AlSi10Mg, AlSi10Mg-TiC, and AlSi10-TiC.

The fracture surface morphology is exposed in **Figure 5 - 19** after the tensile tests. For pure AlSi10Mg, as-cast samples show partial dimples and partial brittle morphology (**Figure 5 - 19**a). After the heat treatment, the dimples become shallower yet denser, and the brittle surfaces exhibit more step-like serrated morphology (**Figure 5 - 19**b). For all the TiC-reinforced nanocomposites, the dimple sizes and the fracture plane sizes are all reduced. Specifically, for AlSi10Mg-TiC, the as-cast samples have larger brittle fracture surface, with occasional small dimples (**Figure 5 - 19**c). These features contribute to a higher strength but lower ductility than as-cast AlSi10Mg. After the heat treatment, the AlSi10Mg-TiC samples show similar serrated morphology, and different brittle fracture planes are denser (**Figure 5 - 19**d). Original TiC-dense zone, as well as the reaction-introduced intermetallics, is near the fracture surface. Comparatively, as-cast AlSi10-TiC have the

similar brittle fracture surface to as-cast AlSi10Mg-TiC (**Figure 5 - 19**e). However, after the heat treatment, since AlSi10-TiC has less chemical reaction, the fracture surface of heat-treated AlSi10-TiC is more ductile, and brittle surfaces are surrounded with small but dense dimples (**Figure 5 - 19**f). More importantly, no large pieces of intermetallics are observable on the fracture surfaces. The above fractography observation is consistent with the phase and chemical composition analysis in the previous section and the results from AlSi10Ag-TiC (see the following section).

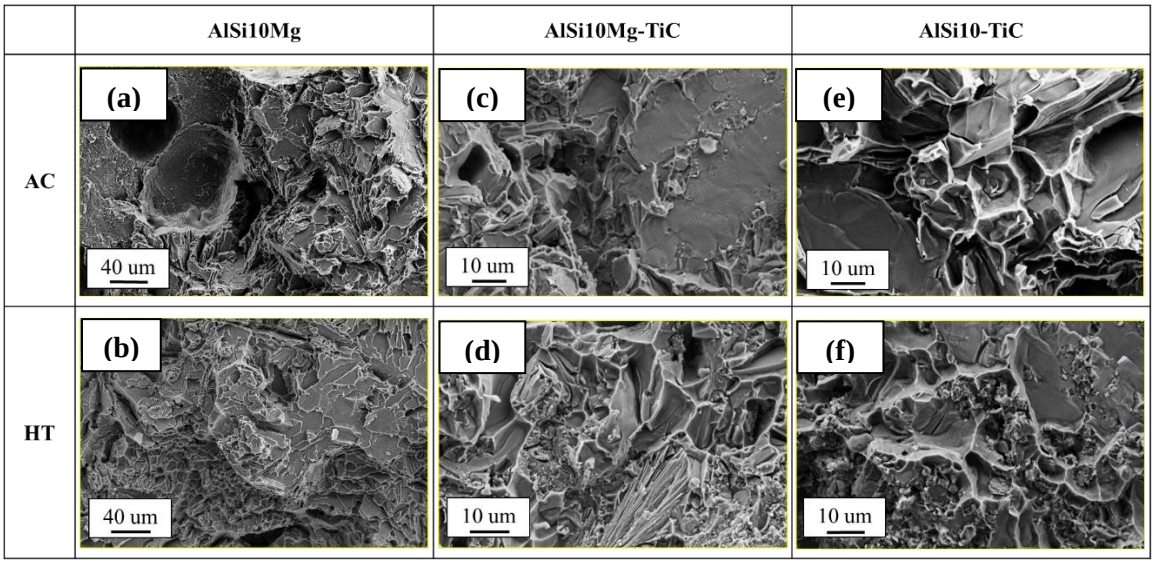

Figure 5 - 19 The fractography images for as-cast and heat-treated AlSi10Mg, AlSi10Mg-TiC, and AlSi10-TiC.

Reaction dynamics: To reveal the reaction dynamics between Si and TiC and make clear ofMg's contribution, AlSi7-TiC system has been added for comparison.

As shown in **Figure 5 - 20**, after the casting process, there are still TiC particles in their original shape and size in the AlSi7-TiC system, and the intermetallic phases are not observable. When the Si concentration is increased (i.e., in AlSi10-TiC), clear chemical reaction happens in the TiC-dense zone, and the reaction precursors are observed. However, due to the reasonable reaction speed, the reaction products are not agglomerating or sintering into big pieces. After

adding Mg in AlSi10Mg-TiC, the reaction happens even faster, and the chemical products already grow into big clusters.

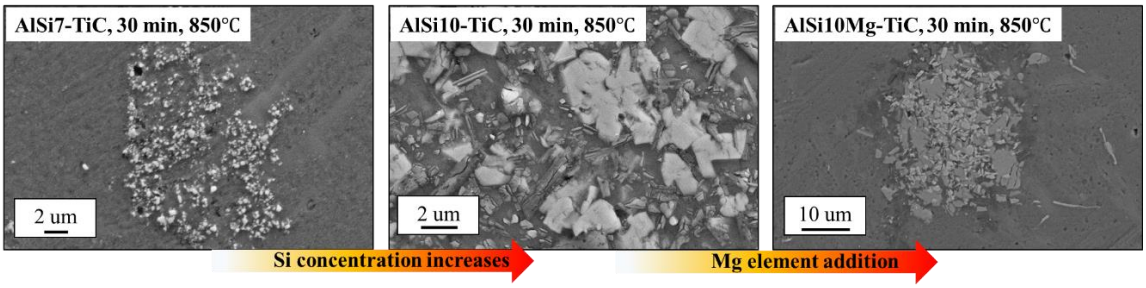

Figure 5 - 20 The reacted product near the (residual) TiC-dense zone in as-cast AlSi7-TiC, AlSi10-TiC, and AlSi10Mg-TiC after 30 min isothermal holding at 850℃.

As summarized in **Figure 5 - 21**, the chemical reaction dynamics could be illustrated to show the effects of increasing Si and adding Mg. When Si concentration is increased, the chemical potential of Si in molten Al-Si is higher, and the energy needed to cross the activation energy barrier is compensated by the increased chemical potential. This is why AlSi10-TiC has a higher chemical reaction speed than AlSi7-TiC. In addition, higher Si concentration in Al-Si-Mg will make the intersection of the Si concentration contour line easier (See **Figure 5 - 22**), which raises the possibility of introducing meta-stable Mg_2Si to the interface near TiC-dense zone. After adding Mg, according to **Eq. 5 - 8**, Mg and Si collides in the molten Al and form Mg_2Si embryo to release heat, and this energy will lower the activation barrier directly, therefore the Si-TiC reaction will be facilitated by the Mg_2Si formation.

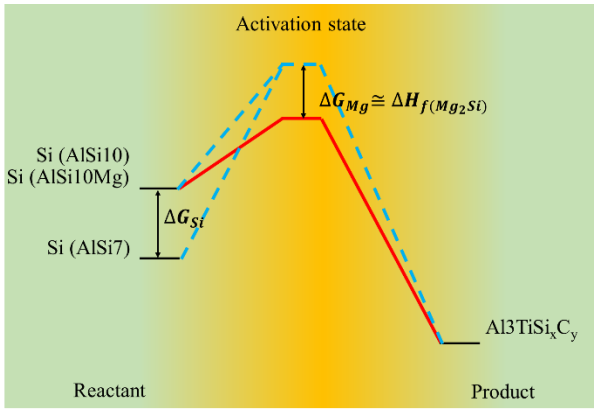

Figure 5 - 21 The schematic picture to show the influence of Si concentration and Mg addition on the reaction dynamics between Si and TiC.

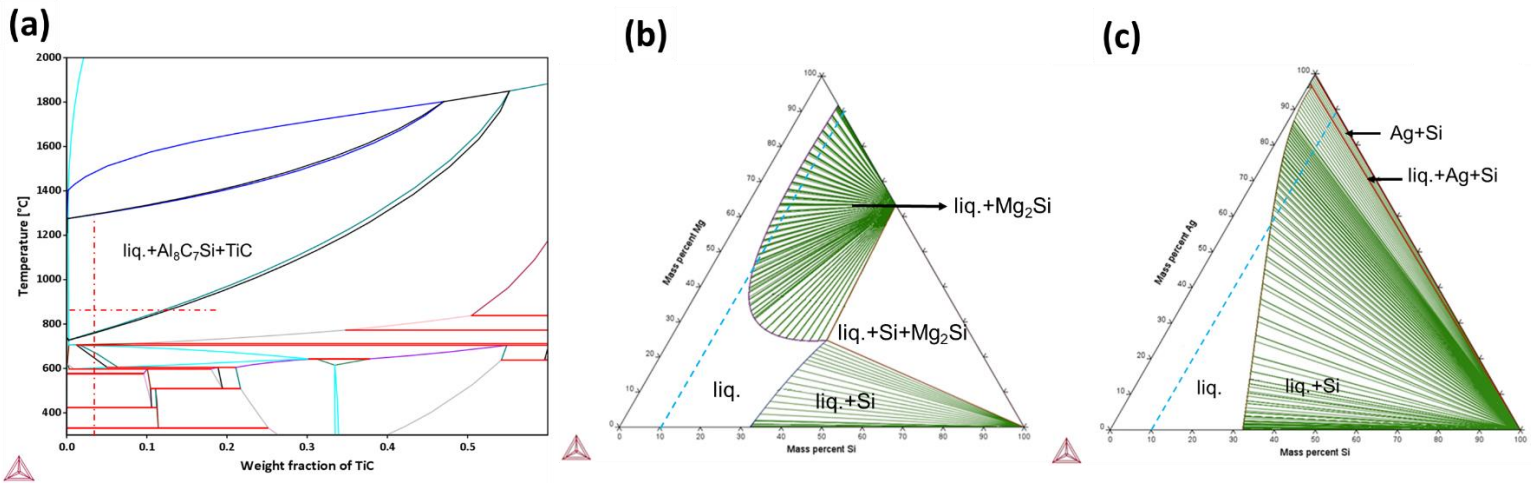

Figure 5 - 22 The CALPHAD-calculated (a) pseudo-phase diagram associated with AlSi10-TiC system and ternary phase diagrams for (b) Al-Si-Mg system and (c) Al-Si-Ag system at 850 ℃.

<u>*Guidance for new TiC-reinforced Al-Si-X composite design*</u> With the understanding of the reaction dynamics (see **Figure 5 - 21**), to fully make advantage of the incorporated TiC in the Al-Si systems, other novel Al-Si-X (X=non-reacting element) could be potentially designed [265]. Here, we use AlSi10Ag as a model system to prove our findings. Ag is designed to be ~0.2-0.45 wt.%, which is the same as the original Mg concentration.

Ag has the following advantages in Al-Si systems: First, Ag-Si phase diagram shows that Ag and Si could not form intermetallic phase via an exothermal route. Second, Since Ag and Si have negligible solubility into each other, the solidification process will also tend to segregate these elements, whose coating/interfacial layer could be favorable to TiC stability [176].

The microstructure and phase composition results are summarized in **Figure 5 - 23** and **Figure 5 - 24**, and the corresponding tensile test results are shown in **Figure 5 - 25**. As shown in **Figure 5 - 23 (a)**, the original TiC-dense zone has the similar morphology as AlSi10-TiC nanocomposites, which indicates a mitigated chemical reaction compared with AlSi10Mg system.

When analyzing the phase change by **Figure 5 - 24** and **Figure 5 - 13**, a clearer advantage of adding Ag instead of Mg could be seen: Comparing the calculated $Al_3TiSi_xC_y$ (104) crystal plane distance change between AlSi10-TiC and AlSi10Mg-TiC from the XRD results,[266] the increased lattice plane distance is introduced by replacing C with Si (and a little Al). Thus, less crystal plane distortion indicates a less rapid chemical reaction (see **Figure 5 - 24 (b)**).

Second, the energy needed for the lattice distortion during the stimulated reaction can be estimated from the energy stored by lattice change, which is:

Eq. 5 - 9 $$\Delta E = G \cdot \Delta d \cdot a^2 \cong 0.076\ eV$$

where G and a are the Young's modulus and lattice parameter for $Al_3TiSi_xC_y$ (adapted from Ti_3SiC_2), respectively. Δd idenotes the lattice plane distance difference to that in AlSi10-TiC. The Mg_2Si formation enthalpy is estimated to be [267]:

Eq. 5 - 10 $$\Delta H \cong 0.183\ eV$$

However, due to the simple phase dynamics of Ag and Si, no formation enthalpy could be used to trigger the faster chemical reaction.

Therefore, in AlSi10Mg-TiC, the formation of Mg_2Si would supply the enough energy for both the chemical reaction activation and the final product lattice distortion by taking more Si atoms, whereas AlSi10Ag-TiC would be more advantageous to minimize the distortion energy and suppress the reaction process.

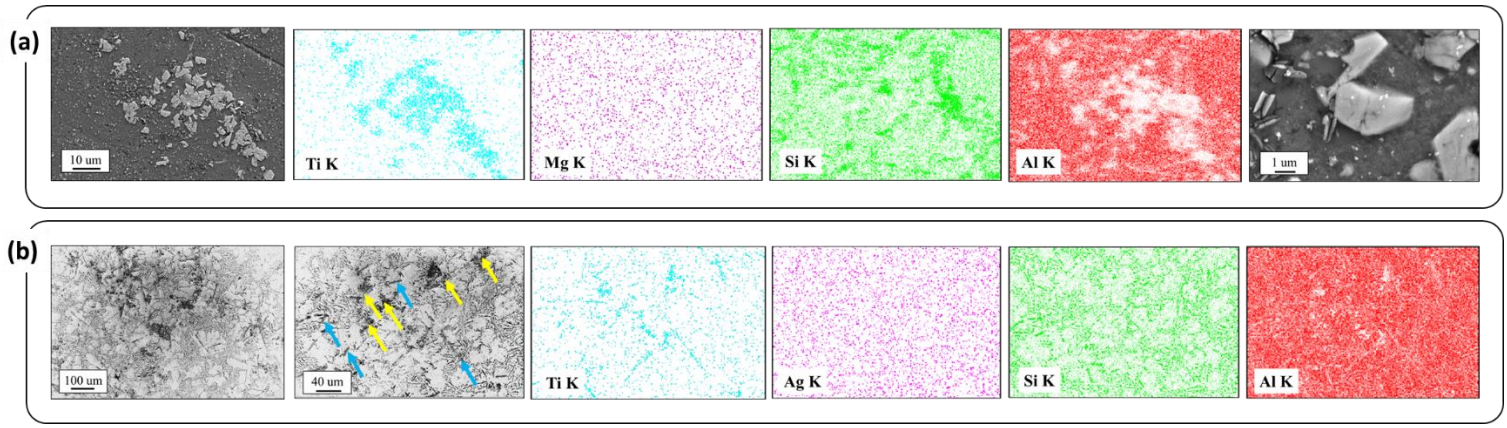

Figure 5 - 23 The microstructure and the elemental mapping of **(a)** as-cast AlSi10Ag-TiC nanocomposite. **(b)** is showing the initiation of the chemical reaction near the nanoparticle-dense zone in as-cast AlSi10Ag-TiC (yellow arrow: TiC-dense zone; blue arrow: Formed $Al_3TiSi_xC_y$ pieces).

The reaction control effect by Ag could be clearer when investigating the tensile properties: Based on the tensile properties between as-cast and heat-treated AlSi10Ag-TiC samples in **Figure 5 - 25**, it is clear that the heat treatment is promoting the ductility (if further comparing the fracture surface morphology in **Figure 5 - 26**), while increasing the strength slightly. This mechanical behavior, as well as the fractography change by the same heat treatment, is also similar to that of AlSi10-TiC, and different with AlSi10Mg-TiC (see **Figure 5 - 18** and **Figure 5 - 25**). Given the similar mechanical property change and microstructure evolution, it could be seen that Ag addition to Al-Si system will alleviate the Si-TiC chemical reaction, and this observation proves our theory on the chemical reaction dynamics in **Figure 5 - 21**.

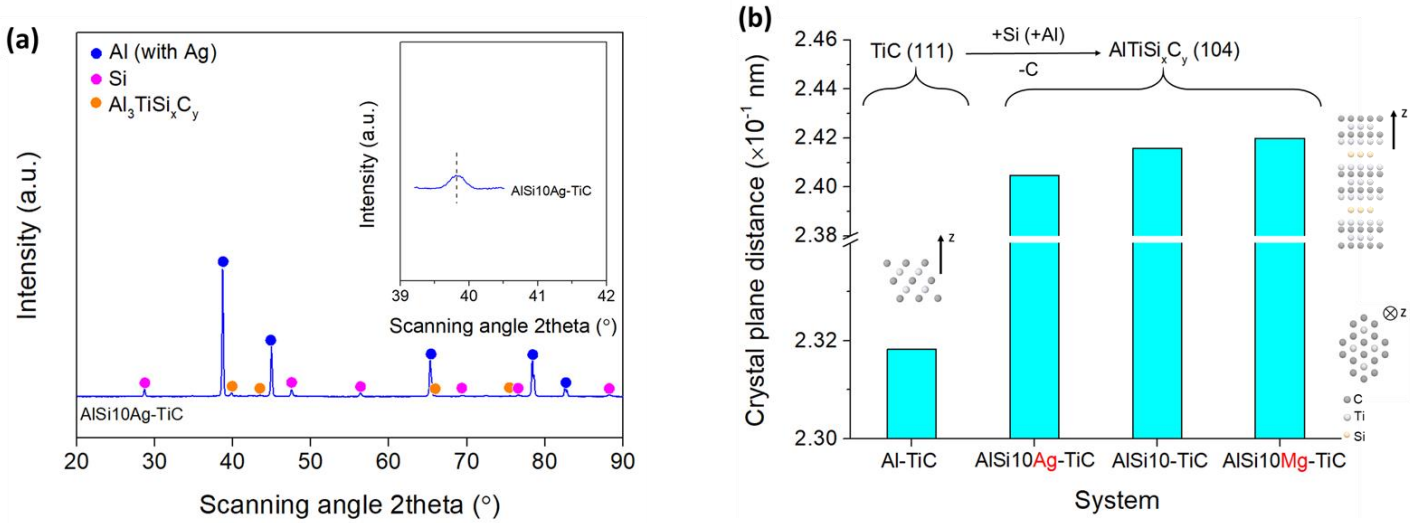

Figure 5 - 24 (a) The phase composition of as-cast AlSi10Ag-TiC nanocomposite. **(b)** The calculated crystal plane distance for $Al_3TiSi_xC_y$ (104) in as-cast AlSi10Ag-TiC, AlSi10-TiC, and AlSi10Mg-TiC.[261,268]

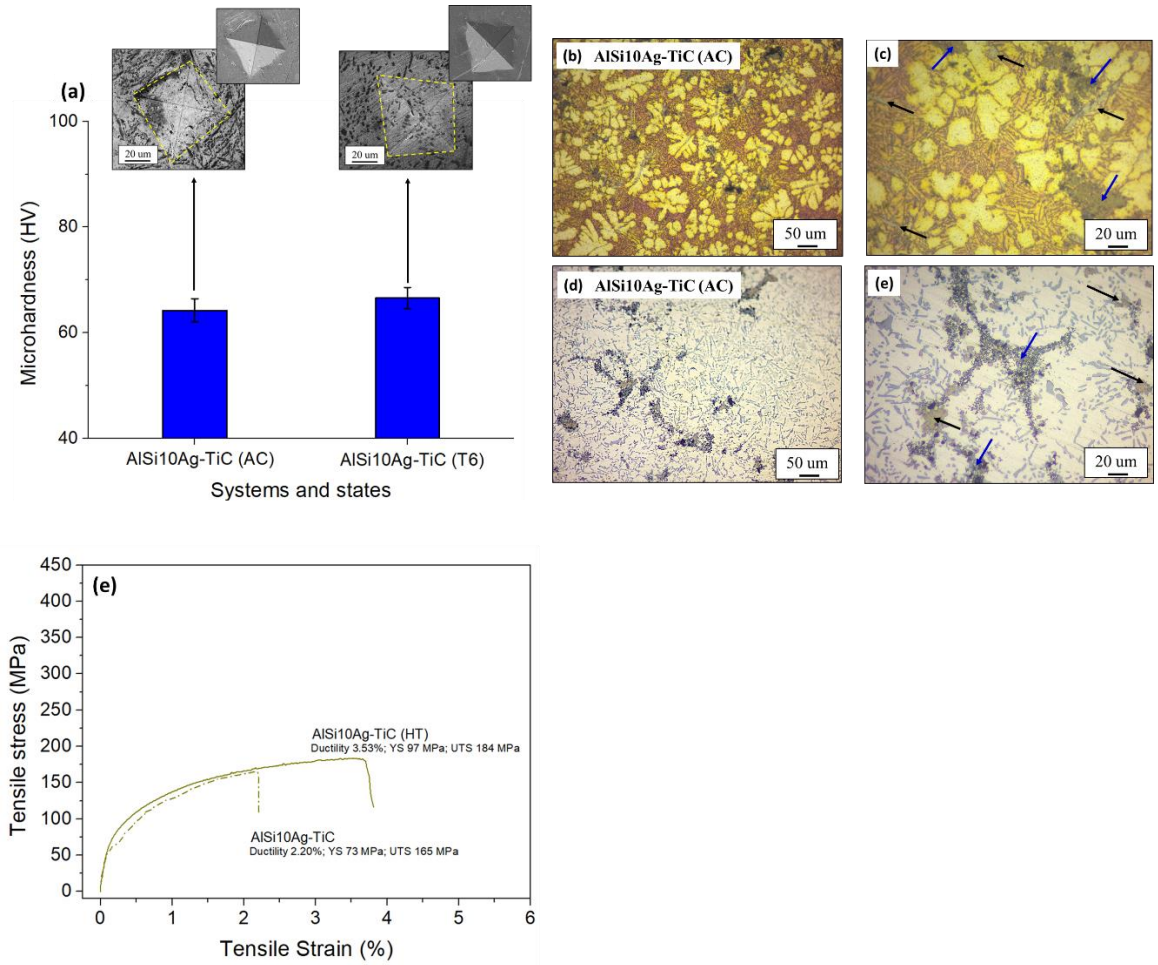

Figure 5 - 25 (a) The stress-strain curve for as-cast and heat-treated AlSi10Ag-TiC; **(b)** and **(c)** The etched microstructure and grain size comparison of as-cast AlSi10Ag alloy (black arrow indicates the formed intermetallic phases; blue arrow indicates the TiC-dense zone).

As the results indicate a promising processing route by changing Mg to Ag, other elements sharing the similar characteristics to Ag (e.g., Bi which is immiscible to Si; Zn, Be, Au, and Sn which have no complex intermetallic phase and minimal solubility with Si) could potentially be used to fabricate the stable Al-Si nanocomposites with TiC. This understanding would be important for the rational design to gain the benefits from Al-Si alloy and nano-reinforcements like TiC.

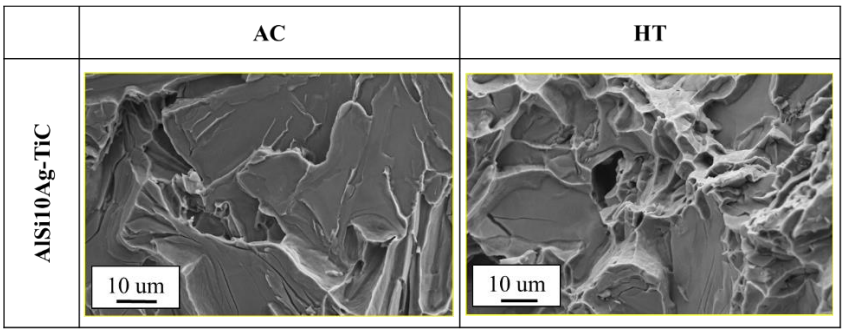

Figure 5 - 26 The fractography images for as-cast and heat-treated AlSi10Ag-TiC.

5.2.3 Thermal oxidation of Naval Brass/WC nanocomposite

As-cast Cu-40 wt.% Zn/WC nanocomposites were prepared via a salt-assisted stirring method.[41,70] For comparison, nanocomposites with 10 vol.% WC were made to balance the enhanced mechanical properties and decreased electrical conductivity, according to a previous study [41]. Besides, this volume percentage of WC nanoparticles is chosen, because it can help make the differences in properties stand out and satisfy the measurement resolution requirements (e.g.,

XRD has certain detectable limit). Then, both the pure alloy and the nanocomposite were analyzed via *in situ* XRD from room temperature to 700°C (~80% melting temperature of the alloy) to obtain information on phase transition and oxidation, as shown in **Figure 5 - 27**. For phase transitions, DSC (*PerkinElmer*) was also used to obtain the detailed phase evolution from 200 to 600°C at a constant speed of 7.5°C/s. At the same time, the oxidation rate was quantitatively analyzed with the surface ZnO concentration under different temperatures with energy dispersive scanning (EDS, *Zeiss Supra 40VP*) and XRD peak intensity [269]. Furthermore, the microstructures of as-cast Cu-40 wt.% Zn and Cu-40 wt.% Zn/10 vol.% were characterized with SEM imaging (*Zeiss Supra 40VP*), and FIB milling (*Nova 600 Focused Ion Beam*) was used to expose the morphology and reveal the inner structure and layer configuration before and after thermal oxidation. Surface profiles were collected via *Wyko NT3300 Optical Profile* at an area scale of 1.234 um × 0.939 um.

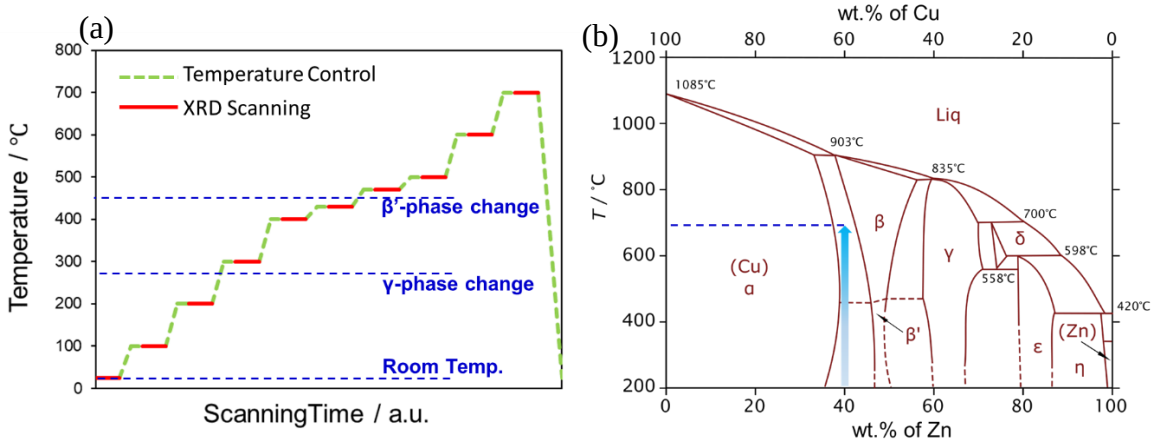

Figure 5 - 27 (a) Temperature curve during the in situ XRD scanning; (b) Phase diagram of Cu-Zn system with the range of our study.

<u>*Microstructure*</u> The microstructure for as-cast Cu-40 wt.% Zn/10 vol.% WC nanocomposite is shown in **Figure 5 - 28**. Based on the energy balance of WC nanoparticles in Cu and Zn systems, pseudo-dispersion (i.e., the nanoparticles' tendency to form denser and sparser

areas with no agglomeration or cluster, as indicated in **Figure 5 - 28** (b) and (c)) is expected.[41] Since 10 vol.% WC is reasonably dense, the choice of this volume percentage can minimize the local property fluctuations in our samples. The curtain-like morphology in **Figure 5 - 28** is mainly due to the scattering and impedance of the focused ion beam by WC.

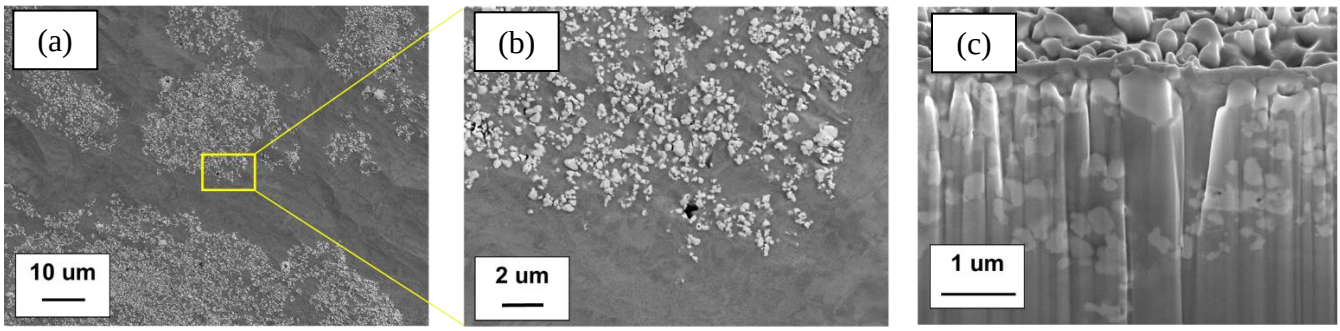

Figure 5 - 28 SEM images for WC nanoparticle dispersion in as-cast Cu-40 wt.% Zn/10 vol.% WC nanocomposites: (a) Low magnification; (b) Large magnification to show the pseudo-dispersion condition; (c) FIB image for embedded WC nanoparticles dispersed inside Cu-40wt.% Zn matrix. (the brighter phase is nanoparticles)

The *in situ* XRD results for Cu-40 wt.% Zn and Cu-40 wt.% Zn/10 vol.% WC systems are shown in **Figure 5 - 29** and **Figure 5 - 30**, respectively, with a focus on room temperature (25°C), 100°C, 200°C, 300°C, 400°C, 430°C, 470°C, 500°C, 600°C, and 700°C. Summarized in **Figure 5 - 31** with XRD peak and EDS mapping information, the oxidation rate is also analyzed. After incorporating WC nanoparticles into Cu-40 wt.% Zn alloy, the $\gamma \rightarrow \beta'$ transition temperature is elevated from below 300°C to above 300°C, and the $\beta' \rightarrow \beta$ transition temperature is also increased above 470°C (see **Figure 5 - 29** (c), **Figure 5 - 30** (c), and **Figure 5 - 32**). Moreover, the oxidation of Cu-40 wt.% Zn is also delayed from ~430-470°C (the same range as the $\beta' \rightarrow \beta$

transition [270]) to above 500℃ (the XRD peak for β' doesn't disappear even after 500℃ in Cu-40 wt.% Zn/10 vol.% WC nanocomposite in **Figure 5 - 30** (c) [271]). The surface patterns after oxidation are compared in **Figure 5 - 33**. The average profile roughness of Cu-40 wt.% Zn/ 10 vol.% WC nanocomposite is measured to be 990 nm (about half of the oxide thickness), much smaller than that of Cu-40 wt.% Zn alloy with 1703 nm roughness.

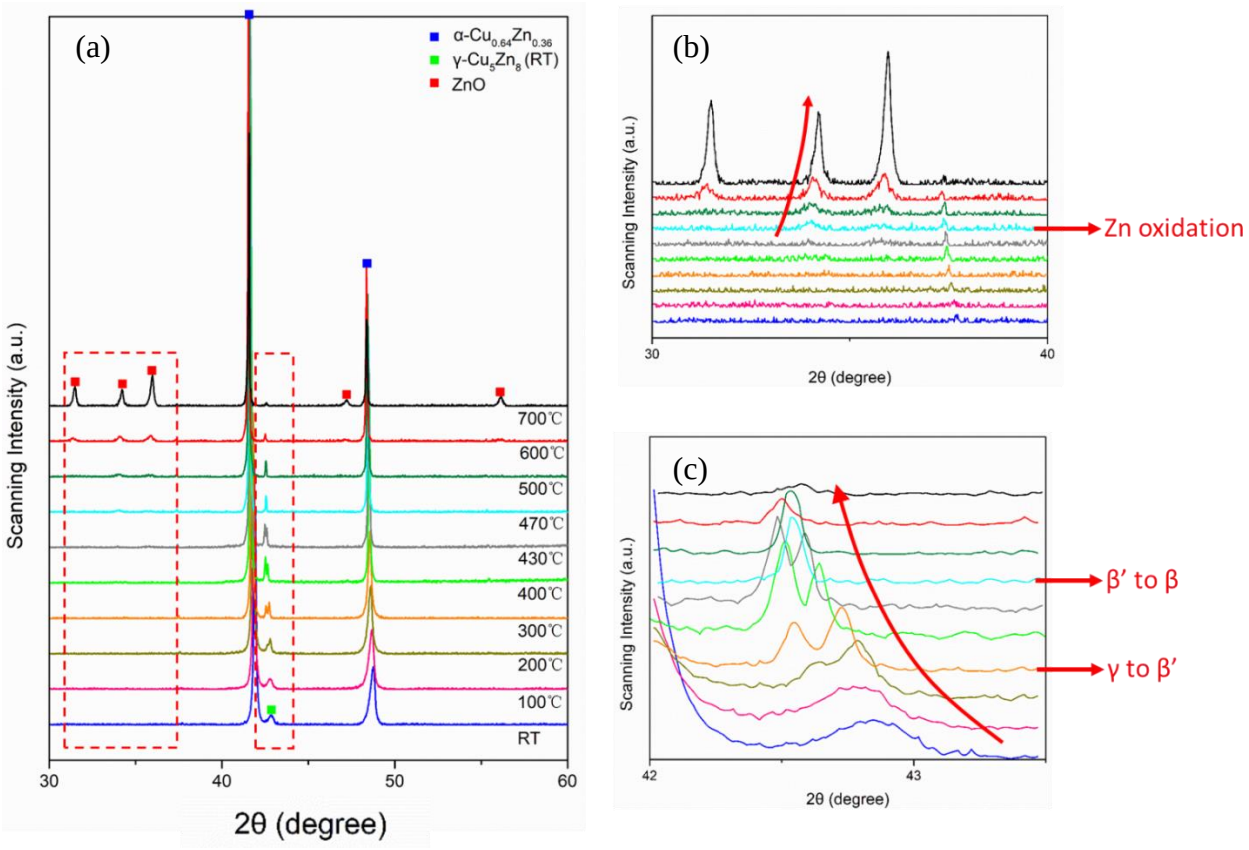

Figure 5 - 29 (a) In situ XRD results for Cu-40 wt.% Zn with increasing temperature; (b) Enlarged XRD for the observation of ZnO in Cu-40 wt.% Zn; (c) Enlarged XRD for the observation of Cu-Zn phase transition in Cu-40 wt.% Zn.

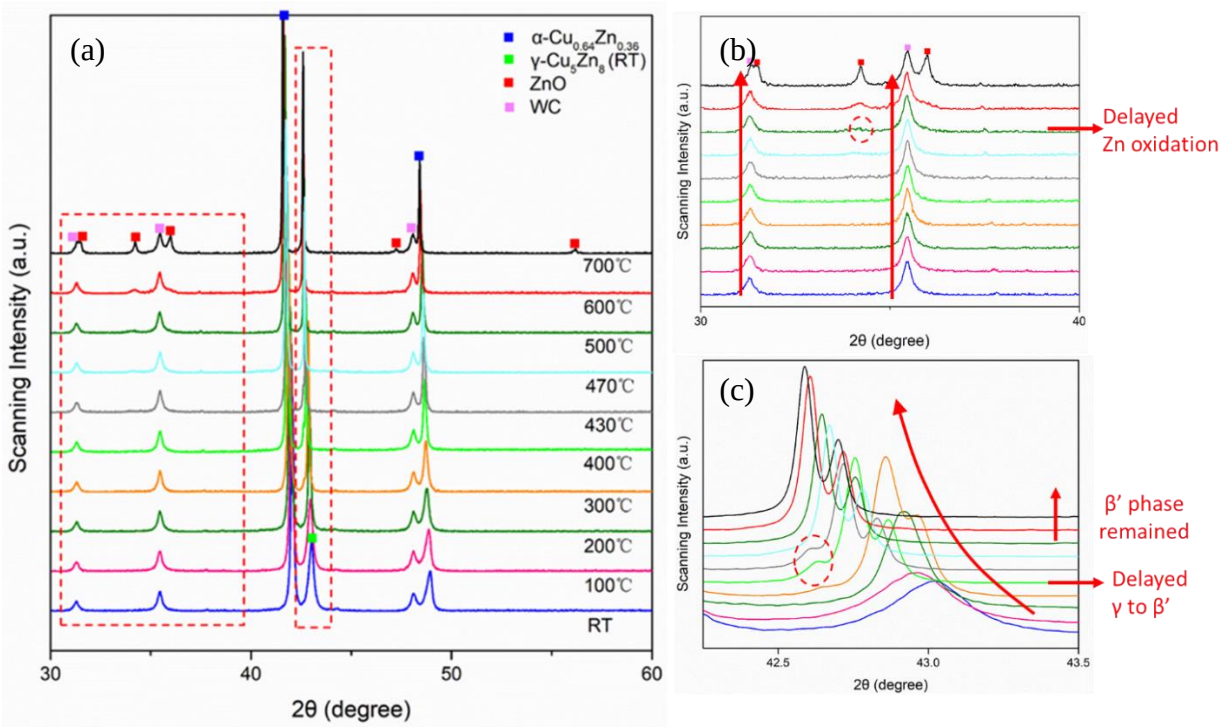

Figure 5 - 30 (a) In situ XRD results for Cu-40 wt.% Zn/10 vol.% WC with increasing temperature; (b) Enlarged XRD for the observation of ZnO in Cu-40 wt.% Zn/10 vol.% WC; (c) Enlarged XRD for the observation of Cu-Zn phase transition in Cu-40 wt.% Zn/10 vol.% WC.

XRD Peak Shift The leftward peak shift of Cu-40 wt.% Zn alloy phases is clear in both **Figure 5 - 29** (a) and (c) and **Figure 5 - 30** (a) and (c). The main phases of Cu-40 wt.% Zn systems experience much larger thermal expansions with increased temperatures, as indicated in **Table 5 - 3**. This leads to a significant thermal compression strain, especially when WC nanoparticles exhibit higher strength with a smaller lattice constant. This is also why WC-phase XRD peaks witness little to no shift during the *in-situ* heating, as demonstrated by **Figure 5 - 30** (b). Thermal mismatch strengthening by nanoparticles in metal matrices can also be supported by this observation.

Contrary to the thermal expansion and lattice strain model, the rightward shift of XRD peaks of the ZnO phase (as shown in **Figure 5 - 29**(b) and **Figure 5 - 30** (b)) is observed. It should

be noted that Zn is oxidized to ZnO with constantly diffusive O_2. As more and more ZnO appear on the surface, pure Zn will also need to cross the surface to get oxidized. The diffusion-governed process will cause oxygen vacancies in the ZnO layer (i.e., $\mathrm{Zn} + \frac{x}{2} O_2 \rightarrow ZnO_x, 0 < x \leq 1$), which will lead to the diffraction peak shifting right, to higher 2θ angles [272]. The semi log-linear relationship of the approximated ZnO concentration and the scanning temperature also support the diffusive oxidation limit of Zn from a dynamics side [106,273]. Since metal vacancies will appear during the early stages of oxidation at the metal/oxide interface [274], the eventually produced voids or cracks (as shown in **Figure 5 - 33** (a) and (b)) will also help release compressive stress by providing more energy and mobility and creating tension in ZnO structures [275,276]. Therefore, unlike the XRD peaks of the alloy matrix, the newly formed ZnO will tend to diffract x-rays at a higher angle.

Table 5 - 3 Lattice constants and CTEs of the relevant materials

Materials	**Single Atomic volume / $\times 10^{-29}\ m^3$**	**CTE / $\times 10^{-6}$ m/(m · ℃)**
Zn	1.182	34.2
Cu	1.528	17.6
Cu-40 wt.% Zn	/	20.9
WC	1.016	5.5
ZnO	/	4.26 (c-axis) ~7.47

<u>*Thermal Oxidation Rate*</u> The thermal oxidation of Cu-40 wt.% Zn occurs between ~430-470℃, whereas oxidation of Cu-40 wt.% Zn/10 vol.% WC nanocomposite starts at ~500℃. The quantitative ZnO concentration on the detected surface is calculated from EDS mapping and XRD

peak intensity in **Figure 5 - 31**. The surface roughness R_a of the oxidized surfaces in **Figure 5 - 33** (e) and (f) also supports a slower oxidation rate in Cu-40 wt.% Zn/10 vol.% WC. Referring to the theory of metal oxidation [106], the ZnO growth and concentration should obey the following rule:

Eq. 5 - 11 $$v \propto \frac{d}{dt} C_{ZnO} \cong \frac{d}{dt}\left[C_0 \cdot exp\left(-\frac{B(Zn)}{k_B \cdot T}\right)\right]$$

Here, $B(Zn)$ is the effective thermal oxidation constant of Zn in Cu-40 wt.% Zn alloy and is mainly determined by the process of $\mathrm{Zn} + \frac{1}{2}O_2 \rightarrow ZnO$. Since the experimental temperature is far less than the activation temperature determined by $\frac{B(Zn)}{k_B} \sim 10^4 K$, based on the linear fitting of the inserted figure in **Figure 5 - 31**, the major role of WC nanoparticles is to reduce the diffusion-limited Zn oxidation rate $\frac{\mathrm{d}}{\mathrm{dt}}\mathrm{C}_0$. WC does not serve as an adverse catalyst in oxidation [277] because the fitting curves' similar slopes prove the negligible change in activation energy. Since copper and zinc belong to the materials with linear oxidation evolution,[105] the activation energy is estimated to be ~0.778 eV by the curve fitting. Given pure zinc's oxidation activation energy and its concentration in the alloy systems [278], the theoretical value is ~0.720 eV, which fits our experiment well. The reason for this difference in diffusion hindrance will be further discussed in the proceeding section**.**

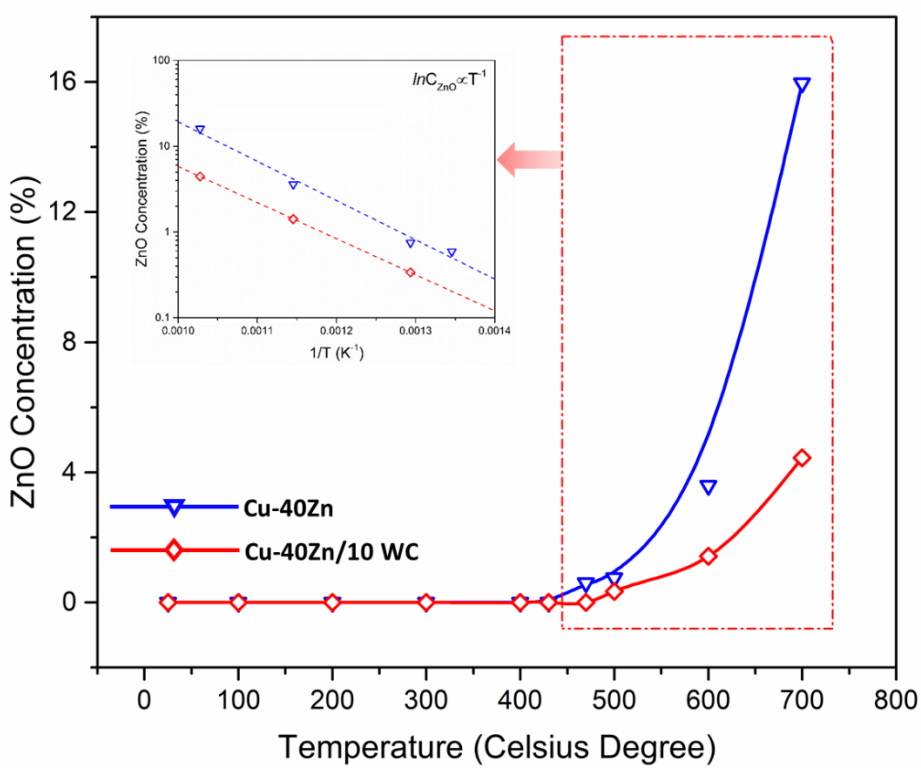

Figure 5 - 31 ZnO concentration as a percentage of the scanned surface atoms with increasing temperatures (inserted: fitting by activation energy model)

Enhanced thermal stability In Cu-40 wt.% Zn/10 vol.% WC nanocomposites, the enhanced thermal stability of both phase transition and thermal oxidation is correlated. As partially revealed by the FIB images in **Figure 5 - 28** (c) and **Figure 5 - 33**, WC nanoparticles would hinder the mobile particles, even high-energy ions. As demonstrated in **Figure 5 - 34**, the phase transition (governed by the phase diagram in **Figure 5 - 27** (b)) and thermal oxidation in Cu-40 wt.% Zn alloy are greatly related to the motion of Zn atoms or cations [106].

WC will prevent Zn from interacting with O_2 by blocking diffusion paths along grain boundaries [91,103]. The diffusive oxidation of metals can be estimated by:

Eq. 5 - 12

$$J = \frac{D_{path} \cdot \delta \cdot V}{k_B \cdot T} \cdot \frac{\partial \sigma_n}{\partial s}$$

Here, J is the Zn flux along a grain boundary of width δ, and D_{path} is the diffusivity of Zn in the diffusion path S. V is the effective atomic volume per atom and is related to the chemical potential gradient, and σ_n demotes the stress introduced perpendicular to the diffusive path, as shown in **Figure 5 - 33** (c).

In Cu-40 wt.% Zn/WC nanocomposite, WC nanoparticles will reduce the diffusive path D_{path} (as supported by **Figure 5 - 28** (c)). Since they will provide a reasonably smaller atomic volume (as listed in **Table 5 - 3**), WC nanoparticles will also decrease the stress-related volume V on the diffusion path. Last but not least, according to the load-bearing mechanisms of WC nanoparticles in metal matrices,[279] the stress will be partially transferred to WC nanoparticles (i.e., σ_n is changed into $\sigma_{WC-alloy}$) instead of being fully exerted along the grain boundary paths; this will give a smaller $\frac{\partial \sigma_n}{\partial s}$. In this way, by adding WC nanoparticles, reduced D_{path}, V, and $\frac{\partial \sigma_n}{\partial s}$ will contribute to a slower oxidation rate by limiting the diffusion rate of Zn. The morphology of changing needle-like ZnO nanorods in Cu-40 wt.% Zn to flake-like ZnO plates in Cu-40 wt.% Zn/10 vol.% WC also supports this argument [103,280].

The phase transitions of $\gamma \rightarrow \beta'$ and $\beta' \rightarrow \beta$ are also associated with Zn diffusion for the re-arrangement of Cu-Zn configuration (as supported by **Figure 5 - 33** (e-1) and (e-2)). The similar hindrance and changes can be introduced by WC nanoparticles to mitigate the phase transition kinetics and dynamics [281,282]. This process is the result of high-temperature Zn dezincification due to Zn content variation. The evidence for the more retarded phase transitions of $\gamma \rightarrow \beta'$ and $\beta' \rightarrow \beta$ (corresponding to the *λ-shaped endothermic reaction* curve [283]) is shown in the DSC results in **Figure 5 - 32**. Since the high oxygen permeability at elevated temperatures is usually associated with order-disorder transition in materials,[270] the lower oxygen penetration probability in Cu-40 wt.% Zn/10 vol.% WC nanocomposites (as verified by the oxide layer thickness in **Figure 5 - 33**

(d) and (e) and the analyses for thermal oxidation rate) also helps with the stabilization of ordered β' phase. Additionally, from an atomic aspect, the smaller average atomic size of WC (see **Table 5 - 3**) means the system will be more favorable towards ordered intermetallic configuration [284,285]. Indeed, the phase transition trend with WC nanoparticle incorporation into Cu-40 wt.% Zn is different from the previously reported phenomena, since WC nanoparticle introduces hindrance, endures stress, and provides heterogeneous configuration and properties [286].

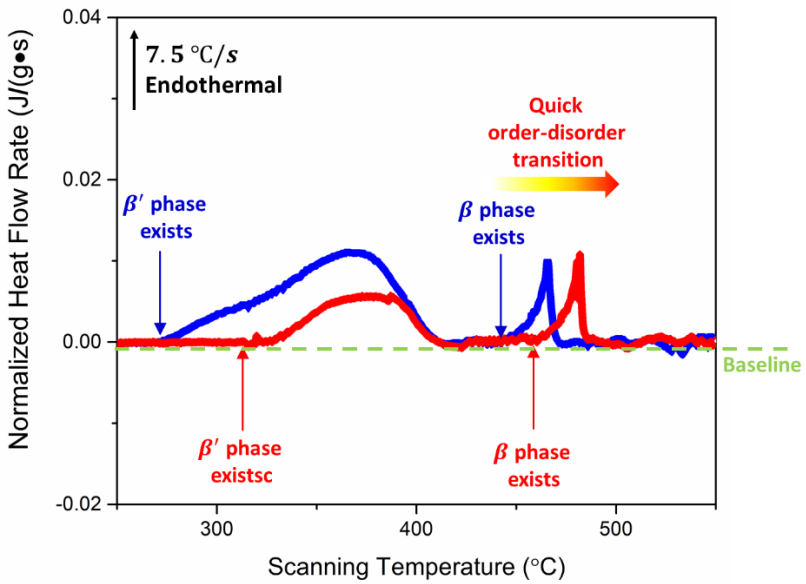

Figure 5 - 32 DSC scanning curve for phase transition observation in Cu-40 wt.% Zn alloy (*blue line*) and Cu-40 wt.% Zn/10 vol.% WC nanocomposite (*red line*) under N_2 protection

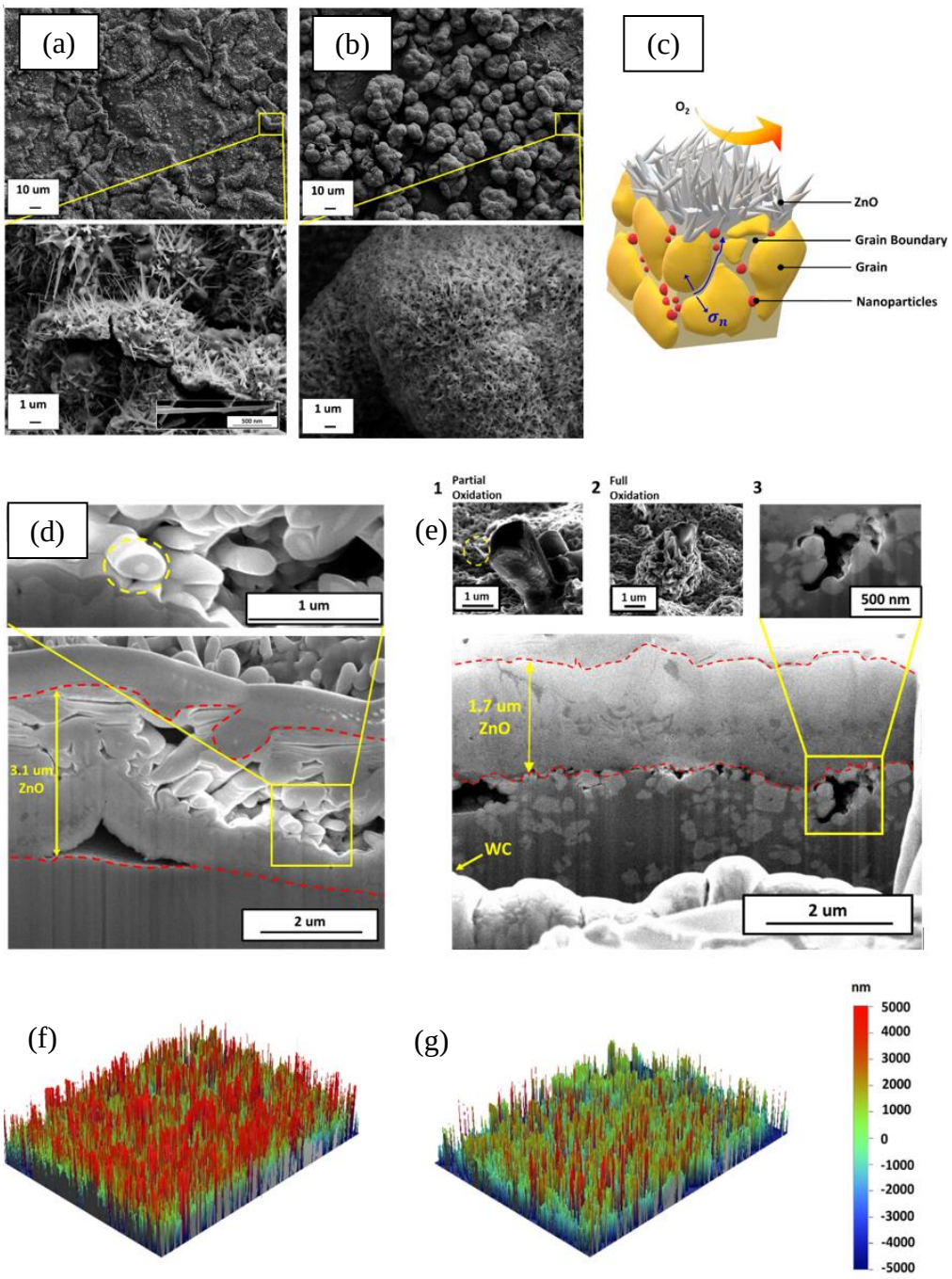

Figure 5 - 33 The oxidized surface morphology after in situ XRD scanning of (a) Cu-40 wt.% Zn and (b) Cu-40 wt.% Zn/10 vol.% WC; (c) The dynamic illustration of Zn thermal oxidation; FIB cross-section image of (d) Cu-40 wt.% Zn and (e) Cu-40 wt.% Zn/10 vol.% WC nanocomposite to show the oxidation interface of alloy nanocomposite-ZnO; (e-1) The partially

oxidized region in Cu-40 wt.% Zn/ 10 vol.% nanocomposites (with sparse ZnO nanorods shown in the inserted yellow circle); (e-2) The fully oxidized region in Cu-40 wt.% Zn/ 10 vol.% nanocomposite with nanoplate structures; (e-3) The enlarged image of WC nanoparticle as the interface hindrance; (f) The relative surface roughness of Cu-40 wt.% Zn alloy after oxidation; (g) The relative surface roughness of Cu-40 wt.% Zn/10 vol.% WC nanocomposite.

In summary, this part systematically analyzed the thermal stability (i.e., phase stability and anti-oxidation in this study) of Cu-40 wt.% Zn up to high temperatures and confirmed the beneficial role of WC nanoparticles in the enhanced thermal stability of Cu-40 wt.%/WC nanocomposites. The facile as-cast Cu-40 wt.% Zn/10 vol.% WC nanocomposite showed well-dispersed WC nanoparticles. After performing *in situ* XRD studies, the higher temperatures for the phase transition and Zn oxidation were confirmed. On one hand, the oxidation rate analysis, SEM surface, and FIB cross-section images proved the different morphology from nanorod to nanoplates introduced by WC nanoparticles and the important role of WC nanoparticles as path hindrance. On the other hand, DSC analysis validated the postponed phase transition trend in the Cu-40 wt.% Zn/10 vol.% WC nanocomposites. The results are summarized in **Figure 5 - 34**.

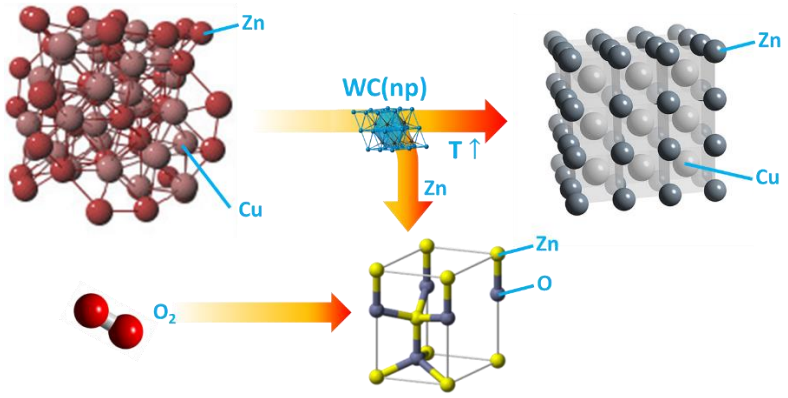

Figure 5 - 34 Descriptive illustration of phase transitions (with different crystal structures) and chemical reactions in Cu-40 wt.% Zn/ WC nanocomposite with increased temperatures.

This mechanism of alloy incorporated with ceramic nanoparticles (e.g., WC in Cu-40 wt.% Zn/WC nanocomposite) to increase thermal stability will be of great potential for metal/alloy systems working under high-temperature, high-enthalpy, oxygen-sufficient, and/or high-humidity conditions. As for the Cu-40 wt.% Zn alloy, the enhanced thermal stability by WC nanoparticles broadens its usage in fields as naval brass for heat exchangers and beyond.

5.2.4 Thermal oxidation of Al/ZrB_2 nanocomposite

Al-5 vol.% ZrB_2 was fabricated via the in-situ route shown in **Eq. 5 - 13**.[287] The 5 vol.% ZrB_2 is chosen, because this volume percentage can give better castability with reasonable molten metal flowability, avoid ZrB_2 segregation by the density difference, and balance its functional properties including electrical conductivity.[2,179]

Eq. 5 - 13 $$10Al + 3K_2ZrF_6 + 6KBF_4 \xrightarrow{1023K,20min} 3ZrB_2 + 10KAlF_4 + 2KF$$

The as-cast Al-5 vol.% ZrB_2 was characterized by SEM on equipment model *Zeiss* Supra 40VP. For the size distribution, the ZrB_2 nanoparticles were extracted out from the Al matrix by dilute HCl etching. A suspension liquid with ZrB_2 nanoparticles was then subjected to 30 min of ultrasonic vibration before measurement. The size distribution of the ZrB_2 nanoparticles was characterized by Dynamic Light Scattering (DLS) on an *N4-PLUS DLS Machine*.

Then, the in situ XRD scanning was performed on both pure Al and Al-5 vol.% ZrB_2 nanocomposites from room temperature up to 873K on a *PANalytical X'Pert Pro* model (Cu Kα, 40KV acceleration voltage with 0.05° step size). Each sample has been scanned twice. The *in situ* heating took 15 mins to achieve each temperature, and then the in situ scanning started. The post-oxidation surface morphology of pure Al and Al-5 vol.% ZrB_2 nanocomposites was characterized by SEM imaging and EDS mapping on *Zeiss Supra 40VP*. The surface characteristics were gauged

via XPS (*Kratos Axis Ultra* model) for element composition and status analyses before and after oxidation. 3 different spots on the surface were gauged for XPS analysis.

Further, to quantitatively analyze the anti-oxidation performance, the XRD peak intensity (by Al peaks) and EDS surface mapping were used to quantify the oxidized surface ratio. Since the low-temperature oxidation created amorphous Al_2O_3, FIB milling (on a *FEI Nova 600 SEM/FIB System*) was utilized to show the oxidation cross-section for layer properties.

TGA measurement (on a *Perkin Elmer Diamond TG/DTA model*) was added to analyze the dynamic and kinetic evolution of the Al_2O_3 oxide layer. The scanning temperature was set from 325K to 875K at 4K/min for 150 min (with 13 min for isothermal keeping at 875K before cooling to guarantee the mass measurement stabilization) and isothermal scanning for 90 min. Each sample has been scanned for 3 times under each investigated condition. The results were summarized as Al_2O_3 weight gain and Al_2O_3 layer thickness. The air flow was set to be 30 mL/min to guarantee the enough oxygen and efficient heating in TGA. All the oxidation was introduced under air condition ($P_{tot} = 10^5\ Pa$; $P_{O_2} = 2.1 \times 10^4\ Pa$).

To demonstrate the functionality of the oxidized surface, wettability and anti-corrosion study has been carried out. The contact angle measurement was performed on a goniometer which consists of a XYZ axis positioning stage and an observation setup (*GO® Edund VZMTM 1000i Zoom Imaging Lens* at ×5 magnification with *Point Grey FL3-U3–13Y3M-C CMOS camera*). During the measurement, a 5µl DI water droplet was crated and placed on the sample by a pipette (*Eppendorf Single-Channel Pipette, Max 10µl*). The contact angle was determined by the air-water interface and the triple phase contact line.

The corrosion test was done on the oxidized surfaces by an EIS spectroscopy. Before the corrosion test, all surfaces were rinsed with anhydrous ethanol (200 proof) to remove surface

impurities. The exposed area for tests was 0.9 cm^2. The anti-corrosion performance was analyzed on an EIS spectroscopy (*Ametek VersaSTAT 4 model*) in 3.5 wt.% NaCl solution (pH=6.5-7; 500 mL for each test) under the temperature of 25°C. A saturated Ag/AgCl reference electrode and 2 graphite rods as counter electrode were used. The sequence of the tests was open current potential (OCP), potentiostatic EIS scanning, linear polarization resistance (LPR), and finally potentiodynamic scanning. For OCP, the stable time was set to 10 mins to minimize the damage from pitting initiation;[288] For potentiostatic EIS scanning, the frequency range of 100KHz to 1Hz was studied at 0V v.s. OCP; For LPR measurement, the scanning range was from -0.02V v.s. OCP to +0.02V v.s. OCP; For potentiodynamic measurement, the scanning range was from -0.25V v.s. OCP to 0.6 v.s. OCP with the potential step of 5 mV; For potentiodynamic measurement, the scanning range was from -0.25V v.s. OCP to 0.6 v.s. OCP with the potential step of 5 mV. Each material has been tested with 2 samples.

<u>*Microstructure before Oxidation*</u> As shown in **Figure 5 - 35** (a) and (b), due to the reasonable wettability (~75 °) between ZrB_2 and molten Al, pseudo-dispersion of ZrB_2 nanoparticles is expected.[1] **Figure 5 - 35** (c) shows the size distribution of in situ synthesized ZrB_2 nanoparticles. The average size of the ZrB_2 nanoparticles is ~96 nm in diameter.

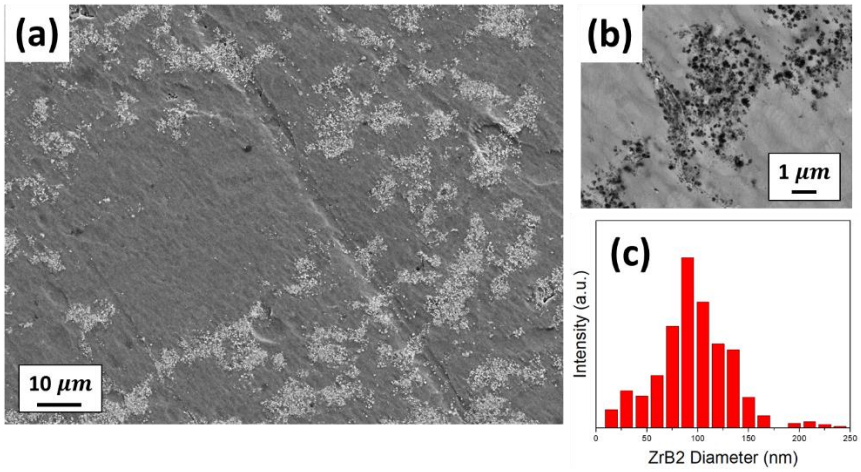

Figure 5 - 35 (a) SEM image of in situ ZrB_2 nanoparticles distributed in the Al-5 vol.% ZrB_2 nanocomposite; (b) Enlarged SEM image of the ZrB_2-dense zone (under InLens/SE combined mode); (c) Distribution of ZrB_2 nanoparticle size in the Al-5 vol.% ZrB_2 nanocomposite.

Al Matrix Stability: With the incorporation of nanoparticles, the Al matrix characteristics will also be influenced in thermal oxidation.[289] As shown in the in situ XRD results of **Figure 5 - 36**, with the increased oxidation temperature and prolonged oxidation time, unstable crystalline planes including (200), (220), and (311) in pure Al disappear (**Figure 5 - 36** (a)); while in Al-5 vol.% ZrB_2 nanocomposites, all the Al crystalline planes are stable even under the oxidation temperature of 873K near the Al melting temperature (**Figure 5 - 36** (b)). It indicates that the in situ ZrB_2 nanoparticles could greatly increase the matrix crystal plane stability. This is understandable: For pure Al, the closely packed crystal plane is (111) and amorphous Al_2O_3 is more stable on (200) and (220) planes due to the favorable interfacial energy;[290] therefore, under high-temperature oxidation, (111) is the only plane observable after pure Al oxidation. When ZrB_2 nanoparticles are introduced, they have a higher oxidation initial temperature and have been synthesized with (001), (100) and (101) planes in relatively equal possibility (See **Figure 5 - 36** (b)). These three planes would correspondingly form less mismatch with all Al (111), (200), (220), and (311) planes and show strong interfacial stability,[291] which prevents these planes from high-temperature dynamic oxidation.

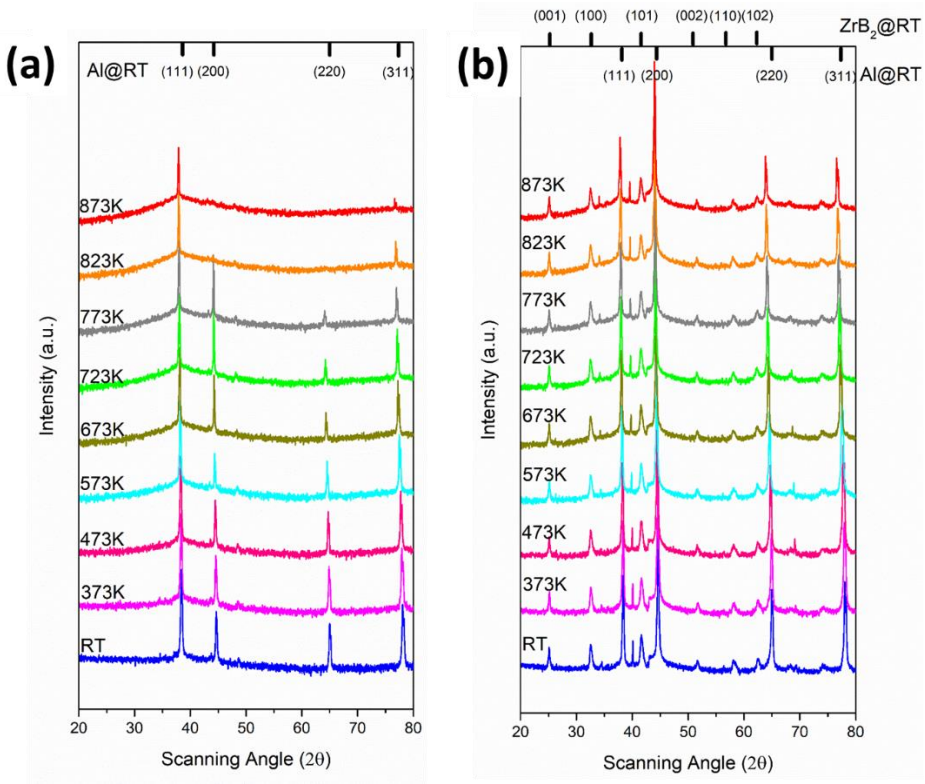

Figure 5 - 36 The in situ XRD observation for the oxidation process from room temperature to 873K for (a) pure Al, and (b) Al-5 vol.% ZrB_2 nanocomposites.

Thermal Oxidation Performance: The post-oxidation surface morphology of pure Al and Al-5 vol.% ZrB_2 nanocomposites after XRD scanning are shown in **Figure 5 - 37**. It is clear that the oxide growth of Al follows the well-established island-by-layer mode in air.[292] Under lower temperature (<673K), due to this growth mode, the ZrB_2 nanoparticles in the system will slow the covering process of Al_2O_3 and break the oxide layer continuity,[292] which could result in a thicker self-limiting oxide layer. However, under higher temperature (≥673K), **Figure 5 - 37** (a) and (b) show that amorphous Al_2O_3 has partially transferred to crystalline Al_2O_3 with regular geometry in pure Al.[106] The observation will influence the anti-oxidation performance at different temperature range and will be further discussed when quantifying the oxidation rate.

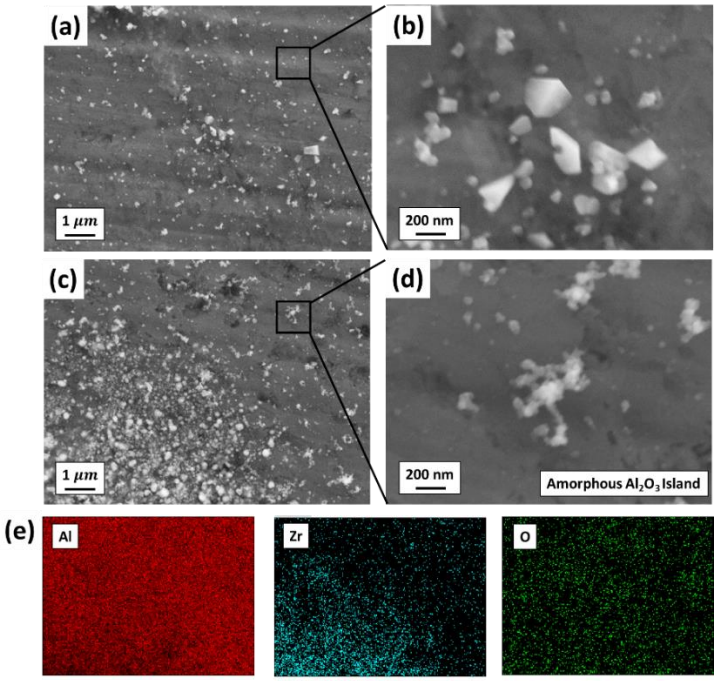

Figure 5 - 37 (a) and (b) The SEM image of the post-oxidation surface of pure Al after in situ XRD measurement; (c) and (d) The SEM image of the post-oxidation surface of Al-5 vol.% ZrB_2 nanocomposites after in situ XRD measurement; (e) The EDS mapping for the post-oxidation surface of Al-5 vol.% ZrB_2 nanocomposites after in situ XRD measurement to confirm the homogeneous distribution of amorphous Al_2O_3.

Comparing the XPS results for the surfaces before (**Figure 5 - 38** (a) and (b)) and after (**Figure 5 - 38** (c) and (d)) oxidation, no Zr and B signal of the post-oxidation surface indicates that amorphous Al_2O_3 covers the surface up. The detailed scanning for Al 2p (**Figure 5 - 38** (e) and (f)) and O 1s (**Figure 5 - 38** (g) and (h)) reveals that the Al 2p and O 1s peaks in the oxides of Al-5 vol.% ZrB_2 nanocomposites have a left shift compared with that of pure Al. The left shift of ~1.5-2 eV at O 1s is more obvious, which indicates a higher oxygen vacancy in the oxides formed

on Al-5 vol.% ZrB_2 nanocomposites. A smaller O(1s)/Al(2p) ratio of Al-5 vol.% ZrB_2 nanocomposites in **Figure 5 - 39** also proves this difference.

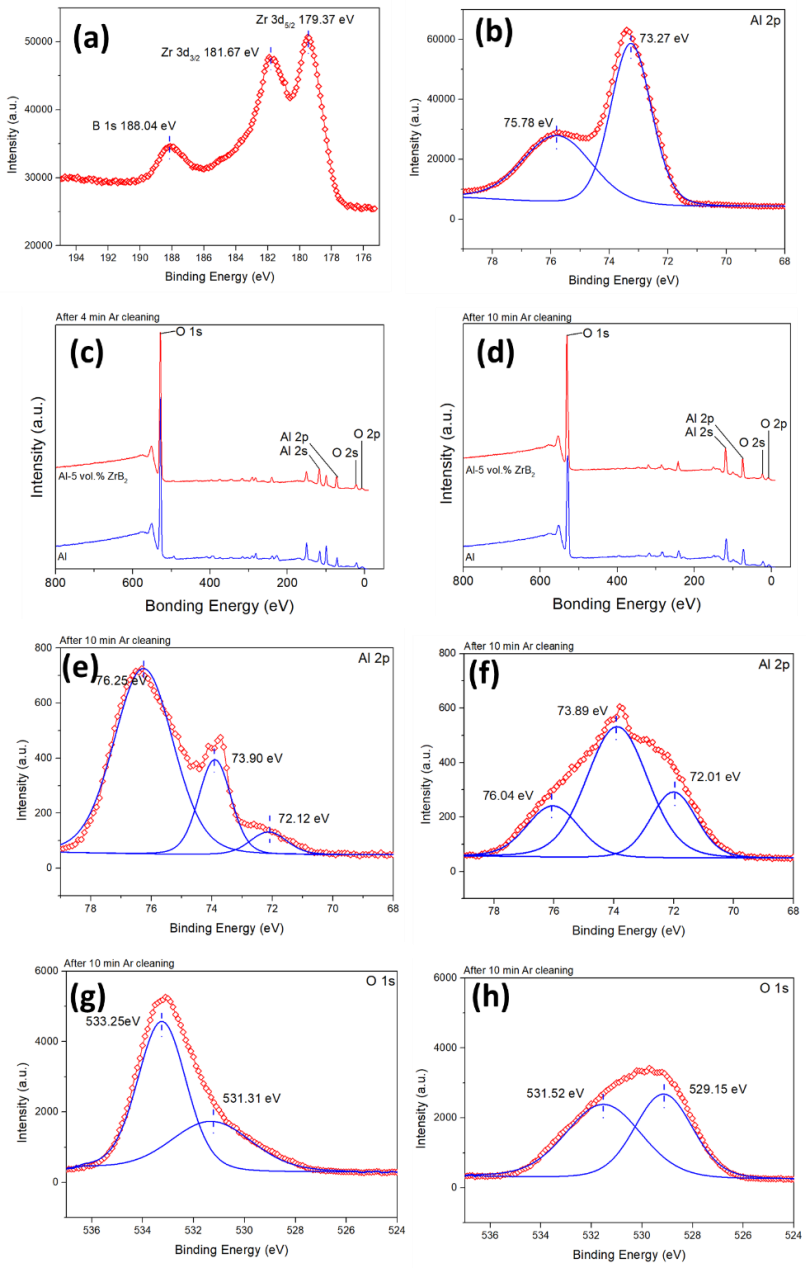

Figure 5 - 38 The detailed XPS spectrum for (a) Zr 3d and B 1s and (b) Al 2p in pre-oxidized Al-5 vol.% ZrB_2 nanocomposites; The XPS survey scanning of post-oxidation surface for in-situ XRD after (c) 4 min and (d) 10 min Ar ion cleaning; The detailed XPS spectrum for Al 2p on the post-oxidized surface for (e) Al-5 vol.% ZrB_2 nanocomposites and (f) pure Al after 10 min Ar

ion cleaning; The detailed XPS spectrum for O 1s on the post-oxidized surface for (g) Al-5 vol.% ZrB_2 nanocomposites and (h) pure Al after 10 min Ar ion cleaning.

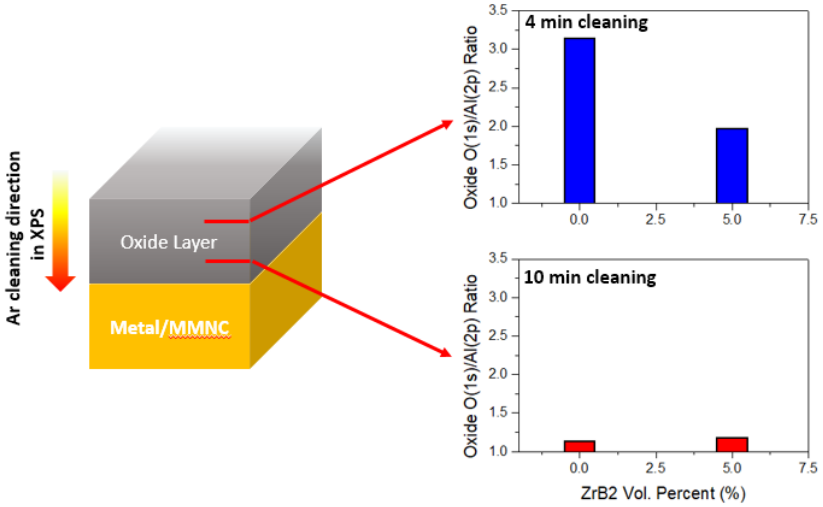

Figure 5 - 39 The O/Al ratio in the formed oxide for both Al and Al-5 vol.% ZrB_2 nanocomposites after in-situ XRD scanning and oxidation.

As shown in the **Figure 5 - 38** and **Figure 5 - 39**, the oxides at different depths (revealed by different Ar ion cleaning in XPS) have changed oxygen and aluminum ratio. Since the oxide forms and grows from the metal-oxide interface, 4 min cleaning reveals amorphous oxide formed in the earlier stage of the oxidation process (i.e., the lower temperature range) than 10 min cleaning (i.e. at the later oxidation stage under high temperature). At lower temperature, as shown in **Figure 5 - 39**, O(1s)/Al(2p)≫1.5 demonstrates an Al cation-deficient growth mode, which makes the process electric field-governed.[90,293] However, at higher temperature, O(1s)/Al(2p)<1.5, which introduces excessive Al cation (as proved by the Al oxidation states of the XPS results in **Figure 5 - 38** (c) and (d)) in the amorphous oxide to cancel the effect of electric field and dominates the oxide growth by activation energy.[90] This will be further discussed and correlated with the

calculation of the Mott potential-introduced electric field and the activation energy barrier with **Table 5 - 4**.

Quantitative Oxidation Rate To quantify the oxidation rate, both dynamic (following the in situ XRD thermal oxidation process) and kinetic measurement by TGA analyses are applied (**Figure 5 - 36** and **Figure 5 - 40**). The cross-section images are provided in **Figure 5 - 41** to prove the good match between the weight gain (in **Figure 5 - 40**) and the oxide layer average thickness after dynamic oxidation.

It is seen in **Figure 5 - 40** that Al-5 vol.% ZrB_2 nanocomposite shows a better anti-oxidation performance only under higher temperature (≥673K) than pure Al. It is because ZrB_2 will disturb the oxide layer covering process under lower temperature (<673K). Nevertheless, under higher temperature (≥673K), the whole surface is covered up and the oxygen diffusion will be more dependent on the morphology of Al_2O_3. Since pure Al already shows amorphous-to-crystalline transition of the formed Al_2O_3 (**Figure 5 - 37**), the interfacial boundaries of the crystalline Al_2O_3 will ease the oxygen diffusion for oxidation.[290,292,294] Therefore, pure Al will have worse anti-oxidation performance under higher temperature (≥673K) with continuous oxidation (**Figure 5 - 40** (a)) and breaks the self-limiting oxide layer under dynamic scanning (**Figure 5 - 40** (b)). The downward trend observed for 450K-700K in **Figure 5 - 40** (b) of Al-5 vol.% ZrB_2 nanocomposites during the dynamic oxidation may be explained by the medium-temperature dehydration of formed precursor $Al_2O_3{\cdot}xH_2O$.[295] This observation is also supported by the TGA analyses in **Figure 5 - 42**.

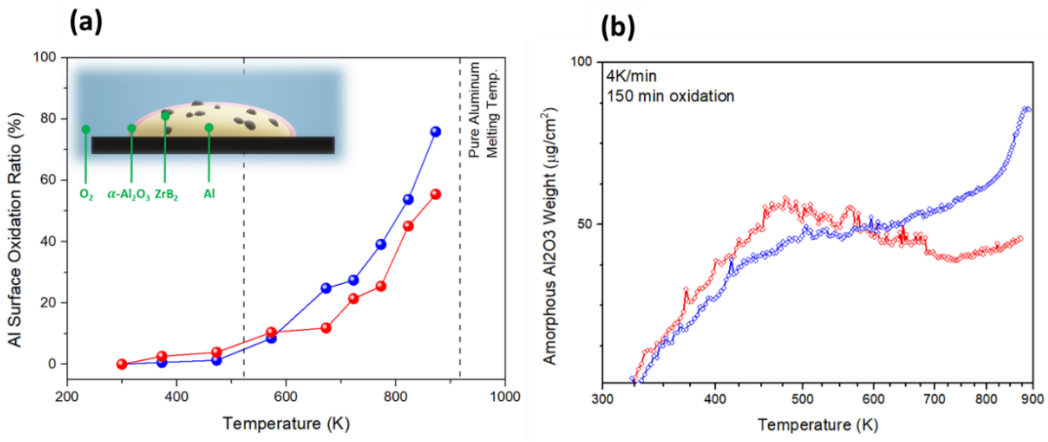

Figure 5 - 40 (a) The surface oxidation ratio analysis by *in situ* XRD and EDS mapping and (b) The TGA analysis to simulate the oxidation process during *in situ* XRD scanning for Al-5 vol.% ZrB_2 (red line) and pure Al (blue line).

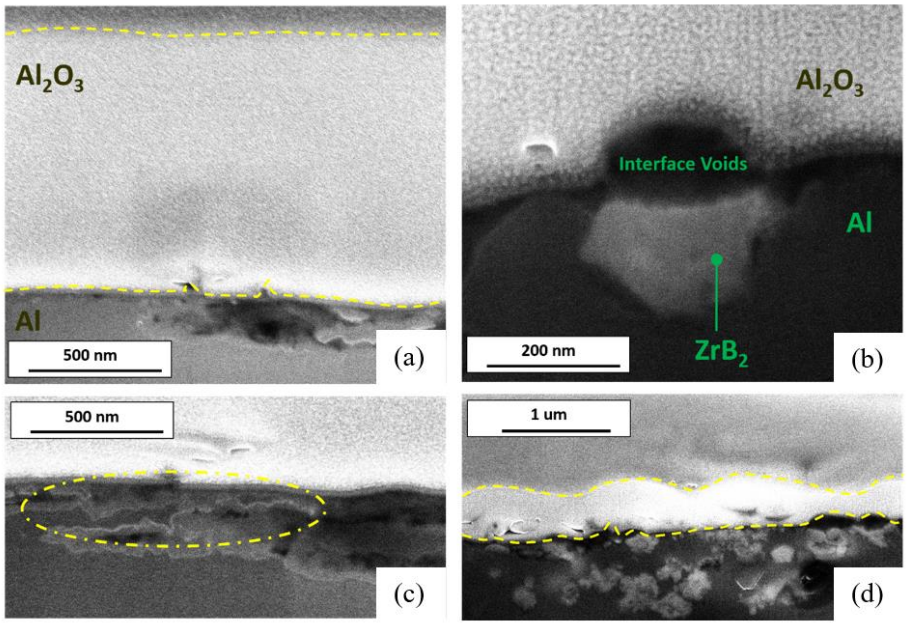

Figure 5 - 41 (a) and (c) The oxide layer cross-section of pure Al after in situ XRD characterization (the interface shows partial contact as the Al oxidation channel in (c)); (b) and (d) The oxide layer cross-section of Al-5 vol.% ZrB_2 after in situ XRD characterization (the interface shows large interface voids and huge interfacial separation with ZrB_2 nanoparticles, as shown in (d))

Using the equations of **Eq. 5 - 14** and **Eq. 5 - 15**,[90,296] together with the kinetic thermal oxidation lines shown in **Figure 5 - 42**, the Mott potential (the limiting threshold electric field strength) and activation energy barrier for oxidation are summarized in **Table 5 - 4**. For Al-5 vol.% ZrB_2 nanocomposite, the Mott potential is higher, which will lead to a faster oxidation rate; however, when the temperature goes higher, the Al cation-deficient growth mode is ended (**Figure 5 - 39**) and the activation energy control is more dominant. Al-5 vol.% ZrB_2 nanocomposite with a higher activation energy barrier will demonstrate better anti-oxidation performance. The good match between our experiment results and the literature data confirms the feasibility of our Al-ZrB_2 anti-oxidation analyses.

Eq. 5 - 14

$$n_{O_2} = \frac{P_{O_2}}{\sqrt{2\cdot\pi\cdot m_{O_2}\cdot k_B\cdot T}} \gg n_{Al}$$

Eq. 5 - 15

$$\frac{1}{z_{lim}} = -\frac{k_B\cdot\ln\left(\frac{10^{-15}}{\Omega\cdot n_{Al}\cdot v}\right)}{q\cdot a\cdot V_M}\cdot T - \frac{U}{q\cdot a\cdot V_M}$$

Where n_{O_2} is the number of O_2 molecules hitting a surface per unit time and area at constant pressure of P_{O_2} and constant temperature of T. m_{O_2} denotes the mass of O_2 molecule, and k_B is the Boltzmann's constant. n_{Al} is the available Al atoms for oxidation process. $n_{O_2} \gg n_{Al}$ under atmospheric pressure indicates that the oxidation of Al is not limited by the availability of O_2.

In **Eq. 5 - 15**, z_{lim} refers to the self-limiting oxidation layer thickness (corresponding to the thickness in **Figure 5 - 43**). Ω is the volume of oxide formed per cation of Al, v is the attempt frequency of the cation jump to get oxidation across the oxidation film, q is the charge of the migrating cation (+3 for Al), $2a$ is the distance from the potential minimum to the next potential

minimum across the rate-limiting activation energy barrier U, and V_M is the Mott potential for Al oxidation.[90]

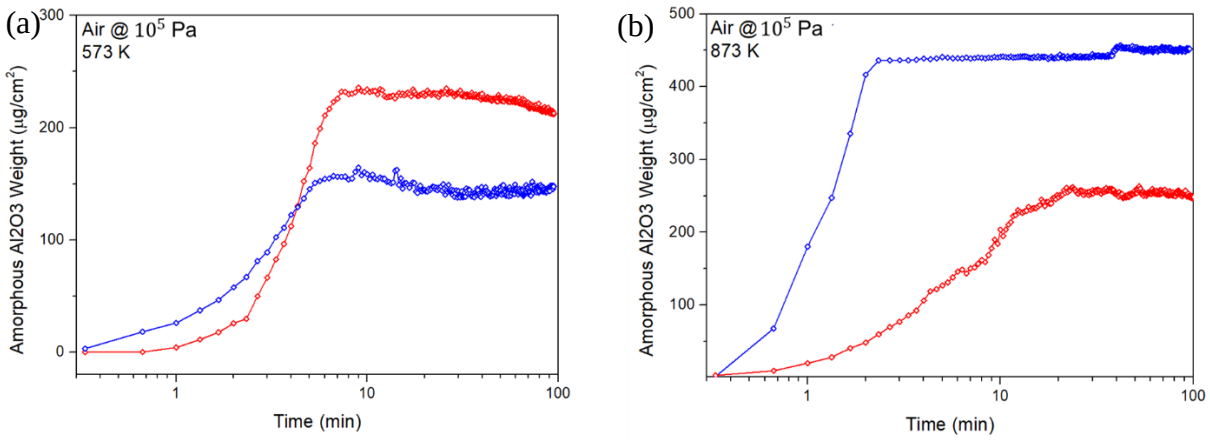

Figure 5 - 42 TGA analysis for the oxidation rate and the observation of self-limiting oxidation behavior in pure Al (blue line) and Al-5 vol.% ZrB_2 (red line) under air condition of 10^5 Pa at (a) 573K and (b) 873K for 90 min.

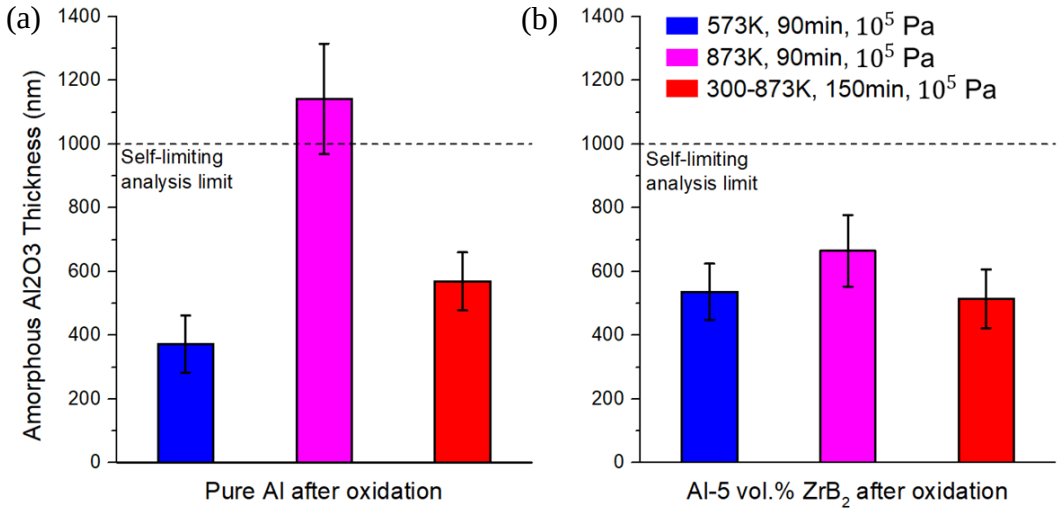

Figure 5 - 43 Thickness comparison between 3 different thermal oxidation processes mentioned above for (a) pure Al and (b) Al-5 vol.% ZrB_2 nanocomposites.

Table 5 - 4 The effect of ZrB_2 nanoparticles on Mott potential and rate-limiting activation energy barrier based on self-limiting Mott-Cabrera model

Materials	**Mott potential by limiting threshold electric field strength at 573K MV/cm**	**Energy barrier eV**	**Oxygen partial pressure Pa**
Al-5ZrB_2	~52.7	3.91	$\sim 2.1 \times 10^4$
Al	~22.7	2.88	$\sim 2.1 \times 10^4$
Al *	19	2.6	$\sim 10^{-5} - 10^{-3}$

* Data from Ref. [90]

Potential Applications Oxide layers may serve as a surface-engineering technique and anti-corrosion barrier. Therefore, thermal oxidation is the most effective way to tune the surface properties (e.g., wettability and anti-corrosion performance) of alloys.

Here, we demonstrated that the incorporation of 5 vol.% ZrB_2 nanoparticles can effectively tune the surface wettability with water both before and after thermal oxidation, as shown in **Figure 5 - 44** (a)-(f). It is clear in **Figure 5 - 44** (f) that after thermal oxidation, the Al-5 vol.% ZrB_2 surface is more hydrophobic than the oxidized pure Al surface, and the wetting angle almost doubled. Since having difference hydrophobicity could introduce different functionalities, the incorporation of ZrB_2 nanoparticles could potentially be used as an effective means to change Al alloys' surface properties for thermal and biological applications.

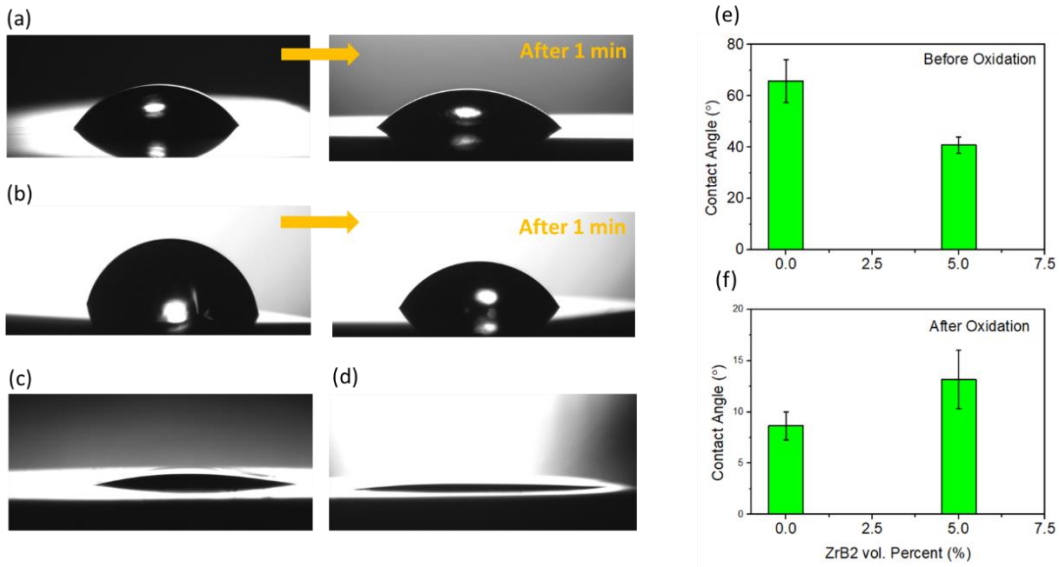

Figure 5 - 44 The wetting condition between water and the pre-oxidation surface of (a) Al-5 vol.% ZrB_2 nanocomposites and (b) pure Al; The wetting condition between water and the post-oxidation surface of (c) Al-5 vol.% ZrB_2 nanocomposites and (d) pure Al. The wetting angle between water and the (e) pre-oxidation and (f) post-oxidation surfaces.

Furthermore, the anti-corrosion performance of the oxidized surfaces is different in pure Al and Al-5 vol.% ZrB_2 nanocomposite. The results of the potentiodynamic curve and the frequency response of the corrosion process in the oxide layer have been summarized in **Figure 5 - 45**. Since the Al_2O_3 layer would be dense after the oxidation process, given the frequency-dependent characteristics in **Figure 5 - 45** (b) and (c), the circuit as shown in **Figure 5 - 45** (d) is used for EIS spectra fitting. The electrochemical results are summarized in **Table 5 - 5**. Here, E_{corr} refers to the corrosion potential (by **Figure 5 - 45**). R_s is the solution resistance, R_p the polarization resistance, and C_{dl} the electrical double layer capacitance. For oxide layer electrochemical properties, R_o denotes the oxide layer resistance, and C_o the oxide layer capacitance. The similar R_s indicates the measurement is accurate and the fitting is feasible.

After thermal oxidation, the oxide layer of Al-5 vol.% ZrB_2 has higher E_{corr}, which means it's much noble against the corrosion in 3.5 wt.% NaCl solution. Besides, Al-5 vol.% ZrB_2 oxide layer has a much larger R_o and R_p, which demonstrates the more supreme anti-corrosion performance than pure Al oxide layer.

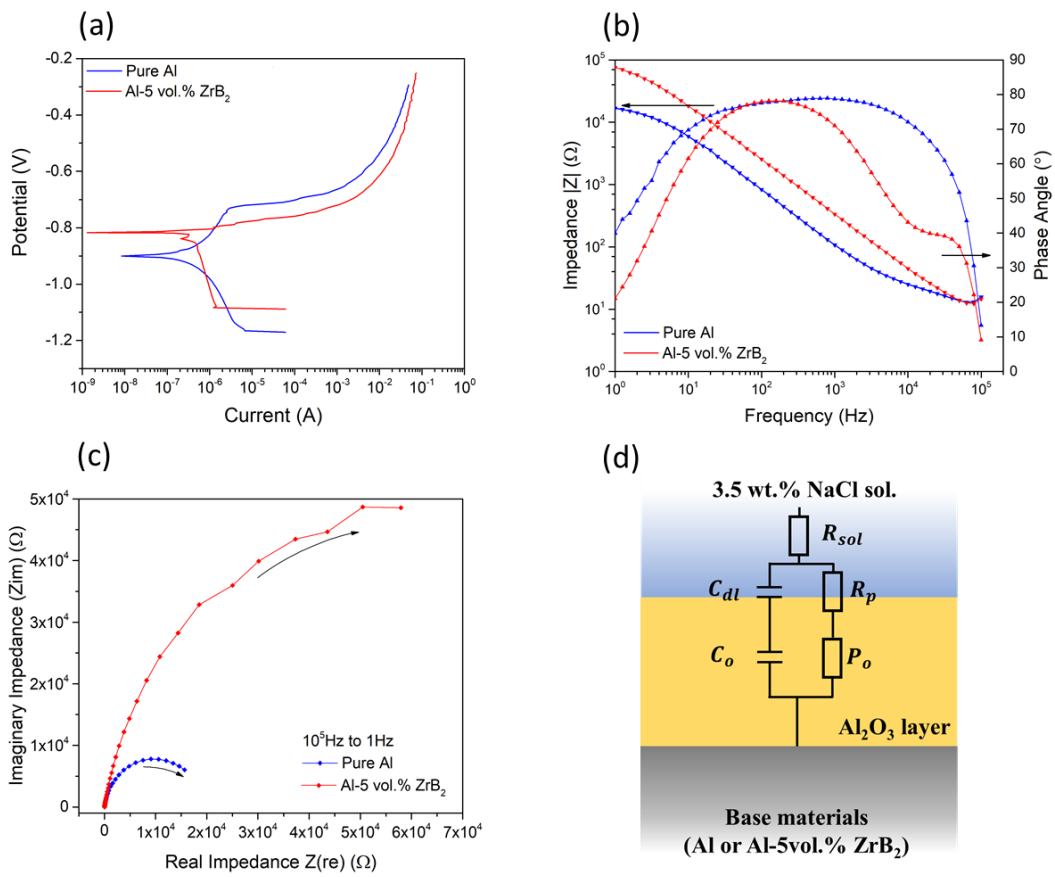

Figure 5 - 45 Anti-corrosion performance analysis for pure Al and Al-5 vol.% ZrB2 after thermal oxidation (in situ XRD route) with (a) potentiodynamic curve, (b) frequency-dependence of total impedance and phase angle, (c) frequency-dependence of real and imaginary impedance, and (d) equivalent electrical circuit for impedance analysis.

Table 5 - 5 Fitting values for simulative EIS spectra of the oxidized surface for pure Al and Al-5 vol.% ZrB_2 samples (in situ XRD route, 0.9 cm^2 surface area)

	E_{corr} (V)	R_s (Ω)	R_p (Ω)	C_{dl} (nF)	R_o (Ω)	C_o (nF)
Pure Al	-0.901	9.783	13129	1969.8	20.91	734.1
Al-5ZrB_2	-0.818	9.578	68243	767.6	433.7	834.4

More importantly, Al-5 vol.% ZrB_2 oxide layer interacts with the solution to have a smaller C_{dl}.The Gibbs free energy G at the interface of the oxide layer and the solution is governed by[297]:

Eq. 5 - 16 $$G = \gamma_{sl} \cdot A + C_{dl} \cdot {U_{dl}}^2$$

Where γ_{sl} is the solid-liquid interfacial energy, A the exposed surface (which could be normalized), and U_{dl} the electrical potential set up in the electrical double layer. Here, since R_p is much larger, U_{dl} will be mostly determined by R_p under disturbance <1Hz and could be considered constant for wettability experiment. So, with the equilibrium criterion $\Delta G = 0$, γ_{sl} and U_{dl} have the relationship of:

Eq. 5 - 17 $$\frac{d\gamma_{sl}}{\mathrm{d}C_{dl}} = -\frac{{U_{dl}}^2}{A}$$

So, Al-5vol.% ZrB_2 oxidized surface would have a higher γ_{sl} with lower C_{dl}. Since the contact angle is determined by $cos\theta = \frac{\gamma_{sg}-\gamma_{sl}}{\gamma_{gl}}$, a larger contact angle (i.e., more hydrophobic) is expected for Al-5 vol.% ZrB_2 oxidized surface than pure Al surface. The EIS measurement is consistent with our observation in **Figure 5 - 44**.

In brief, the thermal oxidation of Al-5 vol.% ZrB_2 surface would provide tunable wettability and anti-corrosion performance for the Al matrix. In our case, Al-5 vol.% ZrB_2 oxidized surface is more hydrophobic and corrosion-resistant than Al oxidized surface.

In summary, this part analyses the oxidation process and oxide layer characteristics of pure Al and in situ Al-ZrB_2 nanocomposites. The effects of ZrB_2 nanoparticles are studied by both dynamical and kinetical measurements: Under lower temperature (<673K), Al-5 vol.% ZrB_2 nanocomposites exhibit a higher oxidation rate than pure Al. The exposed ZrB_2 nanoparticles breaks the continuity of the oxide layer, and the cation-deficient mode makes this temperature-range electric field-controlled. However, under higher temperature (>673K), Al-5 vol.% ZrB_2 has a better anti-oxidation performance, thanks to the delay of the amorphous-to-crystalline phase change of Al_2O_3.

This observation is confirmed by the Mott-Cabrera model analysis: The Al-5 vol.% ZrB_2 nanocomposites have both higher Mott potential and greater activation energy barrier. When the oxidation temperature is lower, Mott potential, as well as higher O/Al ratio, makes Al-ZrB_2 easier to be oxidized initially; on the other hand, when the temperature is higher, the activation energy barrier is more dominant and leads to a slower oxidation rate.

With the different characteristics of the oxide layer, it has been further demonstrated that the post-oxidation surface of Al-ZrB_2 nanocomposites has different wettability and corrosion-performance. The Al-ZrB_2 oxidized surface has a larger contact angle, more noble corrosion potential, and higher corrosion resistance. This understanding is important for thermal oxidation applications (e.g., surface modifications) for various aluminum alloys.

5.2.5 Thermal oxidation of AA7075/TiB_2 nanocomposite

Pre-oxidation microstructure The microstructure of the as-fabricated AA7075-1.5TiB_2 nanocomposites (by hot extrusion, under T6 state) was summarized in **Figure 5 - 46**. The TiB_2 nanoparticles would form bands with some secondary phases inside/near [180]. Before the thermal oxidation experiments, the polished surface will expose secondary phases linked to the sample surface, as shown in **Figure 5 - 46**c for AA7075 alloys and **Figure 5 - 46**d for AA7075-1.5TiB_2 nanocomposites.

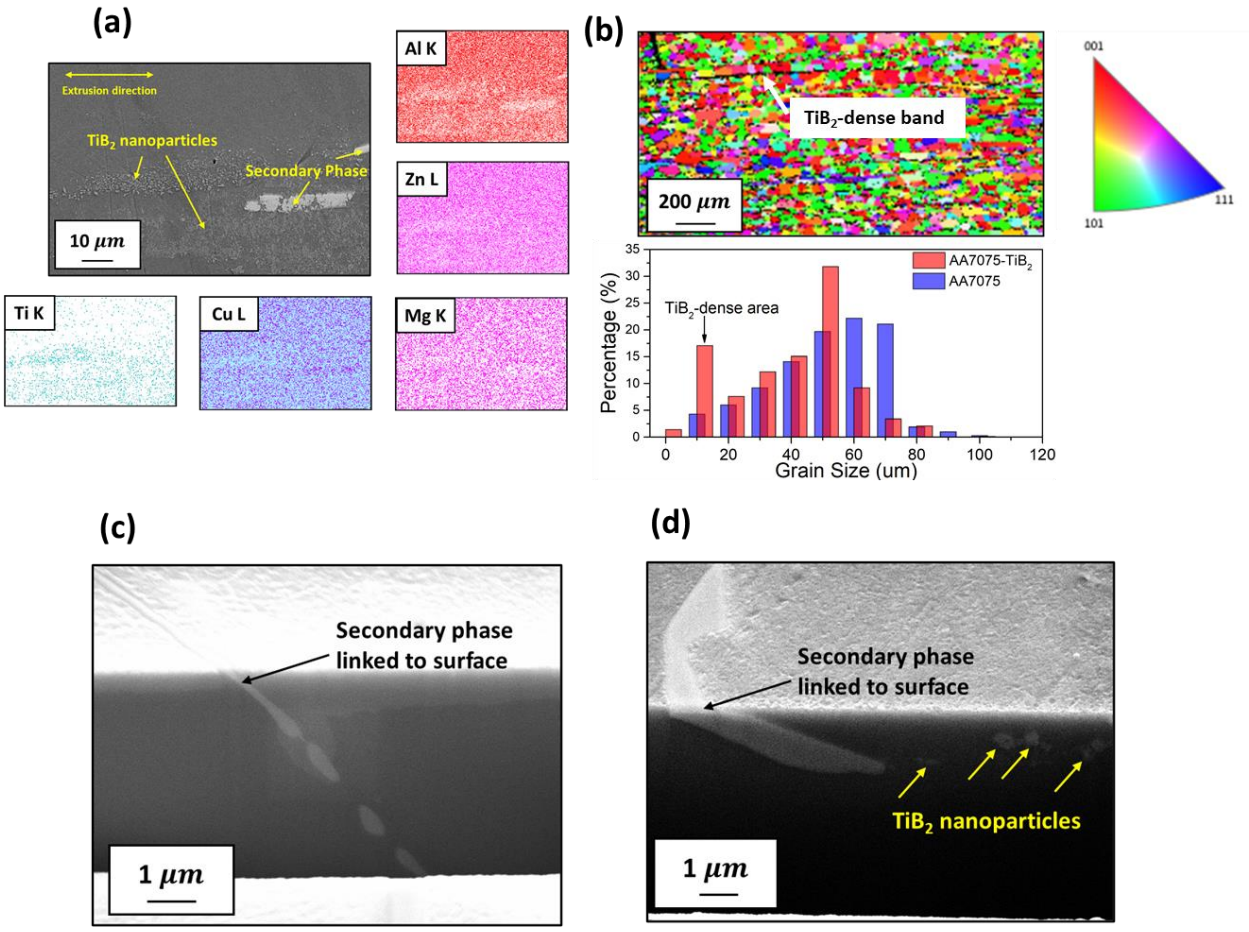

Figure 5 - 46 (a) SEM imaging and EDS mapping and (b) large-area EBSD analysis of AA7075-1.5TiB_2 nanocomposites; Near-surface morphology of secondary phases in (c) AA7075 alloy and (d) AA7075-1.5TiB_2 nanocomposite.

Dynamic oxidation To understand the oxidation behavior of AA7075 and AA7075-1.5TiB_2 nanocomposites, the samples under the dynamic thermal oxidation conditions were first tested, during which the temperature was varying with control (as shown in **Figure 5 - 47**a).

As shown in **Figure 5 - 47** b-d, the AA7075-1.5TiB_2 nanocomposites show a similar oxidation trend as the AA7075 alloy. The surface oxidation ratio increases with the increased temperature. When the temperature approaches the solutionizing temperature of secondary phases like $MgZn_2$, the oxidation process runs into a plateau (see **Figure 5 - 47**b), which is due to the Al_2O_3 coverage[298] and a drastically changed microstructure in these secondary phases (as shown in the dashed box of **Figure 5 - 47**c and d). Since the Gibbs free energy drives the oxidation reaction with $\Delta G = \Delta H - T \cdot \Delta S$, the structural change could contribute to the increased entropy ΔS and, as a result, balance the need of ΔH from mere oxidation reaction and lower the oxidation speed. In this case, $MgZn_2$ as the secondary phase is important for oxidation at a high-temperature range (e.g., 400℃ to 600℃), and this will be further addressed in the isothermal oxidation experiments.

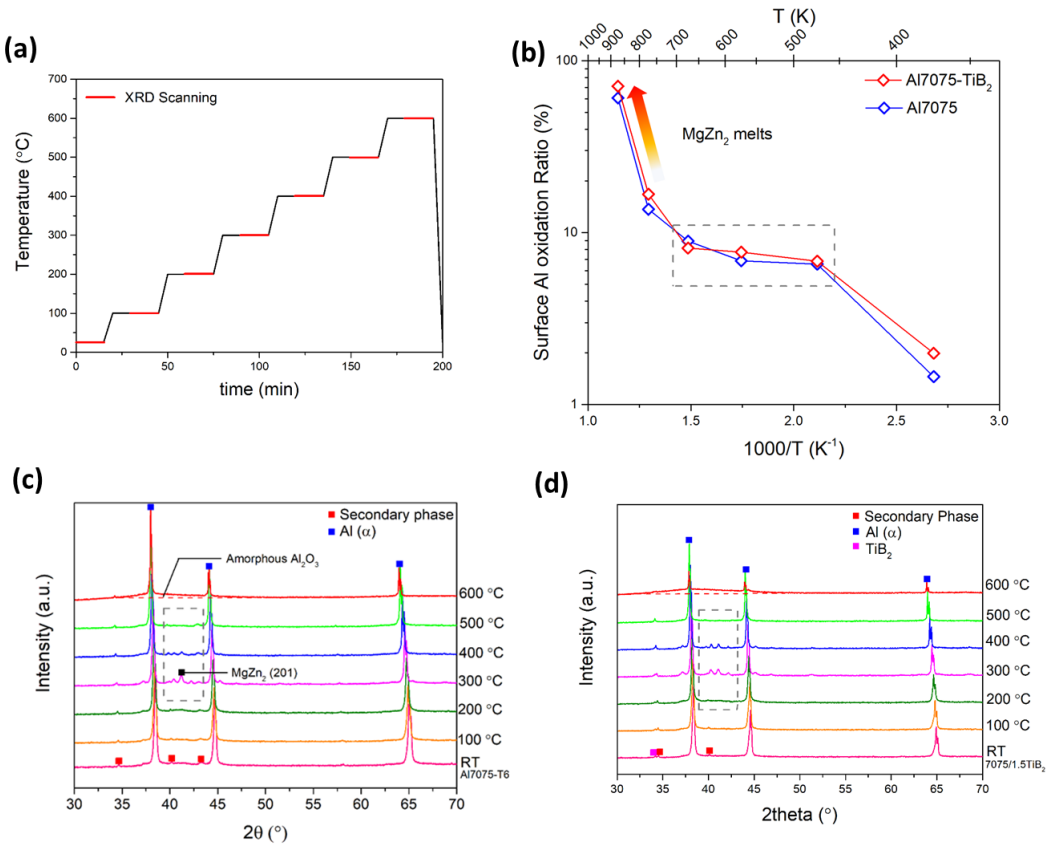

Figure 5 - 47 *In situ* XRD results for surface oxidation and materials' composition analyses (a) the scanning speed, time, and temperature setup; (b) Semi-quantitative dynamic thermal oxidation rate; XRD spectrum for (c) AA7075 alloy and (d) AA7075-1.5TiB_2 nanocomposite at different temperatures.

The surface morphology was first characterized by the surface roughness, as shown in **Figure 5 - 48**. The average surface roughness for the AA7075-1.5TiB_2 nanocomposite is 2.47 um, whereas that of the AA7075 alloy is 25.46 um. Clearly, the AA7075-1.5TiB_2 nanocomposites would have a smoother surface than the AA7075 alloy, which is consistent with the observation of the refined grain size by TiB_2 (as shown in **Figure 5 - 46**b).

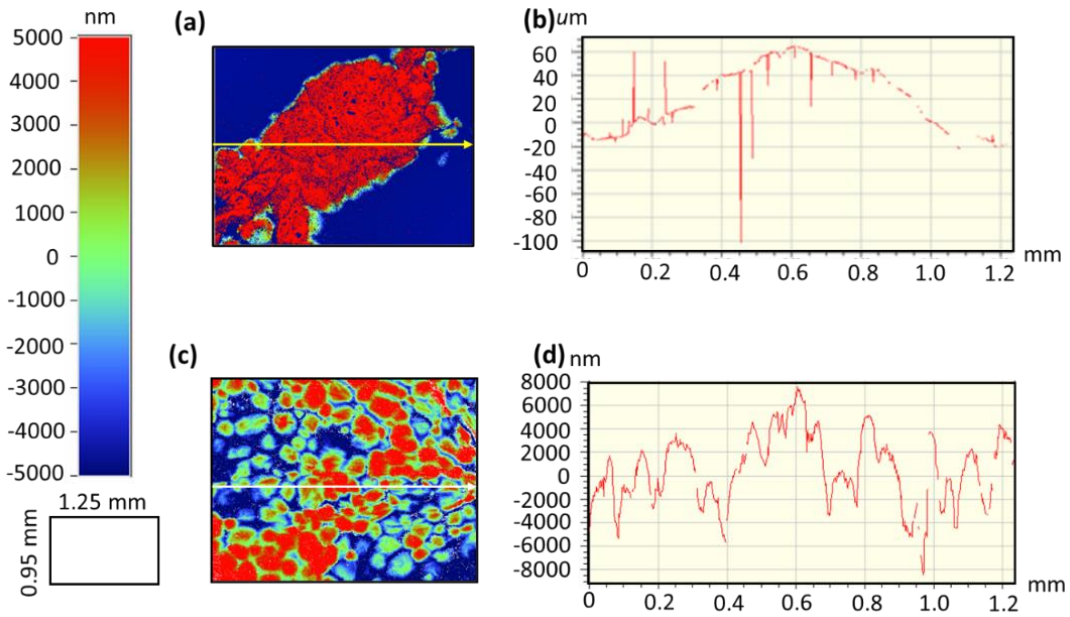

Figure 5 - 48 Post-oxidation morphology by VSI scanning after in situ XRD measurement: (a) 3D morphology and (b) line-scan surface roughness of AA7075; (c) 3D morphology and (d) line-scan surface roughness of AA7075-1.5TiB_2 nanocomposites.

Figure 5 - 49 further demonstrates a similar result to **Figure 5 - 48**. As shown in **Figure 5 - 49**a and b, both AA7075 and AA7075-1.5TiB_2 nanocomposites show an oxidation pattern of bubble-like curved Al_2O_3 oxide film on the grain and wavy-patterned Zn-rich oxides near the grain boundaries (GBs) (as supported by EDS mapping in **Figure 5 - 49**c and d). The wavy-patterned Zn-rich zone is mainly enabled by a stress-assisted oxidation process,[74] and this process is governed by the different oxidation behaviors of Al and Zn: Al oxidation is self-limiting and forming a flat and dense amorphous non-stoichiometric layer [90]; At the same time, Zn tends to oxidize into wire-like patterns by continuous growth [103,273]. During the thermal oxidation, Al will quickly form a thin oxide layer to cover all the surfaces (Phase I, as shown in **Figure 5 - 50**b). When the temperature is higher, meta-stable η-phase $MgZn_2$ goes through a configurational

change, and Zn starts to diffuse out (Phase II, as shown in **Figure 5 - 50**c). When the temperature goes above the solutionizing temperature of $MgZn_2$, Zn participates in the oxidation process: Since Zn is mainly forming GB precipitates near or at GBs, the Zn outward growth will be rapid near the GB precipitates. Stress arises when wire-like ZnO interacts with the Al_2O_3 layer surface, and the interconnected ZnO wires will bend to form patterns. Meanwhile, when the surface is curved, the pressure difference from the surface tension of Al_2O_3 oxide thin films will assist the Zn element diffusion by an inward oxygen flux (Phase III, as shown in **Figure 5 - 50**d). The detailed process and observations for phase I and phase II/III will be further discussed in the following sections.

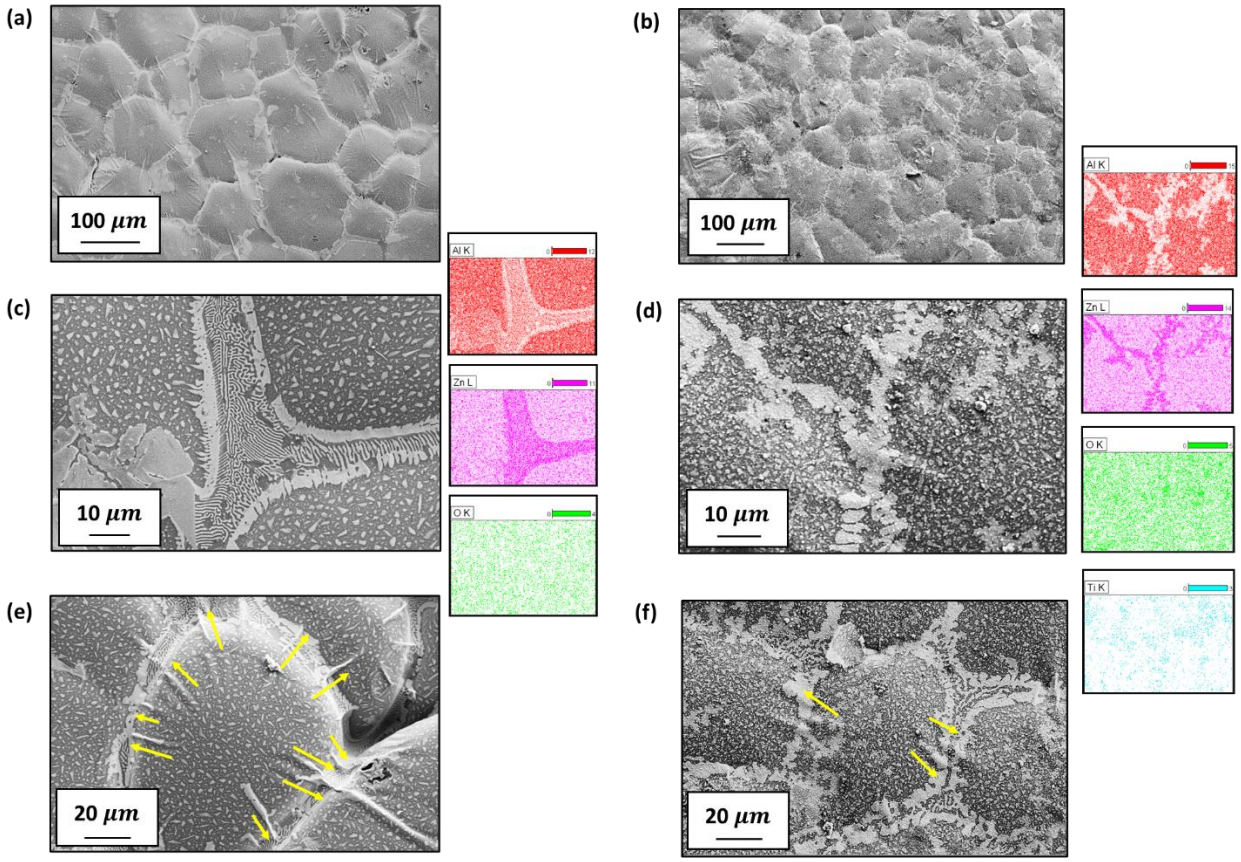

Figure 5 - 49 Post-oxidation surface morphology in *in situ* XRD process: (a) AA7075 and (b) AA7075-1.5TiB_2 after oxidation; The morphology and EDS mapping of the Zn-rich oxidation zone near the GBs of (c) AA7075 and (d) AA7075-1.5TiB_2; The early-stage ruptured Al_2O_3

layer (as well as the formed wrinkles at the GBs) of (e) AA7075 and (f) AA7075-1.5TiB_2 after oxidation (the yellow arrows indicate the tension direction).

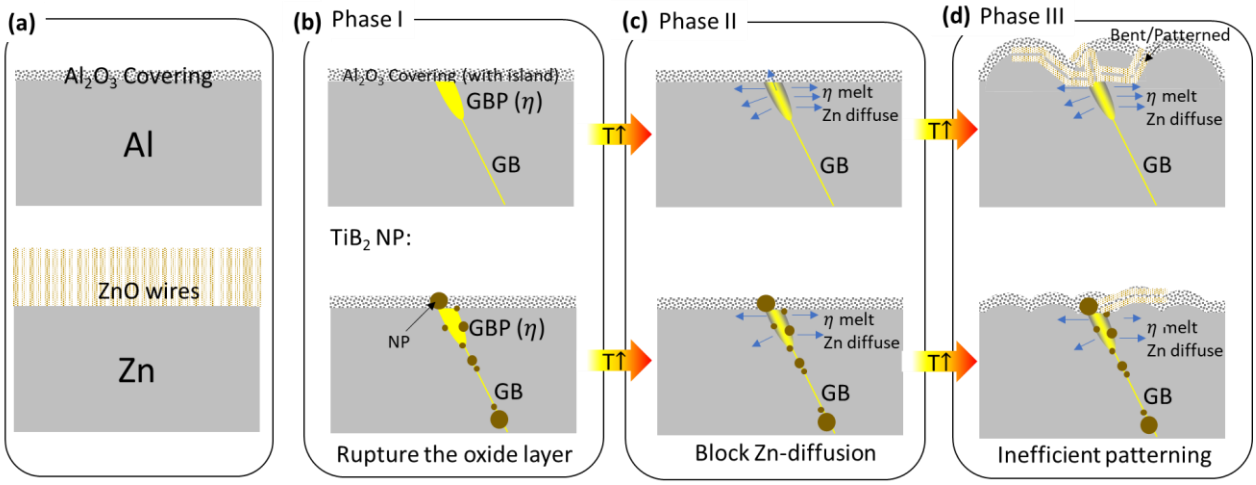

Figure 5 - 50 (a) Illustration of the difference between Al and Zn oxidation processes; (b) The initial Al-oxidation stage (Phase I), (c) η-phase reconfiguration, melting, and Zn-diffusion starting stage (Phase II), and (d) the Zn-oxidation and pattern-forming stage (Phase III) during AA7075 oxidation, and the associated role of TiB_2 nanoparticles.

Isothermal oxidation below solutionizing temperature (600 ℃) To further confirm the above experimental observation in AA7075 and AA7075-1.5TiB_2, the results of isothermal oxidation at 400℃ for 3 hours have been summarized in **Figure 5 - 51**. The period of 3 hours was chosen to be comparable to the dynamic oxidation time.

As shown in **Figure 5 - 51**a-1, a-3, b-1, and b-3, since the temperature is below the solutionizing temperature, the secondary phase keeps its shape, and the matrix Al undergoes an island-shaped self-limiting oxidation [110,298]. The EDS scanning result in **Figure 5 - 51**b-2 also indicates that the TiB_2 nanoparticle is still within the detection depth, which proves the formation of a uniform thin oxide layer. More importantly, the surface keeps reasonably flat. The cross-

section characterization also shows that the $MgZn_2$-linked surface area and the matrix surface area have no observable difference in their oxidation behavior of AA7075 and AA7075-1.5TiB_2, and the Al oxidation solely dominates at this temperature.

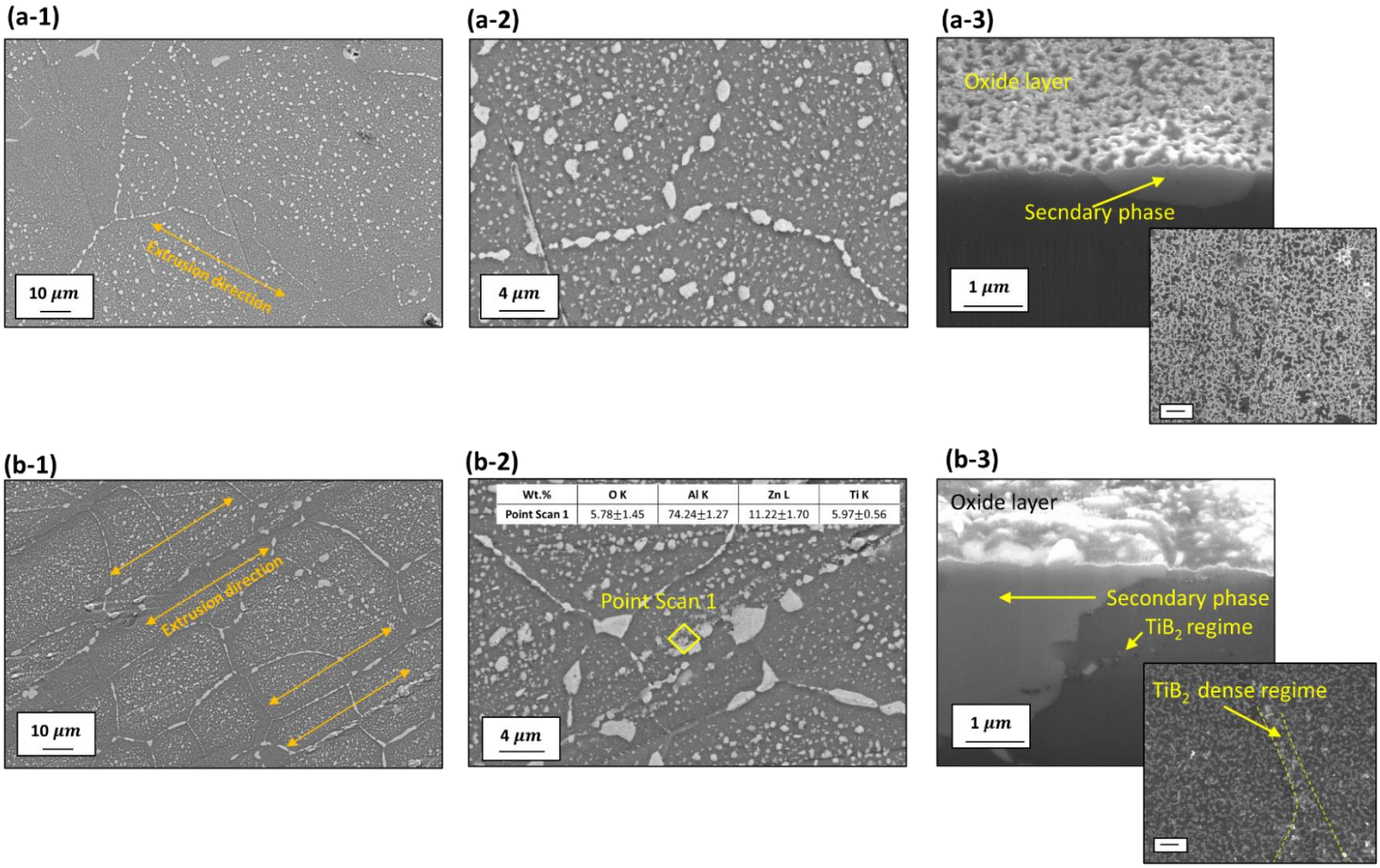

Figure 5 - 51 Post-oxidation surface morphology and cross-section view for (a-1) to (a-3) pure AA7075 and (b-1) to (b-3) AA7075-1.5TiB_2 after isothermal oxidation for 3 hours at 400 ℃.

Isothermal oxidation above solutionizing temperature (600 ℃) Similarly, the 3-hour isothermal oxidation under 600 ℃ was conducted to make a comparison. After this isothermal oxidation process, the surface of both AA7075 and AA7075-1.5TiB_2 exhibits wavy curvatures (in **Figure 5 - 52** a-1 to a-3 and b-1 to b-3). Unlike the mere Al oxidation to create island-like oxidation

mode, the oxidation products yield similar patterns on the surface (**Figure 5 - 52** a-2 and b-2) and near the surface secondary phases (**Figure 5 - 52** a-3 and b-3) to the dynamic oxidation results of **Figure 5 - 49** c and d. Given the element distribution in **Figure 5 - 52** a-4 and b-4 and the flat oxidized surface under 400 ℃, this observation at 600 ℃ indicates that the wavy surface morphology and abnormal oxidized patterning are induced by the solutionizing/melting process of Zn-rich phases. This understanding supports the mechanistic illustration in **Figure 5 - 50**. In this case, under high-temperature oxidation (e.g., 600 ℃), contrary to the typical investigation for the metallic systems with Al [299–301], the pre-formed Al_2O_3 oxide layer does not provide efficient oxygen inhibition to protect the substrate from oxidization (Phase II and Phase III in **Figure 5 - 50**), even though the Al_2O_3 appears intact (see **Figure 5 - 49**). A new model is needed to show the interaction of the pre-formed Al_2O_3 oxide layer and Zn oxidation for morphology patterning and oxygen penetration.

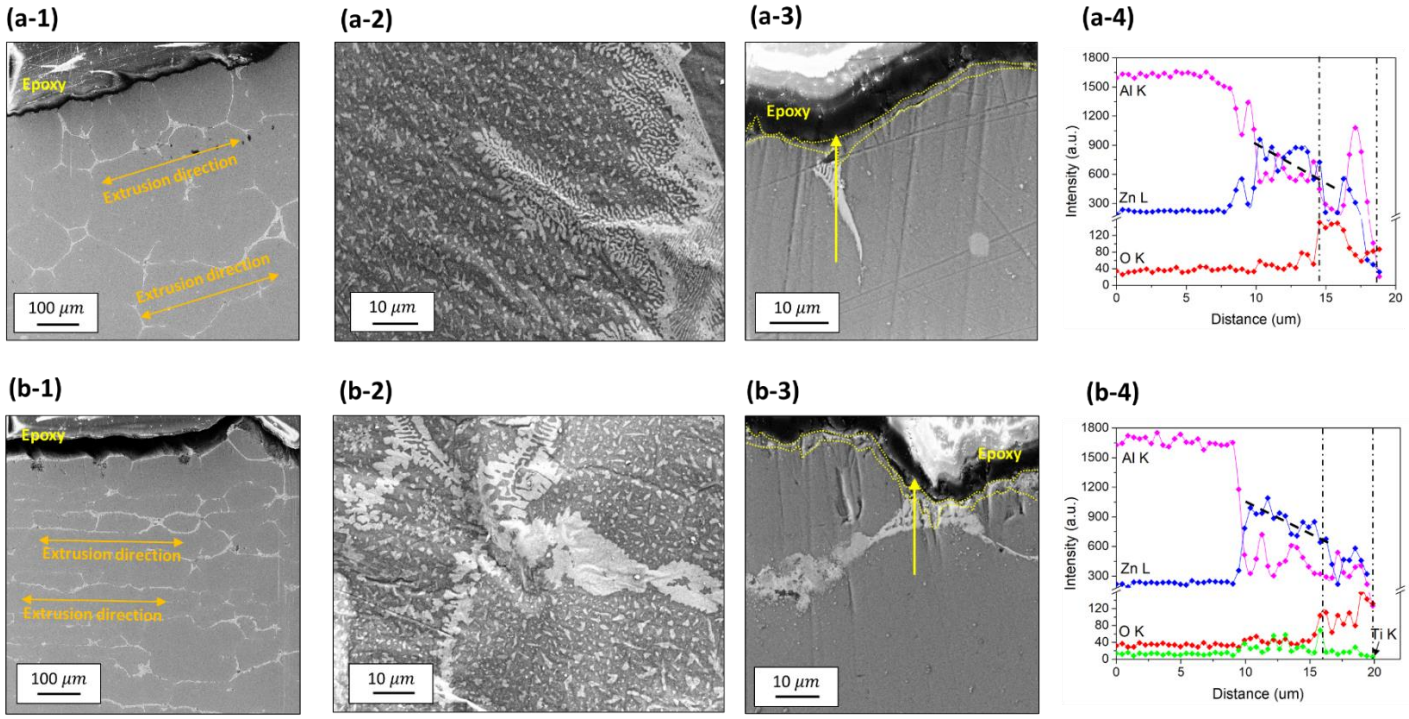

Figure 5 - 52 Post-oxidation cross-section morphology after isothermal oxidation at 600 ℃ for 3 hours for (a-1) pure AA7075 and (b-1) AA7075-1.5TiB_2; Post-oxidation surface morphology for (a-2) pure AA7075 and (b-2) AA7075-1.5TiB_2; EDS line scanning from matrix to surface for Al, Zn, and O elements in (a-3) and (a-4) pure AA7075 and (b-3) and (b-4) AA7075-1.5TiB_2.

<u>*Oxidation mechanism*</u> Since the Zn is oxidized after the thin amorphous Al_2O_3 film is formed, the growth of ZnO will be influenced by the Al_2O_3 film, as shown in **Figure 5 - 50** d. **Figure 5 - 49** e and f and Figure 7 also indicate a surface tension-induced wrinkled morphology after ZnO starts growing above the solutionizing temperature. Therefore, the growth of ZnO will need to sustain an energy consumption from surface tension (per unit area) E_{growth} by:

Eq. 5 - 18 $$dE_{growth} = \frac{2 \cdot \gamma_{Al_2O_3}}{R} \cdot dx$$

Where $\gamma_{Al_2O_3}$ is the surface tension for the thin Al_2O_3 film, R the characteristic curvature radii after the oxide film is ruptured, and x the effective outward moving distance if the oxide film is to be expanded/ruptured.

This energy is supplied by Zn oxidation enthalpy mainly (i.e., $2Zn + O_2 \rightarrow 2ZnO$). Then, the energy supply by oxidation (per unit area) $E_{oxidation}$ will be linked with the Zn diffusion flux to the surface:

Eq. 5 - 19 $$dE_{oxidation} = \Delta H \cdot J_{Zn} \cdot dt \cong \Delta H \cdot J_O \cdot dt$$

Where ΔH denotes the oxidation reaction enthalpy of Zn. J_{Zn} and J_O are the diffusion flux of Zn and oxygen respectively in a short time interval dt.

At equilibrium oxidation condition with $dE_{growth} = dE_{oxidation}$, the Zn oxidation speed and the oxygen penetration speed will be primarily determined by:

Eq. 5 - 20 $$v = \frac{dx}{dt} = \frac{J_{Zn} \cdot \Delta H \cdot R}{2 \cdot \gamma_{Al_2O_3}} \cong \frac{J_O \cdot \Delta H \cdot R}{2 \cdot \gamma_{Al_2O_3}}$$

As shown in **Figure 5 - 52** a-3 and b-3, Zn oxidation in AA7075 is different from its oxidation process in Zn-dominant system [74], because the secondary phase enriched with Zn in AA7075 systems directly contributes as a Zn reservoir. This condition requires minimum GB stress-assisted Zn transport to the surface,[103,273] as the oxygen gradient leads to an inward oxidation and diffusion trend, as shown in **Figure 5 - 54** and **Figure 5 - 58**. Besides, high temperature will also give the (near-)surface enough stress relaxation by softening the matrix. Thus, the Zn oxidation is minimally influenced by the stress gradient but largely depend on the concentration gradient, as shown in the following equation:

Eq. 5 - 21 $$J_{Zn} \cong D_{Zn} \cdot \frac{\partial C_{Zn}}{\partial x}$$

Eq. 5 - 22 $$J_O \cong D_O \cdot \frac{\partial C_O}{\partial x}$$

Where D_{Zn} and D_O are the elemental diffusivity for Zn and oxygen in the AA7075 system, respectively. C_{Zn} and C_O denotes the concentration of these elements along the presumed Al_2O_3 rupture normal direction.

Here, the quantification of the Zn oxidation process uses **Eq. 5 - 21** and **Eq. 5 - 22**, because Zn is forming complex intermetallic compounds like $MgZn_2$ and the Zn concentration gradient may be heavily influenced by other secondary phases, including AlCu-rich phases (see **Figure 5 - 53**).

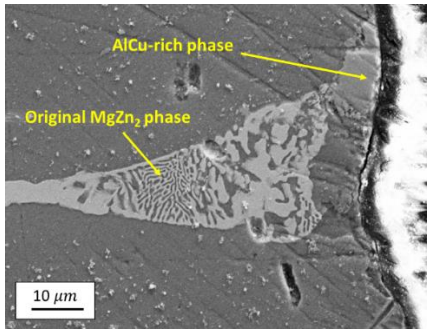

Figure 5 - 53 Illustration of complex intermetallic compounds on the gradient-driven thermal oxidation path of Zn. (6-hour thermal oxidation at 600 ℃ in AA7075-1.5TiB_2 as an example)

Besides, the interchangeable relationship between Zn and oxygen is also valid, because the higher Zn concentration gradient leads to a higher O concentration gradient by mass conservation and vice versa (see **Figure 5 - 54** c and d and **Figure 5 - 58** c and d).

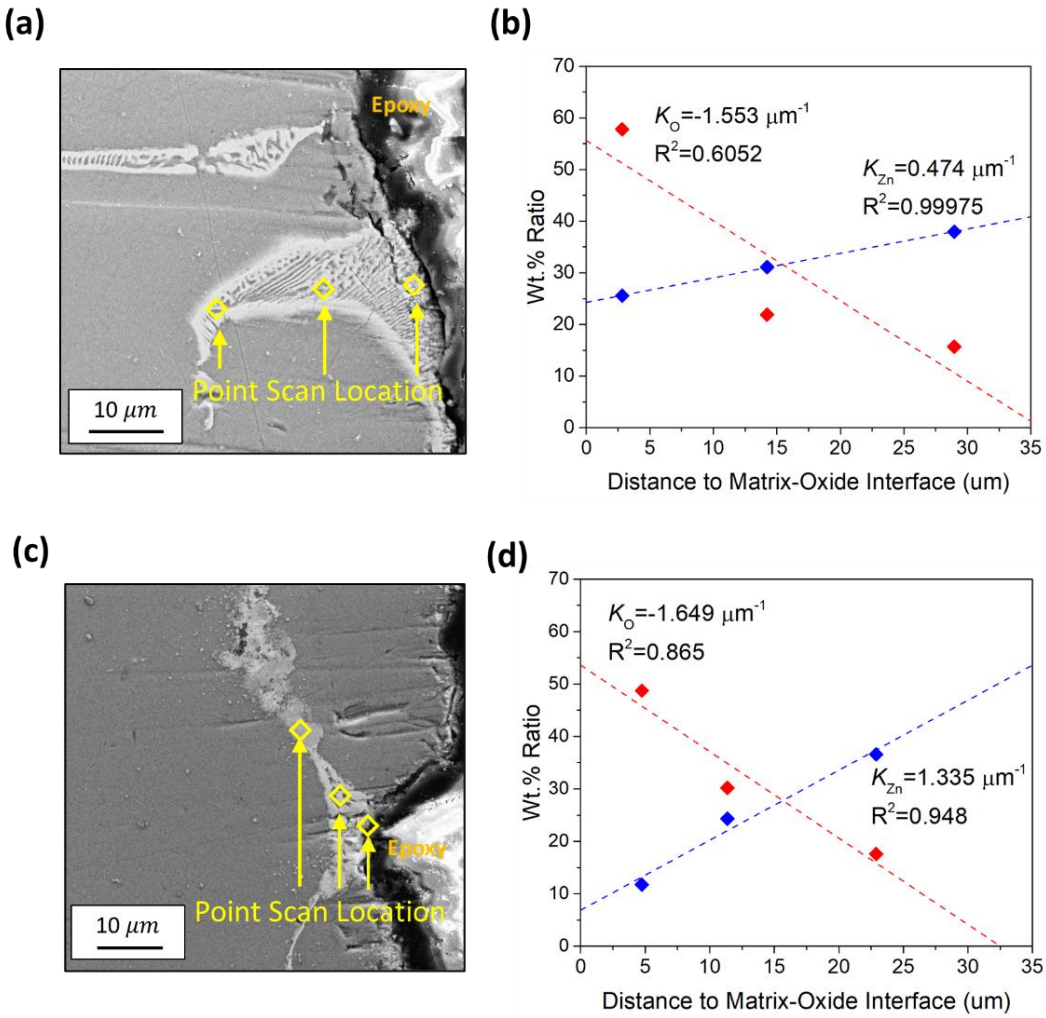

Figure 5 - 54 Element concentration gradient of Zn and O along the diffusion path within the secondary phase after 3-hour thermal oxidation at 600 ℃ for (a) pure AA7075 with EDS point-scanning in (b) and (c) AA7075-1.5TiB_2 with EDS point-scanning in (d).

Therefore, considering the interchangeable equivalence between **Eq. 5 - 21** and **Eq. 5 - 22** and the simple chemical composition of oxygen, **Eq. 5 - 22** will be mainly used to quantify the Zn oxidation process. With this equation substitution, the oxidation penetration depth (illustrated by the oxygen depletion depth) could be derived quantitatively in **Eq. 5 - 23**:

Eq. 5 - 23 $$\frac{dz}{dt} \propto v \cong \frac{D_{Zn} \cdot \frac{\partial C_{Zn}}{\partial x} \cdot \Delta H \cdot R}{2 \cdot \gamma_{Al_2O_3}} \cong \frac{D_O \cdot \frac{\partial C_O}{\partial x} \cdot \Delta H \cdot R}{2 \cdot \gamma_{Al_2O_3}} \propto \left(\frac{\partial C_O}{\partial x} \cdot R\right)$$

As measured by VSI (in **Figure 5 - 48**) and surface morphology and grain size characterization (in **Figure 5 - 49** and **Figure 5 - 55**), the average ratio of curvature radii between AA7075-1.5TiB_2 and pure AA7075 is R_{NP}/R_{pure} ≈0.78.

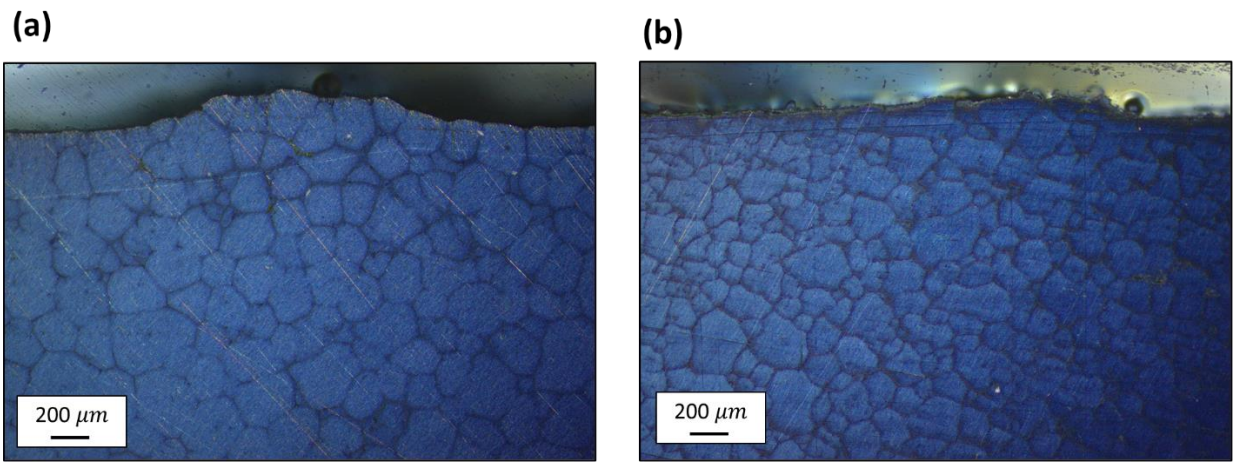

Figure 5 - 55 Post-oxidation grain size of (a) AA7075 and (b) AA7075-1.5TiB_2 nanocomposite after 6 hours at 600 ℃ (under microscope with polarization directly after polishing).

According to **Figure 5 - 54**, the oxygen concentration gradient ratio between AA7075-1.5TiB_2 and pure AA7075 is $(\frac{\partial C_O}{\partial x})_{NP}/(\frac{\partial C_O}{\partial x})_{pure}$ ≈1.07. Thus, the average oxygen depletion depth ratio between AA7075-1.5TiB_2 and pure AA7075 would be ~0.84. It suggests that oxygen could not be prevented from reacting with Zn by Al_2O_3 film. Therefore, the oxidation process would be

different in AA7075-1.5TiB_2 than in AA7075 under the high temperature (see **Figure 5 - 47**b). This newly discovered mechanism related to the interaction between the pre-formed Al_2O_3 oxide layer and related element diffusion is illustrated in **Figure 5 - 57**. The proposed model could be further proved by **Figure 5 - 56**, and the clear inward oxygen diffusion across the Al_2O_3 layer to oxidize Zn can be observed in **Figure 5 - 56**.

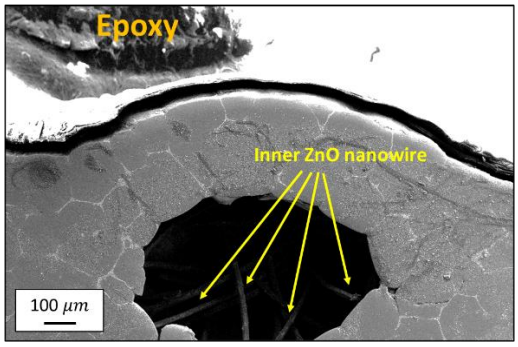

Figure 5 - 56 Cross-section morphology of AA7075-1.5TiB_2 after 3-hour thermal oxidation at 600 ℃ (without being pre-heated at 400°C for 5 mins)

To further validate our theory, the isothermal oxidation at 600 ℃ for 6 hours has been conducted and summarized in **Figure 5 - 58** and **Figure 5 - 59**. Clearly, with the prolonged 6-hour thermal oxidation time, Zn is continuously consumed, so the Zn concentration gradient (as well as the O concentration gradient) will be less steep than the 3-hour oxidation, which also indicates a diffusion-controlled nature in Zn oxidation. By considering the concentration gradient after 6 hours, the corresponding oxygen penetration depth ratio between AA7075-1.5TiB_2 and pure AA7075 is calculated to be ~1.25. After plotting and comparing the theoretical and experimental values, the theory matches the experimental observation.

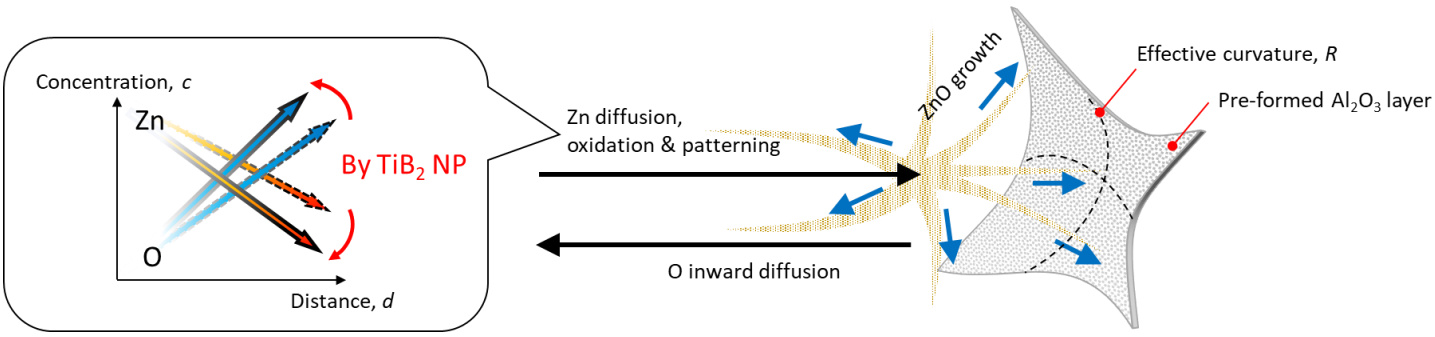

Figure 5 - 57 Illustration of the oxidation process in **Figure 5 - 50**d: the interaction of pre-formed Al oxide film and Zn oxidation above the solutionizing temperature.

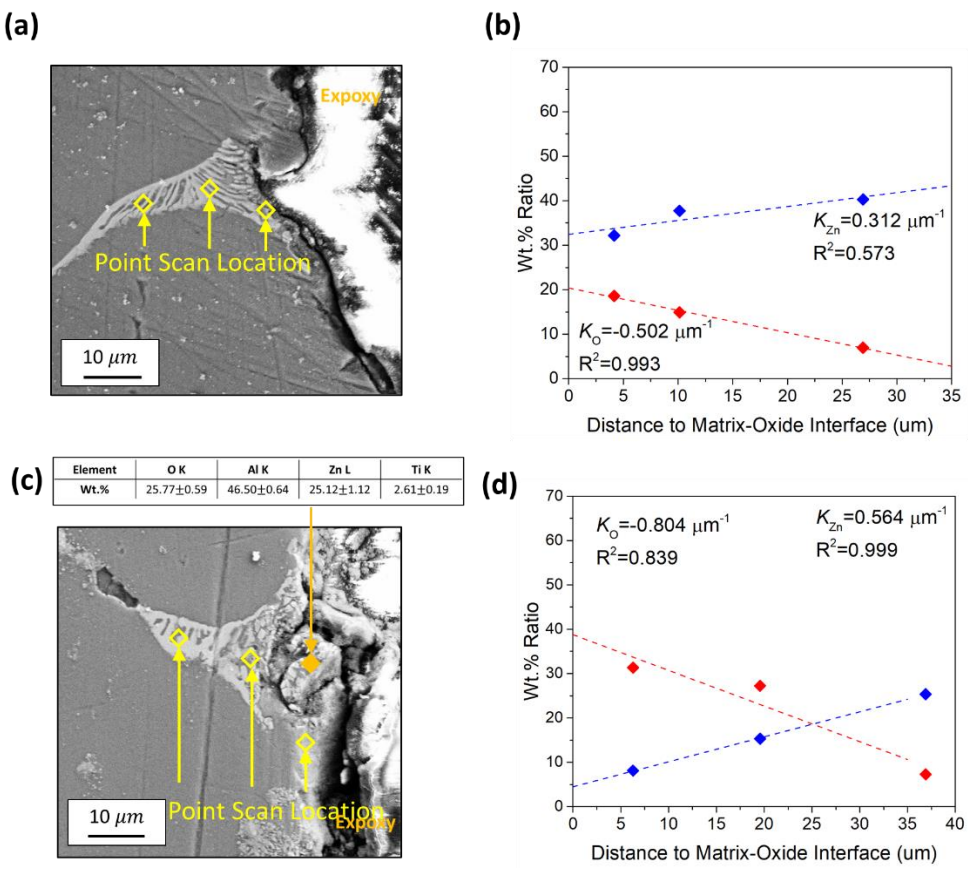

Figure 5 - 58 Oxidation-induced and oxide layer growth-driving element concentration gradient along the diffusion path within the secondary phase after 6-hour thermal oxidation at 600 ℃ for (a) pure AA7075 by EDS point-scanning in (b) and (c) AA7075-1.5TiB_2 by EDS point-scanning in (d).

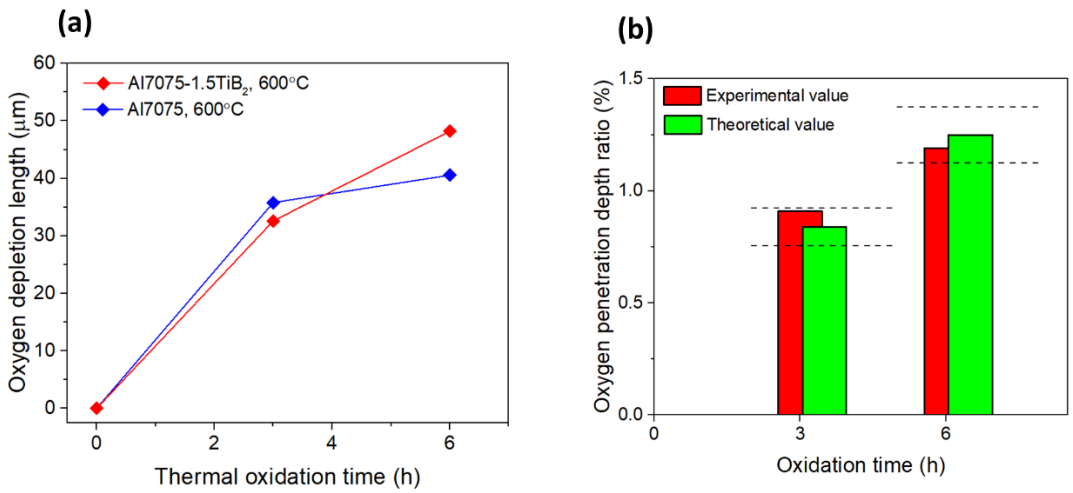

Figure 5 - 59 (a) Oxygen depletion depth of AA7075 and AA7075-1.5TiB_2 nanocomposite at 600 ℃ by oxygen concentration gradient in **Figure 5 - 54** and **Figure 5 - 58**; (b) The comparison between the experimental and theoretical values.

At this point, the role of TiB_2 nanoparticles in the thermal oxidation of AA7075-1.5TiB_2 alloys becomes clear: First, the element (Zn) concentration gradient is increasing, because the TiB_2 nanoparticles block the diffusion path (see **Figure 5 - 50**); at the same time, the oxide layer rupturing and grain refining from TiB_2 tune the thermal oxidation morphology (with curvatures) to balance the oxidation driving force from Al_2O_3 and change the Zn oxidation patterning (see **Figure 5 - 57**).

Summary: There is a strong interaction between TiB_2 nanoparticles and oxide formation during the oxidation of AA7075 nanocomposites: At a lower temperature (e.g., 400 ℃), the TiB_2 nanoparticle will rupture the self-limiting Al_2O_3 film to tune the oxidation speed [298]. When the temperature is above the solutionizing temperature (e.g., 600℃) of the $MgZn_2$ secondary phases, TiB_2 nanoparticles will help increase the element (Zn and O) concentration gradient, while reducing the roughness of the wavy Al_2O_3 film due to much-refined grains. The nanoparticles

generate a different oxide surface pattern and change the inward oxidation penetration depth in AA7075-TiB_2. Generally speaking, Zn can be oxidized to a large depth in AA7075 and AA7075-TiB_2 even after the Al_2O_3 oxide film is formed. The TiB_2 nanoparticles can dynamically regulate the whole process by controlling the Zn oxidation rate. Considering the large oxygen penetration depth along the Zn-rich phase and the oxidation control from TiB_2, this understanding would be of significance for the processing AA7075 and its nanocomposites under high temperature or high temperature gradient.

5.2.6 Corrosion performance of cast AA7075/TiC and AA7075/TiB_2 nanocomposite

Microstructure and Mechanical Properties: Previous studies have shown that grain size is important to determining the corrosion performance in an alloy: the smaller the grain size, the more resistant to corrosion. As shown in **Figure 5 - 60**, with the incorporation of TiC and TiB_2 nanoparticles, the grain size of Al will be greatly refined while TiC is more effective than TiB_2.

Besides, grain boundaries (GBs) are serving as the preferential path for diffusion-related phenomena, and are vulnerable to corrosion, when high-angle GBs (HAGBs) are dominating. Knowing this, when looking into the grain boundary misorientation of the same scanning area by EBSD, it clearly shows that the incorporation of nanoparticles (TiC and TiB_2) could both promote the formation of low-angle GBs (LAGBs). We should note that the LAGB ratio in AA7075-1.5 vol.% TiB_2 (cast, T6) is slightly lower than pure AA7075 (cast, T6), and the average GB misorientation is similar, because the TiB_2 nanoparticles have the coherent interface with Al of Al(11-1)//TiB_2 (0001) (planes) and Al[011]//TiB_2 [11–20] (direction). [302] The misorientation angle between crystal planes of (11-1) interfaced with the same TiB_2 (0001) could have stable GB angles

of ~45°. This means the GB misorientation in AA7075-1.5 vol.% TiB_2 (cast, T6) could still have a more stable configuration than AA7075 (cast, T6).

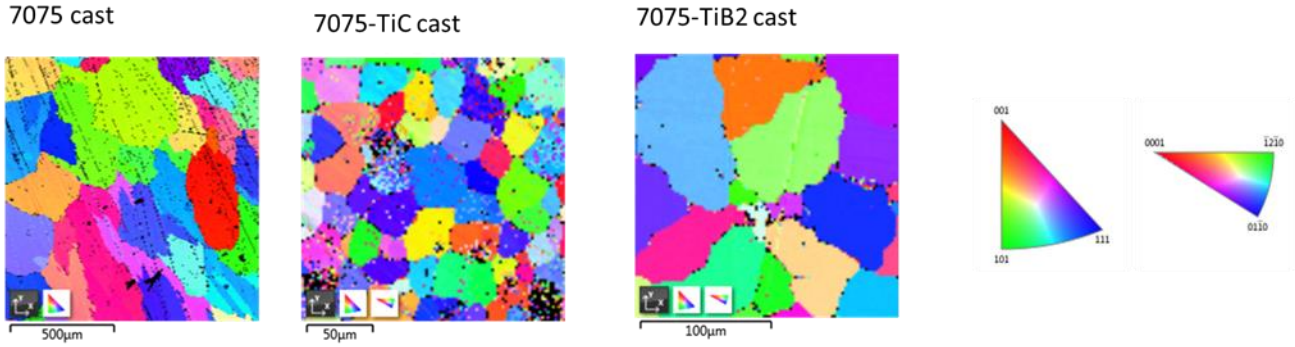

Figure 5 - 60 IPF figures and grain size distribution of **(a)** AA7075 (cast, T6), **(b)** AA7075-1.5 vol.% TiC (cast, T6), and **(c)** AA7075-1.5 vol.% TiB_2 (cast, T6). (the thick dark lines indicate the HAGBs)

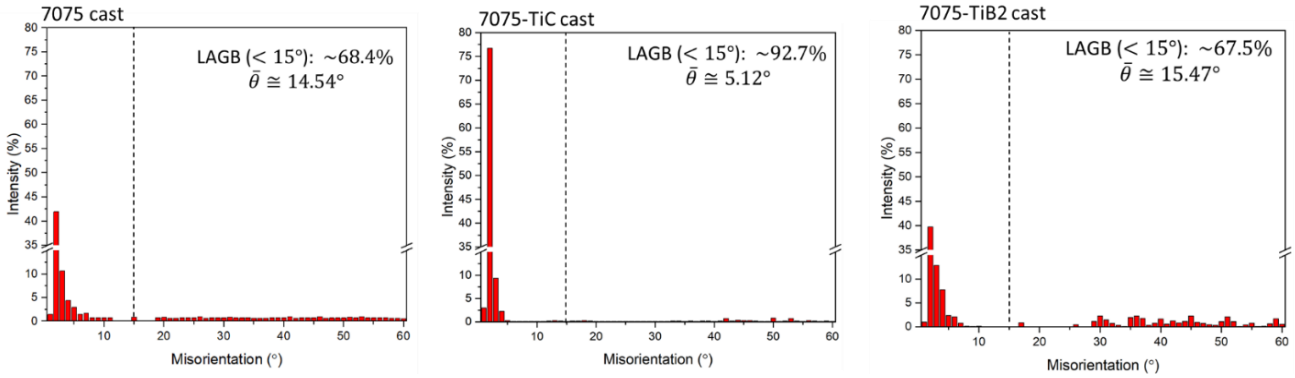

Figure 5 - 61 Grain boundary misorientation distribution (as well as the LAGB ratio and the average GB angles) of **(a)** AA7075 (cast, T6), **(b)** AA7075-1.5 vol.% TiC (cast, T6), and **(c)** AA7075-1.5 vol.% TiB_2 (cast, T6).

In addition to grain and GB characteristics, the sub-feature of PFZ zones could also potentially determine the corrosion degradation, because the drastic composition change exists in the PFZs. As shown in **Figure 5 - 62**, the PFZs in AA7075-1.5 vol.% TiB_2 (cast, T6) and AA7075-1.5 vol.% TiC (cast, T6) (37 nm and 26 nm, respectively) are narrower than that in AA7075 (cast,

T6), with a width of 58 nm, which acts favorably to an enhanced corrosion resistance in nanocomposites.

Moreover, **Figure 3 - 18** shows that the incorporation of TiB_2 and TiC nanoparticles could offer a higher hardness and lower electrical conductivity. The reduced electrical conductivity is introduced by the localized electrons at the matrix-nanoparticle interfaces, which could potentially lower the reactivity in corrosionfor an enhanced corrosion resistance in AA7075 nanocomposites (cast, T6).

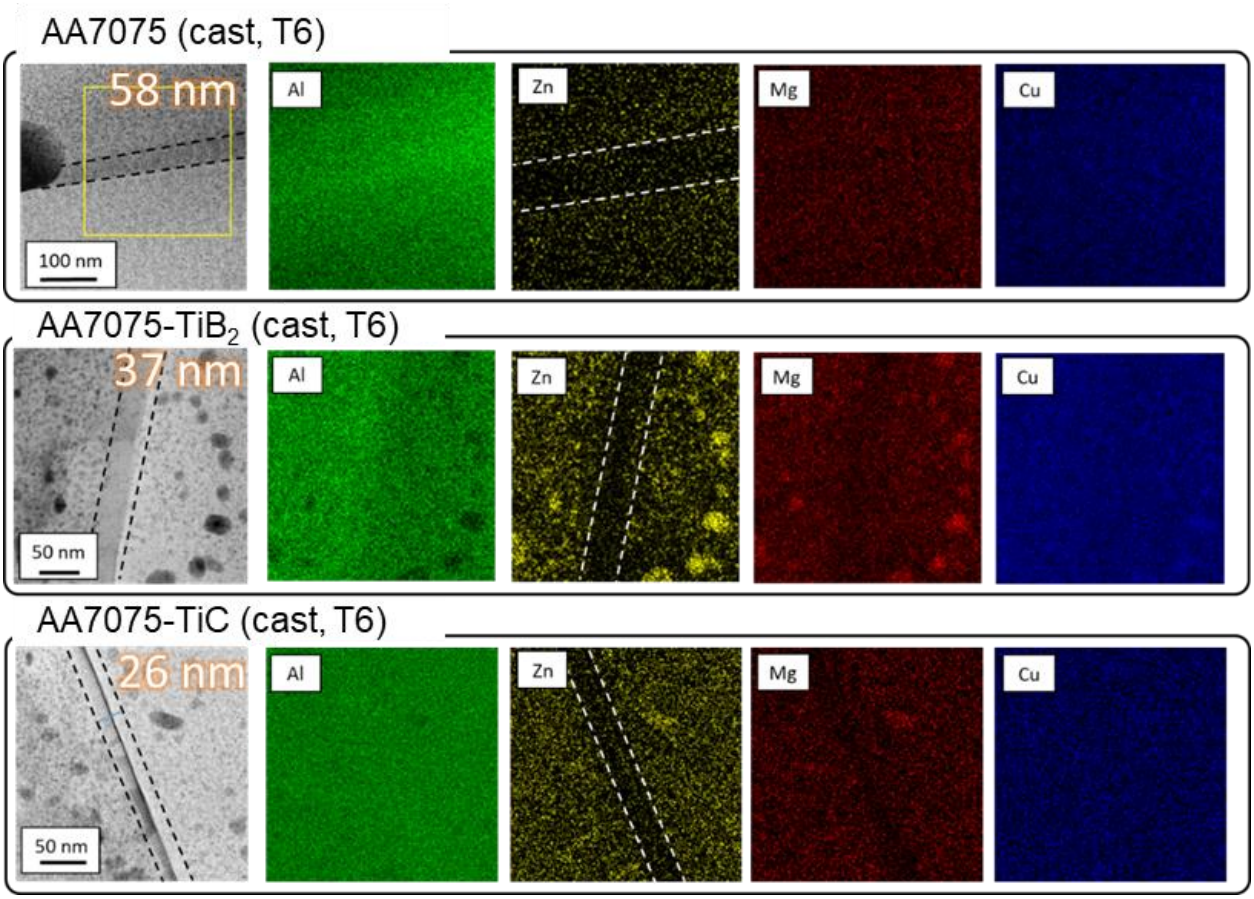

Figure 5 - 62 PFZ width under aberration-corrected HRTEM of AA7075 (cast, T6), AA7075-1.5 vol.% TiC (cast, T6), and AA7075-1.5 vol.% TiB_2 (cast, T6).

Corrosion electrochemistry: As mentioned earlier in the experimental methods, the electrochemical response for AA7075 alloy and nanocomposites (cast, T6) is examined on three different types of surfaces (i.e., fresh, passivated, and immersed and pitted surfaces). Since the pitting and repassivation behavior is easy to be blurred in Al alloy system, this design of measurement could distinguish the influences of different passivation, corrosion, and repassivation.

The potentiodynamic curves are summarized in **Figure 5 - 63**. As shown in **Figure 5 - 63 (a)**, in the fresh surface corrosion experiment, a higher electrochemical potential is gained in both AA7075-1.5 vol.% TiB_2 (cast, T6) and AA7075-1.5 vol.% TiC (cast, T6), which suggests that the incorporation of nanoparticles makes the alloy system intrinsically nobler. **Figure 5 - 63 (b)** shows the V-I curve for cast AA7075 alloy (T6) with the oxide layer-passivated surface. It suggests that, during the cyclic tests, only AA7075-1.5 vol.% TiB_2 (cast, T6) and AA7075-1.5 vol.% TiC (cast, T6) have effective repassivation with a clear intersected point as the repassivation potential. Further examing the corrosion on cast AA7075 alloys (T6) with the immersed and then pitted surface in **Figure 5 - 63 (c)**, the pre-existent pitting surfaces suppress the repassivation behavior in AA7075-1.5 vol.% TiB_2 (cast, T6) and AA7075-1.5 vol.% TiC (cast, T6) and distinguishes the process with those on fresh and oxide layer-passivated surfaces.

Comparing the electrochemical characteristics and quantifying the process with the corrosion models from the later **Figure 5 - 83**, the corrosion impedance and the corresponding Nyquist and Bode plots are plotted in **Figure 5 - 64**, and the corresponding electrochemical parameters are summarized in **Table 5 - 6**. As shown in **Figure 5 - 64 (a)** and **(b)**, the impedance loops of AA7075-1.5 vol.% TiB_2 (cast, T6) and AA7075-1.5 vol.% TiC (cast, T6) on passivated and immersed surfaces are larger than AA7075 (cast, T6), which indicates a higher corrosion resistance. Considering the larger oxide layer resistance (R_o) and polarization resistance (R_p) from

Table 5 - 6, it suggests that the better corrosion resistance on the passivated surface of AA7075 nanocomposites (cast, T6) is mainly due to a more resistant oxide layer. Based on the recommended standard EIS fitting for aluminum alloy and its composites,[303] the larger polarization resistance R_p in the AA7075-TiB_2/-TiC (cast, T6) could be mainly due to the lower electrical conductivity in its cast nanocomposites (**Figure 3 - 18**), and the AA7075 matrix-nanoparticle interface will add up the polarization capacitance (C_p) due to the interfacial electron localization.[2,189]

Meanwhile, comparing the phase angle in **Figure 5 - 64 (c)** and **(d)**, transitioning from fully passivated surface to immersion-induced pitted surface, the phase angle peak of AA7075-1.5 vol.% TiB_2 (cast, T6) and AA7075-1.5 vol.% TiC (cast, T6) did not change; however, the phase angle peak of AA7075 (cast, T6) shifts from ~100 Hz to ~10 Hz, indicating an accelerated pitting process. In this sense, AA7075-1.5 vol.% TiB_2 (cast, T6) and AA7075-1.5 vol.% TiC (cast, T6) after passivation are more stable and resistant to pitting corrosion.

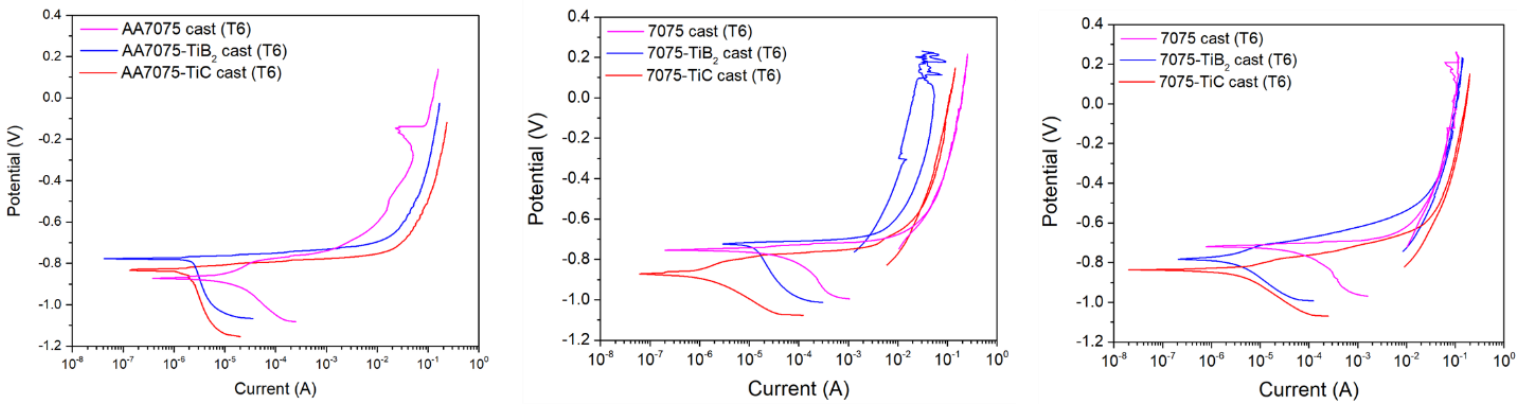

Figure 5 - 63 Potentiodynamic corrosion curve for AA7075 (cast, T6), AA7075-1.5 vol.% TiB_2 (cast, T6), and AA7075-1.5 vol.% TiC (cast, T6) with **(a)** freshly exposed surface, **(b)** passivated surface, and **(c)** immersed surface after passivation.

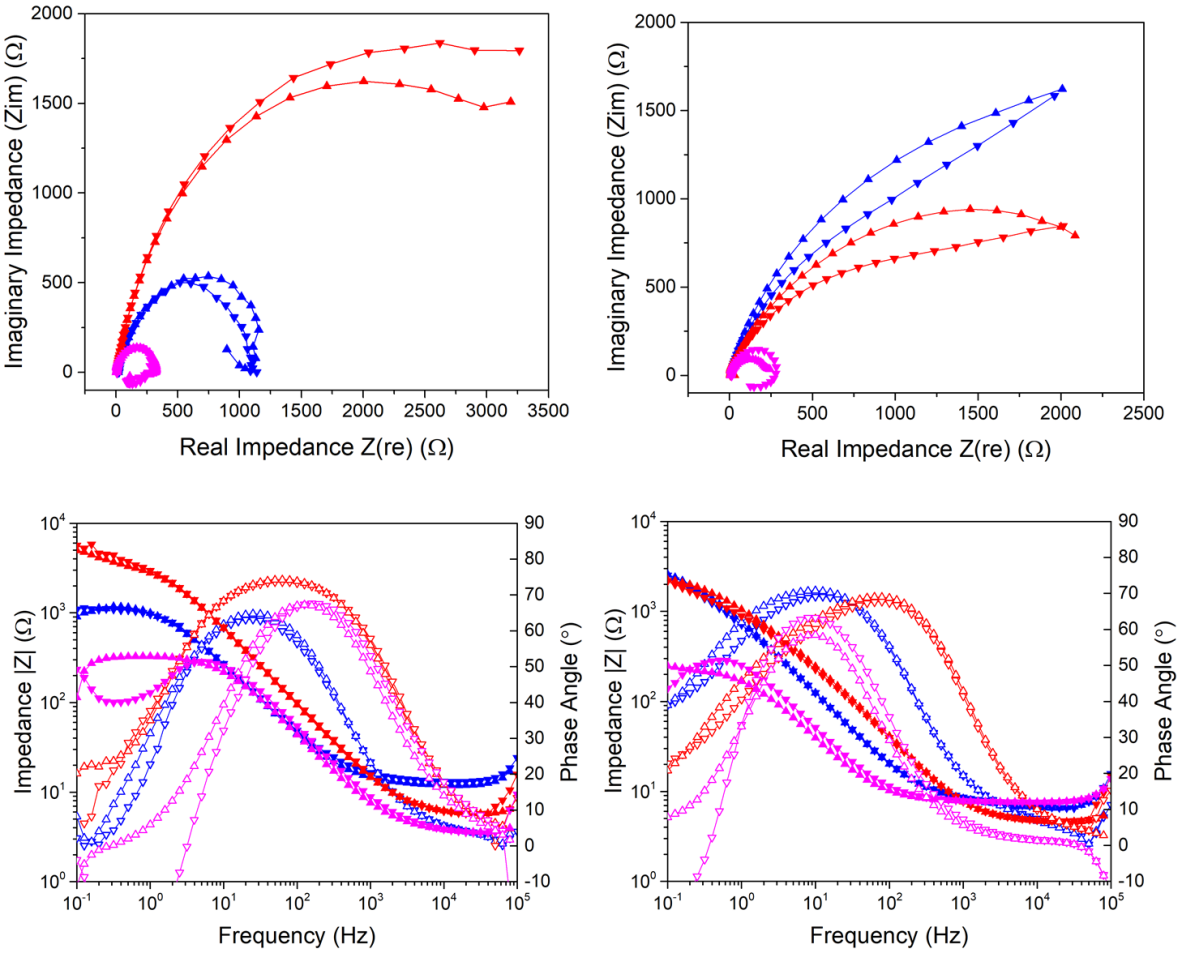

Figure 5 - 64 Comparison of the Nyquist plot and impedance- and phase-frequency figures for AA7075 (cast, T6), AA7075-1.5 vol.% TiB_2 (cast, T6), and AA7075-1.5 vol.% TiC (cast, T6) with **(a)** and **(c)** passivated surface, and **(b)** and **(d)** immersed surface after passivation.

Table 5 - 6 Fitted electrochemical impedance parameters for AA7075 (T6), AA7075-1.5 vol.% TiB_2 (T6), and AA7075-1.5 vol.% TiC (T6) (with a homogeneous passivation oxide layer)

	AA7075 (cast, T6)	**AA7075-1.5 vol.% TiB_2 (cast, T6)**	**AA7075-1.5 vol.% TiC (cast, T6)**
R_s **(Ω)**	4.352	13.95	6.231
R_p **(Ω)**	289.4	832	2610
C_{dl} **(μF)**	49.919	59.59	22.12
R_o **(Ω)**	15.72	29.34	39.73
C_o **(μF)**	65.335	51.42	25.93

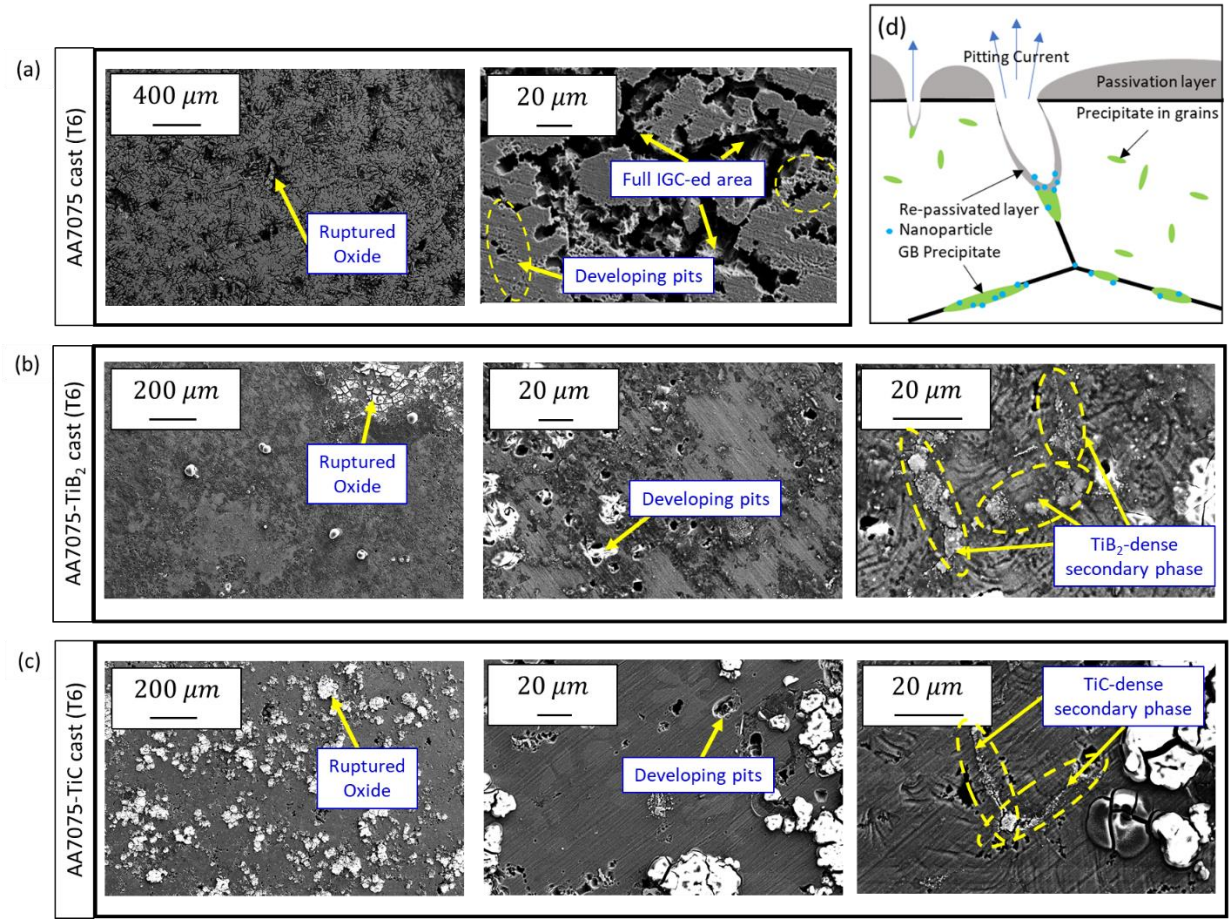

Figure 5 - 65 Surface morphology after corrosion electrochemical measurement on passivated surface in **(a)** AA7075 (cast, T6), **(b)** AA7075-1.5 vol.% TiB_2 (cast, T6), and **(c)** AA7075-1.5 vol.% TiC (cast, T6).

IGC Susceptibility Another important corrosion failure in AA7075 alloys and nanocomposites is intergranular corrosion (IGC). It stems from the initiation and penetration of pitting corrosion, and creates drastic damage to the materials' integrity, as it propagates along the weakened GBs and GBPs [304] as well as the electrochemically different precipitate particles inside grains, as shown in **Figure 5 - 65** (d) [305].

The IGC susceptibility of AA7075 alloys and nanocomposites (cast, T6) is summarized in **Figure 5 - 66**. The shorter IGC penetration depth and the fully protected IGC path by oxides in AA7075-1.5 vol.% TiC (cast, T6) and AA7075-1.5 vol.% TiB_2 (cast, T6) confirms the beneficial role of nano-reinforcements in enhancing (re-)passivation capacity. The relatively intact secondary phases along the grain boundaries in **Figure 5 - 65** also proves the enhanced IGC resistance in AA7075-1.5 vol.% TiB_2 (cast, T6) and AA7075-1.5 vol.% TiC (cast, T6). The possible strengthening mechanism is associated with a more stable and nobler GBPs by nanoparticles that mitigate the localized possibilities in GBP-adjacent areas, as shown in **Figure 5 - 65** (d). Further comparison with A206 alloy and mechanistic illustration will be discussed in section **5.2.8**.

Further characterization of the surface oxidation states of Al by XPS after the IGC immersion tests (see **Figure 5 - 68**) confirms that the oxide protection of AA7075-1.5 vol.% TiC (cast, T6) and AA7075-1.5 vol.% TiB_2 (cast, T6) is more efficient. First, AA7075-1.5 vol.% TiC (cast, T6) and AA7075-1.5 vol.% TiB_2 (cast, T6) both expose less metallic Al, which will mitigate the corrosion and IGC speed. Second, AA7075-1.5 vol.% TiC (cast, T6) and AA7075-1.5 vol.% TiB_2 (cast, T6) both have higher hydroxide contents, which could serve as an effective pH buffer to suppress the drastic pitting-initiation environments [306].

Generally speaking, based on the results in **Figure 5 - 63 (b)**, **Figure 5 - 64**-**Figure 5 - 66**, and **Table 5 - 6**, it suggests that the better corrosion resistance in AA7075 (cast, T6) with TiC and TiB_2 nanoparticles is closely related to and effectively promoted by the modified oxidation behavior. As the previous study shows that nanoparticles could introduce oxidation behavior more easily under the room temperature,[298] the better protection from the oxide layer is the reason for the enhanced anti-corrosion performance in AA7075 (cast, T6) nanocomposite systems.

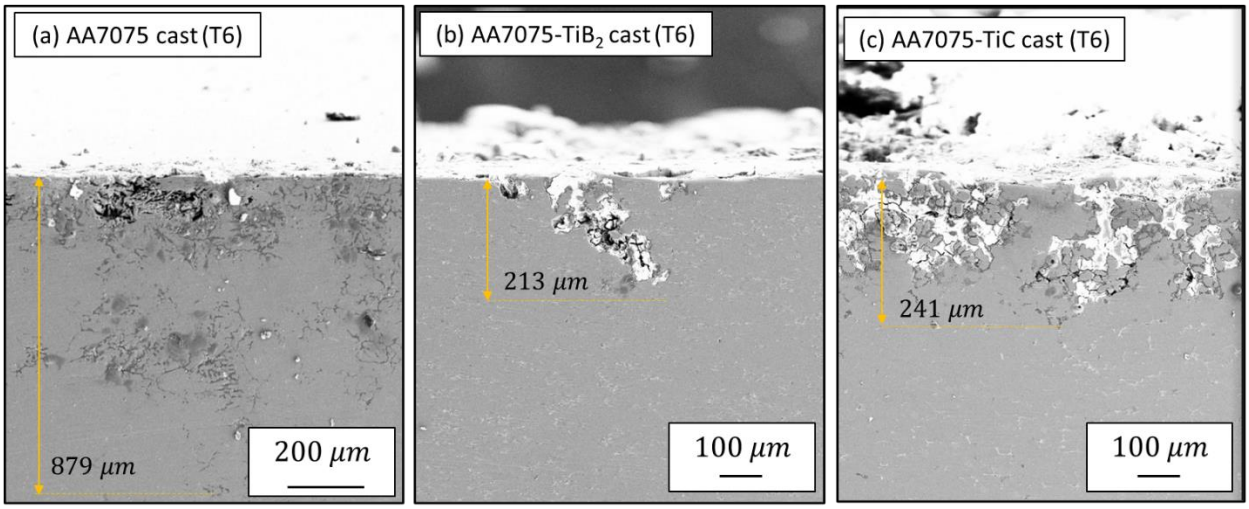

Figure 5 - 66 IGC-susceptibility measurement of **(a)** AA7076 (cast, T6), **(b)** AA7075-1.5 vol.% TiB_2 (cast, T6), and **(c)** AA7075-1.5 vol.% TiC (cast, T6).

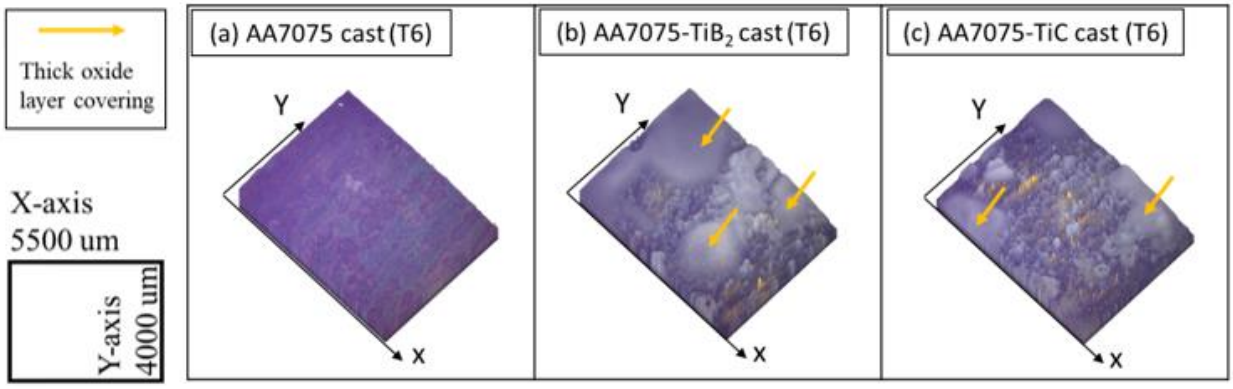

Figure 5 - 67 Microscopy and pseudo-3D imaging of **(a)** AA7076 (cast, T6), **(b)** AA7075-1.5 vol.% TiB_2 (cast, T6), and **(c)** AA7075-1.5 vol.% TiC (cast, T6).

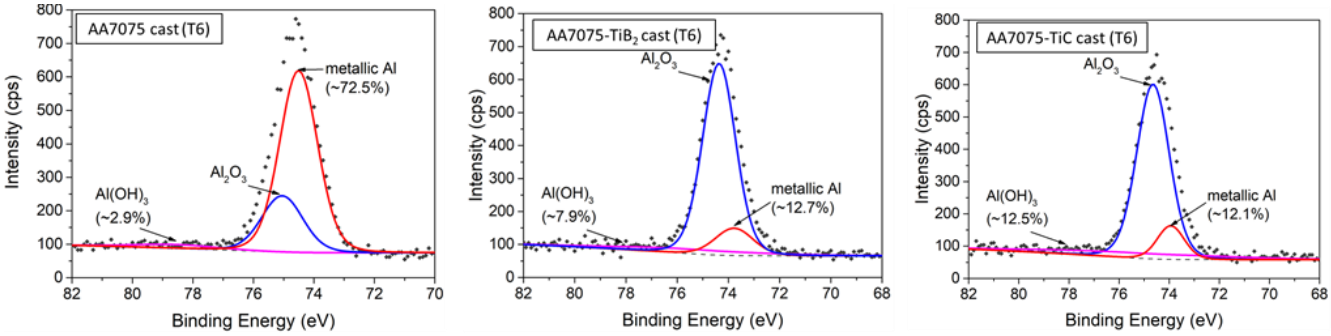

Figure 5 - 68 XPS results for Al 2s peak of **(a)** AA7076 (cast, T6), **(b)** AA7075-1.5 vol.% TiB_2 (cast, T6), **(c)** AA7075-1.5 vol.% TiC (cast, T6)

Stress Corrosion Cracking After examing the corrosion behavior of the cast AA7075 and its nanocomposites, the stress corrosion cracking behavior was studied by a double cantilever beam setup, as shown in **Figure 5 - 2**.

The results are summarized in **Figure 5 - 69**. The general trend of SCC in cast AA7075 systems indicates that, with the incorporation of TiC and TiB_2, the critical stress intensity for crack propagation in SCC is enhanced (3.59 $MPa \cdot m^{0.5}$ for AA7075-1.5 vol.% TiC and 7.06 $MPa \cdot m^{0.5}$ for AA7075-1.5 vol.% TiB_2, whereas the pure cast AA7075 could only have a critical stress intensity of 1.84 $MPa \cdot m^{0.5}$).

For lower stress intensity range (<10-15 $MPa \cdot m^{0.5}$), the benefits of TiC and TiB_2 nanoparticles for SCC could come from the enhanced chemical stability in corrosive media and the more rapid passivation/oxidation, which is consistent with the experimental observation in **Figure 5 - 65**-**Figure 5 - 68**.

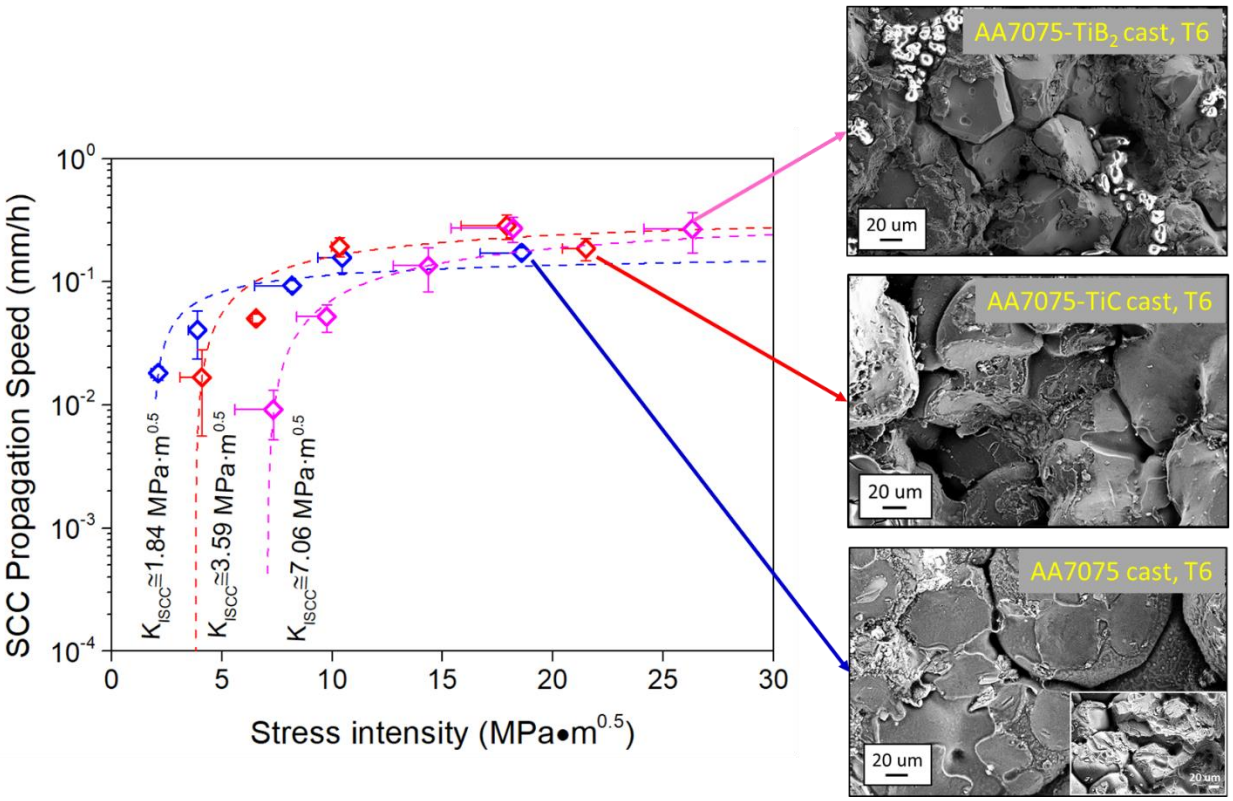

Figure 5 - 69 SCC crack propagation speed and the near-the-crack-tip fracture morphology of AA7075 (cast, T6), AA7075-1.5 vol.% TiB_2 (cast, T6), and AA7075-1.5 vol.% TiC (cast, T6) in 3.5 wt.% NaCl solution.

When the stress intensity goes higher (>15 $MPa \cdot m^{0.5}$), the incorporation of TiC and TiB_2 will only offer a comparable SCC crack propagation speed. The less significant SCC-mitigation than in the lower stress intensity range is possibly due to the fact that the crack under this stress intensity range is determined by both electrochemical and mechanical factors. At this range, the mitigation of SCC propagation requires more strength and ductility in GBs to withhold the crack initiation from stress accumulation. Besides, if the stress intensity is high, after the passivation and oxidation occur, the oxide will also easily grow near the stress-accumulated sites, and adversely contributes to a quicker crack growth (see the inserted SEM images for the crack-tip in **Figure 5 -**

69). The crack-tip morphology is consistent with the previous study on AA7075 systems by various cast procedures[307].

Supplementary Comparison for Stress Corrosion Cracking The previous results in **Figure 5 - 69** for cast AA7075 and AA7075 nanocomposites with TiC and TiB_2 in T6 heat treatment confirm the beneficial role of adding nanoparticles in the low stress intensity range, and the post-SCC cracking tip under high stress intensity possibly shows a mechanics-dominated feature by the reduced ductility near the grain boundaries. Therefore, rationally designing the nanoparticles volume percentage (to a lower value) could be helpful to mitigate SCC behavior under high stress intensity range.

Besides, in the practical applications, SCC-insensitive T73 heat treatment(i.e., solutionizing at 460 ℃ for 1 h and 475 ℃ for 2 h, water quenching at room temperature, aging at 120 ℃ for 24 h, and then aging at 160 ℃ for 18 h) [308] will be used for AA7075 alloys. The anti-SCC performance in AA7075 nanocomposites under T73 with less nanoparticles was studied as shown in **Figure 5 - 70**.

Figure 5 - 70 (a) shows the SCC performance in AA7075, AA7075-0.75 vol.% TiC, and AA7075-0.75 vol.% TiB_2 after T73 heat treatment. It shows that the benefits of TiC and TiB_2 nanoparticles at low stress intensity have been maintained, while in the high stress intensity range the SCC propagation speed slows to be very close to that of pure AA7075 (T73). The result is consistent with that under T6 heat treatment.

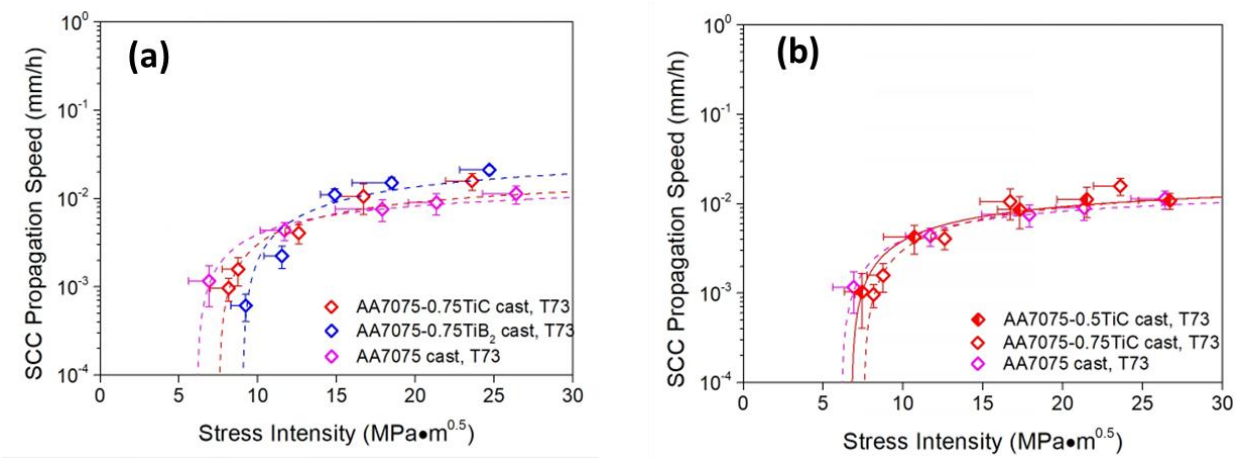

Figure 5 - 70 SCC crack propagation speed of (a) AA7075 (cast, T73), AA7075-0.75 vol.% TiB_2 (cast, T73), and AA7075-0.75 vol.% TiC (cast, T73) in 3.5 wt.% NaCl solution and (b) AA7075 (cast, T73), AA7075-0.75 vol.% TiC (cast, T73), and AA7075-0.5 vol.% TiC (cast, T73) in 3.5 wt.% NaCl solution.

Figure 5 - 70 (b) compares SCC performance of AA7075 (T73) with even less TiC nanoparticle volume percentages. It seems that the SCC speed in samples with 0.5 vol.% TiC nanoparticles is only slightly lower that in samples with 0.75 vol.% TiC nanoparticles.

In brief, the SCC result of AA7075 (T73) without TiC nanopaticles and with 0.5 vol.% and 0.75 vol.% TiC nanoparticles still confirms the advantages of less nanoparticles for SCC mitigation at high stress intensity by possibly retarding the embrittlement process and regaining partial ductility via grain boundary modification and segregation,[309–311] but it has a limit. It is reasonable as less nanoparticles will reduce the microstructural modification effects (including PFZs, GB and GBP strengthening, etc.). In addition to the mechanical behavior, the direct interface between nanoparticles and adjacent area would contribute to the SCC propagation both electrochemically and mechanically. As indicated in **Figure 5 - 90**, if treated individually, TiC and TiB_2 have a much higher electrochemical potential than GBs and GBPs, this potential difference could lead to a

selective corrosion of the interface areas [310], even though the nanoparticle-dense GBPs and GBs have the overall strengthening effects against corrosion. In fact, this localized corrosion in an even more microscopic view will interact with the mehanics for cracking tip propagation (e.g., by quick hydrogen generation and oxygen depletion for passivation [95,310]). This could explain why the effects of lowering the volume percentage of inert TiC and TiB_2 could not bypass the SCC propagation limits. More SCC experimental observation of the similar trend will be provided in section **5.2.8**, and more future work is needed as discussed in **Chapter 8**.

5.2.7 Corrosion performance of extruded AA7075/TiC and AA7075/TiB_2 nanocomposite

Though AA7075 (cast, T6) is important for research purpose, AA7075 (extruded, T6) is more popular in various industrial applications. Therefore, how nanoparticles would tune the corrosion performance in AA7075 (extruded, T6) is of great importance for a stable long-term service. Following the abovementioned methods, the corrosion behavior of AA7075 (extruded, T6), AA7075-1.5 vol.% TiC (extruded, T6), and AA7075-1.5 vol.% TiB_2 (extruded, T6) is further studied.

Microstructure and Mechanical Properties Similarly, the distribution of nanoparticles in AA7075 (extruded, T6) could be further confirmed by the EBSD scanning in **Figure 5 - 71**. With the band-like structure formed by nanoparticles, the grain size of AA7075-1.5 vol.% TiC (extruded, T6) and AA7075-1.5 vol.% TiB_2 (extruded, T6) shows different features, when compared with the cast AA7075 nanocomposites (T6). Away from the nanoparticle bands, the grains of AA7075-1.5 vol.% TiC (extruded, T6) and AA7075-1.5 vol.% TiB_2 (extruded, T6) are comparable to those in pure AA7075 (extruded, T6). Moreover, pure AA7075 (extruded, T6) exhibits smaller

recrystallized grains inside these large grains, whereas AA7075-1.5 vol.% TiC (extruded, T6) and AA7075-1.5 vol.% TiB_2 (extruded, T6) do not have these features, which indicates nanoparticles could suppress the recrystallization process during hot extrusion by nanoparticles. On the contrast, in the nanoparticle-dense areas, the grain size is much refined in AA7075-1.5 vol.% TiC (extruded, T6) and AA7075-1.5 vol.% TiB_2 (extruded, T6). Generally, the observation will introduce different corrosion response from the cast AA7075.

Furthermore, given the ability to mitigate the recrystallization, the GB angles of AA7075 systems (extruded, T6) show the similar trend as those of cast AA7075 samples (see **Figure 5 - 72**). Both TiC and TiB_2 nanoparticles could introduce a higher concentration of LAGBs, which might be conducive to the anti-corrosion performance for AA7075 (extruded, T6) samples.

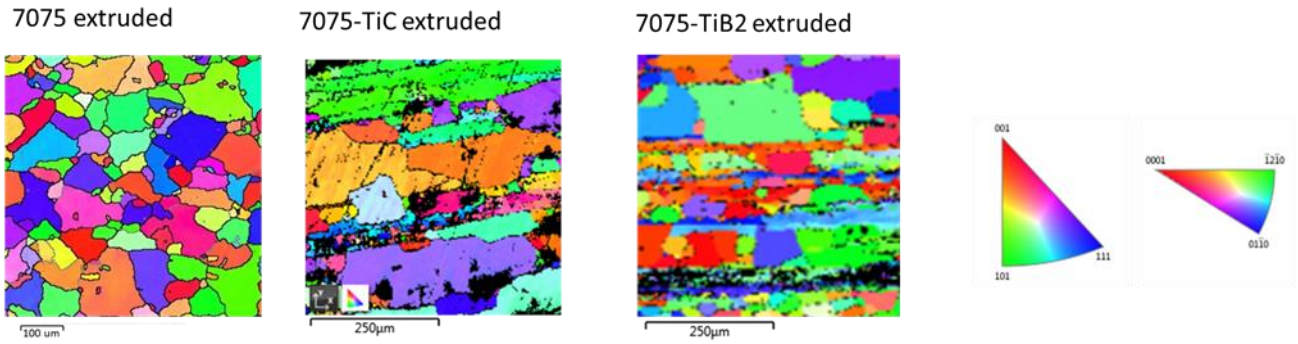

Figure 5 - 71 IPF figures and grain size distribution of **(a)** AA7075 (extruded, T6), **(b)** AA7075-1.5 vol.% TiC (extruded, T6), and **(c)** AA7075-1.5 vol.% TiB_2 (extruded, T6). (the thick dark lines indicate the HAGBs)

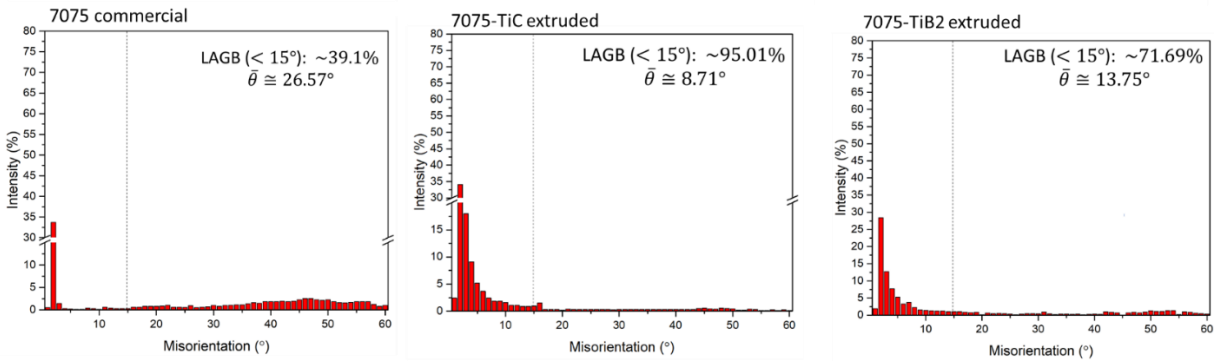

Figure 5 - 72 Grain boundary misorientation distribution (as well as the LAGB ratio and the average GB angles) of **(a)** AA7075 (extruded, T6), **(b)** AA7075-1.5 vol.% TiC (extruded, T6), and **(c)** AA7075-1.5 vol.% TiB_2 (extruded, T6).

Figure 5 - 73 shows the widths of the PFZ in extruded AA7075 (~34 nm), AA7075-1.5 vol.% TiC (~19 nm), and AA7075-1.5 vol.% TiB_2 (~26 nm). Clearly, the PFZ width is smaller in these extruded samples than in the cast ones (compared with **Figure 5 - 62**). The reason for this change is that extrusion process as a deformation processing method could significantly segregate Cu to GBs, reduce the grain boundary energy, and provide the extra Cu near the original PFZ range.[150]

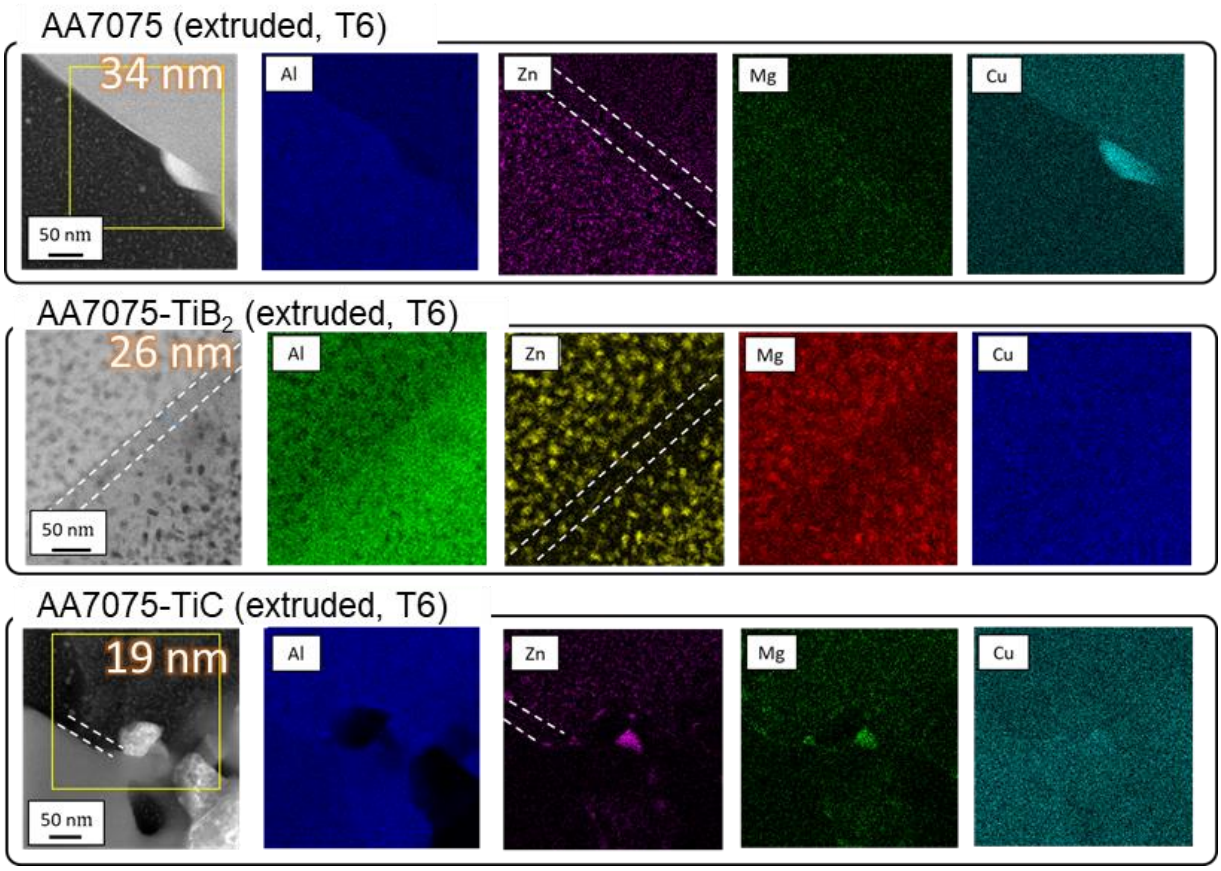

Figure 5 - 73 PFZ width under aberration-corrected HRTEM of AA7075 (extruded, T6), AA7075-1.5 vol.% TiC (extruded, T6), and AA7075-1.5 vol.% TiB_2 (extruded, T6).

Corrosion electrochemistry As shown in **Figure 5 - 74**, the electrochemical responses in extruded AA7075 systems are different from the cast samples. On the fresh exposed surfaces (see **Figure 5 - 74 (a)**), both AA7075-1.5 vol.% TiB_2 (extruded, T6) and AA7075-1.5 vol.% TiC (extruded, T6) have a higher corrosion potential, which indicates a better anti-corrosion performance than AA7075 (extruded, T6) and confirms a consistent trend to their cast counterparts (**Figure 5 - 63 (a)**).

Figure 5 - 74 (b) shows the V-I curve for extruded AA7075 (T6) samples with the oxide layer-passivated surface. Unlike the results of cast AA7075 (T6) samples in **Figure 5 - 63 (b)**, no

effective repassivation is observed in extruded AA7075 (T6) samples at this stage during the cyclic tests. When further examining the post-corrosion surface in **Figure 5 - 76**, it suggests that the main difference is caused by the nanoparticle distribution. **Figure 5 - 76 (b)** and **(c)** shows that the repassivation process in AA7075-1.5 vol.% TiB_2 (extruded, T6) and AA7075-1.5 vol.% TiC (extruded, T6) is largely retarded by the pitting process near the nanoparticle band (even when the corrosion potential still proves a better nobility in these nanocomposites), and the preferential corrosion near the nanoparticle bands expose the corrodible surface more quickly than the oxide re-covering during the cyclic electrochemical tests. The smaller impedance loop in **Figure 5 - 74 (b)** is therefore introduced by this preferential accelerated corrosion and oxide layer consumption.

After introducing the natural pitting on the passivated surface following the process in **Figure 5 - 1**, the corrosion signatures (as shown in **Figure 5 - 74 (c)**) in AA7075-1.5 vol.% TiB_2 (extruded, T6) and AA7075-1.5 vol.% TiC (extruded, T6) have shown a huge difference from their cast counterparts. The repassivation behavior is clear with the hysteresis current loop in AA7075-1.5 vol.% TiB_2 (extruded, T6) and AA7075-1.5 vol.% TiC (extruded, T6). In addition, the higher stability enabled by a higher corrosion potential at this state also proves the advantages from nanoparticles by introducing more efficient passivation process.

Considering the results from **Figure 5 - 74 (c)**, the smaller Nyquist impedance loop of AA7075-1.5 vol.% TiB_2 (extruded, T6) and AA7075-1.5 vol.% TiC (extruded, T6) is reasonable: Even though the whole system is nobler after the surface is immersed for 24 h, the rapid continuous (re-)passivation contributes to a larger corrosion current (i.e., chemical current) and a smaller loop. The Nyquist curves showing the no low-frequency tails in **Figure 5 - 75 (b)** also indicate that the corrosion process is mainly dominated by the interface redox electron transfer process. Thus, the

results of **Figure 5 - 74 (c)** and **Figure 5 - 75 (b)** and **(d)** show a different influencing parameter to **Figure 5 - 74 (b)** and **Figure 5 - 75 (a)** and **(c)**.

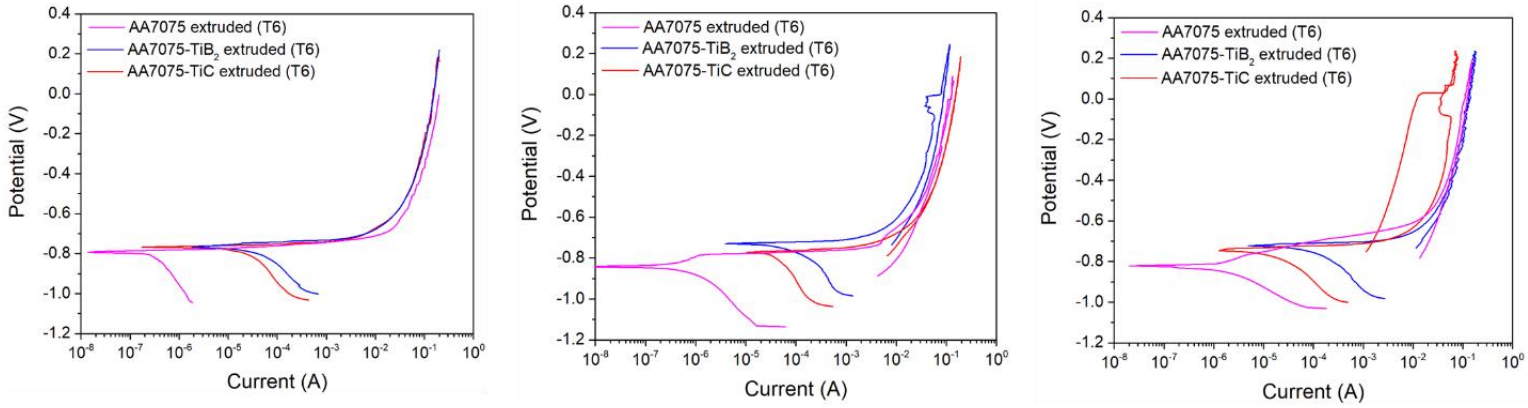

Figure 5 - 74 Potentiodynamic corrosion curve for AA7076 (extruded, T6), AA7075-1.5 vol.% TiB_2 (extruded, T6), and AA7075-1.5 vol.% TiC (extruded, T6) with **(a)** freshly exposed surface, **(b)** passivated surface, and **(c)** immersed surface after passivation.

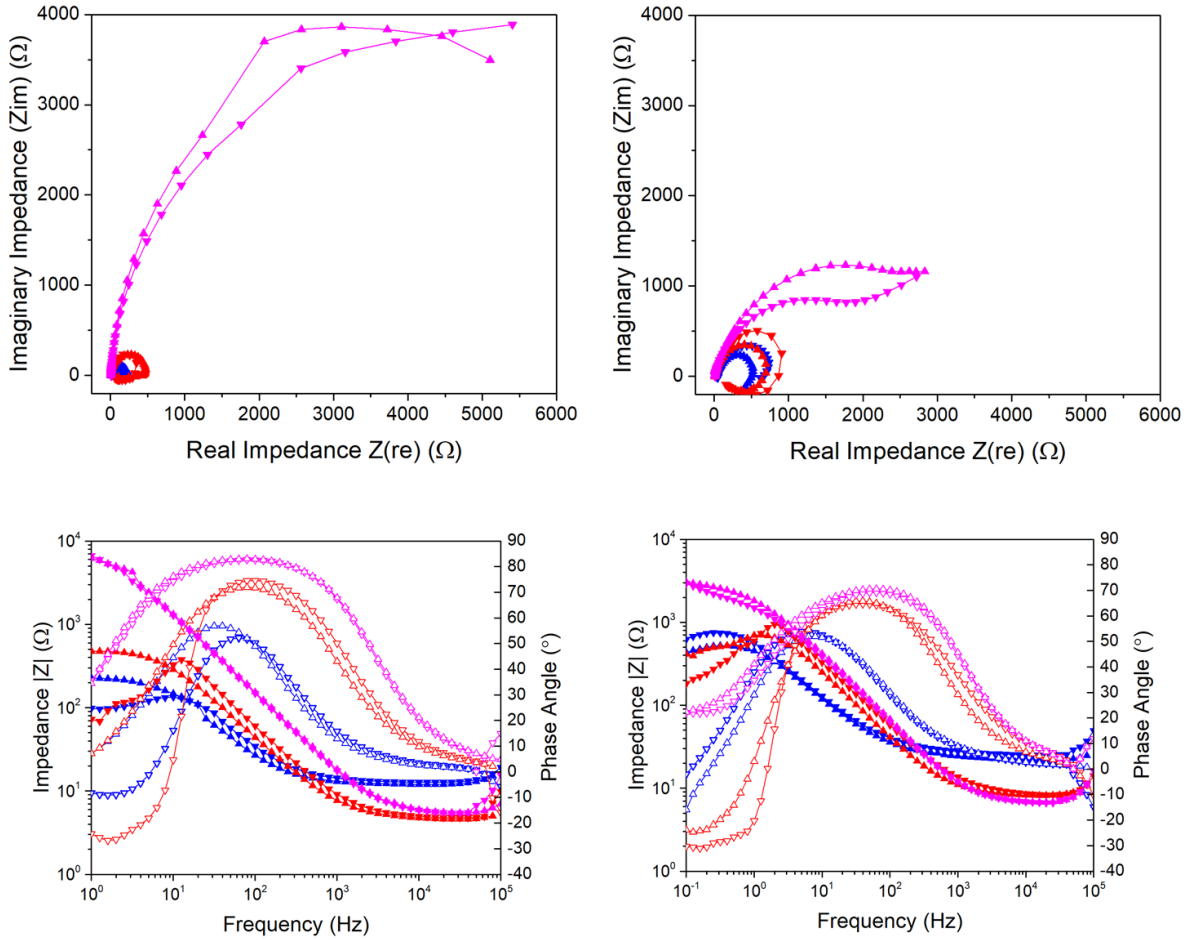

Figure 5 - 75 Comparison of the Nyquist plot and impedance- and phase-frequency figures for AA7075 (extruded, T6), AA7075-1.5 vol.% TiB_2 (extruded, T6), and AA7075-1.5 vol.% TiC (extruded, T6) with **(a)** and **(c)** passivated surface, and **(b)** and **(d)** immersed surface after passivation.

Table 5 - 7 Fitted electrochemical impedance parameters for AA7075 (extruded, T6), AA7075-1.5 vol.% TiB_2 (extruded, T6), and AA7075-1.5 vol.% TiC (extruded, T6) (with a homogeneous passivation oxide layer)

	AA7075 (extruded, T6)	**AA7075-1.5 vol.% TiB_2 (extruded, T6)**	**AA7075-1.5 vol.% TiC (extruded, T6)**
$\boldsymbol{R_s}$ **(Ω)**	5.649	12.41	5.133

R_p (Ω)	7578	193.7	424.3
C_{dl} (μF)	11.454	84.223	42.44
R_o (Ω)	20.61	24.05	27.45
C_o (μF)	44.135	162.35	102.66

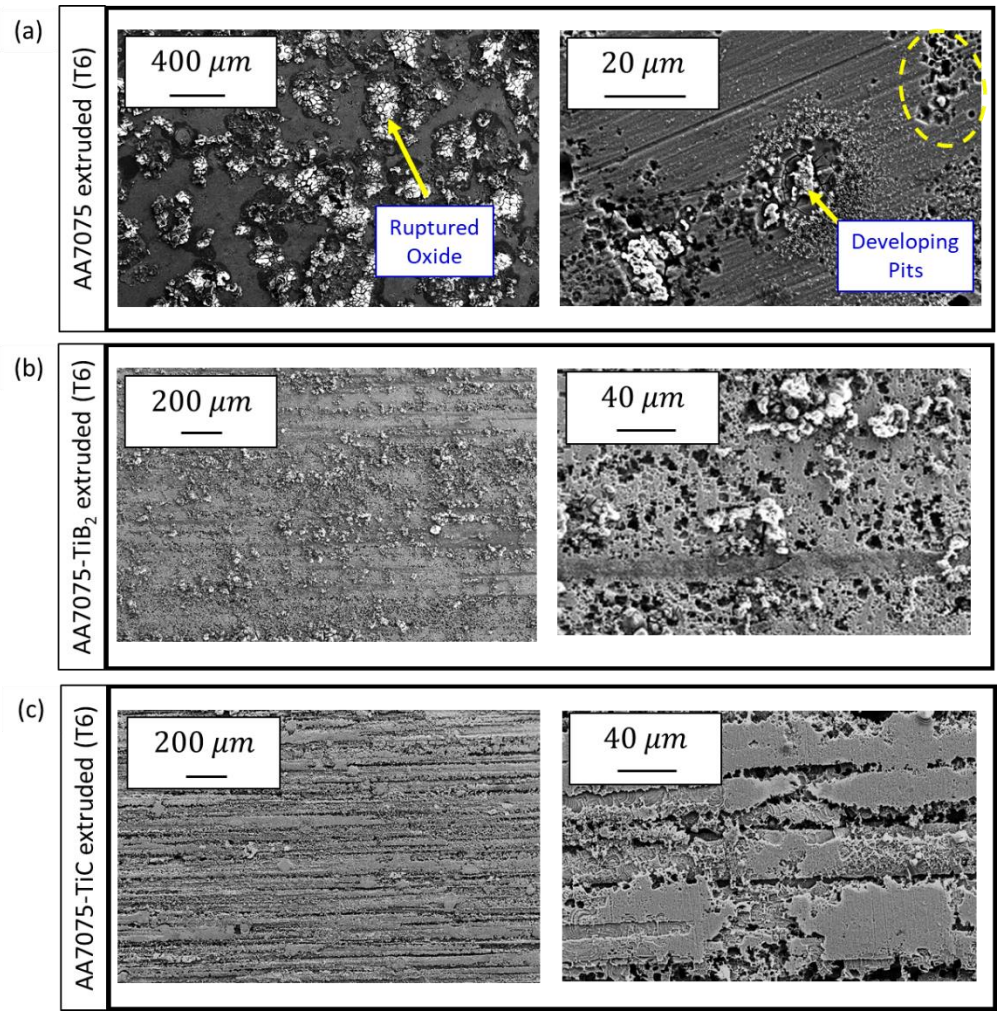

Figure 5 - 76 Surface morphology after corrosion electrochemical measurement on passivated surface in **(a)** AA7076 (extruded, T6), **(b)** AA7075-1.5 vol.% TiB_2 (extruded, T6), and **(c)** AA7075-1.5 vol.% TiC (extruded, T6).

IGC Susceptibility: The IGC-resistance was investigated by the same accelerated corrosion test. As shown in **Figure 5 - 77**, AA7075-1.5 vol.% TiB_2 (extruded, T6) and AA7075-1.5 vol.% TiC (extruded, T6) both have shorter intergranular corrosion cracking traces than that in AA7075 (extruded, T6). Similarly, the clear inner oxidation protection and denser surface corrosion sites are obvious in AA7075-1.5 vol.% TiB_2 (extruded, T6) and AA7075-1.5 vol.% TiC (extruded, T6). This is consistent with our results for cast AA7075: The nanoparticles dispersed in the extruded AA7075 resulted in a quicker corrosion and oxidation with a less sensitive pitting corrosion initiation and evolution at or near the GBs; Due to the more uniform corrosion and less sensitive GBs with oxide covering (see **Figure 5 - 78** and **Figure 5 - 79**), the IGC susceptibility dictated by corrosion penetration is reduced in AA7075-1.5 vol.% TiB_2 (extruded, T6) and AA7075-1.5 vol.% TiC (extruded, T6).

Besides, the difference of the corrosion performance between the cast and extruded AA7075 systems is also illustrated by the surface composition in **Figure 5 - 68** and **Figure 5 - 79**. The nanoparticles in the extruded AA7075 still contribute to an increased oxidation and passivation behavior. However, the extruded AA7075 nanocomposites have nanoparticle bands, which transform the oxides into hydroxide (indicated by $Al(OH)_3$ content in **Figure 5 - 68** and **Figure 5 - 79**); This transition leads a chemical current and make the apparent impedance by the EIS measurement smaller in AA7075-TiC/-TiB_2 (extruded, T6) (**Figure 5 - 75**). Thus, the band-structure will greatly influence the dissolution equilibrium during the corrosion polarization.

Since the oxidation process is still promoted in extruded samples with nanoparticles, when the $Al(OH)_3$ formation is quicker, it needs a longer time to achieve fully effective passivation under the electrically unbiased condition (e.g., immersion process as shown in **Figure 5 - 1**), which results in a retarded repassivation process (as compared in **Figure 5 - 63 (b)** and **Figure 5 - 74 (c)**).

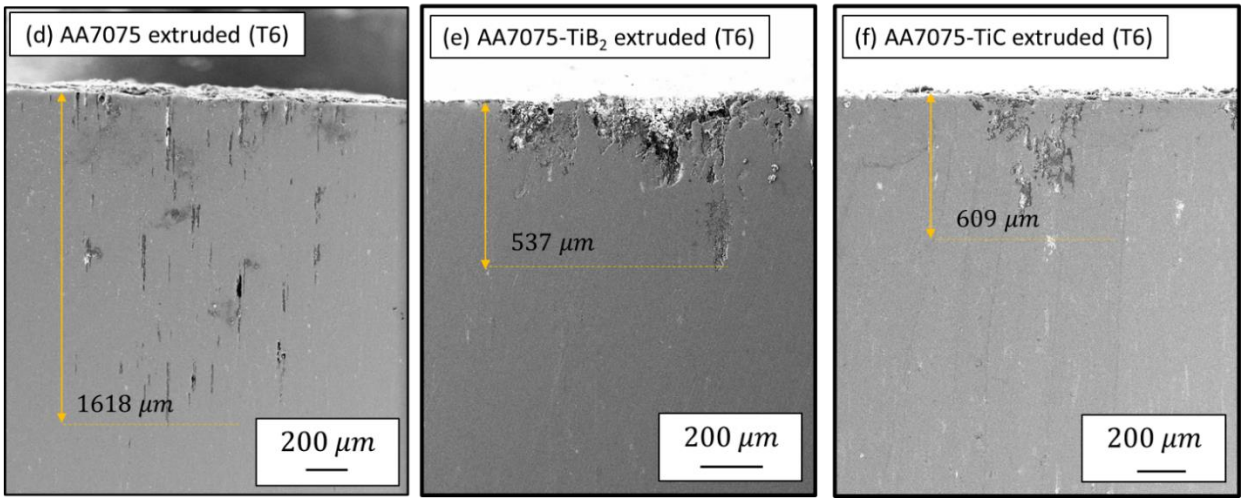

Figure 5 - 77 IGC-susceptibility measurement of **(a)** AA7076 (extruded, T6), **(b)** AA7075-1.5 vol.% TiB_2 (extruded, T6), and **(c)** AA7075-1.5 vol.% TiC (extruded, T6).

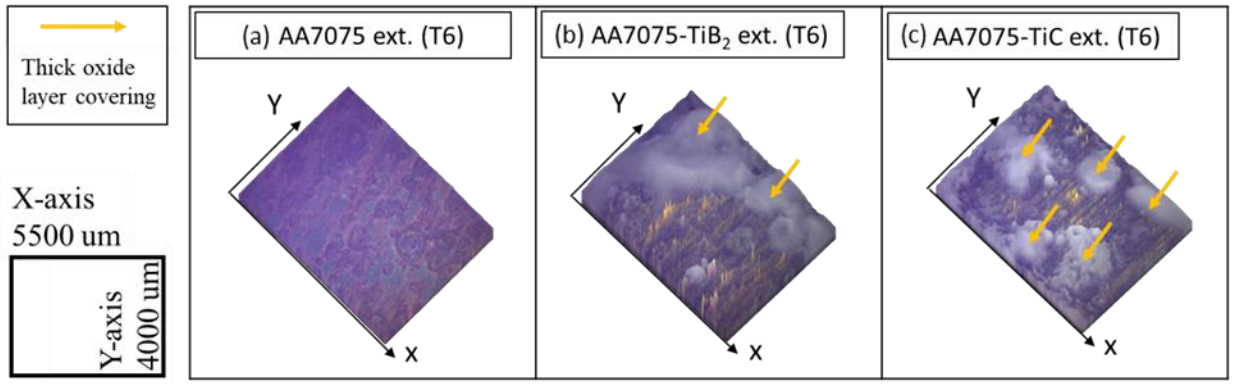

Figure 5 - 78 Microscopy and pseudo-3D imaging of **(a)** AA7076 (extruded, T6), **(b)** AA7075-1.5 vol.% TiB_2 (extruded, T6), and **(c)** AA7075-1.5 vol.% TiC (extruded, T6) to show the thick oxide layer distribution.

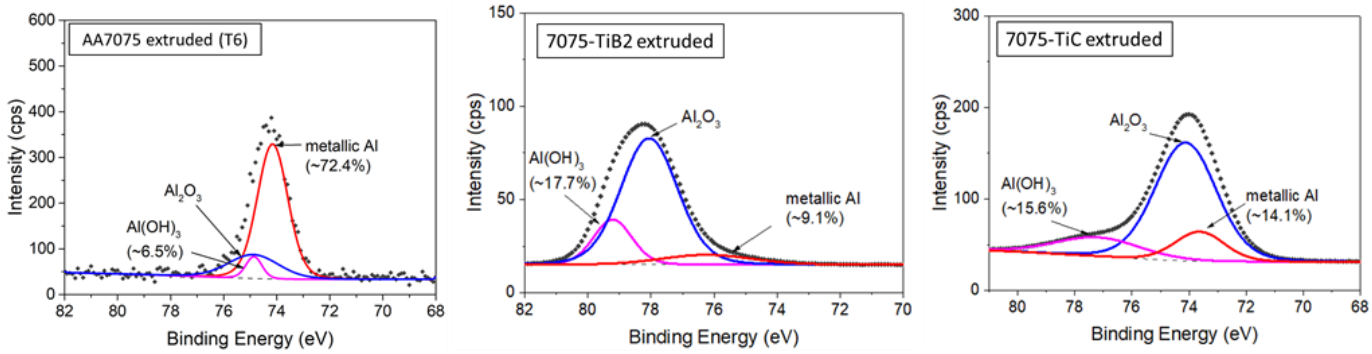

Figure 5 - 79 XPS results for Al 2s peak of **(a)** AA7076 (extruded, T6), **(b)** AA7075-1.5 vol.% TiB_2 (extruded, T6), and **(c)** AA7075-1.5 vol.% TiC (extruded, T6) to show surface oxide layer component ratio after IGC test.

Stress Corrosion Cracking The SCC results of AA7075 (extruded, T6) is summarized in **Figure 5 - 80**. It shows that, with the nanoparticles' incorporation and at the lower stress intensity, the SCC crack propagation speed in AA7075-1.5 vol.% TiC (extruded, T6) and AA7075-1.5 vol.% TiB_2 (extruded, T6) is much slower than AA7075 (extruded, T6). In addition, this leads to a higher SCC-initiating critical stress intensity (K_{ISCC}) in both AA7075-1.5 vol.% TiC (extruded, T6) and AA7075-1.5 vol.% TiB_2 (extruded, T6). At low stress intensity, the SCC could be mainly dominated by the corrosion process, and the effective oxide covering (after a long-term immersion) could mitigate the pitting-induced IGC process, which enhanced SCC resistance.

However, when the stress intensity is larger (>15 MPa·$m^{0.5}$), the SCC propagation speed in AA7075-1.5 vol.% TiC (extruded, T6) and AA7075-1.5 vol.% TiB_2 (extruded, T6) exceeds that of AA7075 (extruded, T6). The main reasons for this transition are due to the band-like nanoparticles and the brittleness by more rapid oxidation. First, as shown in **Figure 3 - 16**, **Figure 3 - 17**, **Figure 5 - 71** and **Figure 5 - 76**, the nanoparticle-dense band has distinctive corrosion morphology, which indicates the dense nanoparticle zones actually deteriorate the general

corrosion resistance and localize the corrosion behavior in the band areas (e.g., carbides are advantageous for the stable interfacial hydrogen entrapment [312,95]). Second, as shown in the fractography, the cracking surface near the tip of AA7075-1.5 vol.% TiC (extruded, T6) and AA7075-1.5 vol.% TiB_2 (extruded, T6) shows more brittle features, where more ductile dimples are observed in AA7075 (extruded, T6). As mentioned for corrosion and IGC behavior, nanoparticles could introduce a quicker passivation by oxides. The formation of oxides could potentially release hydrogen, and the oxide layer in between the grains could add to the brittleness of GBs, which reduce the ductility necessary for cracking mitigation and localize the plasticity under higher stress intensity.

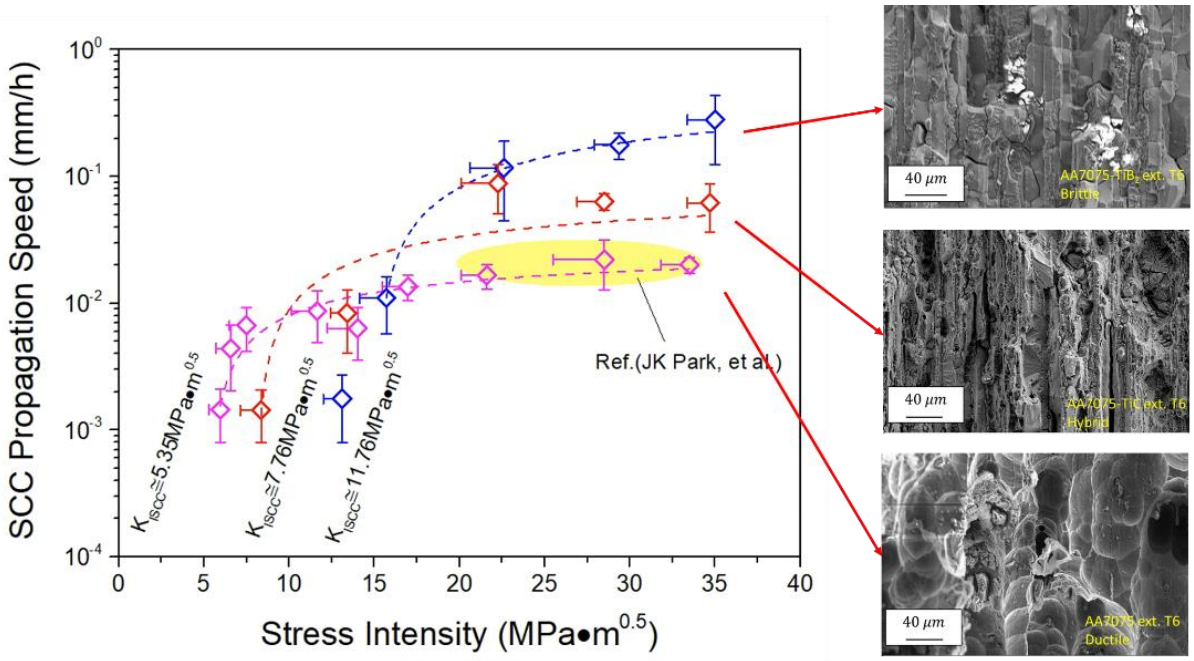

Figure 5 - 80 SCC crack propagation speed and the near-the-crack-tip fracture morphology of AA7075 (extruded, T6), AA7075-1.5 vol.% TiB_2 (extruded, T6), and AA7075-1.5 vol.% TiC (extruded, T6) in 3.5 wt.% NaCl solution.

Generally speaking, for the cast and extruded AA7075 nanocomposites with TiC and TiB_2 nanoparticles:

1) The incorporation of nanoparticles will refine the grains, increase the LAGB fraction, reduce the PFZs, and reduce the electrical conductivity, which is advantageous to anti-corrosion;

2) AA7075 with nanoparticles will introduce a more effective passivation behavior, compared to their pure AA7075 matrix, either TiC or TiB_2 is used;

3) This passivation activity change by nanoparticles will lead to an enhanced anti-corrosion performance, particularly IGC resistance;

4) The distribution of nanoparticles will cause the different electrochemical performance of cast and extruded AA7075 nanocomposites. XPS and surface morphology study confirms the accelerated hydration process of the passivation layer in the extruded AA7075 nanocomposites with the pseudo-dispersed nanoparticle bands.

The results indicate that the incorporation of nanoparticles will introduce different distribution and microstructure in AA7075-TiC (extruded, T6) and AA7075-TiB_2 (extruded, T6) to AA7075-TiC (cast, T6) and AA7075-TiB_2 (cast, T6). The band-like features will heavily interact with the oxide passivation (by changing the oxide hydration process and tuning the electrochemical potential near the nanoparticle-band areas), oxide layer consumption process, and the resultant corrosion behavior. The anti-corrosion behavior of AA7075-TiC (extruded, T6) and AA7075-TiB_2 (extruded, T6) could be further enhanced, if the nanoparticles could achieve a more homogeneous distribution.

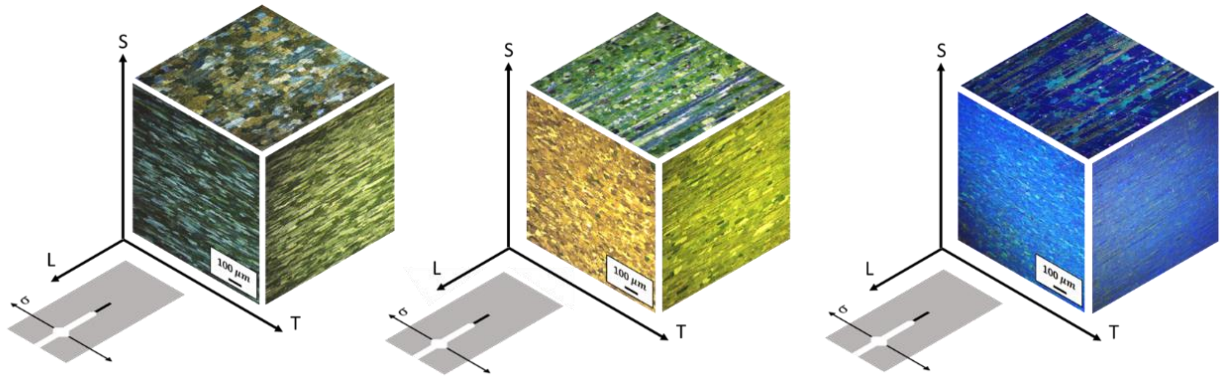

Figure 5 - 81 Grain characteristics and SCC test direction of **(a)** AA7076 (extruded, T6), **(b)** AA7075-1.5 vol.% TiB_2 (extruded, T6), and **(c)** AA7075-1.5 vol.% TiC (extruded, T6). (For cast samples, since the grains have no orientation preference, the directional figure is not shown here)

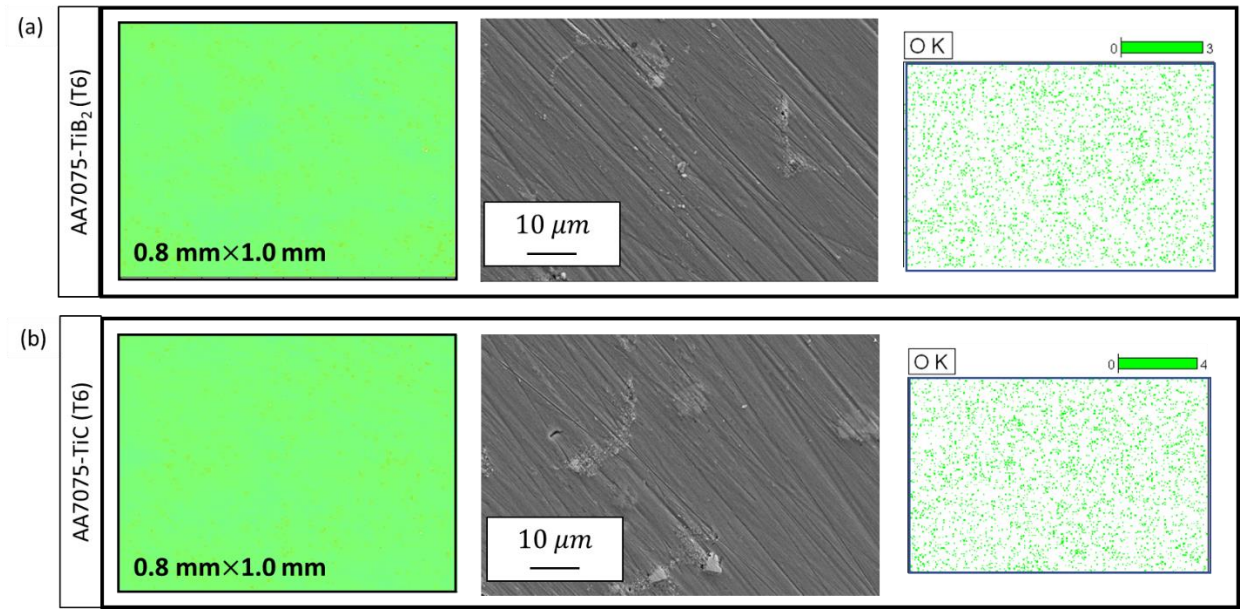

Figure 5 - 82 VSI mapping, SEM imaging, and EDS mapping of AA7075-1.5 vol.% TiB_2 (T6) and AA7075-1.5 vol.% TiC (T6) in as-cast state after 1 min HNO_3 passivation with their fresh surface, showing that the uniformly passivated surface has not presented early pits and will not affect electrochemical measurements.

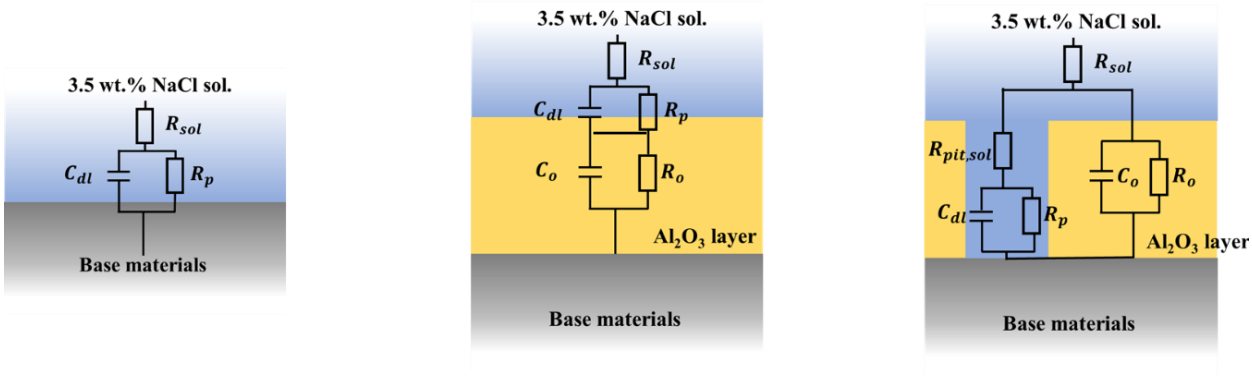

Figure 5 - 83 Potential corrosion modes for (a) freshly exposed surface, (b) passivated surface, and (c) immersed surface after passivation in the electrochemical measurements.

5.2.8 Corrosion performance of A206/TiC nanocomposites

For cast A206 alloy, the effects of TiC nanoparticles on its corrosion performance are studied in its different heat treatment states, i.e., SCC-insensitive T4 state and SCC-sensitive T6 state.

Electrochemistry in A206-TiC nanocomposites: The most common case for corrosion in Al alloys and composites is when their surfaces are exposed and oxidized before immersed, due to the high chemical reactivity of fresh Al. Therefore, to distinguish the effects of the pre-formed oxide layer on the corrosion process, the passivated surface is of interests in this study (as shown in **Figure 5 - 84**), and will be compared with the corrosion behavior taking place on the freshly exposed (see **Figure 5 - 94**) and immersed/pitted surfaces (see Appendix **Figure 5 - 95**).

For the passivated surface corrosion in T4 and T6 heat treatment states, the corrosion potential of A206-1.5 vol.% TiC is both higher than A206 (76 mV higher in T4 state and 39 mV higher in T6 state, respectively), which indicates a nobler reactivity. Second, the corrosion current near the corrosion potential of A206-1.5 vol.% TiC is also smaller than or similar to that of pure A206, which further confirms a slower corrosion speed. Third, since the cyclic polarization is used

for measurement, the intersecting point will demonstrate the (re-)passivation range, above which the corrosion current during back-scanning is smaller than that during forth-scanning. As shown in **Figure 5 - 84** (b) and (c), the TiC nanoparticles will introduce a clear re-passivation potential in A206 alloys and demonstrate the re-passivation protection on the corroded surfaces, whereas pure A206 in T4 and T6 does not have this advantage.

Further looking into the EIS results from impedance values and phase angle in **Figure 5 - 84** (b) and (c), the phase angle evolution trend is similar between A206 and A206-1.5 vol.% TiC under both T4 and T6 heat treatment. However, the EIS loop of A206-1.5 vol.% TiC is smaller than pure A206 after both T4 and T6 heat treatment. Given the beneficial re-passivation behavior by TiC nanoparticles, it could be concluded that the smaller EIS loop is introduced by the quicker oxidation process (mainly $4\mathrm{Al} + 3O_2 \rightarrow 2\mathrm{Al}_2O_3$)

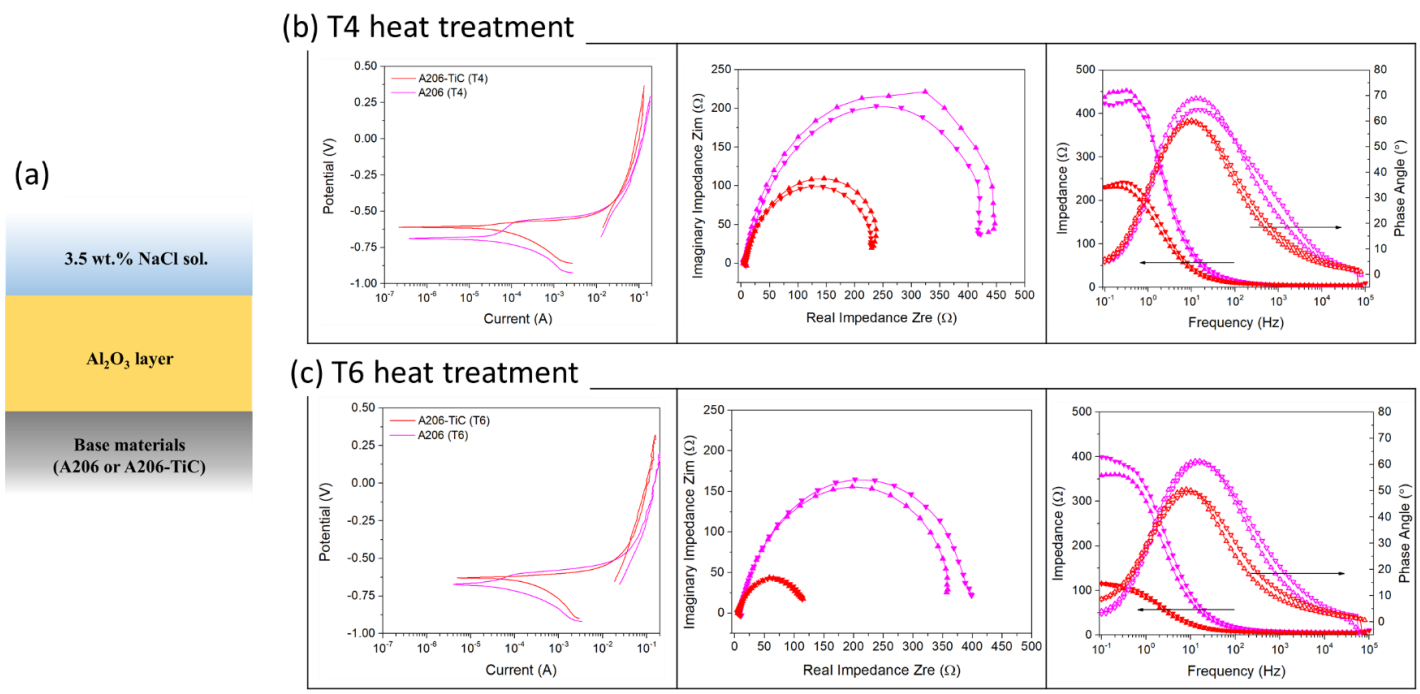

Figure 5 - 84 (a) The illustrative impedance model for corrosion with passivation layer; the potentiodynamic scanning curve and the EIS impedance plots for A206 and A206-1.5 vol.% TiC in (b) T4 and (c) T6 heat treatment state.

The post-corrosion surface morphology in **Figure 5 - 85** and **Figure 5 - 86** supports the effects of quick passivation by TiC nanoparticles. In both T4 or T6 state, the TiC-incorporated A206 nanocomposites have more intact oxide layer covering (see **Figure 5 - 85** (b) and **Figure 5 - 86** (b)). Particularly, since T6 state is the IGC- and SCC-sensitive state, the grain boundaries and adjacent areas are heavily attacked, as shown in **Figure 5 - 86** (a). However, after TiC nanoparticles are added, the corrosion process will yield dense oxide layer that sticks to the grain boundaries and adjacent areas tightly (see **Figure 5 - 86**). The surface oxygen element estimation by EDS mapping in **Figure 5 - 87** supports this hypothesis. Therefore, though the nanocomposites in different heat treatment states have a smaller corrosion-resistance as indicated by the smaller impedance loop, the uniform corrosion and the rapid covering of corrosion-susceptible locations are more advantageous for reducing the localized corrosion.

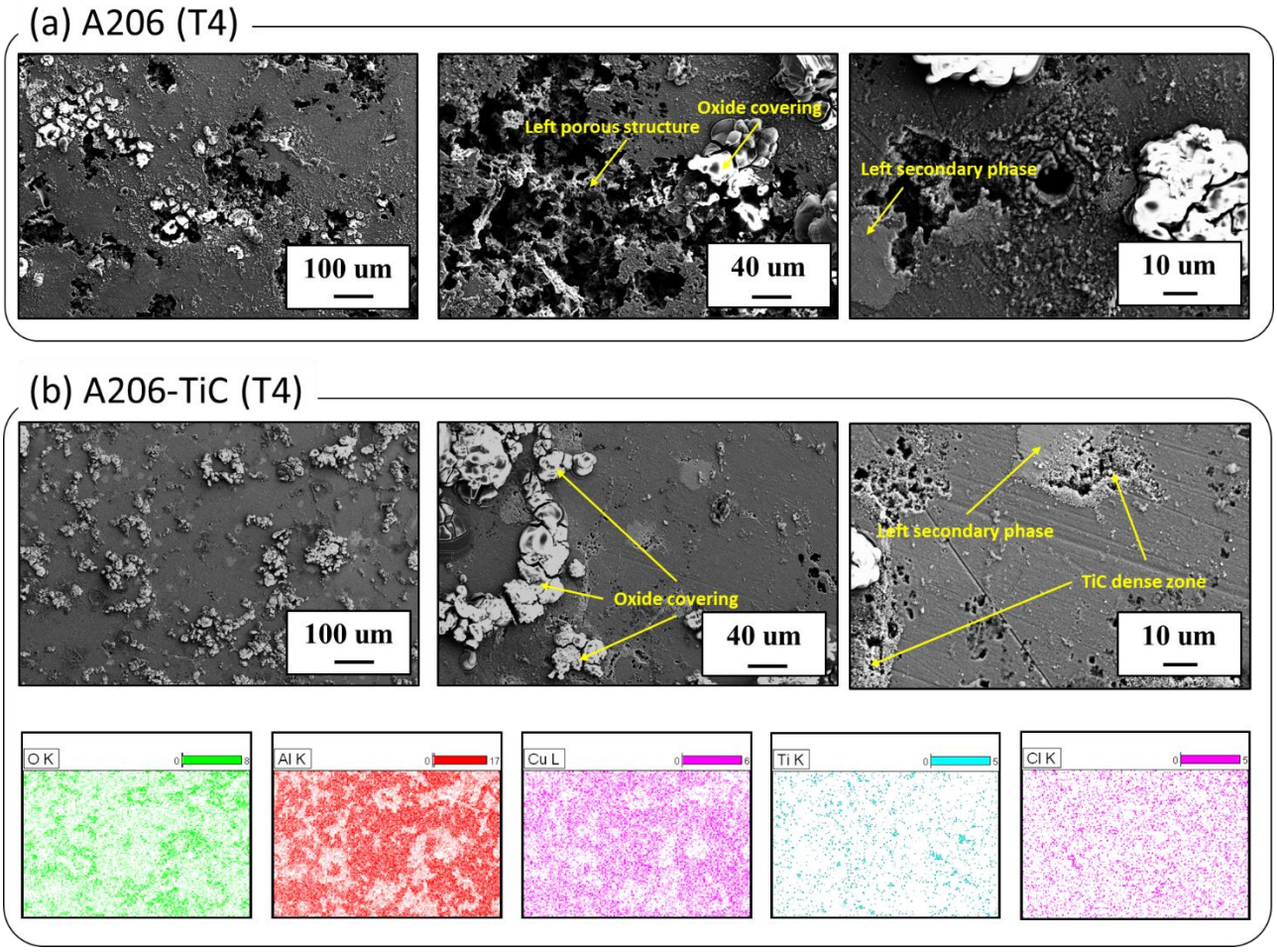

Figure 5 - 85 The post-corrosion surface morphology and microstructure of (a) A206 (T4) and (b) A206-1.5 vol.% TiC (T4).

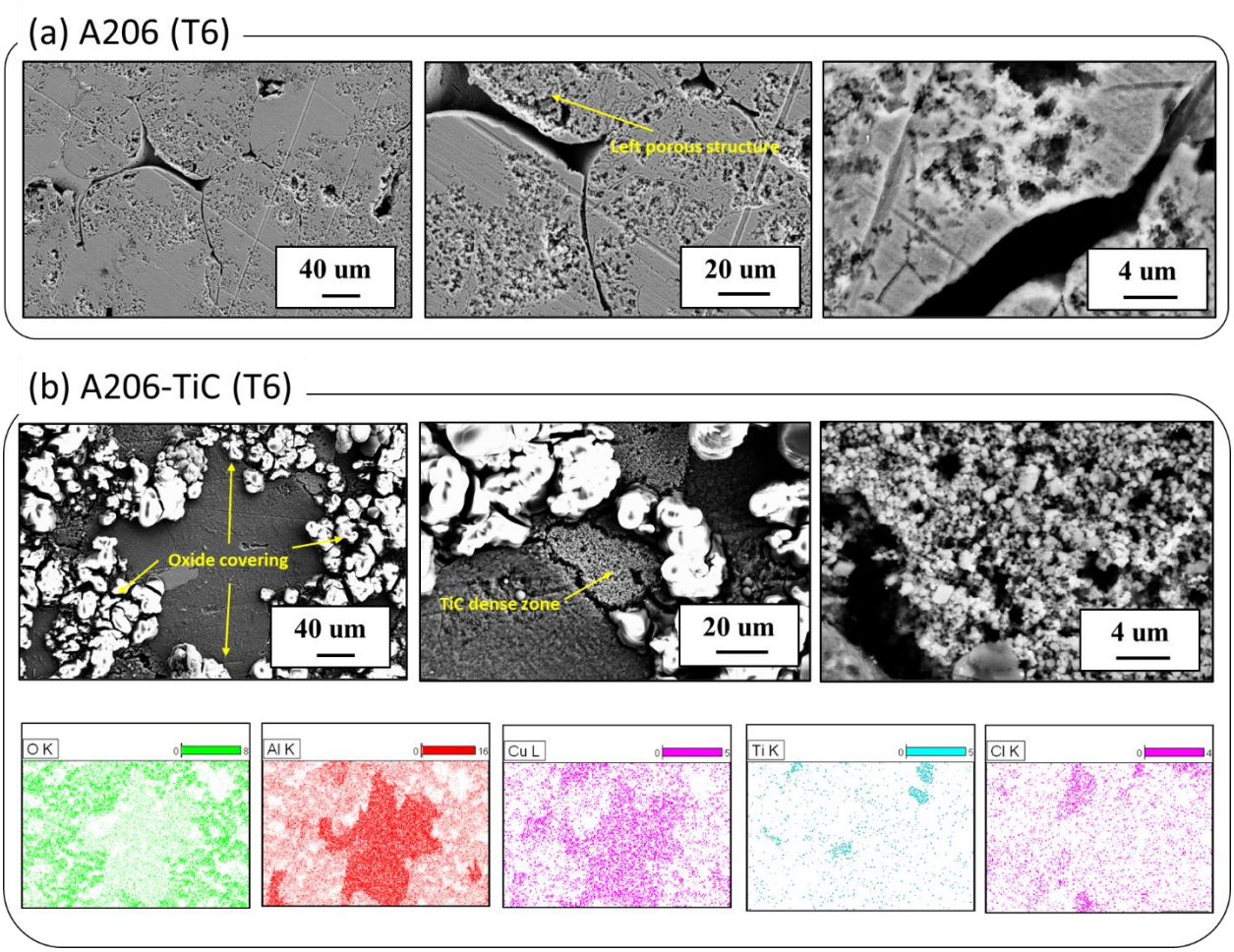

Figure 5 - 86 The post-corrosion surface morphology and microstructure of (a) A206 (T6) and (b) A206-1.5 vol.% TiC (T6).

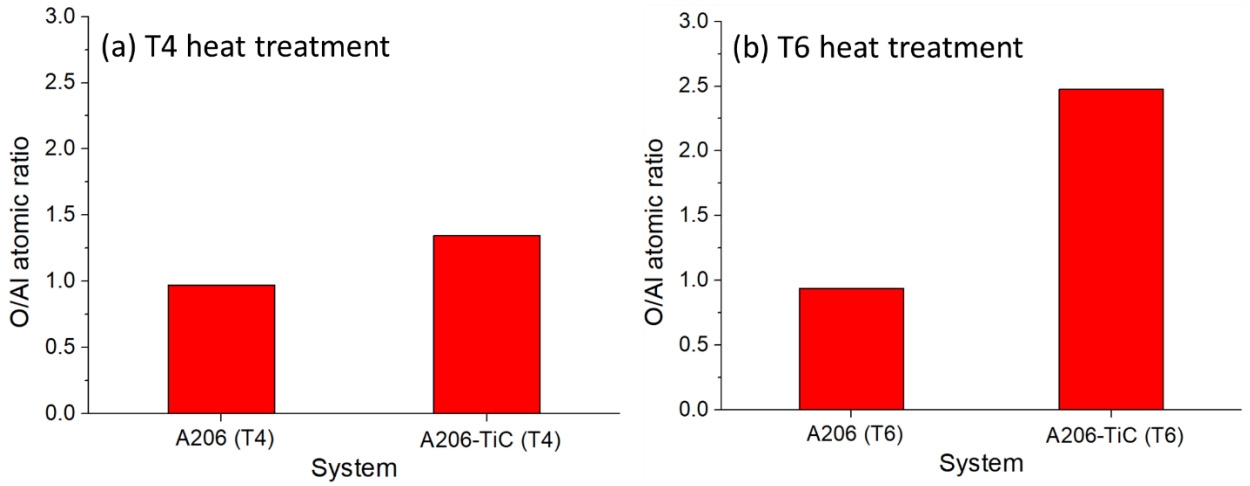

Figure 5 - 87 The O/Al element ratio on the post-corrosion surface of A206 and A206-1.5 vol.% TiC under (a) T4 and (b) T6 heat treatment state.

IGC behavior in A206-TiC nanocomposites IGC-corrosion is a corrosive degradation attacking grain boundary and adjacent areas specifically. Due to the easy diffusion along the grain boundaries, the potential stress concentration near the corrosion tip, and the complex interaction with grain boundary precipitates, the IGC propagation would be detrimental to the localized properties and may lead to the initiation and propagation of SCC.

Figure 5 - 88 and **Figure 5 - 89** show the IGC susceptibility test results for A206 and A206-1.5 vol.% TiC in T4 and T6 states. It can be seen that the TiC incorporation could reduce the IGC penetration depth greatly and seal the corroded grain boundaries to resist the further preferential IGC attack. The IGC susceptibility results in **Figure 5 - 88** and **Figure 5 - 89** are consistent with the passivation-mitigated corrosion process observed in **Figure 5 - 85** and **Figure 5 - 86**.

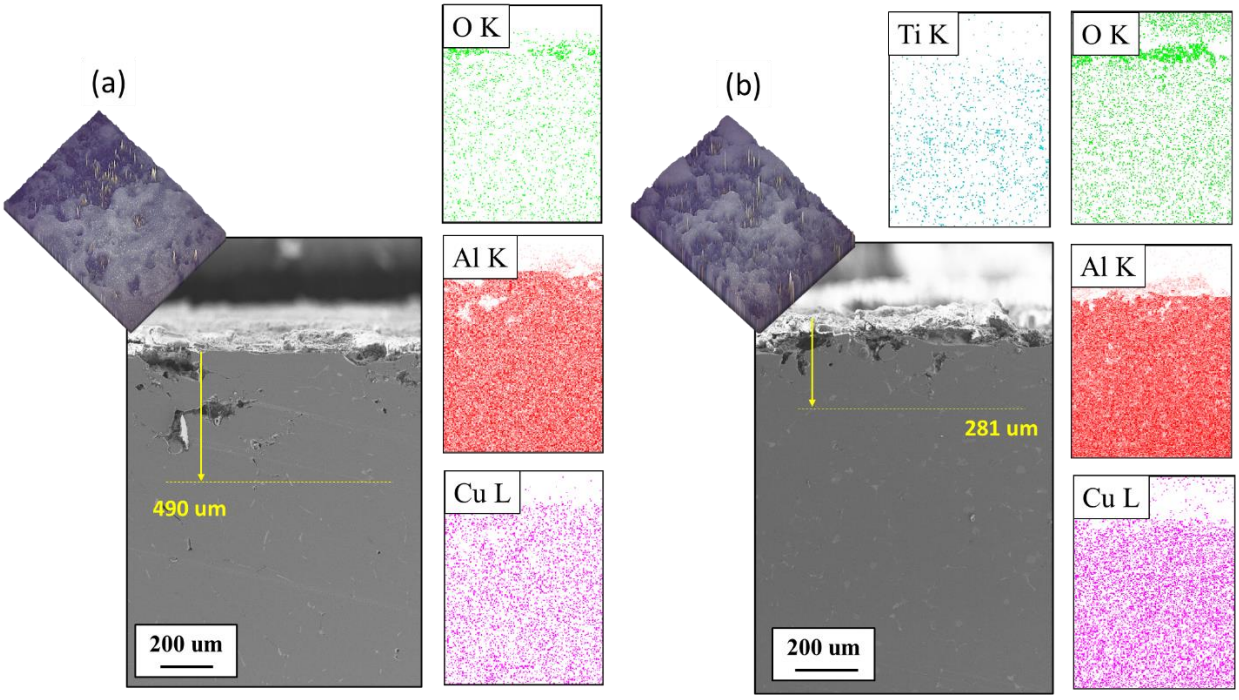

Figure 5 - 88 The IGC test results of (a) A206 and (b) A206-1.5 vol.% TiC in T4

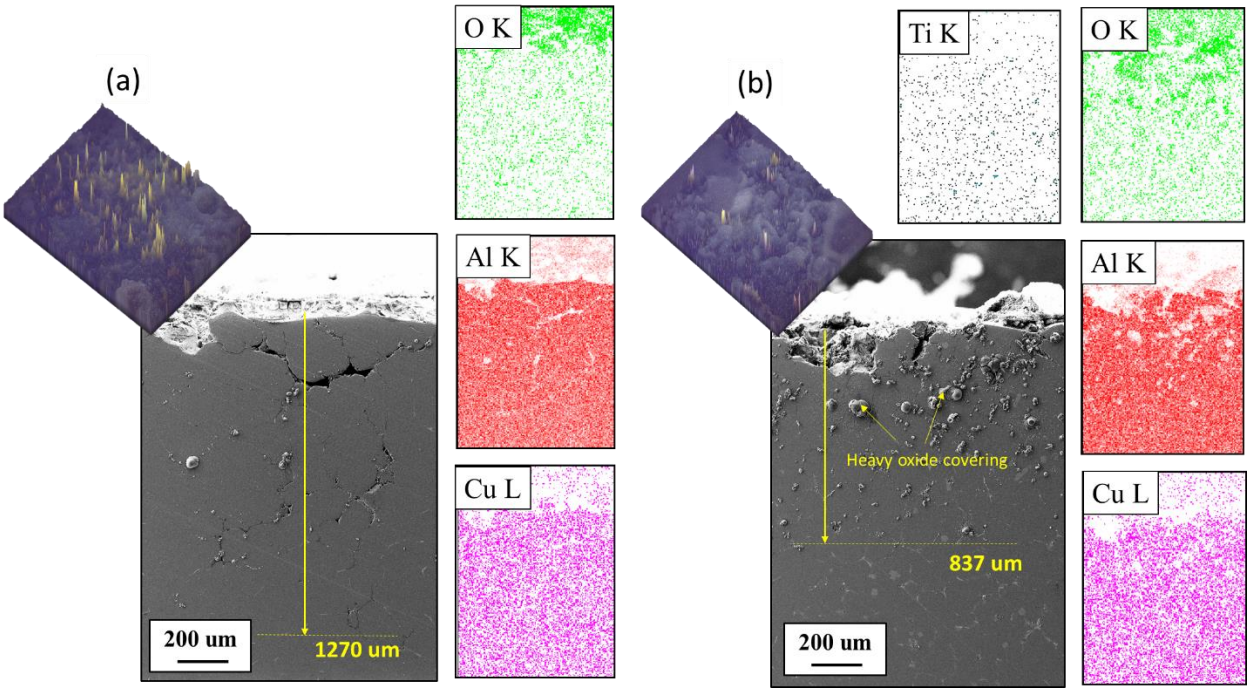

Figure 5 - 89 The IGC test results of (a) A206 and (b) A206-1.5 vol.% TiC in T6

Here, although A206 nanocomposites show a similar IGC mitigation effect to that of AA7075 nanocomposites (see **Figure 5 - 66** and **Figure 5 - 77**), the electrochemical mechanism, particularly the preferential localized corrosion initiation, is different.

As shown in **Figure 5 - 90** (a-1) and (a-2), for AA7075 alloys, since the electrochemical potential for the different features (e.g., TiC has the corrosion potential of -107 mV, [313] whereas the electrochemical potential for TiB_2 is -432 mV [122]), the most susceptible microstructure to corrosive media is grain boundary precipitates (GBPs). However, no matter in peak-aged (T6) or overaged (T73) state, the GBPs linked to the surface is little. Therefore, since the inner-grain precipitates are in higher concentration and the GB has a similar potential with the matrix, during the first step of corrosion on the surface, the corrosion process would be mostly uniform (see the illustration in **Figure 5 - 65** (d)). Only when the corrosion uniformly proceeds and penetrates to

the GBPs at different locations, shall the localized corrosion (to introduce IGC, etc.) be initiated. Since the incorporated nanoparticles like TiB_2 and TiC would pseudo-disperse at GBs and near GBPs, the nanoparticles will slow down the localized corrosion near the GBs by strengthening GBPs, as shown in **Figure 5 - 90** (a-2).

However, since the GB is denser than the GBPs on the surfaces and has the lowest corrosion potential in A206, the corrosion initiation is directly dominated by a localized mode (See **Figure 5 - 90** (b-1)). The generally longer IGC penetration depth in **Figure 5 - 88** and **Figure 5 - 89** of A206 than AA7075 in **Figure 5 - 66** and **Figure 5 - 77** supports this mechanism. Considering the distribution of nanoparticles in the GB-adjacent areas (including PFZs), the nanoparticle-introduced IGC-mitigation in A206 alloys is enabled by the GB-strenghtening effects, instead of GBP-strengthening effect. Knowing GBs act as the corrosion-susceptible paths in A206, **Figure 5 - 90** (b-1) and (b-2) would then show different meaning for the A206 in T4 and T6 states. A206 (T6) would have larger PFZ zones due to the element depletion by larger and more continuous GBPs than A206 (T4) near GBs. Therefore, because of the initial exposed dense GBs with PFZs to the surface, A206 (T6) is generally more susceptible to localized corrosion than A206 (T4) (as shown by the comparison of **Figure 5 - 88** and **Figure 5 - 89**).

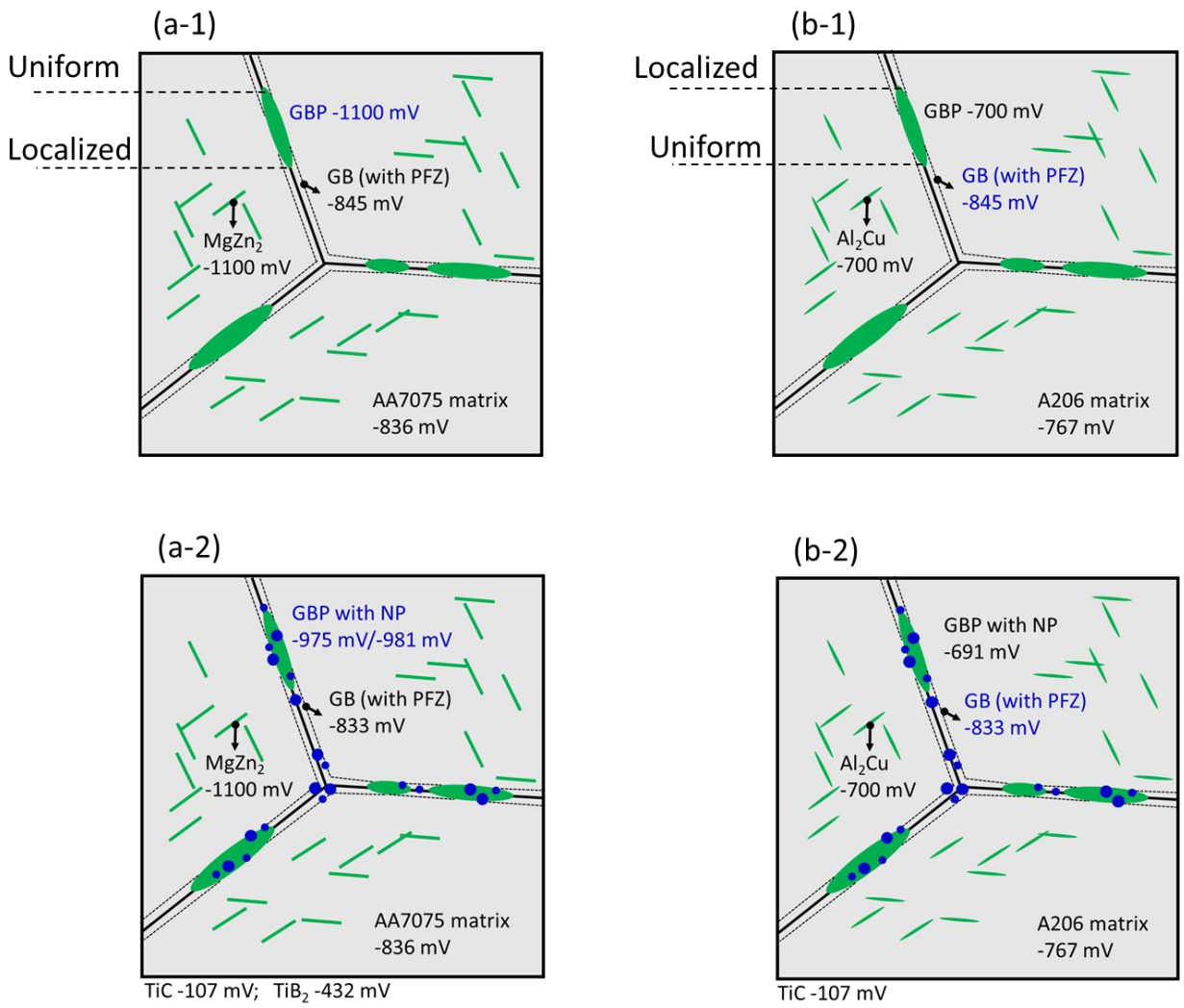

Figure 5 - 90 The localized corrosion initiation and IGC mitigation mechanisms in (a-1) and (a-2) AA7075 and its nanocomposites and (b-1) and (b-2) A206 and its nanocomposites with TiC and TiB_2 incorporation.

SCC behavior in A206-TiC nanocomposites: Knowing the beneficial effects of TiC nanoparticles to suppress the IGC susceptibility and introduce more homogeneous corrosion by more efficient rapid oxidation process, it is also of great interests to quantify the SCC susceptibility in these A206-TiC nanocomposites.

Figure 5 - 91 shows the SCC comparison between A206 and A206-1.5 vol.% TiC in their SCC-sensitive T6 state. The crack propagation speed by the immersion tests could be divided into 2 parts. Under the lower stress intensity range ($< 10\ \mathrm{MPa} \cdot m^{0.5}$), the incorporation of TiC nanocomposites reduces the SCC sensitivity by lowering the crack propagation speed. This mitigation of SCC failure gives a higher critical stress intensity of ~6.67 $\mathrm{MPa} \cdot m^{0.5}$ in A206-1.5 vol.% TiC (T6). Under this stress intensity range, the improved SCC behavior is associated with the effective surface oxide layer covering/passivation (see **Figure 5 - 85**-**Figure 5 - 87**) and the resultant better anti-IGC performance (see **Figure 5 - 89**).

Under the high stress intensity range (>15 $\mathrm{MPa} \cdot m^{0.5}$), the crack propagation speed of A206-1.5 vol.% TiC (T6) is slightly higher than that of pure A206 (T6). The less effective SCC control under high stress intensity range is likely due to the reduced ductility and microscopic interfacial corrosion couple by nanoparticles and their immediate adjacent areas in A206-1.5 vol.% TiC (T6).[311] As shown in the previous studies [314], the incorporation of TiC nanoparticles can narrow down the PFZ zone width, particularly near the TiC-dense zone [315]. However, the incorporation of TiC nanoparticles also induce more matrix/precipitate-nanoparticle interfaces, which could efficiently serve as the void/porosity nucleation sites under stress [316] or by dynamic chemical change (e.g., local corrosion depletion enabled by these micro-interfaces) [4,311]. When the nanoparticles are pseudo-dispersed, the apparent void/porosity spacing is smaller, and the denser corrosion porosity near the TiC-dense area could have a higher chance to coalesce through the heterogenous micro-interfaces. Thus, the smaller PFZ length to void spacing ratio will introduce an easier intergranular fracture [311]. Particularly, the higher stress intensity will also give a higher chance of intergranular fracture [311]. The fracture mechanics dominates the SCC cracking under the higher stress intensity and counteract on the beneficial effects of passivation in the corrosion,

which lead to a weaker SCC control by pseudo-dispersed nanoparticles. It would be of interest to investigate how A206 with less TiC nanoparticles, thus possibly better plasticity at GB areas, will behave in SCC testing.

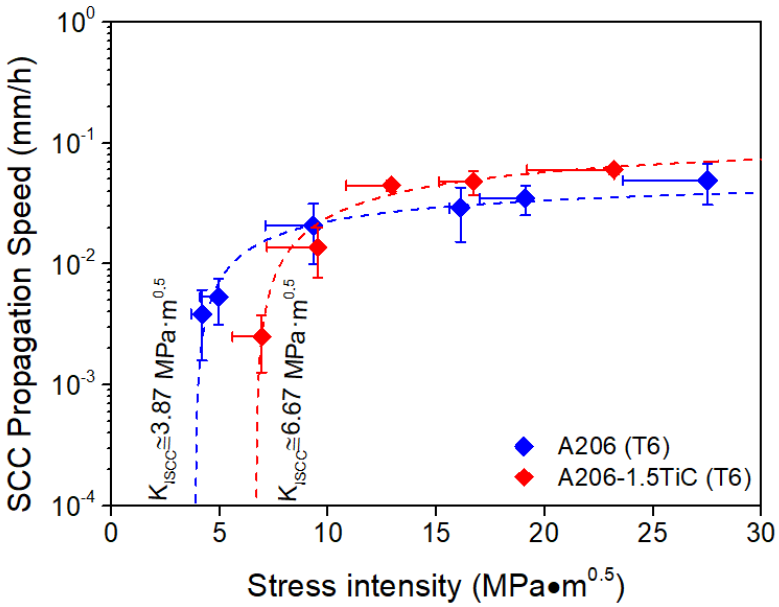

Figure 5 - 91 The SCC crack propagation test results of (a) A206 and (b) A206-1.5 vol.% TiC under T6 heat treatment state.

For the SCC behavior of A206 and A206-1.5 vol.% TiC in their T4 state, the results are similar. Due to the natural SCC-insensitivity of alloy matrix, **Figure 5 - 92** shows that the SCC propagation speed is plateaued and comparable though the whole measurable stress intensity range. The overall SCC-resistance is also likely determined by the balanced passivation protection during corrosion and plasticity mechanics by nanoparticle incorporation. Given the results in AA7075 (T73) system from **Figure 5 - 70**, as the 1.5 vol. % TiC nanoparticles seems to be overdosed for the high stress intensity range, it is expected that a lower volume percentage (~0.75 vol.%) of TiC (see **Figure 5 - 92**) would give a better SCC-resistance under the high stress intensity range. This

observation supports that, under higher stress intensity, the ductility change near the grain boundary (along with the grain boundary precipitates) is the key to further mitigate the SCC problems in A206 alloy, which is also consistent with the findings in **Figure 5 - 70**.

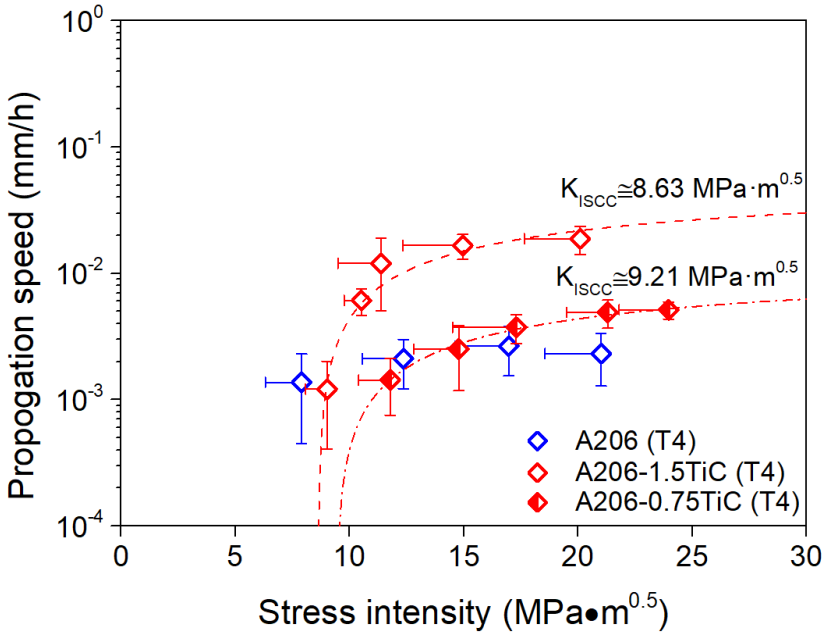

Figure 5 - 92 The SCC crack propagation test results of A206 and A206-1.5 vol.% TiC in T4

In short, for A206-TiC nanocomposites, the corrosion behavior is also largely determined by the TiC nanoparticles. The pseudo-dispersion of TiC near and along the grain boundary and secondary phase strengthen the grain boundaries, and the more rapid passivation near the TiC-dense zone introduces a more uniform corrosion feature. Though quicker, the uniform corrosion accompanying rapid passivation help reduce its IGC susceptibility. As a results, the mitigated IGC performance contributes to a much lower SCC-susceptibility in A206-TiC nanocomposites under the lower stress intensity. However, under higher stress intensity, due to the strengthening effect and microstructural modification in A206-TiC nanocomposites, the likely lowered ductility along GBs by pseudo-dispersed nanoparticles makes the SCC-control less effective. Moreover, as

mentioned for cast AA7075 and its TiC- and TiB_2-reinforced nanocomposites, the direct interface between nanoparticles and adjacent area would have an abrupt electrochemical potential change, due to the inertness of TiC and TiB_2 (see **Figure 5 - 90**) [310]. Even though the nanoparticle could strengthen GBPs and GBs against corrosion, this microscopic galvanic corrosion process will compromise the strengthening effects against corrosion and could lead to the interaction with cracking tip propagation by oxygen depletion for passivation, etc. [95,310] Therefore, the addition of even lower percentage of inert TiC and TiB_2 could not outcompete the SCC propagation in pure A206 alloy.

Generally speaking, the T4 and T6 states have the similar corrosion effects, but a lower volume percentage of TiC nanoparticles could help with the anti-SCC behavior under the higher stress intensity range, likely due to the less plasticity loss near and along grain boundary and less microscopic interfacial galvanic corrosion at the nanoparticle-matrix/precipitate boundaries.

Appendix **Figure 5 - 93** shows that the pre-passivation by 70.0 wt.% concentrated HNO_3 will not change the surface integrity and introduce sensible corrosion during the process.

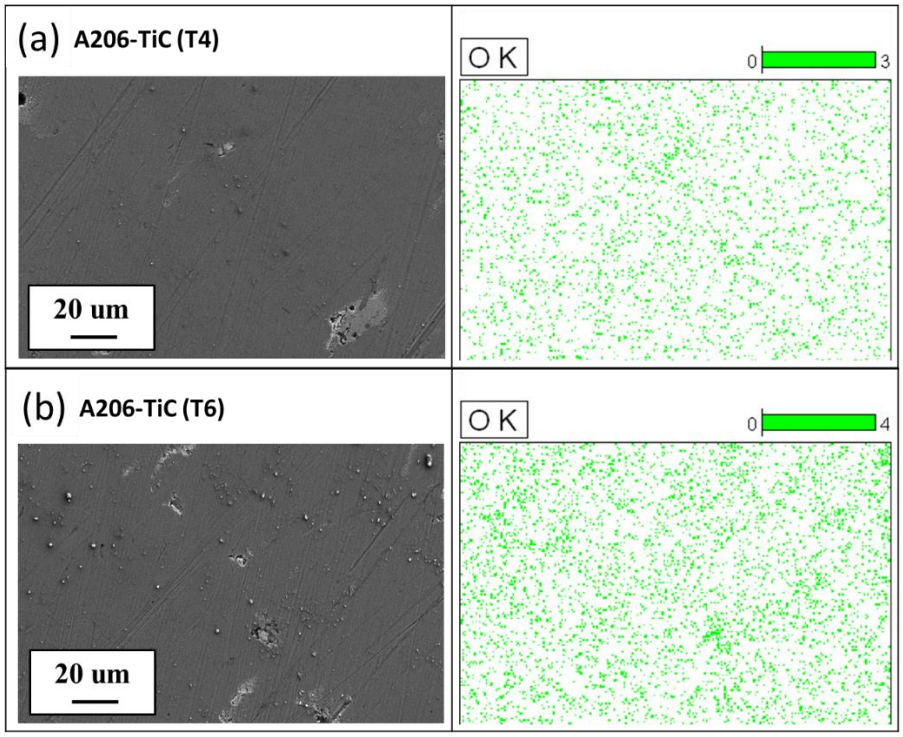

Figure 5 - 93 The post-passivation surfaces with oxides of A206-1.5 vol.% TiC in (a) T4 and (b) T6 heat treatment state.

Figure 5 - 94 considers the corrosion process on the freshly exposed A206 and A206-1.5 vol.% TiC surfaces of both T4 and T6 states. In this process, since the surface has very high reactivity in the 3.5 wt.% NaCl solution, the forth and back EIS scanning shows a less overlap (see **Figure 5 - 94** (b) and (c)). Clearly, due to the higher anti-corrosion performance, the T4 state generally has a larger impedance than the T6 state. Besides, considering the effects of the TiC nanoparticles, the smaller impedance loop confirmed that A206-TiC could introduce the electrochemical reaction more easily. As the same case with the previous studies [317] and our study for AA7075 systems, this electrochemical change indicates a more rapid oxidation process to give more passivation and obtain more uniform surface corrosion. For the samples after 24h immersion in the corrosion medium, **Figure 5 - 95** indicates a similar phenomenon with **Figure 5 - 94**.

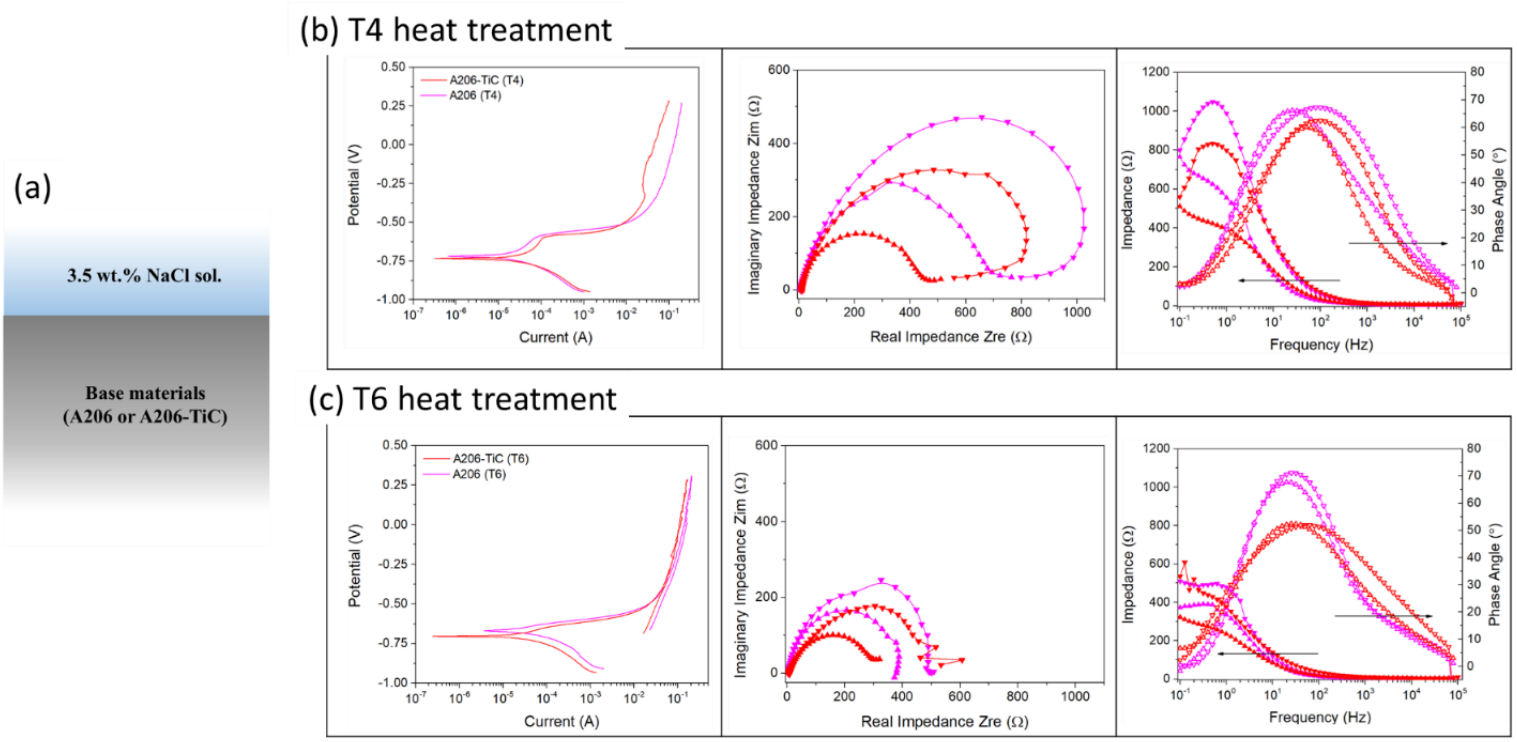

Figure 5 - 94 (a) The illustrative impedance model for corrosion with freshly exposed surface; the potentiodynamic scanning curve and the EIS impedance plots for A206 and A206-1.5 vol.% TiC in (b) T4 and (c) T6 heat treatment state.

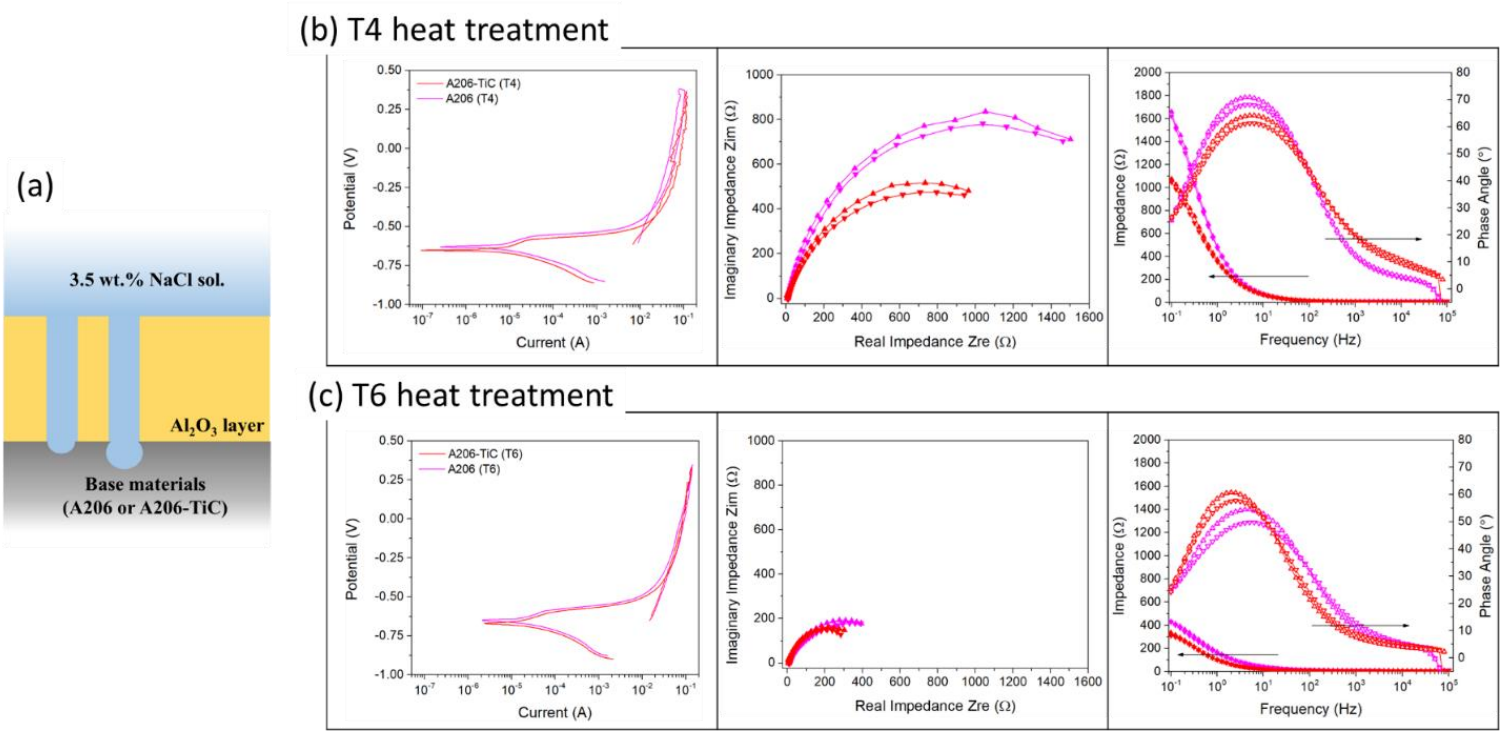

Figure 5 - 95 (a) The illustrative impedance model for corrosion with immersed and pitted surface; the potentiodynamic scanning curve and the EIS impedance plots for A206 and A206-1.5 vol.% TiC in (b) T4 and (c) T6 heat treatment state

5.3 Summary

In this chapter, a systematic study into the chemical stability (i.e., high-temperature stability and anti-corrosion performance) of the nanocomposite systems was conducted.

First, the Mo-enhanced chemical stability of TiC nanoparticles during the solidification processing of Al-TiC nanocomposites was investigated. In brief, the addition of Mo into the Al-TiC system is advantageous for its chemical stability at the favorable Al processing temperature range (~750 °C). Mo increases the reaction activation energy by about 0.069 eV and introduces a lower reaction diffusion coefficient during the reaction between Al and TiC. During the reaction, Mo will form intermetallic products with $Al_3Ti(Mo)$ more slowly, thus making the intermetallic

phase finer. This observation would be important to designing a more robust and wider processing temperature window for Al-TiC nanocomposites and effectively suppressing their chemical reactions below 750 ℃.

Second, as metals and alloys are prone to oxidation, how nanoparticles could tune the thermal oxidation behavior of metal matrix nanocomposites was systematically analyzed.

The Zn-dominant stress-assisted thermal oxidation in Cu-40Zn/WC nanocomposites show continuous oxidation features, and the incorporation of WC share the thermal stress by a similar load-bearing capacity to mitigate the Zn oxidation process. The study in this chapter systematically analyzed the thermal stability (i.e. phase stability and anti-oxidation) of Cu-40 wt.% Zn up to high temperatures and confirmed the beneficial role of WC nanoparticles in the enhanced thermal stability of Cu-40 wt.%/WC nanocomposites. The oxidation rate analysis, SEM surface, and FIB cross-section images proved the different morphology from nano-rod to nano-plates introduced by WC nanoparticles and the important role of WC nanoparticles as oxidation path hindrance. Meanwhile, the DSC analysis validated the postponed phase transition trend in the Cu-40 wt.% Zn/10 vol.% WC nanocomposites. The results are summarized in **Figure 5 - 34**. As for the Cu-40 wt.% Zn alloy, the enhanced thermal stability by WC nanoparticles broadens its usage in fields as naval brass for heat exchangers and beyond.

For Al-ZrB_2 nanocomposites, due to the self-limiting nature of Al oxidation, the incorporation of nanoparticles would speed up the surface oxidation process at lower temperature by rupturing the oxide film and reduce the oxidation rate at higher temperature by increasing atomic-scale electric Mott potential. In this study, the effects of ZrB_2 nanoparticles are studied by both dynamical and kinetic measurements: Under lower temperature (<673 K), Al-ZrB_2 nanocomposites exhibit a higher oxidation rate than pure Al. The exposed ZrB_2 nanoparticles

breaks the continuity of the oxide layer, and the cation-deficient mode makes this temperature-range electric field-controlled. However, under higher temperature (> 673 K), Al-ZrB_2 has a better anti-oxidation performance, thanks to the delay of the amorphous-to-crystalline phase change of Al_2O_3. This observation is confirmed by the Mott-Cabrera model analysis: The Al-5 ZrB_2 nanocomposites have both higher Mott potential and greater activation energy barrier. When the oxidation temperature is lower, Mott potential, as well as higher O/Al ratio, makes Al-ZrB_2 easier to be oxidized initially; on the other hand, when the temperature is higher, the activation energy barrier is more dominant and leads to a slower oxidation rate. With the different characteristics of the oxide layer, it has been further demonstrated that the post-oxidation surface of Al-ZrB_2 nanocomposites has different wettability and corrosion-performance. The Al-ZrB_2 oxidized surface has a larger contact angle, more noble corrosion potential, and higher corrosion resistance.

With this understanding from the oxidation process of Zn and Al individually, the coupled oxidation between Zn and Al is studied in alloy systems (i.e., AA7075 alloy). The study in this chapter shows that there is a strong interaction between TiB_2 nanoparticles and oxide formation during the oxidation of AA7075 nanocomposites: At a lower temperature (e.g., 400 °C), the TiB_2 nanoparticle will rupture the self-limiting Al_2O_3 film to increase its oxidation speed. When the temperature is above the solutionizing temperature (e.g., 600°C) of the $MgZn_2$ secondary phases, TiB_2 nanoparticles will help increase the element (Zn and O) concentration gradient and reduce the roughness of the wavy Al_2O_3 film due to much-refined grains. The nanoparticles generate a different oxide surface pattern and change the inward oxidation penetration depth in AA7075-TiB_2. Generally speaking, Zn can be oxidized to a large depth in AA7075 and AA7075-TiB_2 even after the Al_2O_3 oxide film is formed. The TiB_2 nanoparticles can dynamically regulate the whole process by lowering the Zn oxidation rate. Considering the large oxygen penetration depth along the Zn-

rich phase and the oxidation control from TiB_2, this understanding would be of significance for the processing AA7075 and its nanocomposites under high temperature or high temperature gradient.

After systematically understanding the oxidation behavior in metal nanocomposites (mainly Al alloy nanocomposites), the environmentally assisted degradation (i.e., corrosion) performance in metal nanocomposites have been studied in detail. For the corrosion investigation, industrially important Al alloys AA7075 and A206 via different manufacturing routes (i.e., cast and extrusion) and post-processing states (i.e., T4, peak-aged T6, and overaged T7) have been selected for the study.

The study revealed that the incorporation of nanoparticles will refine the grains, increase the LAGB fraction, reduce the PFZs, and reduce the electrical conductivity slightly, which are all advantageous to increasing the anti-corrosion performance. Moreover, Al alloys with nanoparticles will introduce a more effective passivation behavior, leading to an enhanced anti-corrosion performance, esepcially IGC resistance. Therefore, for SCC behavior, under low stress intensity range where the static corrosion process is dominating, the SCC crack propagation will be advantageously mitigated by nanoparticles. In brief, nanoparticles will introduce different phase distribution and microstructure in AA7075-TiC (extruded, T6) and AA7075-TiB_2 (extruded, T6) to AA7075-TiC (cast, T6) and AA7075-TiB_2 (cast, T6). The pseudo-dispersed nanoparticles will heavily interact with the oxide passivation (by changing the oxide hydration process and tuning the band-surrounded electrochemical potential), oxide layer consumption process, and the resultant corrosion behavior. The nanoparticles in A206 alloy system play a similar role with those in AA7075.

In summary, the effects of nanoparticles on the overall chemical stability in metal nanocomposites have been studied in depth. In this chapter, the intrinsic thermal stability of metal matrix and incorporated nanophases has been investigated by considering the interfacial chemical process, and quantitatively determined the chemical reaction dynamics and kinetics. The method to mitigate Al-TiC reaction and Al-Si-TiC reaction was proposed. Later, the whole system's thermal stability was studied by investigating the thermal oxidation process of Zn- and Al-contained system. The decoupled oxidation features of Zn and Al interact differently with the incorporated nanoparticles, and this understanding is of great importance to understand the coupled oxidation behavior in Al alloys such as AA7075. After the oxidation process is clarified, together with the electrical property study in **Chapter 4**, the interaction between nanoparticles (TiC and TiB_2), metal matrix (Al), grain boundary features, and pecipitates (after different heat treatment) in the corrosion processes including passivation, pitting, IGC, and SCC. For corrosion-dominant processes, due to the stabilized electrons, more rapid (re-)passivation, and microstructural modifications near the GBPs and PFZs, the incorporation of chemically stable ceramic nanoparticles could be conducive to the corrosion mitigation. Particularly, for SCC behavior in AA7075 and A206 alloys, under the lower stress intensity range, the nanoparticles could effectively reduce the crack propagation speed by enhancing the corrosion resistance, which is consistent with the study on immersion corrosion, pitting, and IGC study. For the SCC propagation under the higher stress intensity range, the interplay between corrosion and mechanical behaviors likely makes the SCC speed local mechanics-sensitive [311], which leads to a comparable yet slightly higher propagation speed. The pseudo-dispersion of nanoparticles into the GBs and GBPs could reduce the ductility in these areas and lead to a possible microscopic galvanic corrosion by the high-density nanoparticle-matrix/precipitate interfaces, thus counteracting on the beneficial

corrosion-mitigating effects. Our results indicate that by rationally deisgning and lowering the nanoparticle's volume percentage, other advantageous effects by incorporating nanoparticles could be maintained, while the high-stress-intensity SCC propagation could be further mitigated and improved.

Overall, this chapter provides an in-depth study on the effects of nanoparticles on the chemical stability of metals containing nanoparticles. The understanding into the synthesis chemical reaction, thermal stability against oxidation, and anti-corrosion performance proves the great potential of using nanoparticles to enhance the anti-degradation behavior in metal nanocomposites and could serve as the useful guide for the novel metal/alloy nanocomposite design.

CHAPTER 6 EFFECT OF NANOPARTICLES ON TRIBOLOGICAL PERFORMANCE OF METALS

6.1 Experimental method

Sample Preparation and Characterization: 1.5 vol.% TiB_2 was chosen based on the study from Akbari et al. [318] as the optimal nanoparticle percentage in aluminum alloys for tribological applications. The AA7075(T6)-1.5 vol.% TiB_2 nanocomposite was fabricated via the following method: K_2TiF_6 and KBF_4 were added to molten pure Al at 750-800 °C for 15-20 min to in situ synthesize Al-TiB_2 master [2]. At this stage, TiB_2 was designed to be at 3 vol.%; Then, the Al-TiB_2 master was diluted and alloyed with the elements needed to yield AA7075's composition. T6 heat-treatment (i.e., homogenization at 480°C for 2 hours, then quenching in water at 25°C, finally aging at 120°C for 24 hours) was used to obtain the AA7075(T6)-1.5 vol.% TiB_2 nanocomposite. Commercial AA7075(T6) was used as the reference material. More details could be referred to in **Chapter 3**.

The microstructure and composition distribution were revealed by SEM and EDS (on equipment model *Zeiss Supra* and equipment model *JEOL JED-2300*). The Mohs hardness and the Young's modulus were measured via nanoindentation on *Bruker Nanoindenter Pro* with 9 readings for each sample. For further comparison, the microhardness of the samples was measured on *Microhardness Tester LM800A* (under the load of 200 gf and for 10 sec dwell time, 10 readings for each sample).

New CoF Measurement and Analyses A new CoF measurement setup was built based on a low-profile wall shear sensor developed by Xu et al. [319]. As shown in **Figure 6 - 1** (a), the counterpart plate made of AA5083 (135 HV), Fe-A247 (505 HV), Fe-52100 (848 HV), and Si (1161 HV) was attached to the floating element, and the friction force between the sample and

counterpart displaced the floating element (connected to a set of flexure beams). The displacement of the counterpart plate was precisely measured by an optical encoder (M2000 linear encoder, *Celera Motion Inc.*) with 78 nm resolution and 512 Hz sampling frequency. The friction force on the counterpart plate was linear to the floating element displacement with a spring constant of ~8000 N/m. The resolution of measured friction was therefore ~10-4 N, which cannot be achieved by any pin-on-disc measurement so far. Also, since this setup guaranteed the sensitivity to record the shear force only along the movement direction, it helped reveal the microscopic area-dependent shear nature of the friction contact with minimum wear influence and surface destruction [320]. The whole setup has an absolute uncertainty of 10% [321]. The setup was calibrated with the friction between pure Cu and Al, and the measured values were consistent with previous studies under similar conditions [322]. (See **Table 6 - 1**) The displacement of the counterpart plate was recorded and converted to CoF. Six measurements have been done for each material combination with this new method.

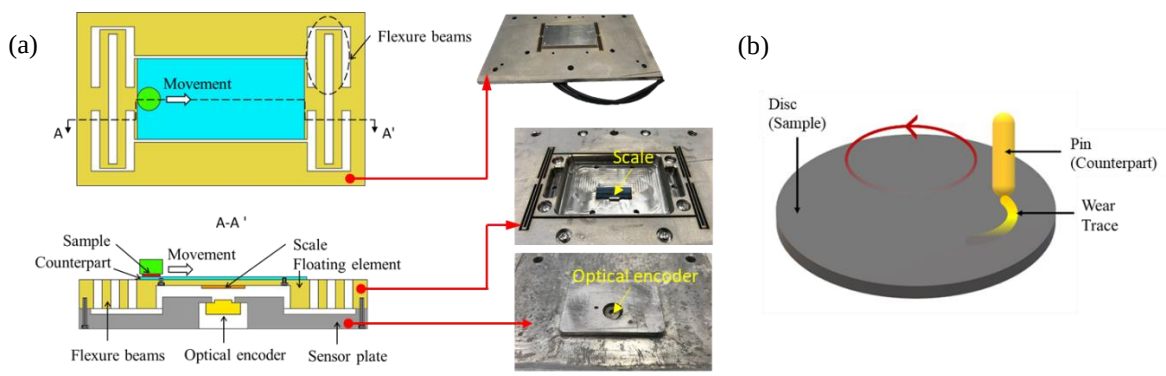

Figure 6 - 1 (a) The illustration and the real model of the precise CoF measurement setup enabled by high-resolution displacement measurement with an optical encoder (overview and cross-section view); (b) The illustration of the traditional pin-on-disc measurement.

For both pure AA7075(T6) and AA7075(T6)-1.5 vol.% TiB_2 nanocomposites, the samples were cut to the size of 1.5 cm in diameter and 0.2 cm thickness by wire EDM. Then, the sample surfaces and the counterpart surfaces were mechanically polished using up to 1200 grit. During polishing, anhydrous ethanol (200 proof) instead of water (i.e., with 0.02 um Al_2O_3-ethanol solution) was used to minimize the surface oxidation effect before the tests. Due to the same reason, relatively shorter time was used for now, because the freshly prepared sample surface would be easily oxidized to influence the measurement of their intrinsic CoF. The total sliding stroke in the test was 100 mm.

After the tests with the proposed method, the counterpart surfaces were characterized via XPS to review the composition change and atom transfer. Also, to confirm that little influence of wear was included, confocal surface profiling by equipment *Wyko NT3000* was used to obtain the surface profile data for the counterpart surface with a scanning area of 300 μm×230 μm.

Figure 6 - 1 (a) The illustration and the real model of the precise CoF measurement setup enabled by high-resolution displacement measurement with an optical encoder (overview and cross-section view); (b) The illustration of the traditional pin-on-disc measurement.

Pin-on-Disc Measurement The pin-on-disc measurement was set up with 400 rpm rotation speed and 1.0 cm wear trace diameter, as shown in **Figure 6 - 1** (b). The pins were made of the counterpart materials of AA5083, Fe-A247, Fe-52100 and Si with a diameter of 7.0 mm, while the discs were fabricated from AA7075(T6) and AA7075(T6)-1.5vol.% TiB_2 samples with a diameter of 1.5 cm, respectively. The load was ≥100 kPa (~1 N with the real contact area of <0.1 cm^2, because the end of the sample pin has been grinded and polished into a circular conical frustum shape with a diameter of ~3.0 mm). The calibrated sliding speed was 0.209±0.006 m/s with 10,000 cycles (i.e., the total sliding length of 315 m) to achieve a steady state for wear (longer than the

steady state for friction). 2 measurements have been done for each material combination to compare with the results from the proposed method.

After the pin-on-disc measurement, the profiles of both the counterpart pins and sample discs were measured, and the pin-surface elements were analyzed with the EDS mapping.

The specific wear rate (SWR) by the Archard method [323] was measured through the surface profiles of the sample discs by means of the following equation:

$$SWR = \frac{VL(mm^3)}{F(N)\times SD(m)} = \frac{M(mm^2)\times \pi d}{F(N)\times (C\times \pi d)} = \frac{M(mm^2)}{F(N)\times C} \times 1000\,\frac{mm}{m} \qquad \textbf{(6-1)}$$

where VL is the worn volume (here the worn volume of the sample disc), F the applied normal load, and SD the sliding distance during the experiment. M means the 2D worn cross-section profile area by the Archard method, d is the wear trace diameter (i.e., 1.0 cm), and C denotes the number of total sliding cycles during the tests. It should be noted that though the new proposed method depends on linear motion and the pin-on-disc test is rotatory, these 2 methods are gauging the same dry sliding tribological behavior [324] with mechanical and chemical wear nature.

6.2 Experimental results

Microstructure and Mechanical Properties As shown in **Figure 6 - 2**, the TiB_2 nanoparticles have been uniformly dispersed in the alloy secondary phases in a pseudo-dispersion state. The mechanical properties are also enhanced in the AA7075(T6)-1.5vol.% TiB_2 nanocomposite: As shown in **Figure 6 - 3**, the AA7075(T6)-1.5vol.% TiB_2 nanocomposite offers a Young's modulus of 79.0 GPa (7.0 GPa higher than the pure samples) and a hardness of 2.8 GPa (0.5 GPa higher) and 193 HV (14 HV higher).

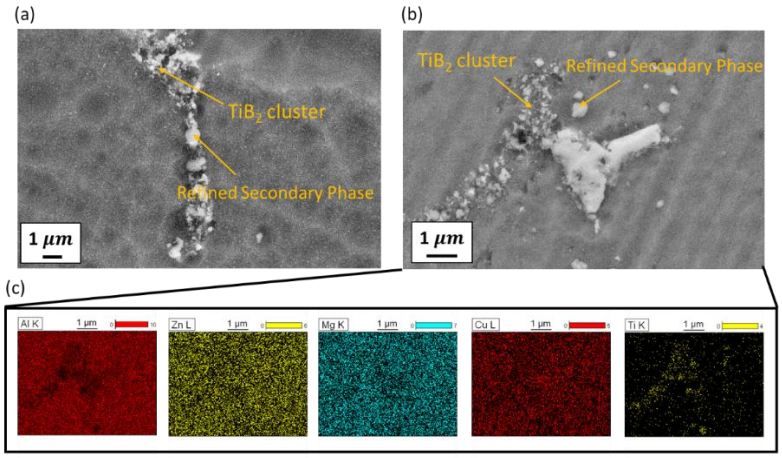

Figure 6 - 2 (a) The microstructure of AA7075(T6)-1.5 vol.% TiB_2 nanocomposites with the refined secondary phases; (b) and (c) The EDS mapping showing the element distribution in AA7075(T6)-1.5 vol.% TiB_2 nanocomposites.

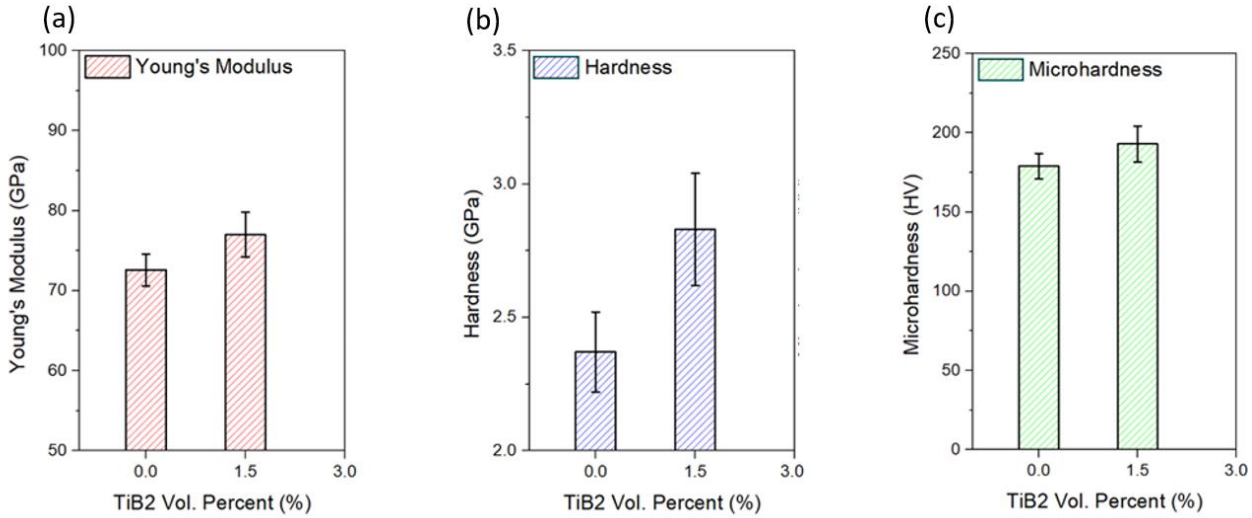

Figure 6 - 3 (a) Young's modulus, (b) Mohs hardness, and (c) Vickers hardness of pure AA7075(T6) and AA7075(T6)-1.5 vol.% TiB_2 nanocomposites.

Tribological Performance by the New Method **Figure 6 - 4** shows the real-time friction evolution of the CoF for pure AA7075(T6) and AA7075(T6)-1.5 vol.% TiB_2 nanocomposite against AA5083, Fe-A247, Fe-52100, and Si wafer counterpart surfaces, respectively. It can be

seen that the proposed measurement method gives continuous rapid CoF data collection and leads to a quicker steady measurement condition.

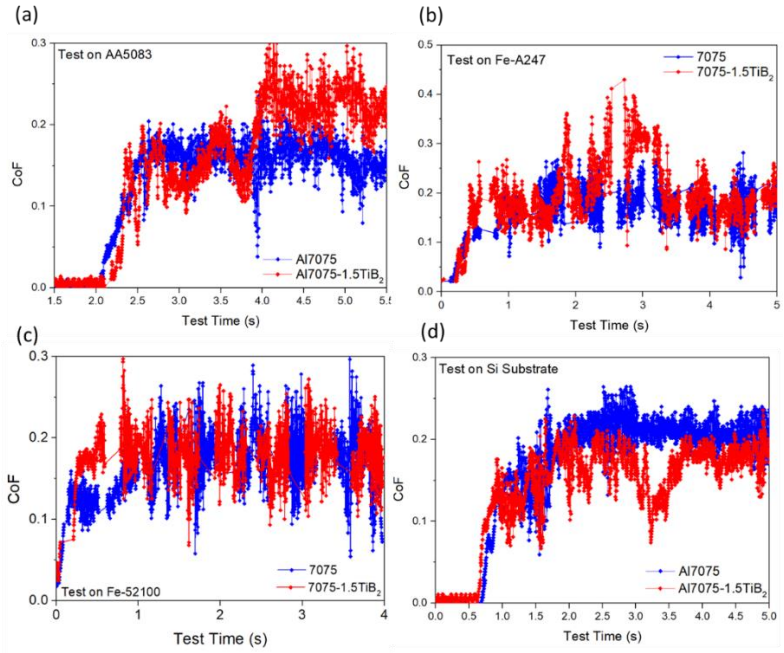

Figure 6 - 4 CoF values for AA7075(T6) and AA7075(T6)-1.5 vol.% TiB_2 nanocomposites during the measurement against (a) Marine grade AA5083 counterpart; (b) Fe-A247 iron counterpart; (c) Fe-52100 iron counterpart; and (d) Si counterpart (wafer).

After the friction tests, the averaged CoF is determined for pure AA7075(T6) and AA7075(T6)-1.5vol.% TiB_2 nanocomposites, as shown in **Figure 6 - 5**. Except for the CoF against AA5083 and Fe-A247 (**Figure 6 - 5** (a) and (b)), the incorporation of 1.5 vol.% TiB_2 in 7075(T6) alloy reduces the CoF of Fe-52100 and Si counterparts (**Figure 6 - 5** (c) and (d)). Considering the different counterpart hardnesses of AA5083, Fe-247, Fe-52100, and Si wafer, the CoF change in pure AA7075(T6) and AA7075(T6)-1.5 vol.% TiB_2 nanocomposites is further plotted in **Figure 6 - 5** (e).

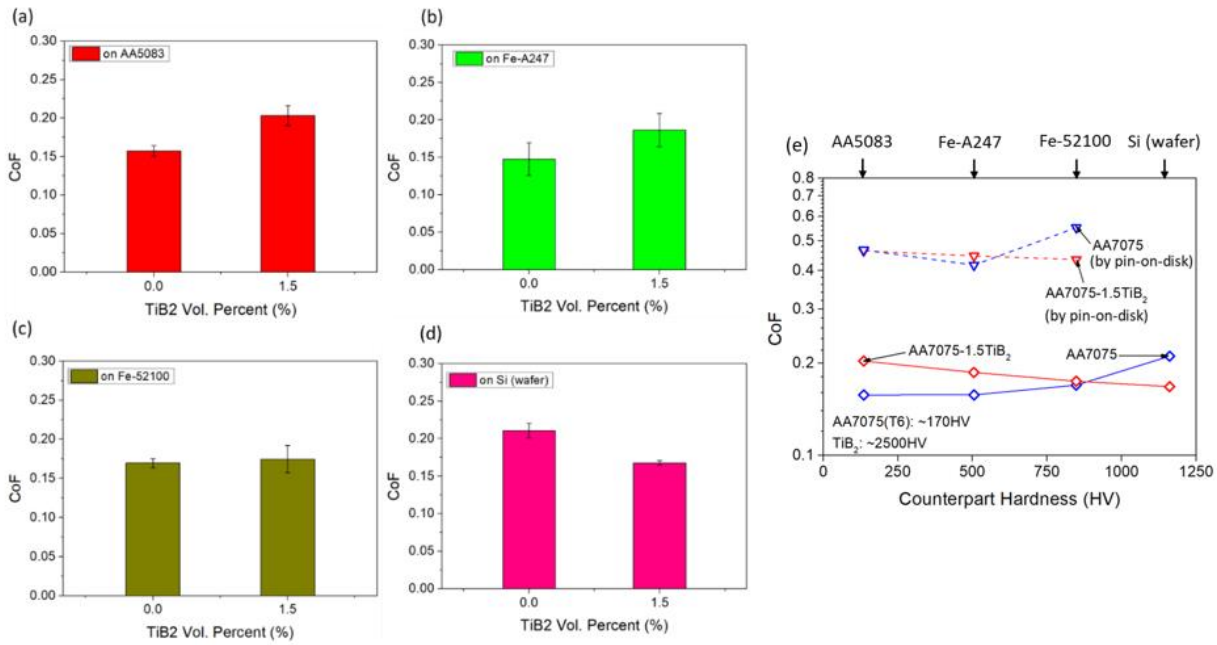

Figure 6 - 5 Comparison of the CoF values for AA7075(T6) and AA7075(T6)-1.5 vol.% TiB_2 nanocomposites during friction against (a) Marine grade AA5083 counterpart; (b) Fe-A247 iron counterpart; (c) Fe-52100 iron counterpart; and (d) Si counterpart (wafer); (e) Summary of the CoF changes with the counterpart hardness for AA7075(T6) and AA7075(T6)-1.5 vol.% TiB_2 nanocomposite, compared to the results from the traditional pin-on-disc tests in **Figure 6 - 12** and **Figure 6 - 14** of **6.4 Appendix**.

Surface Characterization Before the friction tests with the proposed method, the surface roughness of all the counterparts was recorded as a reference to the post-test surfaces, as shown in **Figure 6 - 6**. After the friction tests using the new method, the surface roughness is characterized again, as shown in **Figure 6 - 7**. It's observed that the counterpart surfaces rubbed with AA7075(T6) and AA7075(T6)-1.5 vol.% TiB_2 nanocomposites are still highly smooth, showing no typical grooves and profile changes (whereas the worn grooves and profile change can be

observed in the traditional pin-on-disc tests in **Figure 6 - 15** and **Figure 6 - 17** of **6.5 Appendix**). The roughness is only ~50-150 nm, which is similar to their initial counterpart roughness. **Figure 6 - 8** also partially shows that the proposed method is non-destructive to the surfaces, as the Ti 2p signal is clearly detectable after the proposed tests with AA7075(T6)-1.5 vol.% TiB_2 nanocomposites.

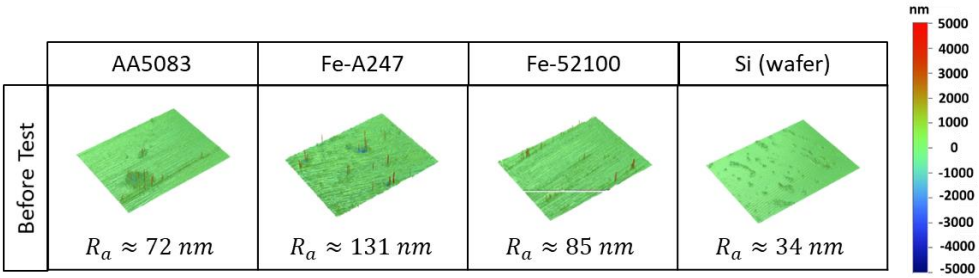

Figure 6 - 6 Surface roughness of the AA5083, Fe-A247, Fe-52100, and Si wafer counterpart surfaces before the friction tests

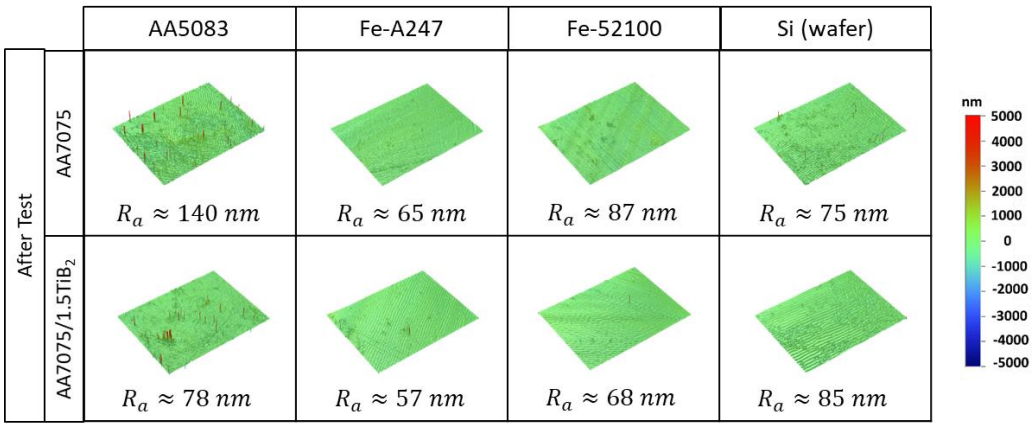

Figure 6 - 7 Surface roughness of the AA5083, Fe-A247, Fe-52100, and Si wafer counterpart surfaces after the friction tests with AA7075(T6) and AA7075(T6)-1.5 vol.% TiB_2 nanocomposites on the test track

The XPS element composition data for the post-test sample surfaces are recorded in **Figure 6 - 8** and **Figure 6 - 9**. Since Fe and Si are not the composition elements for AA7075(T6) and

AA7075(T6)-1.5 vol.% TiB_2 nanocomposites, the results confirm that there exists mutual atom transfer (e.g., Fe and Si atoms) between the 2 surfaces during the new friction tests (whereas the softer part is more likely to attach to the harder part in the traditional pin-on-disc tests, as shown in **Figure 6 - 15** and **Figure 6 - 17** of **6.5 Appendix**). Also, according to **Figure 6 - 9**, after the same new friction test processes, the Fe and Si elements have huge concentration differences between the surfaces of AA7075(T6) and AA7075(T6)-1.5 vol.% TiB_2 samples.

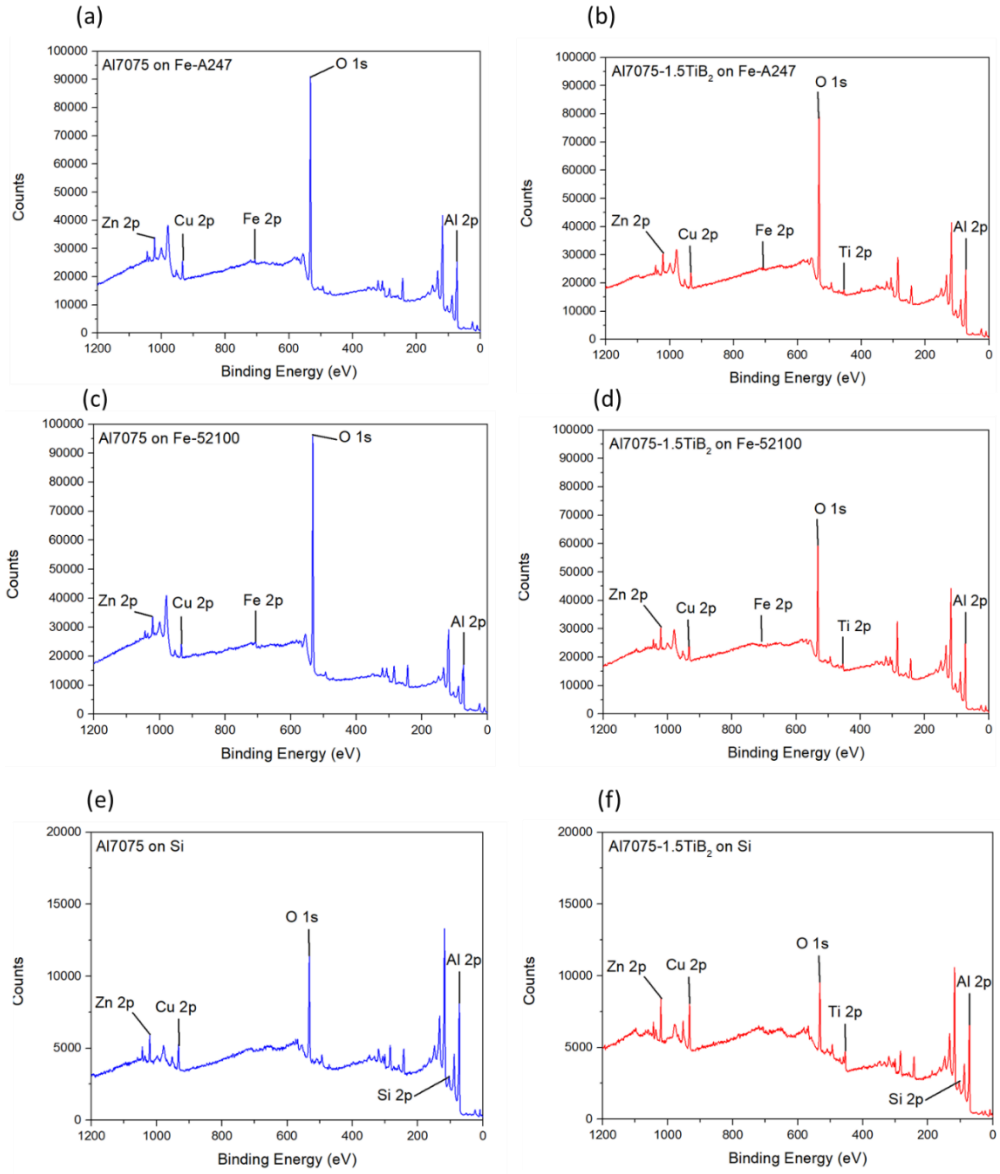

Figure 6 - 8 Surface XPS results of AA7075(T6) and AA7075(T6)-1.5 vol.% TiB_2 nanocomposites after the friction tests against Fe-A247, Fe-52100, and Si wafer counterparts

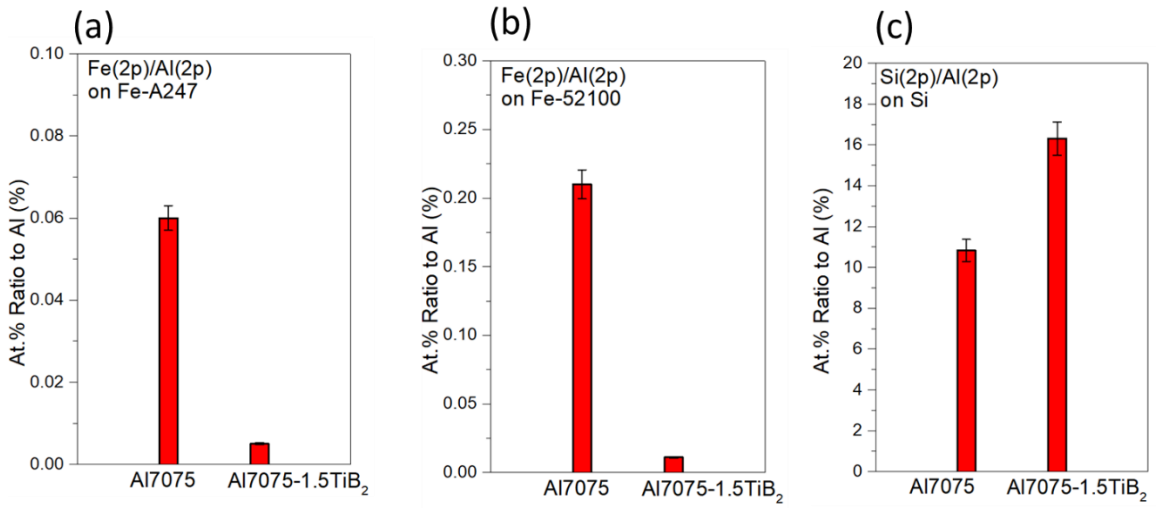

Figure 6 - 9 Surface element composition after the friction tests of AA7075(T6) and AA7075(T6)-1.5 vol.% TiB_2 nanocomposites for the elements of (a) Fe(2p) against Fe-A247 counterpart; (b) Fe(2p) against Fe-52100 counterpart; and (c) Si(2p) against Si counterpart.

6.3 Discussion

As indicated by the results in **Figure 6 - 5** from the new measurement method, the CoF of AA7075(T6) and AA7075(T6)-1.5 vol.% TiB_2 nanocomposite shows the general trend that the harder the counterpart surface is, the more effective TiB_2 nanoparticles are to reduce the CoF values. By further comparing our studies with traditional pin-on-disc test data and previous research on AA7075 nanocomposites (see **Figure 6 - 10**), it can be seen that there exists a significant difference, as almost all of the previous friction investigations underestimated the true CoF change values of the AA7075(T6) nanocomposites.

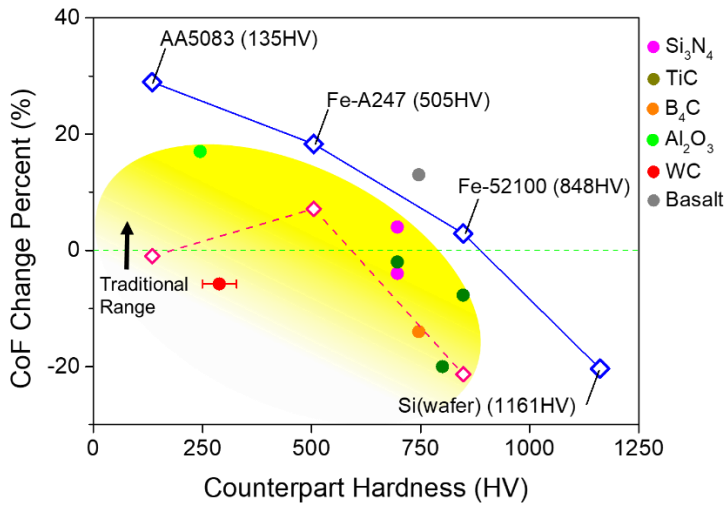

Figure 6 - 10 CoF change ratio (blue line) between AA7075(T6) and AA7075(T6)-1.5 vol.% TiB_2 nanocomposites in relation with the counterpart (i.e., AA5083, Fe-A247, Fe-52100, and Si wafer) microhardness, and the comparison with the data from the traditional pin-on-disc test (pink dashed line) and the previous studies. [164–166], [325–329]

Two characteristics concerning our new technique contribute to the trend difference: At first, the loads of ~0.1-1 kPa are much lower than the traditional tribological tests under ~100 kPa [330]. Secondly, as shown in **Figure 6 - 7**, the new method used to measure the CoF of AA7075(T6) and AA7075(T6)-1.5 vol.% TiB_2 nanocomposite does not obviously change the surface roughness (~50-150 nm). Considering these 2 factors, given the stress-assisted wear mechanism [252], the macroscopic scaling factor S to link stress and roughness could be expressed as:

$$S = exp\left(\frac{\sigma \times V_{act}}{k_B \times T}\right) \quad \textbf{(6-2)}$$

Where σ is the applied stress, and V_{act} is the extended effective activation volume. Here, V_{act} can be expressed with the surface roughness R_a $(\sim 10^{-7} - 10^{-8}\, m)$ as $V_{act} \cong R_a \times a^2$ (where a denotes the lattice parameter of ~1 nm). Therefore, with **equation (6-2)**, using $R_a \approx 10^{-7} m$ and $a \approx 1\, nm$ for calculation, the scaling factor of the pin-on-disc tests is $S \cong 11.45$,

whereas the new measurement method introduces $S \cong 1.03$. Altogether, these 2 factors rule out the effects of wear, and only the friction contribution to CoF is gauged by this new measurement method.

With these measurement method improvements, to understand the observed trend in **Figure 6 - 10**, the following 2 mechanisms are proposed and illustrated in **Figure 6 - 11**:

As shown in **Figure 6 - 5**, the CoF values of pure AA7075(T6) increases with increasing counterpart hardness; while the CoF of AA7075 with TiB_2 decreases as the counterpart hardness increases. Under the extremely low surface roughness (~nm-scale) and low normal load conditions, the effect of the microscopic contact area (i.e., A in **Figure 6 - 11**) will significantly stand out [331]. For AA7075(T6), the increase in counterpart hardness will increase the hardness difference (i.e., ΔHV in **Figure 6 - 11**), which will result in a larger contact area; On the other hand, since TiB_2 in the AA7075(T6)-TiB_2 nanocomposite is harder than any counterparts, as counterpart hardness increases, the real contact area decreases, and less shear force is needed to separate the adhesive contact between the two surfaces.

Secondly, the XPS results from **Figure 6 - 8** and **Figure 6 - 9** confirm the mutual atom transfer (e.g., Fe and Si atoms) between the 2 surfaces during the new friction tests. According to the study by P. Menezes et al. [332], when iron is transferred from the counterpart surface to AA7075(T6) and AA7075(T6)-TiB_2 nanocomposites, the transferred iron atoms and the iron-containing counterpart will interact to decrease the CoF values; It's the same case for Si counterpart. The XPS results in **Figure 6 - 8** and **Figure 6 - 9** match the trend in **Figure 6 - 5** and **Figure 6 - 10** well.

In this sense, if the hardness is close between two materials, mutual atomic-scale transfer layer from the counterparts is easily produced to enable interaction between the atoms of the same

elements (i.e., Fe or Si), and subsequently lowers the CoF. In this study, the combination of hard pin and hard disc or soft pin and soft disc is advantageous for CoF reduction, as shown in **Figure 6 - 11**.

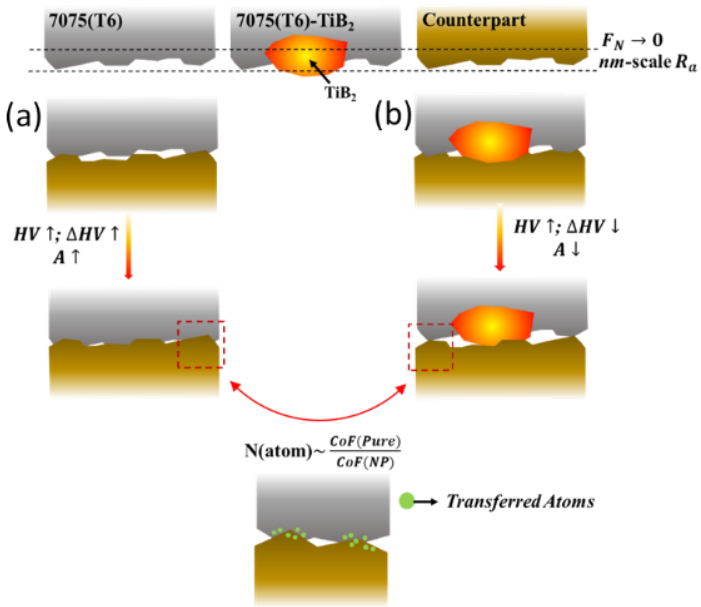

Figure 6 - 11 Illustration of the effects of tribo-pair hardness difference and atom transfer on the tribological performance of (a) AA7075(T6) and (b) AA7075(T6)-TiB_2.

6.4 Appendix: Results from Pin-on-Disc tests

Table 6 - 1 Calibration measurement between pure Cu and pure Al

Methods	Proposed Measurement	Ref. [333]	Ref. [322]
CoF	0.32 ± 0.12	0.25-0.35	~0.3-0.5

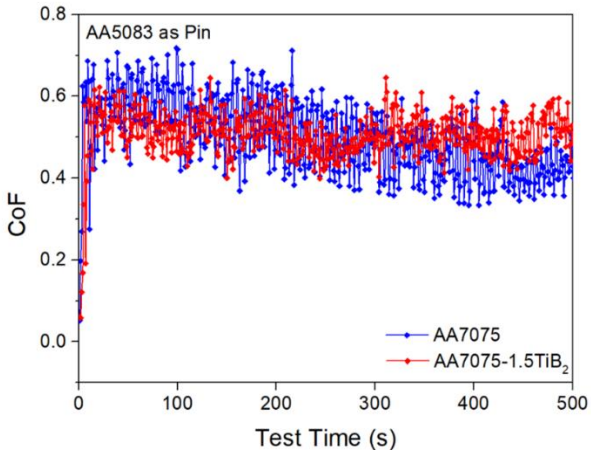

Figure 6 - 12 The CoF evolution during the pin-on-disc test with AA5083 for Al7075(T6) and Al7075(T6)-1.5TiB_2

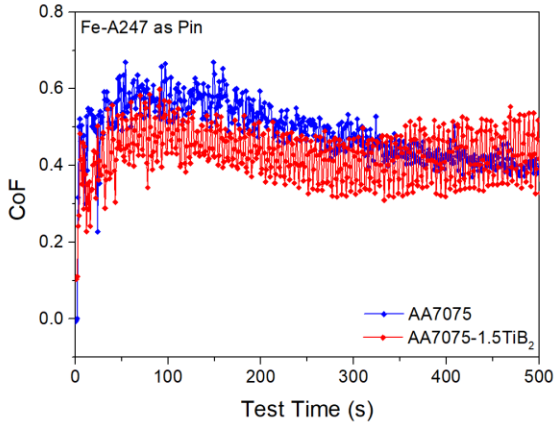

Figure 6 - 13 The CoF evolution during the pin-on-disc test with Fe-A247 for AA7075(T6) and AA7075(T6)-1.5TiB_2

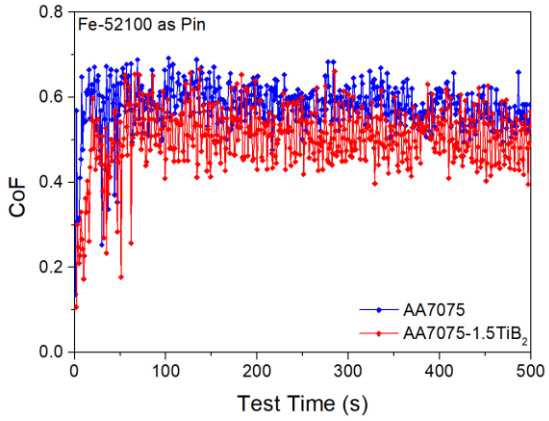

Figure 6 - 14 The CoF evolution during the pin-on-disc test with Fe-52100 for AA7075(T6) and AA7075(T6)-1.5TiB_2

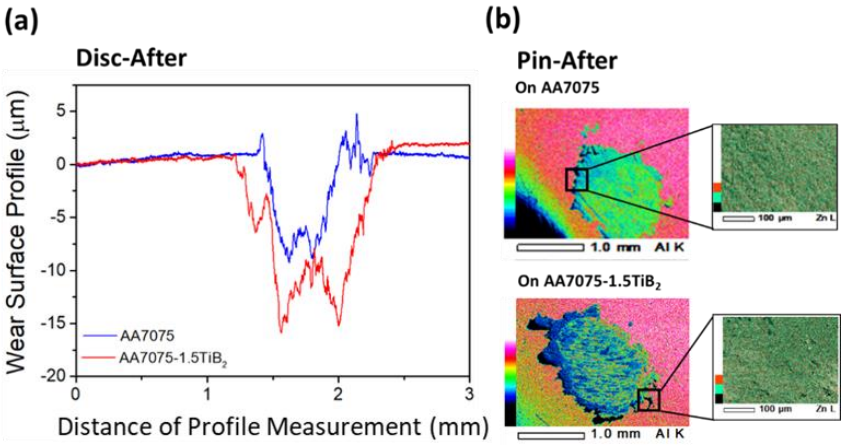

Figure 6 - 15 (a) The disc profile after the pin-on-disc test for AA7075(T6) and AA7075(T6)-1.5TiB_2 with AA5083; (b) The pin EDS mapping for Al after the pin-on-disc test against AA5083 for AA7075(T6) and AA7075(T6)-1.5TiB_2. (* Zn L line is shown, because AA5083 has little-to-no Zn, whereas Zn has a high concentration in AA7075)

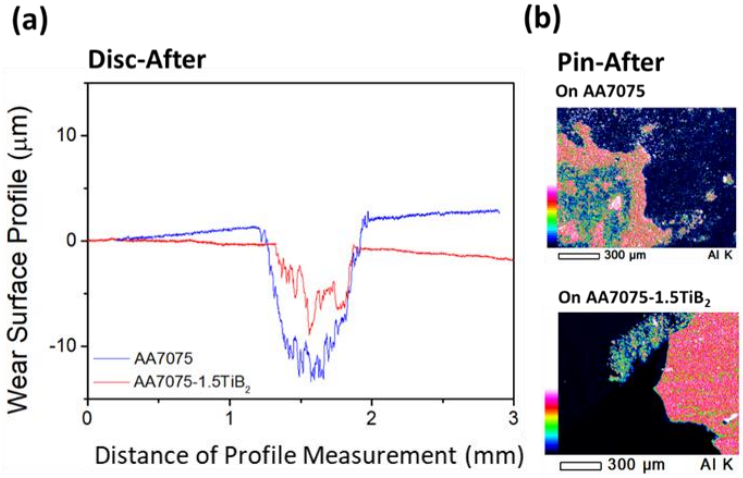

Figure 6 - 16 (a) The disc profile after the pin-on-disc test for AA7075(T6) and AA7075(T6)-1.5TiB_2 with Fe-A247; (b) The pin EDS mapping for Al after the pin-on-disc test against Fe-A247 for AA7075(T6) and AA7075(T6)-1.5TiB_2.

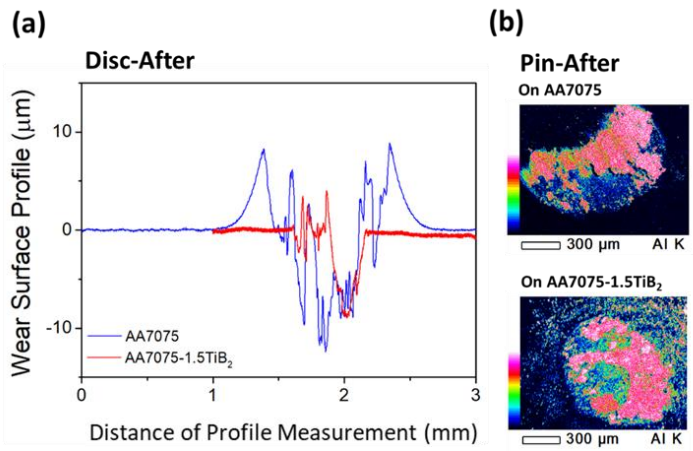

Figure 6 - 17 (a) The disc profile after the pin-on-disc test for AA7075(T6) and AA7075(T6)-1.5TiB_2 with Fe-52100; (b) The pin EDS mapping for Al after the pin-on-disc test against Fe-52100 for AA7075(T6) and AA7075(T6)-1.5TiB_2.

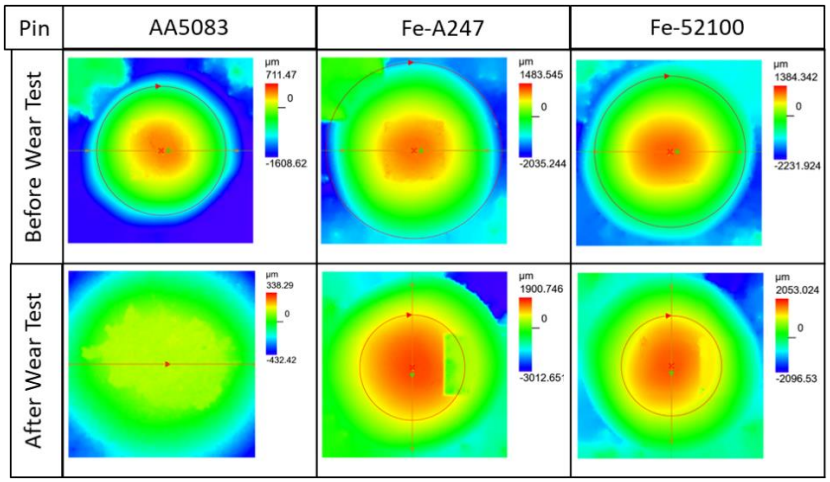

Figure 6 - 18 The pin surface profile of AA5083, Fe-A247, and Fe-52100 before and after the pin-on-disc tests on AA7075(T6)-1.5TiB_2 disc.

Figure 6 - 18 indicates that the pins after the traditional pin-on-disc tests will have severe morphology change (the active area is introduced with the height change from -1500 μm to $+1500$ μm, a magnitude far larger than the roughness change shown in **Figure 6 - 7**)

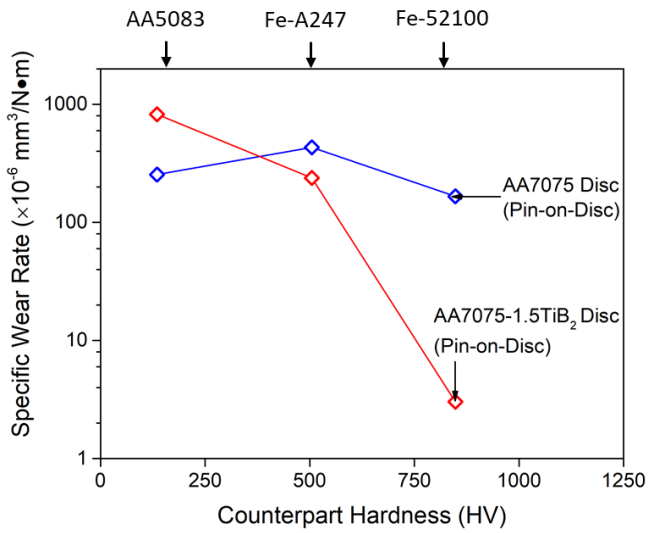

Figure 6 - 19 Wear rate by the disc worn volume of AA7075(T6) and AA7075(T6)-1.5 vol.% TiB_2

6.5 Summary

A new measurement method was applied in the tribological study to distinguish the contributions from pure friction and wear for AA7075 nanocomposites. It provides a new understanding of how TiB_2 nano-reinforcement could change the tribological performance of AA7075 on different substrates. First, the new laser-grating device enabled by a fast-response displacement measurement provides an instant non-destructive surface analysis of the true CoF in AA7075-TiB_2 nanocomposites during tribological tests. Second, an accurate substrate hardness dependence of the CoF in AA7075-TiB_2 nanocomposites is discovered, which shows a different characteristic from the traditional wear-included CoF trend. With detailed surface characterization and a quantitative analysis of wear contribution, a new theory has been established to understand the true CoF dependence on the hardness difference between parts of friction pairs. The new study is able to fully uncover the mystery of previously reported inconsistencies in the tribological performance of AA7075-TiB_2 nanocomposites. The knowledge gained in this study is of

significance for a rational design of AA7075 nanocomposites for optimized tribological performance.

CHAPTER 7 CONCLUSIONS

This study is to understand nanoparticle effects on the overall functional properties of metal matrix nanocomposites (MMNCs). To guide the rational design of high-performance metal matrix nanocomposites with balanced mechanical and functional properties, the study utilizes the nanoparticle-electron interaction as a novel angle. Therefore, the specific objectives of this research were to advance the fundamental understanding of the nanoparticle effects on electron behavior (e.g. electron concentration and electron mobility), thermophysical properties (e.g. heat capacity, thermal diffusivity, and thermal conductivity), intrinsic high-temperature chemical stability, thermal stability against oxidation, anti-corrosion performance (such as pitting, IGC, and SCC resistance), and surface anti-wear performance in Al- and cu-based nanocomposites.

To provide a reliable base for the functional property analysis of bulk MMNCs, two processing routes, i.e., *ex situ* self-dispersion method and *in situ* molten salt-assisted synthesis, were used to prepare samples. In this dissertation, Cu-based metal matrix nanocomposites were successfully fabricated by incorporating WC nanoparticles *ex situ*. This method also produced high-quality Cu-alloy nanocomposites including Cu-40Zn/WC and Cu-xAg/WC (x=10, 20, 40, 50, 60, 71.9, 80 wt.%). For Al-based nanocomposites, *in situ* molten salt assisted method has been used. This economical method produces the size-controllable ZrB_2, TiB_2 and TiC nanoparticles in the Al alloys efficiently.

With high-quality Al nanocomposite master with a high-volume percentage (~3 vol.%) of nanoparticles, high-strength Al alloy nanocomposites was fabricated by alloying and master dilution. AA7075 nanocomposites with different nanoparticles of TiC and TiB_2 (effects of nanoparticle selection) under T6 and T73 heat treatment in both casting and extrusion (effects of processing) conditions were used. Further, A206-TiC nanocomposites were cast and went through

T4 and T6 heat treatments (effects of post-processing and precipitation process). The successful fabrication of the Al alloy nanocomposites built a solid foundation for the systematic study into their functional properties.

To establish the fundamentals for functional properties, the electronic property and electron behavior have been studied first in the model systems of Al-TiB_2, Al-ZrB_2, and Al-TiC. By experimentally investigating into the low-temperature electrical conductivity and electron mobility, the electron localization model to account for the (apparent) free electron concentration in the metal matrix nanocomposites has been proposed. With this understanding, the electrical conductivity prediction model using the Fermi level difference as an indicator in Cu-WC, Cu-40 wt.% Zn/WC, and Cu-60 wt.% Ag/WC systems has been further confirmed.

Since the electrons are a dual carrier for electricity and heat and the electrical conductivity-temperature curve demonstrated a strong electron-phonon coupling, the thermal properties including heat capacity, thermal diffusivity, and thermal conductivity have been examined experimentally in Al-TiB_2, Al-ZrB_2, and Al-TiC systems. The decoupling of electron and phonon contribution to thermal transport in the Al-based nanocomposites also leads to a more accurate and efficient depiction of the interfacial thermal conductance in metals containing metallic ceramic nanoparticles inside (e.g., TiB_2, ZrB_2, TiC, and WC). This understanding gives a consistent picture among the interfacial wettability requirements for successful nanocomposite solidification processing, the electron behavior in nanocomposites, and the ultimate thermophysical response by incorporating these nanoparticles.

After the systematic study into the basic functional properties, the stability of the metal matrix nanocomposites regarding their general chemical stability was studied.

First, to guide the processing and mitigate the interfacial chemical reactions between molten metal and nanoparticles, Al-TiC system was studied as an example. On one hand, to extend the possible lower processing temperature window, Mo micro-alloying was used to mitigate the direct Al-TiC reaction at temperatures lower than 780℃. The effective segregation of Mo to the Al-TiC interface reduced the chemical reaction rate, and the resultant Mo-rich intermetallics were refined and rendered with maintained ductility. On the other hand, to study the alloy's compatibility with various nanoparticles (TiC as an example), the chemical kinetics and dynamics between Al-Si based alloy system and TiC was investigated. The selection of suitable alloying elements is of great importance to reduce or eliminate the Si-TiC reaction in Al-Si-based nanocomposites. The element segregation dynamics still governed the reaction process, and the AlSi10Mg-TiC proved to have a higher chemical reaction of Si and TiC due to the segregation of Mg and Si and the enthalpy-releasing Mg_2Si formation process. Moreover, the replacement of Mg by Ag (i.e., AlSi10Ag-TiC nanocomposites) also provided a deterministic evidence for the less severe reaction by TiC instability in molten Al systems. In brief, this part of the study confirmed the effectiveness of using (micro-)alloying and element segregation for processing Al alloys and increasing the overall nanoparticle stability.

As metal degradation is heavily linked with oxidation and influenced by oxidation kinetics, the anti-oxidation performance in various metal matrix nanocomposites was examined. For diffusion-controlled oxidation process, Cu-40 wt.% Zn/WC nanocomposites were uased to study the crystalline ZnO growth kinetics and dynamics. The WC nanoparticles were found to block the diffusion path of Zn and reduce the normal stress to the diffusion path via the load-bearing transfer. Chemically stable nanoparticles like WC were proven to be effective to control and reduce the diffusion-dominated thermal oxidation. When investigating the self-limiting thermal oxidation

process, Al-ZrB_2 nanocomposites have been used for the surface oxidation characterization. At lower temperature, while the self-limiting oxide layer of amorphous Al_2O_3 would stop at a thinner layer (less than the size of ZrB_2 nanoparticles), the incorporation of nanoparticles would rupture the dense oxide film and increase the oxidation speed. At higher temperature, the self-limiting oxide layer would not be influenced by the nanoparticle size directly. Instead, the ZrB_2 nanoparticles would increase the Mott potential and oxidation activation energy barrier simultaneously. This finding is consistent with the Mott-Cabrera model for Al and confirms the reason for the mitigated oxidation process under higher temperature in Al-ZrB_2. With the information for the interaction between nanoparticles of diffusion-controlled and self-limiting oxidation process, the thermal oxidation process of a more complex, industrially important AA7075 alloy nanocomposites (i.e., AA7075-TiB_2)was studied. At a lower temperature (e.g., 400℃), the TiB_2 nanoparticles also rupture the self-limiting Al_2O_3 film. When the temperature is above the solutionizing temperature (e.g. 600 ℃) of the $MgZn_2$ secondary phases, TiB_2 nanoparticles help increase the element (Zn and O) concentration gradient and reduce the roughness of the wavy Al_2O_3 film. More importantly, Zn can be oxidized to a large penetration depth in AA7075-TiB_2 even after the Al_2O_3 oxide film is formed.

After the oxidation mechanism was clarified, anti-corrosion performance of metal matrix nanocomposites has been studied in detail. The pitting, IGC, and SCC behavior of AA7075 and A206 nanocomposites after casting and extrusion under different heat treatments were systematically studied. To understand the different corrosion mechanisms in pitting, IGC, and SCC processes, the electrochemical signatures of these nanocomposites, as well as their microstructural characteristics (including grain size, grain boundary features, and precipitates) and surface conditions (e.g., element oxidation states and post-corrosion morphology), have been studied. The

incorporation of nanoparticles will refine the grains, increase the LAGB fraction, reduce the PFZs, and reduce the electrical conductivity, which are all advantageous to increasing the anti-corrosion performance. Meanwhile, nanoparticles of TiB_2 and TiC will introduce a more effective passivation behavior than their pure AA7075 matrix, which is consistent with the anti-oxidation performance study influenced by nanoparticles. This passivation activity change by nanoparticles leads to an enhanced anti-corrosion performance, particularly IGC resistance. Moreover, the electrochemical potential analysis proves that the nanoparticles could act differently in AA7075 and A206, because the GBPs are mainly strengthened for anti-corrosion performance in AA7075, and the GBs as the weakest location are made stabler in A206 systems. On the contrary, SCC process is a procedure dominated by both corrosion performance and mechanical response, the anti-SCC performance of AA7075 and A206 nanocomposites is significantly improved under lower stress intensity range, while at the higher stress intensity range they witness a slightly higher crack propagation speed, possibly due to a pseudo-dispersed nanoparticles induced lower ductility at GBs. By lowering the nanoparticle volume percentage (in A206-TiC, T4 as an example), it suggests that a less nanoparticle loading could better mitigate the high-stress-intensity SCC propagation for an improved SCC-susceptibility. It suggsts that the anti-corrosion behavior, particularly the anti-SCC performance, of AA7075 and A206 nanocomposites could be further enhanced, if the nanoparticles could be better dispersed.

To cater to the urgent desires of applying metal matrix nanocomposites in anti-wear and anti-friction applications, the tribological performance of AA7075-TiB_2 was studied with the new setup for ultra-sensitive normal and frictional stress detection. The tribological contributions from pure friction and wear for AA7075-TiB_2 nanocomposites has been distinguished. With this new high-resolution force-sensing setup, an accurate substrate hardness dependence of the CoF in

AA7075-TiB_2 nanocomposites is discovered, and a new theory has been established to understand the true CoF dependence on the hardness difference between parts of friction pairs. The new study is able to fully uncover the mystery of previously reported inconsistencies in the tribological performance of AA7075-TiB_2 nanocomposites. The knowledge gained in this study is of significance for a rational design of AA7075 nanocomposites for optimized tribological performance.

In summary, the study in this dissertation comprehensively investigated the effects of the nanoparticles on the functional properties of important metal/alloy systems. By linking electron behavior among these properties, the systematic study on the electrical and thermophysical property builds a fundamental basis to understand other complicated functional properties in metal matrix nanocomposites. The detailed discussion into the chemical stability governed by the matrix-nanoparticle interface, the anti-oxidation behavior, the overall anti-corrosion performance, and the surface engineering by metal nanocomposites has provided a unique insight for effectively designing the novel metallic systems for a long-term service stability in complex environments.

CHAPTER 8 RECOMMENDATION FOR FUTURE WORK

This chapter is providing a short discussion about potential future work. Scalable and controllable synthesis and fabrication of high-quality metals containing nanoparticles are important for their widespread applications in industry, and their tailored functional properties with enhanced mechanical performance will play an irreplaceable role in new alloy design, advanced manufacturing, and open new space for novel applications.

8.1 Segregation-assisted nanoparticle dispersion and MMNC fabrication

The *in situ* and *ex situ* methods have proven the effectiveness of nanoparticle synthesis and size control. However, the processing route is still largely dependent on the choice of suitable metal matrices and nanoparticles to fulfill the wettability requirements for nanoparticle dispersion. Based on the study in this dissertation, a nanoparticle-involved segregation phenomenon (e.g., Mo-segregation to nanoparticle-matrix interface in Al-Mo alloy, and Mg-/Si-segregation to nanoparticle surfaces for continuing chemical reaction in Al-Si alloy) has already been confirmed. With this insights, the interface between nanoparticles and metal/alloy matrices could be potentially tuned by introducing controllable element segregation or interfacial chemical reaction. With this method, the interface could form an effective interfacial layer (e.g., TiC would form Al_4C_3 to wet Al) with potentially less lattice mismatch. If successful, the traditional limits by interfacial wettability between nanoparticles and metal matrices could be bypassed. More importantly, the tuned interface could offer a better load bearing transfer efficiency (to enhance mechanical properties) and also lead to more exciting interface-dominated functional properties. The homogeneity and uniformness of nanoparticle dispersion could be further improved.

With all these benefits, since the degradation mitigation like anti-SCC performance at high stress intensity also requires a better nanoparticle-matrix/precipitate interface, the interfacial engineering could also potentially introduce a better crack deflection capacility by maintaining the ductility. Second, the better interfacial segregation layer could reduce the abrupt electrochemical property change around the nanoparticles, which will lower the micro-galvanic current, if nanoparticle-induced interfaces adjacent to nanoparticle-dense zone are exposed to corrosive media. Finally, because the controllable interfacial segregation could incorporate a wider variety of nanoparticles, more electrochemically similar nanoparticles (traditionally hard to distribute and easy to sinter/agglomerate) like CrB_2 (with a corrosion potential of -370 mV [334]), ZrB_2 (with a corrosion potential of -600 ~ -400 mV [335]) and Fe(Mo)N (with a corrosion potential of -700 ~ -500 mV [336]) could reduce the interface-determined micro-galvanic corrosion in the nanoparticle-dense region and assist with the SCC-resistance under high stress intensity. Based on these facts, this method could be promising to compensate for lowering the nanoparticle volume percentage directly and losing the advantages of microstructural modification by nanoparticles.

8.2 Application-oriented thermophysical design of MMNCs

Metals are unique due to the high concentration of electrons, which are the fundamental particles determining their overall thermophysical properties. With the interface engineering between various nanoparticles and metal/alloy matrices, given the different electronic structures, band structures, and microstructures after nanoparticle addition, the thermophysical properties could be tuned accordingly. Catering to the needs of practical applications (e.g., heat sinks, DC/AC electrical conductor in power transmission industry, and radiation/electromagnetic shielding materials in telecommunication), metal matrix nanocomposites with tailored properties could

overcome the difficulties encountered by traditional metals/alloys. In brief, the combination of properties from metals/alloys and heterogeneous phases of nanoparticles (e.g., insulating ceramics like Al_2O_3, metallic ceramics like Ti_5Si_3, semi-conductive intermetallics like Mg_2Sn and Mg_2Si) could yield desired non-linear properties for these novel areas.

8.3 Applications of MMNCs in harsh/extreme environments

Owing to the active electrons in metals/alloys, they are also difficult for use in long-term service in harsh environments (e.g., in radiation-influenced nuclearapplications, or in bio-implantation environments). The main reasons for these failures include weak grain boundary, heterogeneous weak points compared with the matrix (e.g., the inner-grain precipitates), and potential activation of electrons to escalate chemical activity, etc. These failures would also result in creep, fatigue, corrosion, wear, or the combination (e.g., tribocorrosion, corrosion fatigue, and wear-creep interaction).

Further study could integrate mechanical property with functional properties for design of novel metal matrix nanocomposites in the harsh and extreme environments. The correlation from mechanical and functional properties to defects (e.g., dislocations, grain boundaries), electrons, matrix (phonons), and nanoparticles could extend the understanding of "(micro-)structure-property" relationship under the framework of "structure-electron-property" interaction. This pathway could have far-reaching impacts for control failure mechanisms to enable anti-failure metal/alloy nanocomposites in the harsh environments. If successful, this direction could contribute significantly to global sustainability through emission reduction and materials' life-time service enhancement.

8.4 Functional properties of MMNCs by advanced manufacturing

Recently, advanced manufacturing techniques are evolving in an unprecedented pace. Methods of additive manufacturing like emergent wire arc additive manufacturing (WAAM), selective laser melting (SLM), and laser solid forming (LSF) offer exciting opportunities to develop and fabricate alloys under far non-equilibrium process (with a typical solidification temperature gradient of $>10^4 - 10^5$ K/s), because the diffusion-controlled manufacturing physics may not be effective. The processing will therefore inevitably change the microstructures (i.e., transition interface and matrix structures) and create a strongly coupled material system for electrons, matrices (phonons), and defects. For example, the ultrafine grains usually made possible by SLM could have a length scale comparable to the MFP of electrons and phonons, which wouldoffer interesting and exciting properties.

Therefore, the study in this dissertation establish a foundation to continue the future study into functional properties of metal matrix nanocomposites in emerging advanced manufacturing techniques. Particularly, the relationship between the non-equilibrium processing parameters and the resultant properties would yield fruitful insights into the development and applications of novel nanotechnology enhanced metals and alloys.

REFERENCE

1. Chen, L.-Y. *et al.* Processing and properties of magnesium containing a dense uniform dispersion of nanoparticles. *Nature* **528**, 539–543 (2015).
2. Pan, S. *et al.* Effect of electron concentration on electrical conductivity in in situ Al-TiB2 nanocomposites. *Appl. Phys. Lett.* **116**, 014102 (2020).
3. Saboori, A., Dadkhah, M., Fino, P. & Pavese, M. An Overview of Metal Matrix Nanocomposites Reinforced with Graphene Nanoplatelets; Mechanical, Electrical and Thermophysical Properties. *Metals* **8**, 423 (2018).
4. Geng, R., Jia, S.-Q., Qiu, F., Zhao, Q.-L. & Jiang, Q.-C. Effects of nanosized TiC and TiB2 particles on the corrosion behavior of Al-Mg-Si alloy. *Corrosion Science* 108479 (2020) doi:10.1016/j.corsci.2020.108479.
5. Javadi, A., Pan, S., Cao, C. & Li, X. High Strength and High Electrical Conductivity Al Nanocomposites for DC Transmission Cable Applications. 10 (2021).
6. Zhang, D. *et al.* Additive manufacturing of ultrafine-grained high-strength titanium alloys. *Nature* **576**, 91–95 (2019).
7. Wen, X. *et al.* Laser solid forming additive manufacturing TiB2 reinforced 2024Al composite: Microstructure and mechanical properties. *Materials Science and Engineering: A* **745**, 319–325 (2019).
8. Kwon, Y.-S., Dudina, D. V., Korchagin, M. A. & Lomovsky, O. I. Microstructure changes in TiB2-Cu nanocomposite under sintering. *Journal of Materials Science* **39**, 5325–5331 (2004).
9. Li, Z. *et al.* Regain Strain-Hardening in High-Strength Metals by Nanofiller Incorporation at Grain Boundaries. *Nano Lett.* (2018) doi:10.1021/acs.nanolett.8b02375.

10. Zhang, Y. & Li, X. Bioinspired, Graphene/Al2O3 Doubly Reinforced Aluminum Composites with High Strength and Toughness. *Nano Lett.* **17**, 6907–6915 (2017).

11. Yi, L.-F., Yoshida, N., Yamamoto, T., Onda, T. & Chen, Z.-C. Microstructure and thermal/mechanical properties of hot-extruded aluminum/graphite composites with Al–Si alloy addition. *J Mater Sci* **54**, 9933–9944 (2019).

12. Fang, H., Bai, S.-L. & Wong, C. P. Microstructure engineering of graphene towards highly thermal conductive composites. *Composites Part A: Applied Science and Manufacturing* **112**, 216–238 (2018).

13. Yoshida, K. & Morigami, H. Thermal properties of diamond/copper composite material. *Microelectronics Reliability* **44**, 303–308 (2004).

14. Cao, C. *et al.* Bulk ultrafine grained/nanocrystalline metals via slow cooling. *Science Advances* **5**, eaaw2398 (2019).

15. Zhang, C. J. *et al.* A titanium composite with dual reinforcements of micrometer sized TiB and submicrometer sized Y2O3. *Materials Letters* **233**, 242–245 (2018).

16. Chen, X.-H. & Yan, H. Solid–liquid interface dynamics during solidification of Al 7075–Al2O3np based metal matrix composites. *Materials & Design* **94**, 148–158 (2016).

17. Liu, Y. Q., Cong, H. T. & Cheng, H. M. Thermal properties of nanocrystalline Al composites reinforced by AlN nanoparticles. *Journal of Materials Research* **24**, 24–31 (2009).

18. Popov, V. A. *et al.* Particulate metal matrix composites development on the basis of in situ synthesis of TiC reinforcing nanoparticles during mechanical alloying. *Journal of Alloys and Compounds* **707**, 365–370 (2017).

19. Yang, H. *et al.* Microstructure and mechanical properties at both room and high temperature of in-situ TiC reinforced Al–4.5Cu matrix nanocomposite. *Journal of Alloys and Compounds* (2018) doi:10.1016/j.jallcom.2018.07.045.

20. Zhang, Y., Choudhuri, D., Scharf, T. W., Descartes, S. & Chromik, R. R. Tribologically induced nanolaminate in a cold-sprayed WC-reinforced Cu matrix composite: a key to high wear resistance. *Materials & Design* **182**, 108009 (2019).

21. Xie, J., Zeng, W., Zhou, D. & Zhang, D. Microstructure and properties of a nanocrystalline Cu-Al-NbC composite with high strength and good conductivity. *Materials Letters* **214**, 174–177 (2018).

22. Eustathopoulos, N., Nicholas, M. G. & Drevet, B. *Wettability at high temperatures*. (Pergamon, 1999).

23. Zou, C. *et al.* Effect of La addition on the particle characteristics, mechanical and electrical properties of in situ Cu-TiB2 composites. *Journal of Alloys and Compounds* **687**, 312–319 (2016).

24. Yao, G., Pan, S., Cao, C., Sokoluk, M. & Li, X. Nanoparticle-enabled phase modification (nano-treating) of CuZrSi pseudo-binary alloy. *Materialia* **14**, 100897 (2020).

25. Sokoluk, M., Cao, C., Pan, S. & Li, X. Nanoparticle-enabled phase control for arc welding of unweldable aluminum alloy 7075. *Nature Communications* **10**, 98 (2019).

26. Pan, S. *et al.* New study on tribological performance of AA7075-TiB2 nanocomposites. *Tribology International* 106565 (2020) doi:10.1016/j.triboint.2020.106565.

27. Zeng, W. *et al.* Bulk Cu-NbC nanocomposites with high strength and high electrical conductivity. *Journal of Alloys and Compounds* **745**, 55–62 (2018).

28. Yao, G. *et al.* Thermally stable ultrafine grained copper induced by CrB/CrB2 microparticles with surface nanofeatures via regular casting. *Journal of Materials Science & Technology* (2020) doi:10.1016/j.jmst.2020.03.052.

29. Xu, C. L. *et al.* Fabrication of aluminum–carbon nanotube composites and their electrical properties. *Carbon* **37**, 855–858 (1999).

30. Huang, G., Shen, Y., Guo, R. & Guan, W. Fabrication of tungsten particles reinforced aluminum matrix composites using multi-pass friction stir processing: Evaluation of microstructural, mechanical and electrical behavior. *Materials Science and Engineering: A* **674**, 504–513 (2016).

31. Lartigue-Korinek, S. *et al.* Interfaces and defects in a successfully hot-rolled steel-based composite Fe–TiB2. *Acta Materialia* **98**, 297–305 (2015).

32. Javadi, A., Pan, S. & Li, X. Manufacturing of Al and Mg nanocomposite microparticles. *Manufacturing Letters* **17**, 23–26 (2018).

33. Cai, Y., Tan, M. J., Shen, G. J. & Su, H. Q. Microstructure and heterogeneous nucleation phenomena in cast SiC particles reinforced magnesium composite. *Materials Science and Engineering: A* **282**, 232–239 (2000).

34. Wang, M. *et al.* Achieving high strength and ductility in graphene/magnesium composite via an in-situ reaction wetting process. *Carbon* **139**, 954–963 (2018).

35. Guan, Z. *et al.* Highly Ductile Zn-2Fe-WC Nanocomposite as Biodegradable Material. *Metall Mater Trans A* (2020) doi:10.1007/s11661-020-05878-y.

36. Candel, J. J., Amigó, V., Ramos, J. A. & Busquets, D. Sliding wear resistance of TiCp reinforced titanium composite coating produced by laser cladding. *Surface and Coatings Technology* **204**, 3161–3166 (2010).

37. Reese, C. W. *et al.* In Situ Al-TiC Composites Fabricated by Self-propagating High-Temperature Reaction: Insights on Reaction Pathways and Their Microstructural Signatures. *Metall and Mat Trans A* (2020) doi:10.1007/s11661-020-05786-1.

38. Zhang, Q. & Chen, D. L. A model for predicting the particle size dependence of the low cycle fatigue life in discontinuously reinforced MMCs. *Scripta Materialia* **51**, 863–867 (2004).

39. Dieter, G. E. & Bacon, D. *Mechanical Metallurgy*. (McGraw-Hill, 1988).

40. Sanaty-Zadeh, A. Comparison between current models for the strength of particulate-reinforced metal matrix nanocomposites with emphasis on consideration of Hall–Petch effect. *Materials Science and Engineering: A* **531**, 112–118 (2012).

41. Pan, S., Sokoluk, M., Cao, C., Guan, Z. & Li, X. Facile fabrication and enhanced properties of Cu-40 wt% Zn/WC nanocomposite. *Journal of Alloys and Compounds* (2019) doi:10.1016/j.jallcom.2019.01.022.

42. Hull, D. & Bacon, D. J. *Introduction to Dislocations*. (Butterworth-Heinemann, 2001).

43. Nardone, V. C. & Prewo, K. M. On the strength of discontinuous silicon carbide reinforced aluminum composites. *Scripta Metallurgica* **20**, 43–48 (1986).

44. Mingo, N., Hauser, D., Kobayashi, N. P., Plissonnier, M. & Shakouri, A. "Nanoparticle-in-Alloy" Approach to Efficient Thermoelectrics: Silicides in SiGe. *Nano Lett.* **9**, 711–715 (2009).

45. Wang, F. *et al.* In-situ fabrication and characterization of ultrafine structured Cu–TiC composites with high strength and high conductivity by mechanical milling. *Journal of Alloys and Compounds* **657**, 122–132 (2016).

46. Bahk, J.-H. *et al.* Thermoelectric power factor enhancement by ionized nanoparticle scattering. *Appl. Phys. Lett.* **99**, 072118 (2011).

47. Yang, M., Weng, L., Zhu, H., Fan, T. & Zhang, D. Simultaneously enhancing the strength, ductility and conductivity of copper matrix composites with graphene nanoribbons. *Carbon* **118**, 250–260 (2017).

48. Subramaniam, C. *et al.* One hundred fold increase in current carrying capacity in a carbon nanotube–copper composite. *Nat Commun* **4**, (2013).

49. Selezneva, E. *et al.* Thermoelectric Transport in InGaAs with High Concentrationof Rare-Earth TbAs Embedded Nanoparticles. *Journal of Elec Materi* **41**, 1820–1825 (2012).

50. Hou, J. P. *et al.* Three principles for preparing Al wire with high strength and high electrical conductivity. *Journal of Materials Science & Technology* **35**, 742–751 (2019).

51. Yao, G. *et al.* High-performance copper reinforced with dispersed nanoparticles. *J Mater Sci* (2018) doi:10.1007/s10853-018-3152-0.

52. Khobragade, N., Sikdar, K., Kumar, B., Bera, S. & Roy, D. Mechanical and electrical properties of copper-graphene nanocomposite fabricated by high pressure torsion. *Journal of Alloys and Compounds* **776**, 123–132 (2019).

53. Chang, S.-Y., Chen, C.-F., Lin, S.-J. & Kattamis, T. Z. Electrical resistivity of metal matrix composites. *Acta Materialia* **51**, 6291–6302 (2003).

54. Tian, L., Anderson, I., Riedemann, T. & Russell, A. Modeling the electrical resistivity of deformation processed metal–metal composites. *Acta Materialia* **77**, 151–161 (2014).

55. Huang, B., Hishinuma, Y., Noto, H. & Muroga, T. Mechanochemical processing of Cu-Y2O3 alloy by MA-HIP for heat sink materials application. *Fusion Engineering and Design* **140**, 33–40 (2019).

56. Zhukov, I. A. *et al*. The Impact of Particle Reinforcement with Al2O3, TiB2, and TiC and Severe Plastic Deformation Treatment on the Combination of Strength and Electrical Conductivity of Pure Aluminum. *Metals* **9**, 65 (2019).

57. Cui, X., Cui, H., Wu, Y. & Liu, X. The improvement of electrical conductivity of hypoeutectic Al-Si alloys achieved by composite melt treatment. *Journal of Alloys and Compounds* **788**, 1322–1328 (2019).

58. Casati, R. & Vedani, M. Metal Matrix Composites Reinforced by Nano-Particles—A Review. *Metals* **4**, 65–83 (2014).

59. Ma, C., Chen, L., Cao, C. & Li, X. Nanoparticle-induced unusual melting and solidification behaviours of metals. *Nature Communications* **8**, 14178 (2017).

60. Parker, W. J., Jenkins, R. J., Butler, C. P. & Abbott, G. L. Flash Method of Determining Thermal Diffusivity, Heat Capacity, and Thermal Conductivity. *Journal of Applied Physics* **32**, 1679–1684 (1961).

61. Fang, H., Bai, S.-L. & Wong, C. P. "White graphene" – hexagonal boron nitride based polymeric composites and their application in thermal management. *Composites Communications* **2**, 19–24 (2016).

62. Davis, L. C. & Artz, B. E. Thermal conductivity of metal-matrix composites. *Journal of Applied Physics* **77**, 4954–4960 (1995).

63. Zhang, Y., Zhang, H. L., Wu, J. H. & Wang, X. T. Enhanced thermal conductivity in copper matrix composites reinforced with titanium-coated diamond particles. *Scripta Materialia* **65**, 1097–1100 (2011).

64. Wagih, A., Abu-Oqail, A. & Fathy, A. Effect of GNPs content on thermal and mechanical properties of a novel hybrid Cu-Al2O3/GNPs coated Ag nanocomposite. *Ceramics International* **45**, 1115–1124 (2019).

65. Uddin, S. M. *et al.* Effect of size and shape of metal particles to improve hardness and electrical properties of carbon nanotube reinforced copper and copper alloy composites. *Composites Science and Technology* **70**, 2253–2257 (2010).

66. Chu, K. *et al.* Thermal conductivity of SPS consolidated Cu/diamond composites with Cr-coated diamond particles. *Journal of Alloys and Compounds* **490**, 453–458 (2010).

67. Zhao, Q., Tan, S., Xie, M., Liu, Y. & Yi, J. A study on the CNTs-Ag composites prepared based on spark plasma sintering and improved electroless plating assisted by ultrasonic spray atomization. *Journal of Alloys and Compounds* **737**, 31–38 (2018).

68. Bakshi, S. R., Lahiri, D. & Agarwal, A. Carbon nanotube reinforced metal matrix composites - a review. *International Materials Reviews* **55**, 41–64 (2010).

69. Kidalov, S., Shakhov, F., Kidalov, S. V. & Shakhov, F. M. Thermal Conductivity of Diamond Composites. *Materials* **2**, 2467–2495 (2009).

70. Guan, Z., Hwang, I., Pan, S. & Li, X. Scalable Manufacturing of AgCu^40 (wt.%)-WC Nanocomposite Microwires. *J. Micro Nano-Manuf* (2018) doi:10.1115/1.4040558.

71. Gobalakrishnan, B., Lakshminarayanan, P. R. & Varahamoorthi, R. Mechanical Properties of Al 6061/TiB2 In-Situ Formed Metal Matrix Composites. https://www.ingentaconnect.com/contentone/asp/jamr/2018/00000013/00000001/art00019 (2018) doi:info:doi/10.1166/jamr.2018.1368.

72. Gasparov, V. A. *et al.* On electron transport in ZrB12, ZrB2, and MgB2 in normal state. *Jetp Lett.* **80**, 330–334 (2004).

73. Kim, J. & Kang, S. Elastic and thermo-physical properties of TiC, TiN, and their intermediate composition alloys using ab initio calculations. *Journal of Alloys and Compounds* **528**, 20–27 (2012).

74. Pan, S., Yao, G., Sokoluk, M., Guan, Z. & Li, X. Enhanced thermal stability in Cu-40 wt% Zn/WC nanocomposite. *Materials & Design* 107964 (2019) doi:10.1016/j.matdes.2019.107964.

75. Hasselman, D. P. H., Donaldson, K. Y. & Geiger, A. L. Effect of Reinforcement Particle Size on the Thermal Conductivity of a Particulate-Silicon Carbide-Reinforced Aluminum Matrix Composite. *J American Ceramic Society* **75**, 3137–3140 (1992).

76. Ma, C., Zhao, J., Cao, C., Lin, T.-C. & Li, X. Fundamental Study on Laser Interactions With Nanoparticles-Reinforced Metals—Part I: Effect of Nanoparticles on Optical Reflectivity, Specific Heat, and Thermal Conductivity. *J. Manuf. Sci. Eng* **138**, 121001-121001–7 (2016).

77. Pan, S., Guan, Z. & Li, X. Unusual thermal performance in Cu-60Ag by WC nanoparticles. *Materials Science and Engineering: B* **265**, 115010 (2021).

78. Kida, M., Weber, L., Monachon, C. & Mortensen, A. Thermal conductivity and interfacial conductance of AlN particle reinforced metal matrix composites. *Journal of Applied Physics* **109**, 064907 (2011).

79. Kawai, C. Effect of Interfacial Reaction on the Thermal Conductivity of Al–SiC Composites with SiC Dispersions. *Journal of the American Ceramic Society* **84**, 896–898 (2001).

80. Bai, G. *et al.* Tailoring interface structure and enhancing thermal conductivity of Cu/diamond composites by alloying boron to the Cu matrix. *Materials Characterization* **152**, 265–275 (2019).

81. Guo, L., Hodson, S. L., Fisher, T. S. & Xu, X. Heat Transfer Across Metal-Dielectric Interfaces During Ultrafast-Laser Heating. *J. Heat Transfer* **134**, 042402-042402–5 (2012).

82. Hong, Y., Li, L., Cheng Zeng, X. & Zhang, J. Tuning thermal contact conductance at graphene–copper interface via surface nanoengineering. *Nanoscale* **7**, 6286–6294 (2015).

83. Cao, H. *et al.* Thermal properties of in situ grown graphene reinforced copper matrix laminated composites. *Journal of Alloys and Compounds* **771**, 228–237 (2019).

84. Gao, F., Qu, J. & Yao, M. Interfacial thermal resistance between metallic carbon nanotube and Cu substrate. *Journal of Applied Physics* **110**, 124314 (2011).

85. Hopkins, P. E. Thermal Transport across Solid Interfaces with Nanoscale Imperfections: Effects of Roughness, Disorder, Dislocations, and Bonding on Thermal Boundary Conductance. *International Scholarly Research Notices* https://www.hindawi.com/journals/isrn/2013/682586/abs/ (2013) doi:10.1155/2013/682586.

86. Jagannadham, K. Thermal Conductivity of Copper-Graphene Composite Films Synthesized by Electrochemical Deposition with Exfoliated Graphene Platelets. *Metall and Materi Trans B* **43**, 316–324 (2012).

87. Czerwinski, F. The reactive element effect on high-temperature oxidation of magnesium. *International Materials Reviews* **60**, 264–296 (2015).

88. Kaur, M. *et al.* Growth and branching of CuO nanowires by thermal oxidation of copper. *Journal of Crystal Growth* **289**, 670–675 (2006).

89. Yan, X. *et al.* Stress corrosion crack of ZnAl15 alloys in hot and humid environment. *Materials Letters* **93**, 183–186 (2013).

90. Jeurgens, L. P. H., Sloof, W. G., Tichelaar, F. D. & Mittemeijer, E. J. Growth kinetics and mechanisms of aluminum-oxide films formed by thermal oxidation of aluminum. *Journal of Applied Physics* **92**, 1649–1656 (2002).

91. Zhang, B. *et al.* Unmasking chloride attack on the passive film of metals. *Nature Communications* **9**, 2559 (2018).

92. Rao, A. C. U., Vasu, V., Govindaraju, M. & Srinadh, K. V. S. Stress corrosion cracking behaviour of 7xxx aluminum alloys: A literature review. *Transactions of Nonferrous Metals Society of China* **26**, 1447–1471 (2016).

93. Badwe, N. *et al.* Decoupling the role of stress and corrosion in the intergranular cracking of noble-metal alloys. *Nature Materials* 1 (2018) doi:10.1038/s41563-018-0162-x.

94. Huo, W. *et al.* Simultaneously enhanced mechanical strength and inter-granular corrosion resistance in high strength 7075 Al alloy. *Journal of Alloys and Compounds* **781**, 680–688 (2019).

95. Chen, Y.-S. *et al.* Observation of hydrogen trapping at dislocations, grain boundaries, and precipitates. 6 (2020).

96. Senna, L. F., Díaz, S. L. & Sathler, L. Electrodeposition of copper–zinc alloys in pyrophosphate-based electrolytes. *Journal of Applied Electrochemistry* **33**, 1155–1161 (2003).

97. Ranjbar, K. Effect of flow induced corrosion and erosion on failure of a tubular heat exchanger. *Materials & Design* **31**, 613–619 (2010).

98. Liu, Y. C., Wan, J. B. & Gao, Z. M. Intermediate decomposition of metastable Cu5Zn8 phase in the soldered Sn–Ag–Zn/Cu interface. *Journal of Alloys and Compounds* **465**, 205–209 (2008).

99. Screen-Printable Silver Pastes with Metallic Nano-Zinc and Nano-Zinc Alloys for Crystalline Silicon Photovoltaic Cells | ACS Applied Materials & Interfaces. https://pubs.acs.org/doi/abs/10.1021/am1011996?casa_token=Rqk4cvP7MTgAAAAA:RKYaEVBcYMcIijp0fYeYHVyQ1DqQU-aM4G2RyfPCOk2AvXf5o1yRTQLwgtc6r6iy7azyVUnLRqo7sKou.

100. Young, D. J. *High Temperature Oxidation and Corrosion of Metals*. (Elsevier, 2008).

101. Wang, S. G., Sun, M., Han, H. B., Long, K. & Zhang, Z. D. The high-temperature oxidation of bulk nanocrystalline 304 stainless steel in air. *Corrosion Science* **72**, 64–72 (2013).

102. Chen, R. Y. & Yeun, W. Y. D. Review of the High-Temperature Oxidation of Iron and Carbon Steels in Air or Oxygen. *Oxidation of Metals* **59**, 433–468 (2003).

103. Yuan, L., Wang, Y., Mema, R. & Zhou, G. Driving force and growth mechanism for spontaneous oxide nanowire formation during the thermal oxidation of metals. *Acta Materialia* **59**, 2491–2500 (2011).

104. Nguyen, L. *et al.* Atomic-Scale Insights into the Oxidation of Aluminum. *ACS Applied Materials & Interfaces* **10**, 2230–2235 (2018).

105. Kofstad, P. Oxidation of Metals: Determination of Activation Energies. *Nature* **179**, 1362–1363 (1957).

106. Cabrera, N. & Mott, N. F. Theory of the oxidation of metals. *Rep. Prog. Phys.* **12**, 163 (1949).

107. Xu, J. Q., Chen, L. Y., Choi, H. & Li, X. C. Theoretical study and pathways for nanoparticle capture during solidification of metal melt. *J. Phys.: Condens. Matter* **24**, 255304 (2012).

108. Xue, W., Shi, X., Hua, M. & Li, Y. Preparation of anti-corrosion films by microarc oxidation on an Al–Si alloy. *Applied Surface Science* **253**, 6118–6124 (2007).

109. Knight, S. P. *et al.* Some effects of alloy composition on stress corrosion cracking in Al–Zn–Mg–Cu alloys. *Corrosion Science* **98**, 50–62 (2015).

110. Shih, T.-S. & Liu, Z.-B. Thermally-Formed Oxide on Aluminum and Magnesium. *Materials Transactions* **47**, 1347–1353 (2006).

111. Rai, A., Lee, D., Park, K. & Zachariah, M. R. Importance of Phase Change of Aluminum in Oxidation of Aluminum Nanoparticles. *The Journal of Physical Chemistry B* **108**, 14793–14795 (2004).

112. Coulet, M.-V. *et al.* Oxidation Mechanism of Aluminum Nanopowders. *The Journal of Physical Chemistry C* **119**, 25063–25070 (2015).

113. Yang, Y., Kushima, A., Han, W., Xin, H. & Li, J. Liquid-Like, Self-Healing Aluminum Oxide during Deformation at Room Temperature. *Nano Letters* **18**, 2492–2497 (2018).

114. Cai, N., Zhou, G., Müller, K. & Starr, D. E. Temperature and pressure dependent Mott potentials and their influence on self-limiting oxide film growth. *Appl. Phys. Lett.* **101**, 171605 (2012).

115. Lucas, K. A., Lucas, K. A. & Clarke, H. *Corrosion of Aluminium-based Metal Matrix Composites*. (Wiley, 1993).

116. Torbati-Sarraf, H., Stannard, T. J., La Plante, E. C., Sant, G. N. & Chawla, N. Direct observations of microstructure-resolved corrosion initiation in AA7075-T651 at the nanoscale using vertical scanning interferometry (VSI). *Materials Characterization* **161**, 110166 (2020).

117. Venugopal, A. *et al.* Effect of micro arc oxidation treatment on localized corrosion behaviour of AA7075 aluminum alloy in 3.5% NaCl solution. *Transactions of Nonferrous Metals Society of China* **22**, 700–710 (2012).

118. Birbilis, N. & Buchheit, R. G. Electrochemical Characteristics of Intermetallic Phases in Aluminum Alloys An Experimental Survey and Discussion. *J. Electrochem. Soc.* **152**, B140–B151 (2005).

119. Natishan, P. M. & O'Grady, W. E. Chloride Ion Interactions with Oxide-Covered Aluminum Leading to Pitting Corrosion: A Review. *J. Electrochem. Soc.* **161**, C421 (2014).

120. Wang, J. *et al.* Combined Effect of Ag and Mg Additions on Localized Corrosion Behavior of Al-Cu Alloys with High Cu Content. *J. of Materi Eng and Perform* **29**, 6108–6117 (2020).

121. Zaid, B., Saidi, D., Benzaid, A. & Hadji, S. Effects of pH and chloride concentration on pitting corrosion of AA6061 aluminum alloy. *Corrosion Science* **50**, 1841–1847 (2008).

122. Du, Y., Kou, M., Tu, J., Wang, M. & Jiao, S. An investigation into the anodic behavior of TiB2 in a CaCl2-based molten salt. *Corrosion Science* **178**, 109089 (2021).

123. Tian, W., Li, S., Wang, B., Liu, J. & Yu, M. Pitting corrosion of naturally aged AA 7075 aluminum alloys with bimodal grain size. *Corrosion Science* **113**, 1–16 (2016).

124. Naeini, M. F., Shariat, M. H. & Eizadjou, M. On the chloride-induced pitting of ultra fine grains 5052 aluminum alloy produced by accumulative roll bonding process. *Journal of Alloys and Compounds* **509**, 4696–4700 (2011).

125. Jilani, O., Njah, N. & Ponthiaux, P. Transition from intergranular to pitting corrosion in fine grained aluminum processed by equal channel angular pressing. *Corrosion Science* **87**, 259–264 (2014).

126. Popov, B. N. *Corrosion Engineering: Principles and Solved Problems*. (Elsevier, 2015).

127. Jafarzadeh, S., Chen, Z. & Bobaru, F. Computational modeling of pitting corrosion. *Corrosion Reviews* **37**, 419–439 (2019).

128. Yuan, J. *et al.* Nanotreating High-Zinc Al–Zn–Mg–Cu Alloy by TiC Nanoparticles. in *Light Metals 2020* (ed. Tomsett, A.) 318–323 (Springer International Publishing, 2020). doi:10.1007/978-3-030-36408-3_46.

129. Zhao, S., Wolfe, D. A., Huang, T.-S. & Frankel, G. S. Generalized model for IGC growth in aluminum alloys. *Journal of Statistical Planning and Inference* **137**, 2405–2412 (2007).

130. Larsen, M. H., Walmsley, J. C., Lunder, O., Mathiesen, R. H. & Nisancioglu, K. Intergranular Corrosion of Copper-Containing AA6x x x AlMgSi Aluminum Alloys. *J. Electrochem. Soc.* **155**, C550 (2008).

131. Unwin, P. N. T., Lorimer, G. W. & Nicholson, R. B. The origin of the grain boundary precipitate free zone. *Acta Metallurgica* **17**, 1363–1377 (1969).

132. Lervik, A., Wenner, S., Lunder, O., Marioara, C. D. & Holmestad, R. Grain boundary structures and their correlation with intergranular corrosion in an extruded Al-Mg-Si-Cu alloy. *Materials Characterization* **170**, 110695 (2020).

133. Sigworth, G. K. The Corrosion of Al–Cu-Based Alloys and Comments on the Paper "Effect of Solidification Time on Microstructure, Wettability and Corrosion Properties of A205-T7 Aluminum Alloys" by Amir Kordijazi et al. *Inter Metalcast* **15**, 13–16 (2021).

134. Park, J. K. Influence of retrogression and reaging treatments on the strength and stress corrosion resistance of aluminium alloy 7075-T6. *Materials Science and Engineering: A* **103**, 223–231 (1988).

135. Zhao, H., Gault, B., Ponge, D. & Raabe, D. Reversion and re-aging of a peak aged Al-Zn-Mg-Cu alloy. *Scripta Materialia* **188**, 269–273 (2020).

136. Knight, S. P., Birbilis, N., Muddle, B. C., Trueman, A. R. & Lynch, S. P. Correlations between intergranular stress corrosion cracking, grain-boundary microchemistry, and grain-boundary electrochemistry for Al–Zn–Mg–Cu alloys. *Corrosion Science* **52**, 4073–4080 (2010).

137. Wanhill, R. J. H., Byrnes, R. T. & Smith, C. L. 16 - Stress corrosion cracking (SCC) in aerospace vehicles. in *Stress Corrosion Cracking* (eds. Raja, V. S. & Shoji, T.) 608–650 (Woodhead Publishing, 2011). doi:10.1533/9780857093769.4.608.

138. Burnett, T. L. *et al.* The role of crack branching in stress corrosion cracking of aluminium alloys. *Corrosion Reviews* **33**, 443–454 (2015).

139. Monticelli, C., Zucchi, F., Brunoro, G. & Trabanelli, G. Stress corrosion cracking behaviour of some aluminium-based metal matrix composites. *Corrosion Science* **39**, 1949–1963 (1997).

140. Speidel, M. O. & Hyatt, M. V. Stress-Corrosion Cracking of High-Strength Aluminum Alloys. in *Advances in Corrosion Science and Technology* (eds. Fontana, M. G. & Staehle, R. W.) 115–335 (Springer US, 1972). doi:10.1007/978-1-4615-8255-7_3.

141. Knight, S. P., Lynch, S. P., Birbilis, N. & Muddle, B. C. Remedial treatments for stress corrosion cracking in Al-Zn-Mg-Cu alloys. in *49th Annual Conference of the Australasian Corrosion Association 2009: Corrosion and Prevention 2009* 612–623 (2009).

142. Gupta, R. K., Deschamps, A., Cavanaugh, M. K., Lynch, S. P. & Birbilis, N. Relating the Early Evolution of Microstructure with the Electrochemical Response and Mechanical Performance of a Cu-Rich and Cu-Lean 7xxx Aluminum Alloy. *J. Electrochem. Soc.* **159**, C492 (2012).

143. Deschamps, A., Bréchet, Y. & Livet, F. Influence of copper addition on precipitation kinetics and hardening in Al–Zn–Mg alloy. *Materials Science and Technology* **15**, 993–1000 (1999).

144. Reda, Y., Abdel-Karim, R. & Elmahallawi, I. Improvements in mechanical and stress corrosion cracking properties in Al-alloy 7075 via retrogression and reaging. *Materials Science and Engineering: A* **485**, 468–475 (2008).

145. Wang, S., He, C., Luo, B., Bai, Z. & Jiang, G. The role of trace Ag in controlling the precipitation and stress corrosion properties of aluminium alloy 7N01. *Vacuum* **184**, 109948 (2021).

146. Chang, C.-H., Lee, S.-L., Lin, J.-C., Yeh, M.-S. & Jeng, R.-R. Effect of Ag content and heat treatment on the stress corrosion cracking of Al–4.6Cu–0.3Mg alloy. *Materials Chemistry and Physics* **91**, 454–462 (2005).

147. Buha, J., Lumley, R. N. & Crosky, A. G. Secondary ageing in an aluminium alloy 7050. *Materials Science and Engineering: A* **492**, 1–10 (2008).

148. Xu, D. K., Birbilis, N. & Rometsch, P. A. Effect of S-Phase Dissolution on the Corrosion and Stress Corrosion Cracking of an As-Rolled Al-Zn-Mg-Cu Alloy. *Corrosion* **68**, 035001–1 (2012).

149. Qi, H. *et al.* Mechanical properties and corrosion resistance of Al–Cu–Mg–Ag heat-resistant alloy modified by interrupted aging. *Journal of Alloys and Compounds* **657**, 318–324 (2016).

150. Liu, X., Zhang, D., Wang, H., Yan, Y. & Zhang, X. Regulating solute partitioning utilized to decorate grain boundary for improving corrosion resistance in a model Al-Cu-Mg alloy. *Corrosion Science* **181**, 109219 (2021).

151. Shimizu, Y., Nishimura, T. & Matsushima, I. Corrosion resistance of Al-based metal matrix composites. *Materials Science and Engineering: A* **198**, 113–118 (1995).

152. G B, V., Rao, C., Selvaraj, N. & Bhagyashekar, M. S. Studies on Al6061-SiC and Al7075-Al2O3 Metal Matrix Composites. *Journal of Minerals and Materials Characterization and Engineering* **09**, 43–55 (2010).

153. Lai, M. O. & Ferguson, W. G. Fracture toughness of aluminium alloy 7075-T6 in the as-cast condition. *Materials Science and Engineering* **74**, 133–138 (1985).

154. Zhao, Y., Zhai, X. & Wang, J. Buckling behaviors and ultimate strengths of 6082-T6 aluminum alloy columns under eccentric compression – Part I: Experiments and finite element modeling. *Thin-Walled Structures* **143**, 106207 (2019).

155. Prasad, S. V. & Asthana, R. Aluminum Metal-Matrix Composites for Automotive Applications: Tribological Considerations. *Tribology Letters* **17**, 445–453 (2004).

156. Suresh, S., Moorthi, N. S. V. & Prema, C. E. Tribological and Mechanical Behavior Study of Al6061-TiB2 Metal Matrix Composites Using Stir Casting. *Advanced Materials Research* vols 984–985 200–206 https://www.scientific.net/AMR.984-985.200 (2014).

157. Lakshmi, S., Lu, L. & Gupta, M. In situ preparation of TiB2 reinforced Al based composites. *Journal of Materials Processing Technology* **73**, 160–166 (1998).

158. Karthikeyan, L., Kumar, V. S. S. & Padmanabhan, K. A. Investigations on Superplastic Forming of Friction Stir-Processed AA6063-T6 Aluminum Alloy. *Materials and Manufacturing Processes* **28**, 294–298 (2013).

159. Senthilvelan, T., Gopalakannan, S., Vishnuvarthan, S. & Keerthivaran, K. Fabrication and Characterization of SiC, Al2O3 and B4C Reinforced Al-Zn-Mg-Cu Alloy (AA 7075) Metal

Matrix Composites: A Study. *Advanced Materials Research* vols 622–623 1295–1299 https://www.scientific.net/AMR.622-623.1295 (2013).

160. Zhao, M., Wu, G., Jiang, L. & Dou, Z. Friction and wear properties of TiB2P/Al composite. *Composites Part A: Applied Science and Manufacturing* **37**, 1916–1921 (2006).

161. Thakur, S. K. & Dhindaw, B. K. The influence of interfacial characteristics between SiCp and Mg/Al metal matrix on wear, coefficient of friction and microhardness. *Wear* **247**, 191–201 (2001).

162. Roy, P., Singh, S. & Pal, K. Enhancement of mechanical and tribological properties of SiC- and CB-reinforced aluminium 7075 hybrid composites through friction stir processing. *Advanced Composite Materials* **28**, 1–18 (2019).

163. Bai, Y., Guo, Y., Li, J., Yang, Z. & Tian, J. Effect of Al2O3 nanoparticle reinforcement on the mechanical and high-temperature tribological behavior of Al-7075 alloy. *Proceedings of the Institution of Mechanical Engineers, Part J: Journal of Engineering Tribology* **231**, 900–909 (2017).

164. Kar, C. & Surekha, B. Effect of red mud and TiC on friction and wear characteristics of Al 7075 metal matrix composites. *Australian Journal of Mechanical Engineering* **0**, 1–10 (2019).

165. Ul Haq, M. I. & Anand, A. Dry Sliding Friction and Wear Behavior of AA7075-Si3N4 Composite. *Silicon* **10**, 1819–1829 (2018).

166. Mistry, J. M. & Gohil, P. P. Experimental investigations on wear and friction behaviour of Si3N4p reinforced heat-treated aluminium matrix composites produced using electromagnetic stir casting process. *Composites Part B: Engineering* **161**, 190–204 (2019).

167. Tjong, S. C. & Tam, K. F. Mechanical and thermal expansion behavior of hipped aluminum–TiB2 composites. *Materials Chemistry and Physics* **97**, 91–97 (2006).

168. Sulima, I., Jaworska, L., Wyżga, P. & Perek-Nowak, M. The influence of reinforcing particles on mechanical and tribological properties and microstructure of the steel-TiB2composites. *Journal of Achievements in Materials and Manufacturing Engineering* 52--57 (2011).

169. Kumar, S., Chakraborty, M., Subramanya Sarma, V. & Murty, B. S. Tensile and wear behaviour of in situ Al–7Si/TiB2 particulate composites. *Wear* **265**, 134–142 (2008).

170. Rocher, J. P., Quenisset, J. M. & Naslain, R. Wetting improvement of carbon or silicon carbide by aluminium alloys based on a K2ZrF6 surface treatment: application to composite material casting. *J Mater Sci* **24**, 2697–2703 (1989).

171. Prabu, S. B., Karunamoorthy, L., Kathiresan, S. & Mohan, B. Influence of stirring speed and stirring time on distribution of particles in cast metal matrix composite. *Journal of Materials Processing Technology* **171**, 268–273 (2006).

172. Powell, R. W., Ho, C. Y. & Liley, P. E. Thermal Conductivity of Selected Materials. 220.

173. Xu, J. Achieving Uniform Nanoparticle Dispersion in Metal Matrix Nanocomposites. (UCLA, 2015).

174. Dong, B.-X. *et al.* Design of TiCx nanoparticles and their morphology manipulating mechanisms by stoichiometric ratios: Experiment and first-principle calculation. *Materials & Design* 107951 (2019) doi:10.1016/j.matdes.2019.107951.

175. Sokoluk, M., Yuan, J., Pan, S. & Li, X. Nanoparticles Enabled Mechanism for Hot Cracking Elimination in Aluminum Alloys. *Metall Mater Trans A* (2021) doi:10.1007/s11661-021-06302-9.

176. Pan, S., Guan, Z., Yao, G., Yuan, J. & Li, X. Mo-enhanced Chemical Stability of TiC Nanoparticles in Molten Al. *Journal of Alloys and Compounds* 158169 (2020) doi:10.1016/j.jallcom.2020.158169.

177. Birol, Y. In situ synthesis of Al–TiCp composites by reacting K2TiF6 and particulate graphite in molten aluminium. *Journal of Alloys and Compounds* **454**, 110–117 (2008).

178. Kim, S. I. *et al.* Dense dislocation arrays embedded in grain boundaries for high-performance bulk thermoelectrics. *Science* **348**, 109–114 (2015).

179. Pan, S., Guan, Z., Yao, G., Cao, C. & Li, X. Study on electrical behaviour of copper and its alloys containing dispersed nanoparticles. *Current Applied Physics* (2019) doi:10.1016/j.cap.2019.01.016.

180. Wang, J. *et al.* Stress corrosion cracking behavior of in-situ TiB2/7050 composite. *Mater. Res. Express* **5**, 126501 (2018).

181. Roy, R. K. & Das, S. New combination of polishing and etching technique for revealing grain structure of an annealed aluminum (AA1235) alloy. *J Mater Sci* **41**, 289–292 (2006).

182. Ahadi, K., Shoron, O. F., Marshall, P. B., Mikheev, E. & Stemmer, S. Electric field effect near the metal-insulator transition of a two-dimensional electron system in SrTiO3. *Appl. Phys. Lett.* **110**, 062104 (2017).

183. Williams, R. K., Becher, P. F. & Finch, C. B. Study of the Kondo effect and intrinsic electrical conduction in titanium diboride. *Journal of Applied Physics* **56**, 2295–2302 (1984).

184. Qian, L. H., Lu, Q. H., Kong, W. J. & Lu, K. Electrical resistivity of fully-relaxed grain boundaries in nanocrystalline Cu. *Scripta Materialia* **50**, 1407–1411 (2004).

185. Basinski, Z. S., Dugdale, J. S. & Howie, A. The electrical resistivity of dislocations. *The Philosophical Magazine: A Journal of Theoretical Experimental and Applied Physics* **8**, 1989–1997 (1963).

186. Gall, D. Electron mean free path in elemental metals. *Journal of Applied Physics* **119**, 085101 (2016).

187. Holwech, I. & Jeppesen, J. Temperature dependence of the electrical resistivity of aluminium films. *The Philosophical Magazine: A Journal of Theoretical Experimental and Applied Physics* **15**, 217–228 (1967).

188. Selcuk, S. & Selloni, A. Facet-dependent trapping and dynamics of excess electrons at anatase TiO 2 surfaces and aqueous interfaces. *Nature Materials* **15**, 1107–1112 (2016).

189. Mosleh-Shirazi, S., Hua, G., Akhlaghi, F., Yan, X. & Li, D. Interfacial valence electron localization and the corrosion resistance of Al-SiC nanocomposite. *Scientific Reports* **5**, 18154 (2015).

190. Gasparov, V. A., Sidorov, N. S., Zver'kova, I. I. & Kulakov, M. P. Electron transport in diborides: Observation of superconductivity in ZrB2. *Jetp Lett.* **73**, 532–535 (2001).

191. Ahadi, K., Shoron, O. F., Marshall, P. B., Mikheev, E. & Stemmer, S. Electric field effect near the metal-insulator transition of a two-dimensional electron system in SrTiO3. *Appl. Phys. Lett.* **110**, 062104 (2017).

192. Justin, J. F. & Jankowiak, A. Ultra High Temperature Ceramics : Densification, Properties and Thermal Stability. *AerospaceLab* 1–11 (2011).

193. Mosleh-Shirazi, S., Hua, G., Akhlaghi, F., Yan, X. & Li, D. Interfacial valence electron localization and the corrosion resistance of Al-SiC nanocomposite. *Scientific Reports* **5**, 18154 (2015).

194. Tenorio, J. A. S. & Espinosa, D. C. R. Effect of salt/oxide interaction on the process of aluminum recycling. *Journal of Light Metals* **2**, 89–93 (2002).

195. Matsuyama, K. & Mishima, K. Preparation of poly(methyl methacrylate)–TiO2 nanoparticle composites by pseudo-dispersion polymerization of methyl methacrylate in supercritical CO2. *The Journal of Supercritical Fluids* **49**, 256–264 (2009).

196. Shklovskii, B. I. & Efros, A. L. *Electronic Properties of Doped Semiconductors*. (Springer Science & Business Media, 2013).

197. Liu, Z. Y., Xiao, B. L., Wang, W. G. & Ma, Z. Y. Tensile Strength and Electrical Conductivity of Carbon Nanotube Reinforced Aluminum Matrix Composites Fabricated by Powder Metallurgy Combined with Friction Stir Processing. *Journal of Materials Science & Technology* **30**, 649–655 (2014).

198. Pan, S. & Zhang, Z. Fundamental theories and basic principles of triboelectric effect: A review. *Friction* 1–16 (2018) doi:10.1007/s40544-018-0217-7.

199. Kittel, C. Introduction to solid state physics. Fifth edition. (1976).

200. Di Ventra, M. *Electrical Transport in Nanoscale Systems*. (2008).

201. Cohen, M. L. & Louie, S. G. *Fundamentals of Condensed Matter Physics*. (Cambridge University Press, 2016).

202. Pan, S. & Zhang, Z. Triboelectric effect: A new perspective on electron transfer process. *Journal of Applied Physics* **122**, 144302 (2017).

203. Blöchl, P. E. & Parrinello, M. Adiabaticity in first-principles molecular dynamics. *Phys. Rev. B* **45**, 9413–9416 (1992).

204. Colton, R. J. & Rabalais, J. Wayne. Electronic structure to tungsten and some of its borides, carbides, nitrides, and oxides by x-ray electron spectroscopy. *Inorganic Chemistry* **15**, 236–238 (1976).

205. Bennett, L. H., Cuthill, J. R., McAlister, A. J., Erickson, N. E. & Watson, R. E. Electronic Structure and Catalytic Behavior of Tungsten Carbide. *Science* **184**, 563–565 (1974).

206. Kittel, C., Charles, K., Kroemer, H. & Herbert, K. *Thermal Physics*. (Macmillan, 1980).

207. Deligoz, E., Colakoglu, K. & Ciftci, Y. O. Lattice dynamical properties of ScB2, TiB2, and V B2 compounds. *Solid State Communications* **149**, 1843–1848 (2009).

208. Zimmermann, J. W. *et al.* Thermophysical Properties of ZrB2 and ZrB2–SiC Ceramics. *Journal of the American Ceramic Society* **91**, 1405–1411 (2008).

209. Krikorian, O. H. *Estimation of heat capacities and other thermodynamic properties of refractory borides*. http://inis.iaea.org/Search/search.aspx?orig_q=RN:3017730 (1971).

210. Fuchs, G. *et al.* A Comparative Study of MgB2 and Other Diborides. *Journal of Low Temperature Physics* **131**, 1159–1163 (2003).

211. Shen, P., Fujii, H. & Nogi, K. Wettability of some refractory materials by molten SiO2–MnO–TiO2–FeOx slag. *Materials Chemistry and Physics* **114**, 681–686 (2009).

212. Tyson, W. R. & Miller, W. A. Surface free energies of solid metals: Estimation from liquid surface tension measurements. *Surface Science* **62**, 267–276 (1977).

213. El-Kady, O. & Fathy, A. Effect of SiC particle size on the physical and mechanical properties of extruded Al matrix nanocomposites. *Materials & Design (1980-2015)* **54**, 348–353 (2014).

214. Jain, A. & McGaughey, A. J. H. Thermal transport by phonons and electrons in aluminum, silver, and gold from first principles. *Phys. Rev. B* **93**, 081206 (2016).

215. Chou, H.-P., Chang, Y.-S., Chen, S.-K. & Yeh, J.-W. Microstructure, thermophysical and electrical properties in AlxCoCrFeNi (0≤x≤2) high-entropy alloys. *Materials Science and Engineering: B* **163**, 184–189 (2009).

216. Liu, M., Ma, Y., Wu, H. & Wang, R. Y. Metal Matrix–Metal Nanoparticle Composites with Tunable Melting Temperature and High Thermal Conductivity for Phase-Change Thermal Storage. *ACS Nano* **9**, 1341–1351 (2015).

217. Frommeyer, G. & Wassermann, G. Anomalous properties of in-situ-produced silver-copper composite wires I. Electrical conductivity. *phys. stat. sol. (a)* **27**, 99–105 (1975).

218. Kang, J. S., Li, M., Wu, H., Nguyen, H. & Hu, Y. Experimental observation of high thermal conductivity in boron arsenide. *Science* eaat5522 (2018) doi:10.1126/science.aat5522.

219. Arbtin, E. & Murphy, G. Correlation of Vickers hardness number, modulus of elasticity, and the yield strength for ductile metals. *Ames Laboratory ISC Technical Reports* (1953).

220. Abyzov, A. M., Kidalov, S. V. & Shakhov, F. M. High thermal conductivity composite of diamond particles with tungsten coating in a copper matrix for heat sink application. *Applied Thermal Engineering* **48**, 72–80 (2012).

221. Johnson, K. L. & Johnson, K. L. *Contact Mechanics*. (Cambridge University Press, 1987).

222. Towler, M. D. *et al.* Ab initio study of MnO and NiO. *Phys. Rev. B* **50**, 5041–5054 (1994).

223. Stedman, R., Almqvist, L. & Nilsson, G. Phonon-Frequency Distributions and Heat Capacities of Aluminum and Lead. *Phys. Rev.* **162**, 549–557 (1967).

224. Nicklow, R. M., Gilat, G., Smith, H. G., Raubenheimer, L. J. & Wilkinson, M. K. Phonon Frequencies in Copper at 49 and 298 K. *Phys. Rev.* **164**, 922–928 (1967).

225. Tütüncü, H. M., Bağcı, S., Srivastava, G. P. & Akbulut, A. Electrons, phonons and superconductivity in rocksalt and tungsten–carbide phases of CrC. *J. Phys.: Condens. Matter* **24**, 455704 (2012).

226. Liu, W. *et al.* Enhanced thermoelectric properties of n-type Mg 2.16 (Si 0.4 Sn 0.6) 1−y Sb y due to nano-sized Sn-rich precipitates and an optimized electron concentration. *Journal of Materials Chemistry* **22**, 13653–13661 (2012).

227. Lu, L., Shen, Y., Chen, X., Qian, L. & Lu, K. Ultrahigh Strength and High Electrical Conductivity in Copper. *Science* **304**, 422–426 (2004).

228. Hong, S. I. & Hill, M. A. Microstructural stability and mechanical response of Cu–Ag microcomposite wires. *Acta Materialia* **46**, 4111–4122 (1998).

229. Zhang, B. B., Tao, N. R. & Lu, K. A high strength and high electrical conductivity bulk Cu-Ag alloy strengthened with nanotwins. *Scripta Materialia* **129**, 39–43 (2017).

230. Wang, S., Li, M., Ji, H. & Wang, C. Rapid pressureless low-temperature sintering of Ag nanoparticles for high-power density electronic packaging. *Scripta Materialia* **69**, 789–792 (2013).

231. Mao, J. *et al.* High thermoelectric power factor in Cu–Ni alloy originate from potential barrier scattering of twin boundaries. *Nano Energy* **17**, 279–289 (2015).

232. Lindenfeld, P. & Pennebaker, W. B. Lattice Conductivity of Copper Alloys. *Phys. Rev.* **127**, 1881–1889 (1962).

233. Tong, X. *et al.* Effect of grain size on low-temperature electrical resistivity and thermal conductivity of pure magnesium. *Materials Letters* **229**, 261–264 (2018).

234. Tjong, S. C. Recent progress in the development and properties of novel metal matrix nanocomposites reinforced with carbon nanotubes and graphene nanosheets. *Materials Science and Engineering: R: Reports* **74**, 281–350 (2013).

235. Shen, J., Liu, Y. C., Han, Y. J., Tian, Y. M. & Gao, H. X. Strengthening effects of ZrO2 nanoparticles on the microstructure and microhardness of Sn-3.5Ag lead-free solder. *Journal of Electronic Materials* **35**, 1672–1679 (2006).

236. Uher, C. Thermal Conductivity of Metals. in *Thermal Conductivity: Theory, Properties, and Applications* (ed. Tritt, T. M.) 21–91 (Springer US, 2004). doi:10.1007/0-387-26017-X_2.

237. Abyzov, A. M., Kidalov, S. V. & Shakhov, F. M. High thermal conductivity composites consisting of diamond filler with tungsten coating and copper (silver) matrix. *J Mater Sci* **46**, 1424–1438 (2011).

238. Oñoro, J. The stress corrosion cracking behaviour of heat-treated Al–Zn–Mg–Cu alloy in modified salt spray fog testing. *Materials and Corrosion* **61**, 125–129 (2010).

239. Kennedy, A. R., Weston, D. P. & Jones, M. I. Reaction in Al–TiC metal matrix composites. *Materials Science and Engineering: A* **316**, 32–38 (2001).

240. López, V. H., Scoles, A. & Kennedy, A. R. The thermal stability of TiC particles in an Al7wt.%Si alloy. *Materials Science and Engineering: A* **356**, 316–325 (2003).

241. Sheibani, S. & Najafabadi, M. Fazel. In situ fabrication of Al–TiC Metal Matrix Composites by reactive slag process. *Materials & Design* **28**, 2373–2378 (2007).

242. Pan, S., Yao, G., Yuan, J., Sokoluk, M. & Li, X. Manufacturing of Bulk Al-12Zn-3.7Mg-1Cu Alloy with TiC Nanoparticles. *Procedia Manufacturing* **48**, 325–331 (2020).

243. Walford, L. K. The phase diagram of the aluminium-molybdenum system. *The Philosophical Magazine: A Journal of Theoretical Experimental and Applied Physics* **9**, 513–516 (1964).

244. Qiu, C. *et al.* Effect of Fe and Mo additions on microstructure and mechanical properties of TiAl intermetallics. *Transactions of Nonferrous Metals Society of China* **22**, 521–527 (2012).

245. Raghavan, V. Al-Mo-Ti (Aluminum-Molybdenum-Titanium). *Journal of Phase Equilibria & Diffusion* **26**, 357–359 (2005).

246. Pang, Y., Xie, H. & Koc, R. Investigation of Electrical Conductivity and Oxidation Behavior of TiC and TiN Based Cermets for SOFC Interconnect Application. *ECS Transactions* **7**, 2427–2435 (2019).

247. Yang, Z., Lu, H., Liu, Z., Yan, X. & Li, D. Effect of particle size on the surface activity of TiC–Ni composite coating via the interfacial valence electron localization. *RSC Advances* **6**, 18793–18799 (2016).

248. Ao, M., Liu, H. & Dong, C. The effect of La2O3 addition on intermetallic-free aluminium matrix composites reinforced with TiC and Al2O3 ceramic particles. *Ceramics International* **45**, 12001–12009 (2019).

249. Knipling, K. E., Dunand, D. C. & Seidman, D. N. Criteria for developing castable, creep-resistant aluminum-based alloys – A review. *Zeitschrift für Metallkunde* **97**, 246–265 (2006).

250. Jain, A. *et al*. Determination of the thermodynamic stability of TiB2. *Journal of Alloys and Compounds* **491**, 747–752 (2010).

251. Tunca, N., Delamore, G. W. & Smith, R. W. Corrosion of Mo, Nb, Cr, and Y in molten aluminum. *Metallurgical Transactions A* **21**, 2919–2928 (1990).

252. Jacobs, T. D. B. & Carpick, R. W. Nanoscale wear as a stress-assisted chemical reaction. *Nature Nanotechnology* **8**, 108 (2013).

253. Pan, S., Yuan, J., Zheng, T., She, Z. & Li, X. Interfacial thermal conductance of in situ aluminum-matrix nanocomposites. *J Mater Sci* (2021) doi:10.1007/s10853-021-06176-7.

254. Yuan, J., Yao, G., Pan, S., Narayanan, M. & Li, X. Size control of in-situ synthesized TiB2 particles in molten aluminum. *Metall Mater Trans A.*

255. Aboulkhair, N. T., Maskery, I., Tuck, C., Ashcroft, I. & Everitt, N. M. The microstructure and mechanical properties of selectively laser melted AlSi10Mg: The effect of a conventional T6-like heat treatment. *Materials Science and Engineering: A* **667**, 139–146 (2016).

256. Kan, W. H. *et al.* Effect of T6 treatment on additively-manufactured AlSi10Mg sliding against ceramic and steel. *Wear* **482–483**, 203961 (2021).

257. Gao, C. *et al.* Effect of heat treatment on SLM-fabricated TiN/AlSi10Mg composites: Microstructural evolution and mechanical properties. *Journal of Alloys and Compounds* **853**, 156722 (2021).

258. Girelli, L., Tocci, M., Gelfi, M. & Pola, A. Study of heat treatment parameters for additively manufactured AlSi10Mg in comparison with corresponding cast alloy. *Materials Science and Engineering: A* **739**, 317–328 (2019).

259. AlMgSi Alloys :: Total Materia Article. https://www.totalmateria.com/page.aspx?ID=CheckArticle&site=ktn&NM=348.

260. Li, Y. *et al.* Insight into Si poisoning on grain refinement of Al-Si/Al-5Ti-B system. *Acta Materialia* **187**, 51–65 (2020).

261. Xia, F. *et al.* Instability of in situ TiC particles in an Al-12Si alloy. *Journal of Materials Research and Technology* **9**, 11361–11369 (2020).

262. Zhang, J. *et al.* Effect of Si element on the interfacial reaction of Ti3SiC2 reinforced Al matrix aomposites. *Mater. Res. Express* **8**, 026506 (2021).

263. Gupta, A. K., Lloyd, D. J. & Court, S. A. Precipitation hardening in Al–Mg–Si alloys with and without excess Si. *Materials Science and Engineering: A* **316**, 11–17 (2001).

264. Li, W. *et al.* Effect of heat treatment on AlSi10Mg alloy fabricated by selective laser melting: Microstructure evolution, mechanical properties and fracture mechanism. *Materials Science and Engineering: A* **663**, 116–125 (2016).

265. Abdelaziz, M. H., Samuel, A. M., Doty, H. W., Valtierra, S. & Samuel, F. H. Effect of additives on the microstructure and tensile properties of Al–Si alloys. *Journal of Materials Research and Technology* **8**, 2255–2268 (2019).

266. Zhou, Y. & Sun, Z. Crystallographic relations between Ti3SiC2 and TiC. *Materials Research Innovations* **3**, 286–291 (2000).

267. Zhang, H. *et al.* Enthalpies of formation of magnesium compounds from first-principles calculations. *Intermetallics* **17**, 878–885 (2009).

268. Ding, H. & Liu, X. Influence of Si on stability of TiC in Al melts. *Transactions of Nonferrous Metals Society of China* **21**, 1465–1472 (2011).

269. Xu, C. H., Zhu, Z. B., Lui, H. F., Surya, C. & Shi, S. Q. The effect of oxygen partial pressure on the growth of ZnO nanostructure on Cu0.62Zn0.38 brass during thermal oxidation. *Superlattices and Microstructures* **49**, 408–415 (2011).

270. Kruidhof, H., Bouwmeester, H. J. M., v. Doorn, R. H. E. & Burggraaf, A. J. Influence of order-disorder transitions on oxygen permeability through selected nonstoichiometric perovskite-type oxides. *Solid State Ionics* **63–65**, 816–822 (1993).

271. Shah, S. I., Kramer, B., Barnett, S. A. & Greene, J. E. Direct evidence for an order/disorder phase transition at x≈0.3 in single-crystal metastable (GaSb)(1−x)(Ge2)x alloys: High-resolution x-ray diffraction measurements. *Journal of Applied Physics* **59**, 1482–1487 (1986).

272. Li, X., Wang, Y., Liu, W., Jiang, G. & Zhu, C. Study of oxygen vacancies′ influence on the lattice parameter in ZnO thin film. *Materials Letters* **85**, 25–28 (2012).

273. Xu, C. H., Zhu, Z. B., Li, G. L., Xu, W. R. & Huang, H. X. Growth of ZnO nanostructure on Cu0.62Zn0.38 brass foils by thermal oxidation. *Materials Chemistry and Physics* **124**, 252–256 (2010).

274. Oleksak, R. P., Kapoor, M., Perea, D. E., Holcomb, G. R. & Doğan, Ö. N. The role of metal vacancies during high-temperature oxidation of alloys. *npj Materials Degradation* **2**, 1–8 (2018).

275. Farbod, M. & Mohammadian, A. Single phase synthesis of γ-brass (Cu5Zn8) nanoparticles by electric arc discharge method and investigation of their order–disorder transition temperature. *Intermetallics* **45**, 1–4 (2014).

276. Fang, Z. B., Yan, Z. J., Tan, Y. S., Liu, X. Q. & Wang, Y. Y. Influence of post-annealing treatment on the structure properties of ZnO films. *Applied Surface Science* **241**, 303–308 (2005).

277. Han, N. *et al.* Nitrogen-doped tungsten carbide nanoarray as an efficient bifunctional electrocatalyst for water splitting in acid. *Nature Communications* **9**, 924 (2018).

278. Mahapatra, A. K., Bhatta, U. M. & Som, T. Oxidation mechanism in metal nanoclusters: Zn nanoclusters to ZnO hollow nanoclusters. *J. Phys. D: Appl. Phys.* **45**, 415303 (2012).

279. He, X., Luo, X., Liu, J. & An, L. Effects of soft phase on the mechanical behaviors of hierarchical Mg nanocomposites. *Journal of Alloys and Compounds* (2018) doi:10.1016/j.jallcom.2018.07.194.

280. Sekar, A., Kim, S. H., Umar, A. & Hahn, Y. B. Catalyst-free synthesis of ZnO nanowires on Si by oxidation of Zn powders. *Journal of Crystal Growth* **277**, 471–478 (2005).

281. Zhu, J. Z. *et al.* Three-dimensional phase-field simulations of coarsening kinetics of γ′ particles in binary Ni–Al alloys. *Acta Materialia* **52**, 2837–2845 (2004).

282. Troiani, H. E. & Baruj, A. In situ optical microscopy study of a phase transformation induced by the dezincification of beta Cu–Zn. *Materials Science and Engineering: A* **454–455**, 441–445 (2007).

283. Suzuki, T. & Hagiwara, M. CsCl-Type Order-Disorder Transition in δ-VMn Solid Solution. *Transactions of the Japan Institute of Metals* **16**, 473–479 (1975).

284. Yang, X. & Zhang, Y. Prediction of high-entropy stabilized solid-solution in multi-component alloys. *Materials Chemistry and Physics* **132**, 233–238 (2012).

285. Ågren, J. A simplified treatment of the transition from diffusion controlled to diffusion-less growth. *Acta Metallurgica* **37**, 181–189 (1989).

286. Alloyeau, D. *et al.* Size and shape effects on the order–disorder phase transition in CoPt nanoparticles. *Nature Materials* **8**, 940–946 (2009).

287. Pan, S., Yao, G., Yuan, J. & Li, X. Electrical Performance of Bulk Al–ZrB2 Nanocomposites from 2 K to 300 K. in *Nanocomposites VI: Nanoscience and Nanotechnology in Advanced Composites* (eds. Srivatsan, T. S. & Gupta, M.) 63–70 (Springer International Publishing, 2019). doi:10.1007/978-3-030-35790-0_5.

288. Meng, G. *et al.* Effect of microcrystallization on pitting corrosion of pure aluminium. *Corrosion Science* **51**, 2151–2157 (2009).

289. Hua, Q. *et al.* Morphological Evolution of Cu2O Nanocrystals in an Acid Solution: Stability of Different Crystal Planes. *Langmuir* **27**, 665–671 (2011).

290. Jeurgens, L. P. H., Sloof, W. G., Tichelaar, F. D. & Mittemeijer, E. J. Thermodynamic stability of amorphous oxide films on metals: Application to aluminum oxide films on aluminum substrates. *Phys. Rev. B* **62**, 4707–4719 (2000).

291. Luo, K. *et al.* Electronic structures and mechanical properties of Al(111)/ZrB2(0001) heterojunctions from first-principles calculation. *Molecular Physics* **113**, 1794–1801 (2015).

292. Yang, Y., Kushima, A., Han, W., Xin, H. & Li, J. Liquid-Like, Self-Healing Aluminum Oxide during Deformation at Room Temperature. *Nano Lett.* **18**, 2492–2497 (2018).

293. Tan, E., Mather, P. G., Perrella, A. C., Read, J. C. & Buhrman, R. A. Oxygen stoichiometry and instability in aluminum oxide tunnel barrier layers. *Phys. Rev. B* **71**, 161401 (2005).

294. Bobzin, K., Bagcivan, N., Reinholdt, A. & Ewering, M. Thermal stability of γ-Al2O3 coatings for challenging cutting operations. *Surface and Coatings Technology* **205**, 1444–1448 (2010).

295. Shih, T.-S. & Liu, Z.-B. Thermally-Formed Oxide on Aluminum and Magnesium. *Materials Transactions* **47**, 1347–1353 (2006).

296. Cai, N., Zhou, G., Müller, K. & Starr, D. E. Temperature and pressure dependent Mott potentials and their influence on self-limiting oxide film growth. *Appl. Phys. Lett.* **101**, 171605 (2012).

297. Moon, H., Cho, S. K., Garrell, R. L. & Kim, C.-J. "CJ". Low voltage electrowetting-on-dielectric. *Journal of Applied Physics* **92**, 4080–4087 (2002).

298. Pan, S. *et al.* Kinetics and dynamics of surface thermal oxidation in Al-ZrB2 nanocomposites. *Corrosion Science* **176**, 108890 (2020).

299. Li, M., Wiame, F., Seyeux, A., Marcus, P. & Światowska, J. Effect of thermal oxidation on surface chemistry and elemental segregation of Al-Cu-Li alloy. *Applied Surface Science* **534**, 147633 (2020).

300. Zhang, Y., Ma, G.-R., Zhang, X.-C., Li, S. & Tu, S.-T. Thermal oxidation of Ti-6Al–4V alloy and pure titanium under external bending strain: Experiment and modelling. *Corrosion Science* **122**, 61–73 (2017).

301. Xia, J., Li, C. X., Dong, H. & Bell, T. Nanoindentation and nanoscratch of a thermal oxide layer on a FeAl alloy. *J. Mater. Res.* **19**, 10 (2004).

302. Dong, X., Youssef, H., Zhang, Y., Wang, S. & Ji, S. High performance Al/TiB2 composites fabricated by nanoparticle reinforcement and cutting-edge super vacuum assisted die casting process. *Composites Part B: Engineering* **177**, 107453 (2019).

303. Mansfeld, F., Wang, Y., Lin, S., Xiao, H. & Shih, H. Detection and Monitoring of Localized Corrosion by EIS. in *Electrochemical Impedance: Analysis and Interpretation* (eds. Scully, J., Silverman, D. & Kendig, M.) 297-297–16 (ASTM International, 1993). doi:10.1520/STP18076S.

304. Singh, S. S., Loza, J. J., Merkle, A. P. & Chawla, N. Three dimensional microstructural characterization of nanoscale precipitates in AA7075-T651 by focused ion beam (FIB) tomography. *Materials Characterization* **118**, 102–111 (2016).

305. Dey, S., Gunjan, M. K. & Chattoraj, I. Effect of temper on the distribution of pits in AA7075 alloys. *Corrosion Science* **50**, 2895–2901 (2008).

306. Kosari, A. *et al.* In-situ nanoscopic observations of dealloying-driven local corrosion from surface initiation to in-depth propagation. *Corrosion Science* **177**, 108912 (2020).

307. Osaki S. *et al.* Mechanical and SCC properties of rheocast 7075 based aluminum alloys. *J. Japan Inst. Light Metals* **55**, 27–32 (2005).

308. Fooladfar, H., Hashemi, B. & Younesi, M. The Effect of the Surface Treating and High-Temperature Aging on the Strength and SCC Susceptibility of 7075 Aluminum Alloy. *J. of Materi Eng and Perform* **19**, 852–859 (2010).

309. Jin, P., Liu, Y., Li, F., Li, J. & Sun, Q. Realization of structural evolution in grain boundary, solute redistribution and improved mechanical properties by adding TiCnps in wire and arc additive manufacturing 2219 aluminium alloy. *Journal of Materials Research and Technology* **11**, 834–848 (2021).

310. Ajay Krishnan, M., Raja, V. S., Shukla, S. & Vaidya, S. M. Mitigating Intergranular Stress Corrosion Cracking in Age-Hardenable Al-Zn-Mg-Cu Alloys. *Metall Mater Trans A* **49**, 2487–2498 (2018).

311. Pardoen, T., Dumont, D., Deschamps, A. & Brechet, Y. Grain boundary versus transgranular ductile failure. *Journal of the Mechanics and Physics of Solids* **51**, 637–665 (2003).

312. Yao, L. *et al.* Remarkable synergistic effects of Mg2NiH4 and transition metal carbides (TiC, ZrC, WC) on enhancing the hydrogen storage properties of MgH2. *International Journal of Hydrogen Energy* **45**, 6765–6779 (2020).

313. Bakkar, A., Ahmed, M. M. Z., Alsaleh, N. A., Seleman, M. M. E.-S. & Ataya, S. Microstructure, wear, and corrosion characterization of high TiC content Inconel 625 matrix composites. *Journal of Materials Research and Technology* **8**, 1102–1110 (2019).

314. Lin, J.-C., Liao, H.-L., Jehng, W.-D., Chang, C.-H. & Lee, S.-L. Effect of heat treatments on the tensile strength and SCC-resistance of AA7050 in an alkaline saline solution. *Corrosion Science* **48**, 3139–3156 (2006).

315. Yuan, J., Pan, S., Zheng, T. & Li, X. Nanoparticle promoted solution treatment by reducing segregation in AA7034. *Materials Science and Engineering: A* 141691 (2021) doi:10.1016/j.msea.2021.141691.

316. Shrivastava, V., Gupta, G. K. & Singh, I. B. Heat treatment effect on the microstructure and corrosion behavior of Al-6061 alloy with influence of α-nanoalumina reinforcement in 3.5% NaCl solution. *Journal of Alloys and Compounds* **775**, 628–638 (2019).

317. Quiambao, K. F. *et al.* Passivation of a corrosion resistant high entropy alloy in non-oxidizing sulfate solutions. *Acta Materialia* **164**, 362–376 (2019).

318. Karbalaei Akbari, M., Rajabi, S., Shirvanimoghaddam, K. & Baharvandi, H. Wear and friction behavior of nanosized and TiO2 particle-reinforced casting A356 aluminum nanocomposites: A comparative study focusing on particle capture in matrix. *Journal of Composite Materials* **49**, 3665–3681 (2015).

319. Xu, M. *et al.* A low-profile wall shear comparator to mount and test surface samples. *Exp Fluids* **61**, 82 (2020).

320. Mo, Y. & Szlufarska, I. Roughness picture of friction in dry nanoscale contacts. *Phys. Rev. B* **81**, 035405 (2010).

321. Xu, M. *et al.* Superhydrophobic Drag Reduction for Turbulent Flows in Open Water. *Phys. Rev. Applied* **13**, 034056 (2020).

322. Goto, H. & Buckley, D. H. The influence of water vapour in air on the friction behaviour of pure metals during fretting. *Tribology International* **18**, 237–245 (1985).

323. Zeng, G., Tan, C.-K., Tansu, N. & Krick, B. A. Ultralow wear of gallium nitride. *Appl. Phys. Lett.* **109**, 051602 (2016).

324. Knowles, G. D. Mechanisms of wear particle formation and detachment. (University of British Columbia, 1994). doi:10.14288/1.0080930.

325. Rao, V. R., Ramanaiah, N. & Sarcar, M. M. M. Dry Sliding Wear Behavior of TiC – AA7075 Metal Matrix Composites. *Int. J. Appl. Sci. Eng.* **14**, 27–37 (2016).

326. Baradeswaran, A. & Elaya Perumal, A. Study on mechanical and wear properties of Al 7075/Al2O3/graphite hybrid composites. *Composites Part B: Engineering* **56**, 464–471 (2014).

327. Ramkumar, K. R., Sivasankaran, S., Al-Mufadi, F. A., Siddharth, S. & Raghu, R. Investigations on microstructure, mechanical, and tribological behaviour of AA 7075–xwt.% TiC composites for aerospace applications. *Archives of Civil and Mechanical Engineering* **19**, 428–438 (2019).

328. Ayyanar Raja, M., Manikandan, V., Amuthakkannan, P., Rajesh, S. & Balasubramanian, I. Wear resistance of basalt particulate-reinforced stir-cast Al7075 metal matrix composites. *J Aust Ceram Soc* **54**, 119–128 (2018).

329. Kumar, B. M. S. & Girish, D. P. Friction and Wear Behaviour of Tungsten Carbide and E Glass Fibre reinforced Al7075 based Hybrid composites. *IOP Conf. Ser.: Mater. Sci. Eng.* **390**, 012002 (2018).

330. Niederberger, S., Gracias, D. H., Komvopoulos, K. & Somorjai, G. A. Transitions from nanoscale to microscale dynamic friction mechanisms on polyethylene and silicon surfaces. *Journal of Applied Physics* **87**, 3143–3150 (2000).

331. Dedkov, G. V. Friction on the nanoscale: new physical mechanisms. *Materials Letters* **38**, 360–366 (1999).

332. Menezes, P. L., Kishore & Kailas, S. V. On the effect of surface texture on friction and transfer layer formation—A study using Al and steel pair. *Wear* **265**, 1655–1669 (2008).

333. Muhammad Nuruzzaman, D. & Asaduzzaman Chowdhury, M. Effect of Load and Sliding Velocity on Friction Coefficient of Aluminum Sliding Against Different Pin Materials. *American Journal of Materials Science* **2**, 26–31 (2012).

334. Jordan, L. R., Betts, A. J., Dahm, K. L., Dearnley, P. A. & Wright, G. A. Corrosion and passivation mechanism of chromium diboride coatings on stainless steel. *Corrosion Science* **47**, 1085–1096 (2005).

335. Monticelli, C., Bellosi, A. & Colle, M. D. Electrochemical Behavior of ZrB2 in Aqueous Solutions. *J. Electrochem. Soc.* **151**, B331 (2004).

336. Nguyentran, L., Sin, K., Hong, J., Pizzo, P. P. & Wang, S. X. Corrosion resistance of low coercivity, high moment FeXN (X=Rh, Mo) thin film head materials. *IEEE Transactions on Magnetics* **33**, 2848–2850 (1997).